Orbit Determination Design for a Lunar Navigation System

MSc Thesis

Enrique Lara Moreno

Delft University of Technology

TU Delft

gmv

Orbit Determination Design for a Lunar Navigation System

by

Enrique Lara Moreno

to obtain the degree of Master of Science in Aerospace Engineering

at the Delft University of Technology,

to be defended publicly on Tuesday, September 10, 2024, at 14:00.

Student number:	5838029	
Project duration:	December 1, 2023 – August 13, 2024	
Thesis committee:	Dr. *ir.* JG. De Teixeira da Encarnacao,	TU Delft, Supervisor
	Dr. *ir.* E. Mooij,	TU Delft, Chair
	Dr. S. Gehly,	TU Delft, Examiner
	Ir. J. Berzosa Molina,	GMV, Examiner

Cover: ©ESA (Modified)

An electronic version of this thesis is available at `http://repository.tudelft.nl/`.

TU Delft

Preface

My internship in the Mission Analysis and Studies section of GMV was a fulfilling experience and showed me the involvement of the company with its interns. As a result, I decided to do my thesis in the company helped by my colleages in the Precise Orbit Determination section. This thesis is the final product of 8 months of hard work and intense learning. Many people has been by my side during these lengthy process. I would like to dedicate some words of acknowledgement to all of them.

I want to express my profuse gratitude to my supervisor Joao De Teixeira da Encarnacao, who has guided me along this journey. He is responsible for the scientific rigor of this thesis, which has been one of the most difficult things to ensure. I would also like to thank him for his patience and his good will in answering my doubts, which have been more than a few.

On the side of GMV, I would like to thank the Precise Orbit Determination team for their every-day assistance and for making the development of this thesis a much more enjoyable experience. A special mention goes to Javier Berzosa Molina, my supervisor in GMV, who has dedicated great deals of time and effort in helping me during this months, more than I would like to acknowledge. His commitment has been decisive in making the thesis as it is.

I want to dedicate this thesis to my family, for their endless support and their trust in my achievements, in the good and, especially, in the bad times. I could not have gotten here without them.

Lastly, I want to wholeheartedly thank my friends, those here in Madrid, who have brightened up the scarce leisure time during these months, and those I met in Delft, who will always be my best memory of my stay abroad.

Enrique Lara Moreno
Madrid, August 2024

Abstract

Recent years have seen an increasing interest in the Moon, both due to scientific and economic reasons, with a special focus on its South Pole. The consequent large volume of lunar missions forecasted for the coming years exposes the need for reliable Positioning, Navigation and Timing (PNT) services for spacecraft orbiting the Moon or moving across its surface. This thesis assesses the design of the Orbit Determination (OD) system for a Lunar Navigation System (LNS) based on satellites in elliptical lunar orbits tracked from a network of stations on the Earth's surface. The objective is to achieve an OD system that meets the current requirements imposed by several space agencies in terms of accuracy. The thesis also explores the relation between the system average OD accuracy and the positioning accuracy of a user in the lunar South Pole.

As a first step in the design, the relevance of the different parameters affecting the quality of the OD solution is evaluated. This aims to find a reduced group of design parameters that drive the accuracy of the OD system, which is found to be the parameters of the orbit propagation (degree and order of the lunar Spherical Harmonic (SH) and integrator tolerance) and the estimation arc length. The design continues with a more detailed analysis to characterize the relation between these 3 parameters and the system's accuracy for a total of 6 cases of interest. The cases consist of 3 orbit configurations—the most frequent configuration found in the literature, the configuration with the best user performance, and the most demanding configuration for the OD—at 2 noise levels of the tracking observations—a conservative, nominal level, and a more modern, reduced level. The outcome of this analysis is a set of recommended values for the design parameters to produce a computationally cheap OD solution that meets the requirement of 2 m in the average accuracy for each of the cases of interest. The common recommendation for all cases is using a network of 3 ground stations with constant visibility of the lunar orbits, tracking at a minimum elevation of 15° with observations every 5 minutes, and a prediction arc in the range 6–24 h. The recommended values for the accuracy drivers are different in each case, but are in the range of 14–83 for the degree and order of the lunar SH, 1.2×10^{-9}–1.6×10^{-8} for the integrator tolerance, and 0.68–1.3 d for the estimation arc length. A comparison between the recommendations for each case reveals that the choice of orbit configuration is decisive for the design of the OD system, being the unique factor in determining the degree and order of the lunar SH and inducing variations of one order of magnitude in the integrator tolerance. It is also found that an 80% reduction in observational noise entails an approximate 20–30% reduction in the required length of the estimation arc and a 40–60% increase in the required integrator tolerance. The lower noise level requires a shorter estimation arc to mitigate the effect of the noise. The shorter integration interval increases the required integrator tolerance for a certain propagation accuracy. Lastly, the results show a correlation coefficient above 0.78 between the average OD accuracy of the satellites in the system and the user positioning error for all the cases of interest.

Future continuations of the work developed in this thesis are the use of more advanced observational noise modeling techniques, the analysis of the impact of data gaps on the system's performance, and the update of the design with new information about the final orbit configuration and observation properties of the future LNSs.

Contents

List of Figures

List of Tables

Nomenclature

Satellite properties		
m_i	Mass of the i-th satellite	[kg]
$A_{\text{body},i}$	SRP effective cross-sectional area of the i-th satellite's body	[m^2]
$C_{\text{r},i}$	Reflectivity coefficient of the i-th satellite's body	[–]
$A_{\text{panel},i}$	SRP effective area of the i-th satellite's solar panels	[m^2]
$C_{\text{s},i}$	Specular reflection coefficient of the i-th satellite's solar panels	[–]
$C_{\text{d},i}$	Diffusive reflection coefficient of the i-th satellite's solar panels	[–]
Constellation properties		
N_{s}	Number of satellites in the constellation	[–]
$\mathbf{x}_{0,i}$	Initial state of the i-th satellite	[km, km s^{-1}]
a	Semi-major axis of the orbit	[km]
e	Eccentricity of the orbit	[–]
i	Inclination of the orbit	[°]
Ω	RAAN of the orbit	[°]
ω	Argument of pericenter of the orbit	[°]
M	Mean anomaly of the orbit	[°]
Ω_0	RAAN offset; RAAN of the constellation's first orbital plane	[°]
$\Delta\Omega$	RAAN difference; separation in RAAN between the constellation's orbital planes	[°]
Environment properties		
DO_{b}	Maximum degree and order of the SH gravitational potential of the celestial body b	[–]
P_{S}	Mean solar radiation pressure at 1 au	[Pa]
Propagation setup parameters		
t_{ref}	Reference epoch of propagation	[–]
tol	Relative tolerance of the numerical integration	[–]
Ground station properties		
N_{GS}	Number of ground stations	[–]
$\mathbf{x}_k$	State of ground station k at any epoch	[km, km s^{-1}]
$e_{\text{min},k}$	Minimum elevation for the tracking links of ground station k	[°]

Observation properties		
T_{obs}	Time step between consecutive observations of the same station	[s]
f_{signal}	Frequency of the radio signal	[GHz]
σ_{ran}	Standard deviation of the white noise affecting range observations	[m]
σ_{dop}	Standard deviation of the white noise affecting Doppler observations	[m s^{-1}]
b_{ran}	Bias affecting range observations	[m]
b_{dop}	Bias affecting Doppler observations	[m s^{-1}]
$\Delta t_{\text{T},i}$	Delay introduced by the i-th satellite's transponder	[s]
Observation properties		
T_{ran}	Ambiguity of range observations	[s]
T_{dop}	Integration time of Doppler observations	[s]
b_{TEC}	Bias of the ionospheric TEC model	[TECU]
σ_{TEC}	Standard deviation of the ionospheric TEC model	[TECU]
Meteorological data		
T_k	Atmospheric temperature at ground station k at any epoch	[K]
P_k	Atmospheric pressure at ground station k at any epoch	[hPa]
RH_k	Atmospheric relative humidity at ground station k at any epoch	[%]
σ_T	Uncertainty of temperature measurements	[K]
σ_P	Uncertainty of pressure measurements	[hPa]
σ_{RH}	Uncertainty of relative humidity measurements	[%]
OD parameters		
T_{est}	Length of the estimation arc	[d]
T_{pred}	Length of the prediction arc	[h]
$\mathbf{x}_{\text{est}}$	Vector of solve-for or estimated parameters	[*]
σ_{pos}	Standard deviation of the first guess of the position components of the satellites' initial states	[m]
σ_{vel}	Standard deviation of the first guess of the velocity components of the satellites' initial states	[mm s^{-1}]
$\sigma_{C_{\text{r}}}$	Standard deviation of the first guess of the satellite body's reflectivity coefficient	[–]
$\sigma_{C_{\text{s}}}$	Standard deviation of the first guess of the satellite panels' specular reflection coefficient	[–]
$\sigma_{C_{\text{d}}}$	Standard deviation of the first guess of the satellite panels' diffusive reflection coefficient	[–]
w_{ran}	Weight of range observations	[µm]
w_{dop}	Weight of Doppler observations	[nm s^{-1}]
w_l	Weight of estimated parameter l	[*]
Θ_{out}	Relative observation outlier threshold	[–]
Θ_{conv}	Relative convergence threshold	[–]

User data		
$\mathbf{x}_\mathrm{r}$	State of a receiver r at any epoch	[km, km s^{-1}]
$e_{\mathrm{min,r}}$	Minimum elevation for the navigation links of receiver r	[°]
Figures of Merit		
Δr_i	3D position error of the OD of the i-th satellite at any epoch	[m]
$\overline{\mathrm{RMSE}}_{\mathrm{pos}}$	Inter-satellite mean position Root Mean Square Error	[m]
$\Delta r_{\mathrm{r,RMS}}$	Root Mean Square user positioning error	[m]
$\mathrm{PDOP}_{\mathrm{RMS}}$	Root Mean Square Position Dilution Of Precision	[–]
ξ	Fraction of the constellation's period with 3-fold coverage	[–]

Acronyms

AMFIN Advanced Modular Facility for Interplanetary Navigation.

CAD Computer-Aided Design.

CDM Code Division Multiplexing.

CDMA Code Division Multiple Access.

CoM Center of Mass.

CR3BP Circular Restricted 3-Body Problem.

CSA Canada Space Agency.

DE Developmental Ephemeris.

DE 421 Develomental Ephemeris 421.

DE 440/441 Developmental Ephemeris 440/441.

DOP Dilution Of Precision.

DRO Distant Retrograde Orbit.

DSA Deep Space Antenna.

DSN Deep Space Network.

ECOM Extended CODE Orbit Model.

EKF Extended Kalman Filter.

ELFO Elliptical Lunar Frozen Orbit.

EM Earth-Moon.

EME2000 Earth Mean Equator and Equinox of J2000.

EoM Equation of Motion.

EOP Earth Orientation Parameter.

ESA European Space Agency.

ESOC European Space Operations Center.

FoM Figure of Merit.

GDOP Geometric Dilution Of Precision.

GENEOS GEneral Navigation for Earth Orbiting Satellites.

GMV *Grupo Mecánica del Vuelo*.

GNSS Global Navigation Satellite System.

GODOT General Orbit Determination and Optimisation Toolkit.

GPS Global Positioning System.

GPST Global Positioning System Time.

GRAIL Gravity Recovery And Internal Laboratory.

GSO Geosynchronous Orbit.

GST Galileo System Time.

HDOP Horizontal Dilution Of Precision.

IAU International Astronomical Union.

ICRF International Celestial Reference Frame.

ILRS International Laser Ranging Service.

IPF InterPolation File.

IR Infra-Red.

ISL Inter-Satellite Link.

ISRU In Situ Resource Utilization.

ITRF International Terrestrial Reference Frame.

ITRS International Terrestrial Reference System.

JAXA Japanese Aerospace Exploration Agency.

JPL Jet Propulsion Laboratory.

JSON JavaScript Object Notation.

LCNS Lunar Communications and Navigation Service.

LCO Lunar Circular Orbit.

LCRNS Lunar Communication Relay and Navigation Systems.

LEO Low Earth Orbit.

LLO Low Lunar Orbit.

LLR Lunar Laser Ranging.

LNS Lunar Navigation System.

LNSS Lunar Navigation Satellite System.

LP Lunar Pathfinder.

LPO Lagrange Point Orbit.

LRO Lunar Reconnaissance Orbiter.

LRT Lunar Reference Time.

LS Least-Squares.

LSP Lunar South Pole.

LuGRE Lunar GNSS Receiver Experiment.

MAORI Multi-purpose Advanced Orbit Restitution Infrastructure.

MC Monte Carlo.

MEIAUE Moon Mean Equator and IAU-Node of Epoch.

MEO Medium Earth Orbit.

MEPA Mean Earth Polar Axis.

MEPME Moon Mean Equator and Prime Meridian of Epoch.

MER Mean Earth/Rotation.

MSPA Multiple Spacecraft Per Antenna.

NAIF Navigation and Ancillary Information Facility.

NAPEOS NAvigation Package for Earth Orbiting Satellites.

NASA National Aeronautics and Space Administration.

NEU North-East-Up.

NRHO Near Rectilinear Halo Orbit.

NTCM-GL GLobal Neustrelitz Total electron Content Model.

OD Orbit Determination.

ODTS Orbit Determination and Time Synchonization.

OEM Orbit Ephemeris Message.

OOP Object Oriented Programming.

Orekit Orbit Extrapolation KIT.

PA Principal Axes.

PCO Prograde Circular Orbit.

PDF Probability Density Function.

PDOP Position Dilution Of Precision.

PDS Planetary Data System.

PNT Positioning, Navigation and Timing.

PPN Parameterized Post-Newtonian.

PSR Permanently Shadowed Region.

RAAN Right Ascension of the Ascending Node.

RBF Radial Basis Function.

RF Radio Frequency.

RK Runge-Kutta.

RMS Root Mean Square.

RMSE Root Mean Square Error.

RNG Random Number Generator.

SBI Same Beam Interferometry.

SCO Selenocentric Orbit.

SH Spherical Harmonic.

SHA Spherical Harmonic ASCII.

SISE Signal-In-Space Error.

SLA Satellite Laser Antenna.

SLR Satellite Laser Ranging.

SoI Sphere of Influence.

SPICE Spacecraft, Planet, Instrument, C-matrix, Events.

SRIF Square Root Information Filter.

SRP Solar Radiation Pressure.

SSB Solar System Barycenter.

SWaP Size, Weight and Power.

TBP Third-Body Perturbation.

TCB Barycentric Coordinate Time.

TDB Barycentric Dynamical Time.

TEC Total Electron Content.

TECU Total Electron Content Unit.

TLI Trans-Lunar Injection.

TS Time Synchronization.

TT Time Transfer.

TT&C Telemetry, Tracking & Command.

TUD *Technische Universiteit Delft*.

Tudat TU Delft Astrodynamics Toolbox.

VDOP Vertical Dilution Of Precision.

VLBI Very Long Baseline Interferometry.

WLS Weighted Least Squares.

1

Introduction

Over the course of the past few years, a renewed interest in the exploration of the Moon has arisen, resulting in a burst of widely varied space missions focused on it—more than 250 lunar missions with different origins and scopes are planned for this decade [1]. The Moon is envisioned as the first step in humanity's coordinated deep space exploration road map, with intentions of progressing from initial robotic and human exploration missions to permanent settlements and resource exploitation [2]. In the context of such road map, several agencies have established their own lunar program: NASA's Artemis program [3], ESA's Argonaut [4], ISRO's Chandrayaan program and CNSA's Chinese Lunar Exploration Program.

A region of the Moon's surface that has aroused a special interest is its South Pole, due to evidence pointing to the possible presence of water on the region. Due to the Moon's orbital characteristics—a low obliquity (angle between orbit normal and body's spin axis) in combination with a similarly low orbital inclination with respect to the ecliptic—, the maximum solar declination experienced by it is only a rough 1.5°. This, together with the characteristically irregular lunar topography dominated by impact craters, results in the presence of bounded polar areas which are never in direct illumination from the Sun, named Permanently Shadowed Regions (PSRs) [5]. The spectroscopic analysis of measurements obtained from the lunar polar regions (bands within 20° from the poles), and, more specifically, from PSRs, shows absorption features consistent with those of cold-trapped water ice [6][7]. The existence of ice has been identified as a key to In Situ Resource Utilization (ISRU), a strategy that would bolster both human exploration and commercial use of the Moon by reducing the costs and risks involved [8]. An additional feature of interest of the polar regions is the presence of areas of high solar illumination [9], which are attractive sites for surface power generation.

The scientific and commercial enthusiasm for our moon, and the consequent increase in the number of planned lunar missions, has exposed the need for a solid support infrastructure for space vehicles in lunar orbit and surface. As a response to this, and through the collaboration of NASA, ESA, JAXA and CSA, the creation of Gateway is planned. The Gateway is a lunar space station aimed at logistically assisting future lunar missions in aspects such as resupply, scientific research, and communications [10][11]. Another identified necessity is a reliable Positioning, Navigation and Timing (PNT) service. The supply of accurate and robust lunar PNT

would, among other benefits, enhance the ability to precisely maneuver the spacecraft—including precision landing [12]—and to perform consequent surface operations (if any) [13]. These are critical elements in meeting the safety standards required for human presence on the Moon, one key short-term step in the space exploration roadmap [2]. It could also serve to support exploration missions and new lunar activities, such as the mining of resources [14].

1.1. Lunar PNT

Positioning, Navigation and Timing are three capabilities that are usually supplied jointly by *navigation systems*. *Positioning* refers to the ability of a system to know its own position in space. *Navigation* is a system's ability to determine its current and desired position, as well as to adopt the appropriate course to go from the former to the latter. Finally, *timing* is the ability to accurately and precisely maintain a time standard. A navigation system constitutes the necessary infrastructure for a user system to perform these 3 activities. So-called Global Navigation Satellite Systems (GNSSs) have been developed to globally supply these capabilities on Earth.

For this thesis, the concept of *Lunar Navigation System (LNS)* is introduced as a navigation system intended to provide PNT capabilities to users at "lunar altitudes", meaning both on the lunar surface and in-orbit around the Moon. Its implementation is considered to rely on a constellation of satellites that conveys the navigation information to the users by means of a navigation message. Although the implementation does not need to be like this, it is logical that it resembles GNSSs, as it allows a greater technology reusability. Further details on the proposed implementation are found in Chapter 2.

1.2. Satellite constellations for lunar navigation systems

In the context of LNSs, many orbits are considered for the implementation of the system's space segment. GNSS-like constellations, which enjoy a well-developed literature in their regard, are not considered central to this thesis due to the limitations stated in § 2.2.1. Therefore, the focus is put on other types of constellations more suitable for the implementation of a LNS. The orbit types of interest can be classified into two groups: Lagrange Point Orbits (LPOs) and Selenocentric Orbits (SCOs).

LPOs are defined as orbits about any of the Lagrange points of the Circular Restricted 3-Body Problem (CR3BP), in this case, corresponding to the Earth-Moon (EM) system. This group encapsulates numerous orbit families [15], which have extensive literature dedicated to them as well. The concept of an in-orbit relay architecture for the support of lunar missions was first introduced by Farquhar in 1967 [16], proposing the use of a satellite in a halo orbit about the EM L_2 point. Although the original motivation for the idea came from dealing with the telecommunication constraints on the lunar far-side, it was concluded that the proposed configuration could also be used for tracking purposes.

The informal term "Selenocentric Orbit" used in this thesis encompasses all trajectories which apparently orbit around the Moon. This includes both true selenocentric orbits—those that can be studied as keplerian motion about the Moon with added perturbations—and orbits defined in the EM 3-body problem—displaying extremely different behaviors to Keplerian motion. Thus, there is overlap between the definitions of SCO and LPO. For the purpose of this thesis, the orbits contained in this overlap are considered to be SCOs, due to their more similar behavior in the context of LNSs. Generally, four types of SCOs are related to LNSs.

- *Elliptical Lunar Frozen Orbit (ELFO).* The term "frozen" refers to the fact that this type of orbit ideally maintains a (nearly) constant eccentricity and argument of pericenter, on average, by exploiting the perturbation created either by the Earth's gravitational attraction (at high altitudes) or by the lunar zonal harmonics (at low altitudes). To achieve this, the value of the argument of pericenter is fixed and a relation between the inclination and the eccentricity is established [17]. Mention to inclined elliptical orbits can be found in early studies for the development of a lunar communications relay system to improve the satellite visibility from the lunar poles [18].
- *Near Rectilinear Halo Orbit (NRHO).* NRHOs are described in the EM CR3BP as a subset of the halo orbits about the L_1 and L_2 points [19]. They are stable or nearly linearly stable and show orbital periods shorter than those of other halo orbits about the respective Lagrange point [15]. In particular, L_2 NRHOs have received the most attention for navigation satellites.
- *Lunar Circular Orbit (LCO).* LCOs refer to a generic category encompassing a variety of orbits for which there is no formal definition. In the context of LNSs, LCOs include circular orbits up to a few thousands of kilometers [20], thus containing Low Lunar Orbits (LLOs) among others. The dominating perturbation with respect to the pure Keplerian motion is, similarly to ELFOs, either the non-sphericity of the lunar gravitational field at low altitudes or the Earth's gravitational pull at high altitudes.
- *Distant Retrograde Orbit (DRO).* Defined in the context of the CR3BP, the DROs are a family of orbits contained in the plane of the Moon's orbit around Earth and symmetric about the rotating EM direction. They range from near-circular low-altitude trajectories to high-altitude trajectories (even enclosing the EM L_4 and L_5 points) with decreasing values of the Jacobi constant[1]. They were identified in 1935 [21] and better characterized in 1968 [22].

Apart from these orbits, other types are sometimes referenced in literature concerning LNSs. An example of this are Prograde Circular Orbits (PCOs), which, although mentioned recurrently in the literature, do not show a closed definition [23][24].

1.3. Orbit Determination and Time Synchronization

Any navigation system supplies PNT capabilities through observations. All observables[2] in this context are relative magnitudes (e.g., distances or rates at which the distance changes) with respect to a reference. Said reference is a quantity/quantities of the system used for the production of the observations (e.g., its position, velocity, or spatial orientation) and locates the observations in space-time. Thus, the user needs to have knowledge of the LNS satellites' positions, velocities, and clocks to handle the observations. These pieces of information are conveyed by the navigation message in the form of satellite ephemerides and parameters of a clock model.

The Orbit Determination and Time Synchonization (ODTS) system is one of the fundamental elements of any navigation system. Its objective is to generate estimates of the navigation data to be included in the broadcast navigation message. The error associated to these estimates directly relates to the error of the user's navigation solution, and, thus, the needed navigation accuracy drives the ODTS accuracy requirements.

[1] The Jacobi constant, in the context of the CR3BP, is a representation of the orbit's energy in the rotating sidereal frame. An increase in the Jacobi constant transforms linearly into a decrease in orbital energy and vice versa.

[2] An observable is a measurable parameter of a system. An observation is a measurement of an observable.

Orbit Determination (OD)

The ODTS process consists of two tasks: Orbit Determination (OD) and Time Synchronization (TS). OD, in the context of navigation systems, aims at estimating the current orbits of the navigation satellites so that navigation receivers can predict them at future epochs. Due to the large computational load involved in accurate OD, for GNSSs, this task is preferably performed on the ground, and its product is later sent to the satellites. There are three main components of the OD process: the spacecraft's dynamic model, the reconstruction of the tracking observations, and the parameter estimation.

The dynamic models are used to propagate in time the spacecraft's state based on a priori knowledge of the accelerations acting on it. The models must be complex enough to faithfully recreate the pertinent accelerations, but not excessively complex to avoid unnecessarily increasing the computational cost. The impact that distinct phenomena have on the motion of a spacecraft depends on a diversity of factors, and, thus, each specific problem requires a tailored analysis to determine their relative relevance. Once the dynamic environment of a satellite is characterized, its motion can be integrated in time by means of analytical or, more frequently, numerical methods.

Tracking observations can be used to estimate the orbit based on measurements. To do so, the observations need to be reconstructed using models together with an a priori orbit, and compared to the actual value of the measurement. All types of observations are subject to errors. In the context of ODTS, most observations are realized as measurements of a time interval, leading to these errors being also known as *delays*. These delays cause the deviation of the observed quantity (time interval) from the real value of the desired observable (e.g., range). Therefore, the various sources of delay must be considered when reconstructing the observations to produce an accurate OD.

Finally, parameter estimation methods merge the information contributed by the dynamic model and the observations to statistically estimate a set of parameters that best represent the spacecraft's orbit. These parameters can be an initial value of the state in dynamic processes or an epoch-wise state in kinematic processes. In this estimation, the deficient knowledge of both dynamic and observation models is partially compensated, increasing the achievable OD accuracy.

Time Synchronization (TS)

Parallelly to OD, TS seeks establishing and maintaining an estimate of the state of a clock with respect to either a reference time or to another clock. The adherence of the satellite system to a synchronized time is fundamental not only to supply timing services, but navigation through pseudo-range observations as well, as they depend on the difference between the transmitter's and receiver's clocks. This requires the definition of a reference time scale for the LNS. A first strategy to ensure synchronization could be to steer the onboard clock to keep it close to said time scale within the needed accuracy. This strategy is undesirable due to the high effort required for its implementation, and unnecessary in most situations. A more popular option is to model the deviation of the on-board, free-running clock with respect to the reference time scale using a parametrized function (usually polynomials). The application of this model can then be used to estimate the clock state at any epoch.

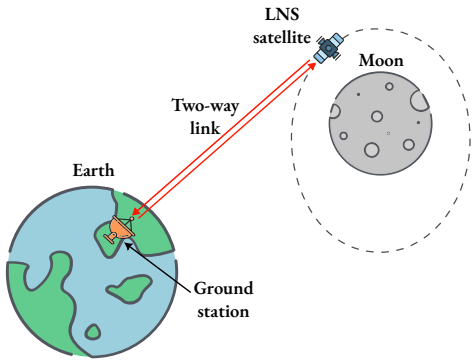

Figure 1.1: Two-way link between a ground station on Earth and a LNS satellite.

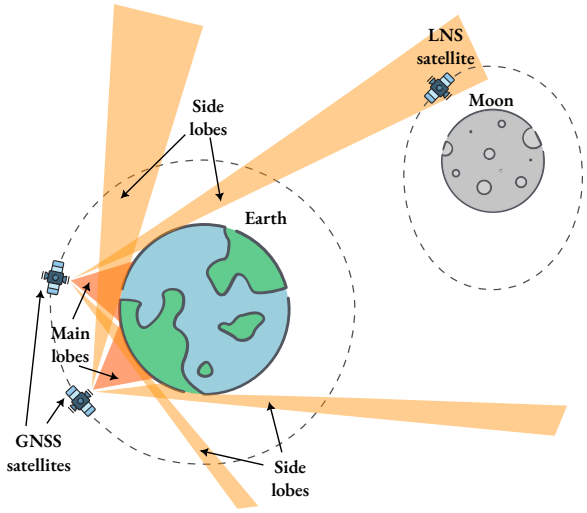

Figure 1.2: Use of existing GNSSs for tracking a LNS satellite.

1.4. Tracking methods for lunar navigation satellites

There is a diversity of tracking options for the navigation satellites of a LNS. They can be categorized in two groups:

- from Earth or terrestrial orbit: Radio Frequency (RF) for Telemetry, Tracking & Command (TT&C), terrestrial GNSS, Satellite Laser Ranging (SLR) and Very Long Baseline Interferometry (VLBI);
- from Moon or lunar orbit: Inter-Satellite Link (ISL), LLO receivers and surface beacons.

All statements in this section are derived from [25], unless otherwise stated.

Radio Frequency for TT&C

The most well-established means of tracking spacecraft beyond Earth orbit is the use of RF, known as radiometric tracking. This technique proposes the use of the communication link for TT&C purposes to obtain two-way range and range-rate observations, as depicted in Figure 1.1. Radiometric tracking has been used for many lunar missions in the past, among which are the Apollo program missions and Lunar Reconnaissance Orbiter (LRO) [26][27].

An issue that strongly affects this method, which is shared with all other Earth-based techniques, is the poor ability to reconstruct the 3D state of a lunar vehicle from the vicinity of Earth (except for extremely high orbits). The range (or range-rate)[3] observations produced are 1D and, to reconstruct the orbit, observability in 3D is beneficial. Due to the long distance between the Earth and the Moon, which leads to small spanned angles in the celestial sphere, all range observations are almost parallel to the line joining both celestial bodies, thus only properly resolving the range along said line. As a consequence, Earth-based tracking must rely on the Moon's orbit around Earth to achieve a more complete observability of a lunar orbit, requiring a 7-day data arc for the relative geometry to have changed by 90°.

[3] As the discussion is applicable to both range and range-rate observations, only range is mentioned hereon to avoid redundancy.

This introduces the concept of Geometric Dilution Of Precision (GDOP), which can be understood as the scaling factor between the uncertainty associated with observations and the resulting uncertainty in position determination [28]. Therefore, small GDOP values are desired to reduce the uncertainty of positioning. The GDOP is defined as

$$\mathrm{GDOP} = \frac{1}{\sigma}\sqrt{\sigma_{\mathrm{E}}^2 + \sigma_{\mathrm{N}}^2 + \sigma_{\mathrm{U}}^2 + \sigma_{dt}^2}, \tag{1.1}$$

where σ is the observations' standard deviation (assumed to be unique), σ_E^2, σ_N^2 and σ_U^2 are the variances of the position estimate along the east, north and up directions, and σ_{dt}^2 is the variance of the receiver clock bias estimate. Other Dilution Of Precision (DOP) concepts can be defined: Position Dilution Of Precision (PDOP), which does not consider the clock component; Horizontal Dilution Of Precision (HDOP), which only accounts for the east and north components; and Vertical Dilution Of Precision (VDOP), which only considers the up component. DOP values are inversely related to the volume of the polyhedron formed by the transmitter-receiver unit vectors. Therefore, a better geometrical arrangement of observations entails having a more disperse distribution of navigation satellites with respect to the receiver, as it leads to a more accurate positioning solution.

GNSS

In recent years, the use of GNSS has been detached from its original restricted purpose (surface use) and expanded to space applications at both LEO and GSO altitudes [29][30]. Consequently, the idea of using a GNSS on-board receiver at lunar altitudes seems a logical following step. Using GNSSs for tracking provides both pseudo-range and range-rate observations, and shows two prominent advantages. First, the number of observational sources is large compared to other techniques—even when accounting for the highly limiting occultation by Earth due to the nadir-pointing of the antennas—, thus increasing the availability of observations. Secondly, the observations are generated by a passive system, which increases the autonomy of the lunar system by alleviating workload from ground operations. A schematic representation of this type of implementation can be observed in Figure 1.2.

Satellite Laser Ranging (SLR)

SLR is a tracking technique that consists of measuring the round-trip time of a laser pulse from a telescope on the ground to a target, which has a reflector, with a similar setup to the one in Figure 1.1. It started being used in the lunar context during the days of the Apollo missions, in which several retroreflectors were left on the lunar surface for performing Lunar Laser Ranging (LLR) that improved our knowledge of the Moon's rotation and helped to produce accurate lunar reference frames. SLR range observations are known for their low levels of residual noise. Two-way SLR tracking of a lunar orbiter has already been achieved for the LRO with a residual Root Mean Square (RMS) of approximately 3 cm [31]. Performing SLR tracking to lunar distances shows some issues, such as the required cooperation by the targeted satellite to orient its retroreflector pointing towards the station and high atmospheric stability during the laser roundtrip time.

Very Long Baseline Interferometry (VLBI)

Unlike the techniques described previously, VLBI produces direction observations relative to the baseline of stations required for the process [32]. Some scientific products regarding the lunar environment have been generated by means of VLBI, as, e.g., the gravity field studies during the SELENE mission [33]. Another existing differential method is Same Beam Interferometry (SBI). Instead of using two stations to observe a single RF source (satellite) and applying single differencing (as done with VLBI), it uses two stations to observe two different

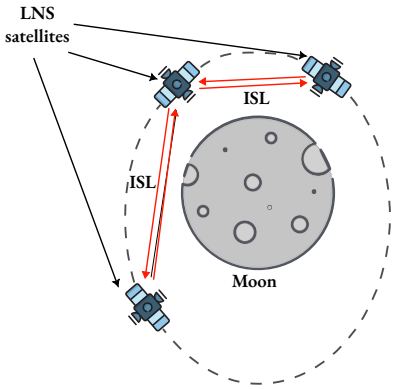

Figure 1.3: Tracking with ISL between LNS satellites.

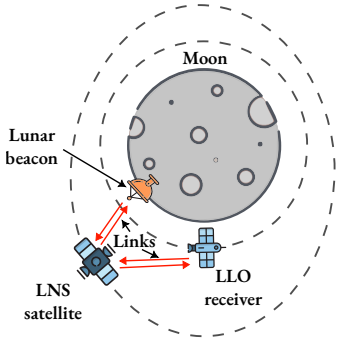

Figure 1.4: Tracking of a LNS satellite from a navigation receiver in LLO and a beacon on the lunar surface.

RF sources (satellites) and apply double differencing [34]. The benefit brought by differential approaches (either VLBI or SBI) is the compensation of errors along the line of sight, which leads to very accurate measurements. An advantage of SBI over VLBI is the compensation of the station biases as well [32]. The use of differential techniques incurs a great operational effort, as it involves at least two coordinated ground stations at a sufficient distance from each other (to increase the baseline) and a correlation center.

Inter-Satellite Link (ISL)

The ISL technique relies on the link between satellites of the LNS, as depicted in Figure 1.3, to produce observations unaffected by Earth's atmospheric effects and with better geometrical arrangements compared to observations from the proximity of Earth. Due to a lack of external reference in the production of ISL observations, it is only possible to resolve the relative position of the navigation satellites forming the constellation, while the 3 degrees of freedom associated to the rotation of the constellation as a rigid body are undetermined. Consequently, ISL requires additional types of observations to determine the absolute position of the satellites with respect to a relevant reference frame. Additionally, ISL needs a dedicated equipment, thus negatively impacting the Size, Weight and Power (SWaP).

LLO receivers and surface beacons

Another concept for the generation of tracking data from the lunar environment uses satellites in LLO carrying LNS high-quality receivers. A small network of these LLO receivers could provide continuous tracking, with a rapidly changing geometry relative to LNS satellites, if suitably distributed.

Another way to exploit the navigation service to produce observations is using stations on the lunar surface. For the OD of GNSSs, several ground stations receive and process the arriving navigation signals [35]. Similarly, a network of lunar surface stations could be used to track LNS satellites, even making use of surface missions with other primary purposes. Both of these strategies are schematically represented in Figure 1.4.

However, there are differences between surface stations on Earth and on the Moon. Firstly, the lunar surface's illumination conditions are more extreme than those found on Earth, with a lunar day being approximately 29.5 Earth days, imposing strict requirements on the power system of a station in an arbitrary surface location. Specific polar areas with high solar illumination are attractive sites for a potential station. The small size and

tight distribution of these areas impose a strict limitation on their location, and it may detrimentally impact the performed ODTS. Moreover, unlike Earth, placing an asset in lunar orbit is logistically easier than landing it on the Moon, and the replacement of a station in case of malfunction may require the same effort as placing it there for the first time.

1.5. Thesis outline

This thesis starts by explaining the motivation behind LNSs and introducing some basic ideas about this type of system. This is done in Chapter 1. Chapter 2 presents the existing programs to instantiate a LNS, along with a summary of the current proposals for the different elements of the system, such as the design of the constellation of satellites, the tracking strategy, and the approach to OD. On the basis of the first two chapters, Chapter 3 specifies the problem assessed in this thesis.

Chapter 4 describes the end-to-end simulation tool used to perform the analyses, including an explanation of the FoMs used to evaluate the OD system, the models and methods involved in the simulation, and the associated software implementation. Chapter 5 reports the verification and validation tasks performed on the simulation tool, and Chapter 6 presents the sensitivity analysis.

Chapter 7 explains the approach to the design of the OD system for a LNS, and discusses the obtained results. Lastly, Chapter 8 summarizes the conclusions of this thesis and makes suggestions to extend it in the future.

2

State of the art

To fulfill the lunar navigation necessities stated in Chapter 1, the scientific community has conducted extensive research on the different aspects involved in providing the service. The objective of this chapter is to gather and summarize the different concepts and ideas for a LNS found in literature.

2.1. Lunar navigation programs

The current supply of navigation services to lunar missions is considerably limited by factors such as occultation by the Moon, restricted observation geometry, and strong dependence on surface infrastructure. The limitations are of special criticality at the polar regions and the far side of the Moon with respect to Earth. The lunar far side, even if not as significantly as the poles, has also received some attention during the last few years, primarily for the study of its seismological, topographical and mineralogical characteristics [36][37] and the impact of meteoroids in the region [38]. Lunar surface missions planned for the short-term future define positioning accuracy requirements on the order of a few tens of meters (1σ) [39][13][12], not achievable at several polar and far side regions of interest with the current techniques [27][40]. Thus, the deep space navigation service currently used for lunar missions is deemed insufficient to meet the PNT requirements arising for the coming generation of lunar missions.

LunaNet

LunaNet has emerged as a NASA initiative in response to the emerging global need for enhanced lunar services. It is an architectural framework with the objective of establishing a comprehensive set of standards, protocols, and specifications that will allow for the interoperability of the lunar services supplied by distinct providers. The architecture is proposed to function as a network of networks, similarly to the Internet [41]. Said network is to be gradually deployed, adapting to the users' number, location and needs, as well as to the technical capabilities of the infrastructure's components, and, therefore, the architecture must account for extensibility. Another objective set for LunaNet is that users can exploit the services without detailed knowledge of the working principles of the system, as happens with terrestrial GNSS and communications [42]. Four main types of services are considered inside the framework, which are: communications, PNT, detection and information, and radio/optical science

[43]. Specific to PNT, several pivotal challenges are identified, which fall into the categories of reference systems, measurement liability, autonomy, timeliness, resource constraints, security and standards [44], which should be accounted for in the system's design.

Proposals of LNSs

The first official initiative to tackle the lunar PNT challenges is the Moonlight program by ESA. In 2020, a call for private collaboration was made in order to elaborate solutions for supplying communications and navigation services at the Moon, referred to as Lunar Communications and Navigation Service (LCNS) [45]. As a result, two independent consortia performed studies assessing business-related and technical aspects as a part of Moonlight's phase A/B1, supported by previous analyses done by the scientific community and internally at ESA [1][46]. More recently, in 2022, NASA established the Lunar Communication Relay and Navigation Systems (LCRNS) project in the context of the LunaNet framework [47]. JAXA has also shown interest in developing a Lunar Navigation Satellite System (LNSS) to support its surface missions [13]. The concepts proposed for all of these programs converge toward a similar system design, which is discussed in the following sections of this chapter.

Lunar Pathfinder (LP)

The Lunar Pathfinder (LP) mission, planned by ESA for 2025, is an early application of the enhanced lunar navigation concept. It serves as an initial step towards the implementation of the LCNS within the Moonlight initiative. One of its objectives is to provide communications and data relay to in-orbit and surface users. Additionally, it also aims at testing technologies of interest for future similar missions, such as a GNSS navigation payload to perform a position fix at lunar altitudes using weak terrestrial GNSS signals [48][49]. Finally, the LP spacecraft is intended to be the first of the LCNS constellation, and, thus, certain aspects of this mission can be used as a reference for the implementation of the final system, as mentioned in § 2.2.1.

OD requirements

The navigation systems proposed in all these programs rely on a space segment consisting of a constellation of dedicated satellites that transmit a navigation signal. The LunaNet Interoperability Specification Document [41] introduces the Signal-In-Space Error (SISE) as the metric to impose requirements on the ODTS accuracy of the LNS. The SISE is usually expressed in two parts, position and velocity SISE, which are defined as

$$\begin{aligned} \mathrm{SISE}_{\mathrm{pos}} &= \sqrt{(x-\tilde{x})^2 + (y-\tilde{y})^2 + (z-\tilde{z})^2 + (ct-c\tilde{t})^2}, \\ \mathrm{SISE}_{\mathrm{vel}} &= \sqrt{(\dot{x}-\tilde{\dot{x}})^2 + (\dot{y}-\tilde{\dot{y}})^2 + (\dot{z}-\tilde{\dot{z}})^2 + (c\dot{t}-c\tilde{\dot{t}})^2}, \end{aligned} \tag{2.1}$$

where x, y, z and t are the true position and time coordinates (with the tilde used to denote their broadcast equivalents) and c is the speed of light. Dotted parameters represent either velocities ($\dot{x}$, $\dot{y}$, $\dot{z}$) or clock drift ($\dot{t}$). With these definitions, the SISE includes orbital errors (e.g., uncertainty of ephemerides and errors in the predicted states), timing errors (e.g., inaccurate clock information and signal misalignment) and calibration errors (e.g., hardware delays and antenna offsets).

The accuracy requirement specified in terms of SISE is not unique. For Moonlight, the most recent requirement sets an allowable position SISE of 10 m (95% of time, namely, $\sim 2\sigma$) [50], with usually 40–60% of the error budget allocated for the orbital error compared to clock error in the studies performed [46][51][52]. The NASA's LCRNS Lunar Relay Services Requirements Document [53] imposes stricter requirements: 3σ 13.43 m position SISE and 3σ 1.2 mm s^{-1} velocity SISE.

2.2. Mission design

This section presents the results and recommendations produced by the literature in terms of mission design, which direct the decisions made in the development of this thesis.

2.2.1. Constellation design

The simplest system implementation in terms of infrastructure consists in using existing GNSSs. The visibility of GNSS satellites is high, with an average number of visible satellites above 10 when considering all 4 systems—Global Positioning System (GPS), Galileo, GLONASS and BeiDou—, for LPOs about the EM L_2 point [24][54]. The good visibility can also be attributed to the consideration of high-sensibility GNSS receivers [55][56] that lower the signal-to-noise ratio floor and allow the reception of GNSS side-lobe signals. Still, many shortcomings are shared with tracking from Earth's surface. Tracking a frozen orbit at low altitude is a significantly worse scenario in terms of occultation by the Moon. In that case, the visibility becomes detrimentally impacted with more than hour-long intervals of complete observational outage [57][1]. For in-orbit spacecraft, information about the dynamic behavior could be used to navigate during GNSS blackout periods [58][59], but that solution is not applicable in all conditions, e.g., a surface mission. Another remaining issue is the poor geometrical distribution of the observations. The GNSS orbits' altitude would theoretically increase the angle spanned by the measurements received by a lunar user compared to surface stations. However, due to the finite aperture of the emitter antenna gain pattern (even when considering side lobes), and the boresight being aimed along the nadir direction towards the Earth, a broad part of the signal is blocked by the Earth. Thus, the acquired advantage is not as significant. A possible solution would be to establish a dedicated GNSS-like constellation at an altitude above Geosynchronous Orbit (GSO) with pointing capabilities towards the Moon. This type of implementation could produce navigation solutions with errors of the order of tens of meters (1σ)[60], with an assumed ephemeris error of the navigation satellites of ~3 m, although it could be an underestimation [58].

The geometric and coverage limitations experienced by GNSS-based lunar navigation require a system outside Earth's vicinity. Different constellations consisting of a variety of LPOs about the EM L_1 and L_2 points have their weakest coverage performance (in terms of number of observable satellites and GDOP) close to the polar regions [61][62][63][64]. When compared to LPOs focused on polar coverage, NRHOs show the best results both in terms of visibility and station-keeping costs [15]. Thus, there is a consensus in literature that SCOs are superior to LPOs for the implementation of a system that targets the polar regions.

Table 2.1 presents a summarized comparison between the types of SCOs. The metrics used for the comparison relate to either the fitness of the orbit to implement a LNS focused on the Lunar South Pole (LSP) or the cost of reaching the orbit from Earth. This relation may not be straightforward for two of the metrics: the orbital period and the maximum altitude. The period of the orbit represents the speed with which the relative position between a satellite and the Moon (or any point on its surface) changes. A more rapidly changing geometry leads to a more varied arrangement of the observations for the same time interval and, thus, to a greater expected accuracy of the navigation solution. The orbit's altitude affects the average distance to a receiver in the lunar environment. A greater altitude, and its consequent greater distance, leads to an increased requirement in the navigation signal power.

[1] Even if this reference only considers the Galileo system, accounting for other systems would not solve the occultation issue.

Table 2.1: Comparison between different types of orbits for the LNS constellation found in literature.

	DRO	ELFO	LCO	NRHO
Orbital period	$\lesssim$10 d [66]	~24 h[67]	>2 h [67]	6-10 d [15]
Maximum altitude over lunar surface	~45000 km [20]	~15000 km [67]	100–7000 km [20]	70000 km [20]
Occultation from Earth	Few hours per orbital period [23]	<0.8% of orbital period [67]*	<40% of the orbital period [67]*	No occultation [15]
Visibility from the LSP	Significant only above $\sim -75°$ [20]	>70% of orbital period [17]**	Greatly dependent on inclination and altitude	>95% of orbital period [15]***
Station keeping ΔV cost (yearly)	1–2 m s^{-1} [68]	<25 m s^{-1} [69]*	25-150 m s^{-1} [70][71][72]	2 m s^{-1} [19][73][74][75]
TLI maneuver delta-V cost	430–560 m s^{-1} [66]	<570 m s^{-1} [76]***	~570 m s^{-1} [76]*	60–400 m s^{-1} [77][78][79]*

*Data may not be perfectly representative of the orbits considered due to a variety of factors (e.g., altitude or inclination).

**Applying a 10° elevation mask

***Applying a 0° elevation mask

Attending to the results in Table 2.1, the most suitable orbits are ELFOs and NRHOs. ELFOs perform better in regard to the orbital period and altitude, while NRHO have better visibility from the LSP and lower costs to reach them. The ELFOs are the most recurrent choice of orbit for the LNS, as shown by the proposals made for the ESA's LCNS [46][51][52], the NASA's LCRNS [65] and the JAXA's LNSS [13]. The LP, which is representative of the future LCNS implementation, is planned to orbit the Moon in an ELFO as well [49]. No definitive choice of number of navigation satellites and their exact orbital elements is given, with a variety of proposals in the literature, but an identified trend considers between 4 and 8 satellites in 2 or 3 planes. However, the most sensible and recurrent recommendation for the early instantiation of a LNS uses 4 satellites in ELFOs in 2 orbital planes. Thus, this constellation concept seems the most adequate for the development of this thesis.

2.2.2. Tracking strategies

Radiometric tracking from Earth has been the most used tracking method for lunar missions, with reported noise levels of the residuals between several tens to hundreds of meters. It exploits a communication link that is still needed for other operations—thus, not requiring additional equipment on board—, it is well-known, and it has been deemed useful by data from previous missions. A preeminent choice for TT&C frequency is X-band [80][65], as it aligns with the interoperability standards in LunaNet [41], while some earlier studies opt for the K-band [81]. The choice of one band or another seems to be a problem more related to interference and occupancy by other signals than to performance. The ODTS system concept currently adopted by ESA uses radiometric tracking as the principal source of tracking observations [82]. However, in case it may not meet the accuracy requirements for a LNS, other methods would be required to improve the solution.

Regarding other tracking techniques from Earth's vicinity, GNSSs have also been considered as sole sources of tracking for LNS satellites, achieving position errors of the order of 30–40 m [83]. Two missions are planned to demonstrate the utilization of GNSS around the Moon, Lunar Pathfinder (LP) and Lunar GNSS Receiver Experiment (LuGRE), which will test two receivers specifically designed for the weak GNSS signal at such long distances. GNSS tracking can also be used as a complement to surface radiometric tracking [80]. The use of SLR is also attractive due to the accuracy of its observations (below 3 cm residual RMS for the LRO). However, its required operational effort make it a technique more suitable for validation than for common operations [80]. Finally, recent use of VLBI and SBI for lunar OD can be traced back mainly to the Chinese space community, mostly in relation to the Chang'e missions, showing values of residual RMS <1 ns [84][85]. Differential techniques are not mentioned in literature for tracking LNS satellites, likely due to their huge required operational effort.

The lunar-based techniques introduced in § 1.4 are also considered for a LNS. ISL tracking can be used for OD with position errors <10 m, using laser ranging to the lunar surface retroreflectors or angular measurements with respect to the celestial sphere to set the absolute reference [86]. It is also proposed for future stages of a more developed LNS [52]. The use of LNS receivers, either on the surface or in-orbit, is also relegated to more advanced stages of the system implementation, probably because of the cost increase due to the inclusion of additional space elements. A proposal to use LEO receivers has been made to cope with the poor (static) observational geometry of BeiDou geostationary navigation satellites from ground stations [87]. This could be used as a demonstration of the effectiveness of this technique prior to its possible application to a LNS.

Ground segment

For the operation of (some of) these tracking techniques, certain ground elements are required. The core paradigm behind the TT&C tracking design is the Multiple Spacecraft Per Antenna (MSPA), which allows communicating and tracking several navigation satellites using one single antenna [25]. In order to achieve this, a Code Division Multiplexing (CDM) procedure is proposed for the uplink, and a Code Division Multiple Access (CDMA) procedure for the downlink. Through this approach, the main constraint in the availability of tracking data from a ground station comes from the satellite-station visibility conditions, instead of from operational planning for tracking the multiple satellites. The MSPA concept requires at least three ground stations with an approximate longitude separation of 120° to ensure (nearly) continuous visibility of the lunar orbits [81]. Each station would include one antenna for MSPA tracking, and another one with single-satellite tracking capability for contingency operations.

To perform SLR tracking on the navigation satellites, regardless of it being done through the International Laser Ranging Service (ILRS) or through dedicated Satellite Laser Antenna (SLA), more than one station is needed due to the strict pointing requirements and the meteorological effects on the measurement. Acquiring VLBI and SBI observations requires a network of RF stations.

2.3. Models and methods for ODTS

In this section, the different models and methods used for the ODTS of recent lunar missions and current navigation systems are discussed. These models and methods intend to be representative of those expected for the implementation of the ODTS of a LNS and can serve to guide the work done in this thesis.

2.3.1. Dynamic models and numerical integration methods

Due to the abundant research in their regard, the models, and methods applied to the OD of GNSSs can serve as a reference for a LNS. For GNSSs, dynamic models accurate to at least $0.1\,\mathrm{nm\,s^{-2}}$ are sought. The most commonly used models are the following [35].

- Earth's gravitational acceleration: Spherical Harmonic (SH) static potential up to degree and order 12 and temporal variations due to polar motion and tides.
- Third-Body Perturbation (TBP): Sun and Moon as major sources, Venus and Jupiter as minor sources.
- Relativistic correction: Schwarzschild effect.
- Solar Radiation Pressure (SRP): Computer-Aided Design (CAD) satellite model with ray tracing technique, or box-wing model.
- Thermal emission: accounted for as a modification to SRP, or as empirical accelerations.
- Earth's radiation pressure: both albedo (reflection) and infrared emission by a grid of points on Earth's surface.
- Antenna thrust.
- Maneuver effects.
- Empirical accelerations: constant and harmonic accelerations (Extended CODE Orbit Model (ECOM)), and piecewise linear, piecewise constant or stochastic pulsed acceleration in radial, along-track and cross-track directions.

It must be noted that the OD products generated for the broadcast navigation message of terrestrial GNSS have error RMS < 1 m in the radial direction and ~1–2 m in the along-track and cross-track directions [88]. The numerical integration schemes employed to solve the resulting Equations of Motion (EoMs) normally use a fixed time step size value, as GNSS orbits are nearly circular. Although multi-step methods can be attractive, they are inadequate for propagations showing discontinuities—which can happen in arcs spanning maneuvers, eclipse transitions, or when using sequential estimation approaches. Therefore, single-step multi-stage methods, such as those from the popular Runge-Kutta (RK) family, are deemed better suited for the task. It is expected that the acceleration models and integration methods needed for the OD of a LNS show some differences, due to discrepancies between the terrestrial and lunar environment, the types of orbits of the navigation satellites and the required accuracy level.

One main source of disparity is, evidently, the lunar gravitational model. The Moon has a more significantly non-spherical gravitational field compared to Earth, and, as such, it could be assumed that higher degrees and orders of the spherical harmonics expansion would be needed. The effect of both the model and its degree and order has been investigated using the 100 km-high orbit of the Lunar Prospector [94]. The SH models derive from the Clementine (1994), Lunar Prospector (1998) and Gravity Recovery And Internal Laboratory (GRAIL) (2011–2012) missions, and the numerical integration scheme employed is the RK78 with a time step size of 30 s. The results show that, to obtain a 3D position error[2] RMS < 10 m in an 84-hour-long OD arc, the more precise models based on GRAIL data must be used. For GRAIL-based models using maximum degree and

[2]The error is computed comparing against a more accurate integration considered as the "true" orbit.

Table 2.2: Dynamic models used for the OD of lunar missions.

		LRO		GRAIL
		Nominal orbit [89]	Extended mission [90]	Primary mission [91]
Orbit	Mean altitude	50 km × 50 km	40 km × 180 km	~55 km × 55 km [92]
Gravitational accelerations	Moon SH	GLGM-3 150/150 D/O	GSFC-GRAIL-270 200/200 D/O	GRG-M900C 350/350 D/O
	Moon tides	$k_2 \approx 0.024$*	$k_2 \approx 0.025$*	$k_2 \approx 0.027$*
	TBP	Unspecified	Earth, Sun, Jupiter	Earth (J_2), Sun, planets
	Ephemerides	DE 421	DE 421	DE 421
	Relativistic corrections	Unspecified	Unspecified	Schwarzschild, Lense-Thirring, De Sitter
Non-gravitational accelerations	Spacecraft model	10-plate macro-model	Cannonball	GRAIL Macro-model [93]
	Radiation sources	Sun, lunar albedo (SH)	Sun	Sun, lunar albedo, lunar IR
Numerical integration	Integration scheme	Unspecified	Unspecified	8th order collocation
	Step size	5 s	5 s	15 s
Results	3D position error RMS**	~59 m	~83 m	$\lesssim$10 m***

*Degree 2 potential Love number of the lunar solid tides.

**Results for the LRO nominal orbit and GRAIL derive from overlaps between consecutive solution arcs. Results for the LRO extended mission derive from overlaps between a solution arc and a prediction based on the previous solution arc.

***Obtained for the better performing parameterizations of empirical accelerations.

order of 70, a comparatively small degradation in the propagation occurs as the relative orientation of the orbit evolves with respect to the EM system. Additionally, further increasing the degree and order reduces the 3D position error RMS of the 84-hour-long OD arc by <1 m. As the orbits considered for the LNS are higher than the Lunar Prospector's orbit, lower values of maximum degree and order of the spherical harmonic model would expectedly produce similar results.

Table 2.2 summarizes the acceleration models used by distinct sources for the OD of different phases of selected lunar missions. Despite the orbits being similar, the lack of uniformity is remarkable. Due to the extremely low mean altitude of the orbits, the used maximum degree and order of the SH expansion of the central body gravity

field is notably high compared to the values used for the geopotential in GNSS OD. The numerous harmonic terms, together with the short period of the orbits, imposes a strict upper limit on the integration step size for the purpose of adequately sampling the gravity field. Additionally, all integrations are done with a fixed step size, a decision favored by the small eccentricities of the orbits. The position error values given in Table 2.2 are not necessarily a proper representation of the quality of the models used for each case, as the results obtained from the OD process are highly influenced by the type, number, and quality of the observations available, but are included as a reference.

2.3.2. Observation models

All types of observations that can be used for the reconstruction of a satellite's orbit are subject to errors. This section summarizes the origin and impact of these errors, together with the strategies used to deal with them. Statements made in this section, unless specified differently, refer to [35].

Clock desynchronization

Two-way range observations—either RF or SLR—use the same clock at transmission and reception. Differently, Doppler observations use the shift in the wave's frequency (unrelated to the clock state). Thus, both observation types are unaffected by clock desynchronization. On the other hand, one-way pseudorange observations, used for the OD of terrestrial GNSSs, are constructed from a measurement of the time interval between the time of transmission and time of reception of a signal measured with different clocks. As the clocks are desynchronized, the offset between them causes an apparent delay. This offset is corrected by solving both the satellite's position and clock, namely, OD and TS, together in a single algorithm.

Time-of-flight

One prominent effect impacting the observations is the so-called *light-time effect*, that refers to the relative motion between transmitter and receiver during the time of flight of the signal from one to the other. For relatively short times of flight, a linear correction of this effect can be applied assuming a constant state of motion and using the derived constant instantaneous relative velocity between both sides of the link (transmitter and receiver). This assumption does not hold for long times of flight, requiring strategies that represent the true state of motion with a higher fidelity (e.g., using an iterative procedure).

Atmospheric effects

Retrieving a distance estimate from a time measurement in relation to an electromagnetic signal in vacuum is trivial, as its propagation speed—the speed of light—is constant. As soon as either the transmitter or receiver are in close proximity to Earth, the signal must traverse at least part of the atmosphere in its path between both. Thus, the signal is affected by different atmospheric layers—coarsely divided into troposphere and ionosphere. The change in medium reduces the propagation speed and direction of propagation of the waves, introducing a delay.

The ionosphere (50–1000 km in altitude) is formed by electrically charged gas particles. It is dispersive, meaning that the introduced delay depends on the frequency. Using this property, the first order ionospheric delay—which can amount to a few tens of meters in the zenith direction—can be corrected by combining measurements at two different carrier frequencies, building the so-called *ionosphere-free* combination. Uncorrected higher order

effects are on the centimeter-level. The stated values are valid for S-band RF, as optical frequencies used for SLR are virtually insensitive to ionospheric effects [95].

On the other hand, the tropospheric and stratospheric layers of the atmosphere are electrically neutral and non-dispersive, so their associated error, usually referred to as only *tropospheric delay*, can only be corrected by models or estimations. The dry component is caused by the dry atmospheric gases and accounts for a delay of a few meters [96]. It can be corrected based on meteorological measurements or models and on the local elevation angle. The wet component is caused by water vapor and condensed water, accounting for a delay of tens of centimeters [96]. For precision applications, it can be included in the estimation process.

Relativity

Some delay can be attributed to relativistic effects as well. Relativity manifests in two ways. Firstly, a satellite's clock suffers an offset due to its fast motion and the difference in gravitational potential with respect to an observer at the station's location. This only affects pseudorange observations and can be simply corrected based on the orbital motion of the satellite. Secondly, the space-time curvature causes a delay due to the presence of a gravitational field, called *Shapiro effect*. The Shapiro effect, which leads to an error of a few centimeters at MEO altitude, can be corrected as a function of the transmitter and receiver positions [97].

Geometric effects

The signal used to perform an observation is generated from a transmitter, which can be an antenna or laser, may be reflected/responded by a reflector/transponder, and is collected by a receiver, which can be an antenna or detector. However, positions of satellites are usually referred to its Center of Mass (CoM) and positions of ground infrastructure to a certain associated reference point. This difference between the transmitter/receiver effective positions and the reference positions must be accounted for. Moreover, the position of the apparent transmission/reception, usually referred to as *phase center* in the context of GNSS, can depend on the frequency and the shape of the equiphase contour. The mean deviation and the contribution dependent on the elevation and azimuth angles, commonly called *Phase Center Offset* and *Phase Center Variation* respectively, can either be corrected by means of calibrations or added to the set of estimation parameters.

Regarding infrastructure on the ground, the position of a ground mark associated to each station is known. The offset between the ground marker (or monument marker) and the device's reference point, which usually consists of a single component along the local vertical, can be corrected using available data. The a priori information regarding the position of the stations' ground markers can be obtained from crustal movement models—frequently a linear model based on a position at an epoch and a velocity—, together with models for solid tides, tidal and non-tidal ocean loading, and pole tides.

Hardware delay

Aside from all the previously mentioned sources of delay, an additional hardware delay is introduced in the process of transmission and reception of the signal [97]. Signal generation is triggered based on clock information, and the transmission of the signal is not immediate due to the hardware path between signal generation and transmission. A similar effect occurs upon reception, when a delay appears due to the path between the receiver and the correlator. In GNSS applications, the transmission delay is broadcast as a signal dependent correction with respect to the reference signal to which the system time is associated. On the other hand, the reception

delay is assumed constant for signals produced by the same GNSS and estimated together with the receiver clock. For the two-way ranging observations performed by the DSN, the ground station delay is corrected using an internally mimicked signal transfer together with additional calibrations and corrections, and the satellite delay is measured during the testing phase [98].

Additional sources

Apart from the mentioned delays, there is also the multipath effect, caused by the reflection of the signal on surrounding surfaces, and the delay due to thermal noise. These effects remain uncorrected (neither modeled nor estimated) and are contained in the final residuals of the observations.

2.3.3. Parameter estimation methods

There exist two major types of parameter estimation algorithms—batch Least-Squares (LS) and sequential estimation methods—which differ in the strategy used to combine both sources of information [35].

The batch LS methods define arcs (intervals) of time, each encompassing a sufficiently large number of observations. It aims at estimating the parameters of the system that minimize the residuals between the observations and the reconstructed observations on every arc. A usual technique to perform the estimation is the Weighted Least Squares (WLS), in which the weighting matrix of the system is the inverse of the observation covariance matrix. By using this weighting strategy, observations with lower uncertainty have a greater impact on the estimation than those with greater uncertainty. The incorporation of a priori information to the estimation process, which can be also weighted by its inverse covariance matrix, is contemplated by the method as well. This allows to include information coming from different sources (e.g., a GNSS-based state solution) into the process. Nevertheless, the LS technique can only be used to solve linear problems, so an iterative linearization process is required to solve the non-linear OD problem.

On the contrary, sequential estimation methods progressively update a previous, already produced OD solution with newly available observations. The most frequently used sequential method, the Extended Kalman Filter (EKF), uses a two-step update of the solution. In the first step, a prediction of the state at the new observation epoch is computed based on the solution at the previous epoch and the dynamic model. Then, in the second step, the prediction, and observations are combined to produce the solution that minimizes the residuals considering the prediction's and observations' uncertainties.

While both of these classes of methods are employed in the ODTS of GNSSs, each of them shows its own advantages and drawbacks. The batch LS allows for the use of observations of both past and future epochs inside the arc to estimate a state, at the cost of severely increasing the dimensionality of the problem. On the contrary, sequential estimation reduces the size of the problem to be solved at every update, but only past observations are effective in the estimation of the updated state—requiring backward filtering to be comparable to LS solutions when offline.

From the studies performed about the feasibility of a LNS, it is observed that the batch LS method—reportedly tolerant to gaps in observation within a batch of data [25]—is predominant to solve the OD problem [80][81][99], while the Kalman filtering approach is more popular for the TS problem [52][80][99].

2.3.4. Time Synchronization (TS) methods/architectures

Current strategies for the estimation of the model parameters used to represent a clock's behavior (see § 1.3) are varied. The most recurring architectures make use of ground infrastructure to generate the TS solution [81][99] and share a similar structure that, among others, relies on

- a clock on each ground station,
- an implementation of a ground Time Transfer (TT) method either to produce the realization of a specifically defined Lunar Reference Time (LRT) or to adhere to an existing reference time (e.g., Global Positioning System Time (GPST) or Galileo System Time (GST)),
- an on-board clock (or clocks) on each navigation satellite,
- an implementation of an Earth-to-Moon TT method to estimate the desynchronization of the realized on-board time scale with respect to the reference time scale.

The choices made for both TT strategies, the followed reference time scale, and the realization methods of both ground and on-board local time scales establish the differences between TS architectures. The strategies proposed for the TS of a LNS, similarly to radiometric tracking, exploit the satellite's TT&C link, and, thus, no additional onboard nor ground equipment is required for the Earth-to-Moon TT [25][81].

2.4. Coordinate systems

Establishing a set of selenodetic reference systems is a fundamental task for the specification of lunar orbits and, more specific to the topic at hand, for the operation of a lunar navigation system. Several inertial systems are defined for the study of orbits around the Moon. One commonly used option is to have the lunar equatorial plane as the principal plane, as done for the Moon Mean Equator and IAU-Node of Epoch (MEIAUE) and Moon Mean Equator and Prime Meridian of Epoch (MEPME) systems, which differ from one another in their principal direction. For their realization, all three of the Moon's polar direction (required to define the equatorial plane), its IAU-Node direction and its prime meridian direction referred to the Earth Mean Equator and Equinox of J2000 (EME2000) are defined by models derived by the International Astronomical Union (IAU) [100]. In the design of particular classes of lunar orbits for which the Earth's gravitational perturbation is a main factor (e.g., ELFOs), an inertial reference system with the principal plane being that of the apparent orbit of the Earth around the Moon and the principal direction being that of the intersection of the Moon's equator with the principal plane can be considered as well to simplify computations [17].

The literature mentions two main types of body-fixed frames, which are the following.

- Mean Earth/Rotation (MER) or Mean Earth Polar Axis (MEPA). This system defines the positive X-axis pointing towards the mean-Earth direction and the Z-axis pointing towards the mean-rotation axis direction of the Moon. The MER frame—in specific, its realization based on Develomental Ephemeris 421 (DE 421)[3]—has been considered as the standard frame for most of the developed lunar cartographic products [101].

[3]The Developmental Ephemeris (DE) is a series of ephemerides developed by the NASA's Jet Propulsion Laboratory (JPL). The inclusion of newly available data or models for the computation of the ephemerides triggers the steady production and release of new versions. The most recent version currently available is DE 440/441, released in 2021 [101].

- Principal Axes (PA). This system's axes are aligned with the principal axes of inertia of the lunar exterior (mantle and crust) [101]. PA frames are useful, e.g., for the determination of the lunar gravitational field [102][103], following the recommendations provided in [104].

There exist several realizations of both MER and PA based on the various ephemeris or models used for their computation. There are simple expressions to transform from MER to PA and back (for realizations using the same or different ephemeris or models), and from/to International Celestial Reference Frame (ICRF) realizations [100][101][105]. By comparing the position of the lunar retroreflectors left by several lunar missions, it is observed that the differences between PA and MER frames are approximately of 1 km at the lunar surface, and between realizations of the same system are of a couple of meters [101][106]. In terms of the ODTS of a lunar navigation system, body-fixed reference frames have an effect on:

1. the perturbations affected by the orientation of the main body (the Moon in this case),
2. the broadcast ephemerides in the navigation message (in body-fixed frame to ease the user's positioning),
3. the incorporation of Moon-based observations.

Each of these three factors concern different aspects of the ODTS process, so it is reasonable to use different frames based on needs: while lunar spherical harmonic gravity models can be found defined relative to PA frames [107], it may be convenient to compress the ephemeris into the navigation message using a MER frame due to it being the standard for cartography.

Regarding time systems, according to [108], the IAU recommends the use of barycentric time scales for coordinate systems having their origin at the Solar System Barycenter (SSB), and the use of geocentric time scales only for coordinate systems with origin at the geocenter. Due to the problem at hand not taking place in the proximity of Earth, the best choice would be to use a barycentric system. Following the same document, the recommended standard barycentric time scale is the Barycentric Coordinate Time (TCB)[4], in supersession of the previous standard, the Barycentric Dynamical Time (TDB)[5]. It is also recognized that, due to the existence of important work developed using TDB prior to the production of the recommendation, the TDB time scale may still be used to avoid discontinuity when desirable. Thus, even the most recent ephemerides products from the DE series are integrated using the TDB time scale [101]. The current definition of the TDB scale is also provided by the IAU as a linear transformation of the TCB scale [109]. Due to TCB and TDB differing in rate—they do not grow parallel one from the other—, quantities with dimensions of time, or length (required to maintain a constant value for the speed of light), need to be rescaled when changing from one time scale to the other [110].

2.5. Software tools

For performing the OD analysis of the LNS, several software options can be considered. A comparison between them is required to determine which is the most suitable for the problem at hand. The contrasted options are the following:

- *Multi-purpose Advanced Orbit Restitution Infrastructure (MAORI):* GMV's internally developed flight dynamics library, written in both C++ and Python.

[4] From the French, *Temps-Coordonnée Barycentrique*.
[5] From the French, *Temps Dynamique Barycentrique*.

- *GODOT*: ESA/ESOC's flight dynamics library, also w in C++ and Python. GODOT is expanded by the GEneral Navigation for Earth Orbiting Satellites (GENEOS) package.
- *Orbit Extrapolation KIT (Orekit)*: a free low-level space dynamics library written in Java by the CS Group.
- *TU Delft Astrodynamics Toolbox (Tudat)*: TUD's free-access astrodynamics library, written in C++ and Python.

These four options are accessible without incurring in any cost, either due to them being free-access (GODOT, Orekit, Tudat) or to the access being granted through the partnership with GMV (MAORI).

In order to select a software tool over the others, they can be comparatively evaluated on the basis of certain aspects. The perhaps more evidently sought feature is the capability to perform OD at lunar altitudes. All four options support the OD process to a certain extent. The most limited option on this field is MAORI, as computations involving spacecraft outside the terrestrial environment (approximately Earth's Sphere of Influence (SoI)) are currently under development and validation. The other three tools include similar capabilities for the reconstruction of observations (of range, range-rate, direction and state observables), as well as orbit propagation and parameter estimation, and have been used for missions at interplanetary distances.

The accessibility of the tools is to be considered in the comparison as well. Python is a very accessible programming language due to its simplicity and, thus, those tools having a Python interface (MAORI, GODOT, Tudat) are deemed superior in this aspect. Nevertheless, an implementation based on MAORI could eventually lead to disclosure issues in relation to this thesis' code, which is avoided with the other open-source alternatives. An additional accessibility advantage shown by GODOT is that it has an active community built around which can give continuous support during the development of the work.

A final advantage of GODOT with respect to the rest of tools is the automatic differentiation feature. GODOT's automatic differentiation analytically computes the partial derivatives of output parameters with respect to the desired input parameters. This feature is helpful in the implementation of new functionality, potentially speeding up the development process, and is of special usefulness for performing sensitivity analyses, as required for the study at hand.

An additional secondary aspect to be considered is the software performance in terms of speed and memory usage. Scientific code written in C++ is noticeably faster than that written in Java, so Orekit is in disadvantage in this aspect. Internal assessments done at GMV have compared the performance of both MAORI and GODOT, showing a higher efficiency by MAORI. Nevertheless, the differences are not deemed relevant for the type of analysis at hand.

Based on this comparison, the most appealing software option is GODOT. It has a solid number of already implemented features required to simulate an OD process, with the addition of a great accessibility, and the automatic differentiation aspect. Its most remarkable advantage comes from the availability of support in the implementation of new functionality, which can become critical during the development of the desired studies. For these reasons, GODOT has been chosen as the software tool to perform the presented work.

3

Problem statement

The work reported in this thesis aims to produce a recommendation for the *OD system specifications* of a LNS. The OD system specifications are the values of the design parameters involved in the OD process. These parameters relate to the modeling of the satellites' dynamics, the network of ground stations used for tracking, the tracking strategy, the properties of the tracking observations, and the orbit configuration of the lunar satellites.

It must be noted that the TS problem is left out of the scope of this thesis. The reason for this is multiple. Firstly, the OD problem is considered to be a more relevant problem given the current state of the art. The navigation observations in the context of the LunaNet framework include both one-way pseudo-range and two-way range measurements [41]. Two-way range observations are not affected by clock desynchronization (§ 2.3.2), and, thus, solving the TS problem relates to just one out of two navigation approaches, while OD remains relevant for both. Secondly, a more complete analysis of different TS architectures is found in literature compared to OD. Therefore, there is a greater interest in exploring the different approaches to solve the OD problem. Finally, the chosen software tool, GODOT, has significantly more limited capabilities to assess TS compared to OD.

As discussed in § 2.1, the current requirements on the position SISE of the ODTS system of a LNS scaled to a 1σ level are of approximately 5 m. Assuming an equal split of the position SISE budget between OD and TS, which is coherent with the fractions found in the literature, the error budget for OD is approximately 2.5 m. This OD error budget includes the error in the estimated satellite ephemerides and other sources of error, among which are the navigation message fit—of the order of a couple of decimeters, according to [52]—, hardware delays, and antenna offsets. To account for these other sources of error, the allocated budget for the estimated satellite ephemerides is set to 2 m. Formulating the system requirement in terms of the OD accuracy of the individual satellites may not be the best approach from the perspective of ensuring a certain user performance. The user positioning accuracy depends on the joint OD accuracy of all satellites that form the LNS, not on their individual accuracy. Thus, this thesis considers a requirement of 2 m on the average accuracy of the estimated OD solutions for all LNS satellites at a 1σ level. To assess the validity of this approach, the thesis must also examine the suitability of this joint OD accuracy evaluation by analyzing its relationship with the user positioning accuracy. Further discussion regarding the Figures of Merit (FoMs) of the problem can be found in § 4.2.

A thorough revision of the state of the art involving LNSs, reported in Chapter 2, reveals the most promising choices regarding certain basic design choices. The most promising constellation design considers 4 satellites placed in ELFOs on 2 orbital planes. The most sensible approach to tracking the satellites of this constellation consists in using range and Doppler observations from stations on the Earth's surface. Thus, this thesis uses these two choices as a baseline for the analysis of the OD of the LNS.

Based on the stated goal, the following research questions and sub-questions are formulated:

RQ-1. How can the accuracy requirements imposed on the OD solution of a LNS be met?

- **RQ-1.1.** What are the OD design parameters that drive the accuracy of the OD solution?
- **RQ-1.2.** What is the sensitivity of the OD solution to the identified accuracy drivers?
- **RQ-1.3.** What are the OD system specifications needed to meet the defined accuracy requirements?
- **RQ-1.4.** How are the OD system specifications affected by uncertainties?

RQ-2. What is the relation between the OD accuracy of a LNS and the accuracy of the positioning capabilities that it offers?

Appendix A contains the research plan developed to answer these questions in the time allocated to the thesis.

4

Methodology

To be able to answer the research questions formulated in Chapter 3, it is necessary to develop an OD simulation tool. The different sections in this chapter are dedicated to describing the different aspects of the simulation: the GODOT/GENEOS functionality employed, the required new implementation, the FoMs defined to assess the system's performance, and the selection of models and methods. The last section specifies the nominal configuration and time frame of the simulations, which is used as a reference for the remainder of the thesis.

4.1. Overview of the end-to-end simulation

Figure 4.1 shows the high-level architecture of the simulator. The general concept behind this flow diagram is a four-step process:

1. generating a reference orbit for each of the satellites in the LNS,
2. simulating observations for the reference orbits from a given network of ground stations,
3. estimating the initial state vector and generating an estimated orbit for each of the navigation satellites using the simulated observations,
4. evaluating the system's performance by comparing the estimated orbits with the reference orbits and computing the resulting FoMs.

Figure 4.1 uses colors to distinguish the level of implementation or modification involved in each of the blocks. Process blocks shaded in green represent those that are (almost) entirely newly included in the simulator layer implemented for this thesis. They may use GODOT functionality, but only at a very low-level. I/O blocks in green make reference to elements that do not follow a format predefined by GODOT or files that follow a predefined format, but are read and written using newly implemented functionality. Red process and I/O blocks mark those elements which are used as provided by GODOT/GENEOS, or requiring a minimal modification. Yellow blocks fall in the middle of the two previous, representing elements that use GODOT/GENEOS as a basis, but have been modified to extend the already available capabilities.

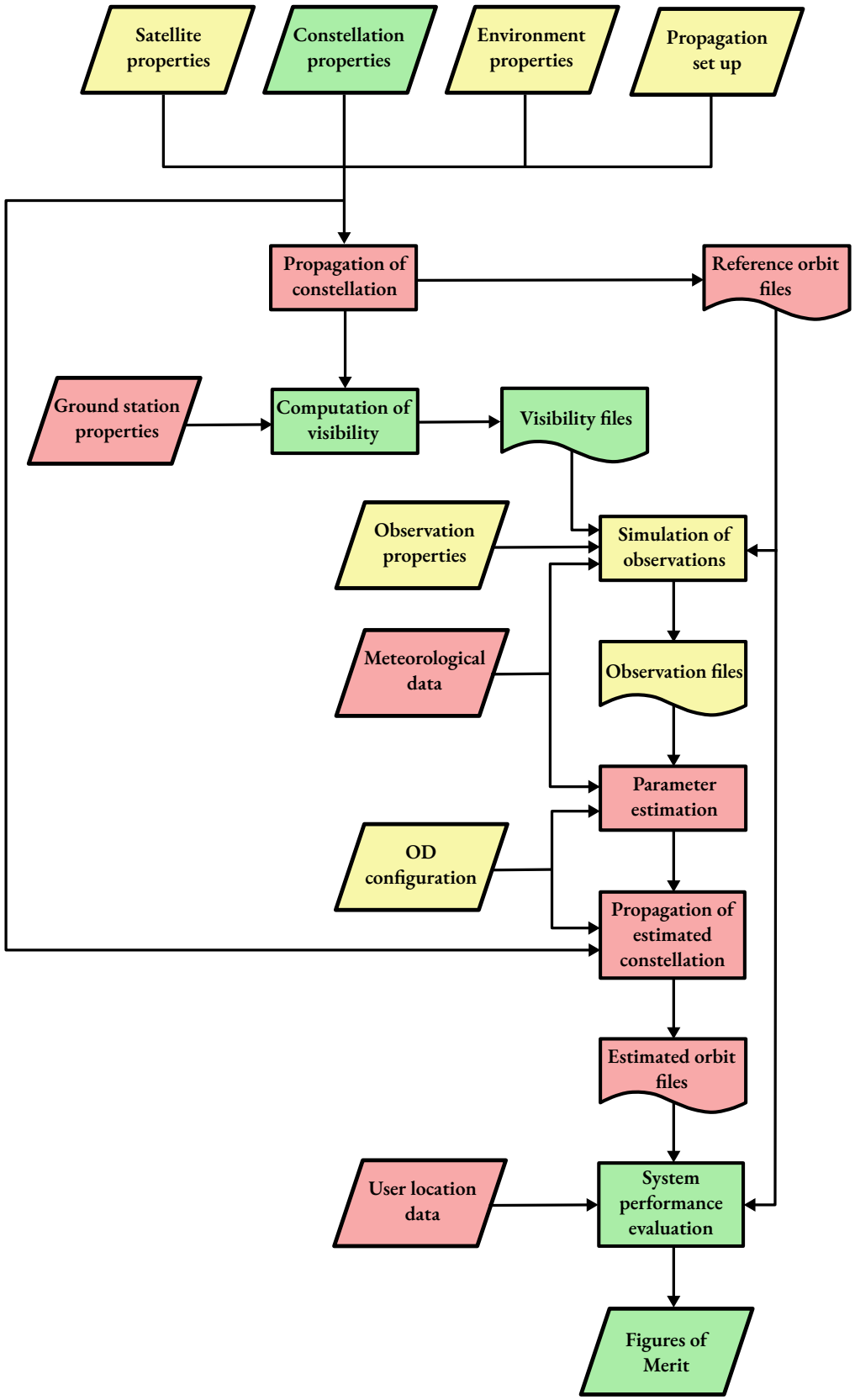

Figure 4.1: Basic flow diagram representing the end-to-end simulation process performed by the software tool. Blocks in green represent new implementation done for this thesis work. Blocks in yellow represent already existing elements in GODOT/GENEOS that has been modified. Blocks in red represent GODOT/GENEOS elements that have required no modification.

Within the end-to-end process, two big parts can be identified. The first one is the simulation part, which encompasses the propagation of the reference orbit and the simulation of observations. The tasks within this part intend to recreate reality in some way, to compensate for the lack of an already instantiated LNS—for example, as there are no real observations to be used in the estimation, they must be simulated. The second part is the OD part, which involves the activities that replicate what the future OD system of a LNS must do. This includes the estimation of parameters and the propagation of the estimated orbit. The computation of the Figures of Merit (FoMs) can also be included in this second part, as it aims at evaluating the quality of the OD product.

To properly account for the inherent difference that should exist between the simulated reality and the OD processing, there are certain parameters of the problem which may need to have different values on one part or the other. These are mainly parameters related to the propagation of the satellites' orbits. For example, the integration tolerance used for the propagation of the reference orbit may be different from that used to propagate the estimated orbit during OD. While the reference orbits are a representation of the real orbits of an implemented LNS, the estimated orbits do not represent real orbits, but fictional orbits used to generate the navigation message, so they only need to be accurate enough to meet the navigation requirements. Thus, it is logical that the integrator tolerance required by either of them may be different. To distinguish between those parameters pertinent to the propagation of the reference orbit and those pertinent to the propagation of the estimated orbit, superscripts r and e are used.

4.2. Figures of Merit (FoMs)

In order to evaluate the performance achieved by using a specific set of input data, we can define a series of FoMs. Besides the accuracy of the OD process, these FoMs should also represent an estimation of the attainable user positioning accuracy and the cost of computing the OD solution.

OD accuracy

The epoch-wise 3D position difference between the reference orbit and the estimated orbit is introduced to assess the OD accuracy. The 3D position difference of i-th satellite of the constellation is defined as

$$\Delta r_i(t) = ||\mathbf{r}_{i,\text{est}}(t) - \mathbf{r}_{i,\text{ref}}(t)||, \tag{4.1}$$

where $\mathbf{r}_{i,\text{est}}(t)$ and $\mathbf{r}_{i,\text{ref}}(t)$ are the position vectors of the estimated and reference orbits of the i-th satellite, respectively. This 3-D position difference is equivalent to the orbital error component of the position SISE defined in (2.1), assuming an ideal representation of the broadcast ephemerides in the navigation message. To condense this multi-satellite epoch-wise information into a single value and allow for an easier quantitative comparison, the inter-satellite mean position Root Mean Square Error (RMSE) is introduced as

$$\overline{\text{RMSE}}_{\text{pos}} = \sqrt{\frac{1}{N}\sum_{j=1}^{N}\left(\frac{1}{N_\text{s}}\sum_{i=1}^{N_\text{s}}\Delta r_i(t=t_j)\right)^2}, \tag{4.2}$$

where N_s is the number of satellites in the LNS constellation and N is the number of epochs at which the 3-D position difference is sampled.

The $\overline{\text{RMSE}}_{\text{pos}}$ is a relevant FoM as it serves as an estimate of the 1σ average OD accuracy of the LNS. Therefore, it is used to assess the fulfillment of the OD accuracy requirement stated in Chapter 3—that is, the OD accuracy

requirement is expressed as $\overline{\text{RMSE}}_{\text{pos}} = 2$ m. Additionally, this FoM is an intuitive and straightforward representation of the correctness of the OD solution, thus easing the understanding and interpretation of the results. Three other FoMs are defined attending to the user aspect of the LNS, which are used to evaluate whether the imposed OD accuracy requirement leads to the expected performance on the user's side.

User positioning accuracy

Given that the navigation service offered to the user is the end product of a LNS, it is interesting to assess the accuracy of the positioning of the user. Firstly, the DOP can be used to analyze the geometrical fitness of the distribution of navigation satellites from the user's location. By modeling a clock-independent navigation observation as

$$R_i = ||\mathbf{r}_\text{r} - \mathbf{r}_i||, \tag{4.3}$$

where $\mathbf{r}_\text{r}$ is the navigation receiver's position and $\mathbf{r}_i$ is the position of the i-th visible satellite from the navigation receiver's position, the resulting design matrix is

$$\mathbf{A} = \begin{pmatrix} \partial R_1/\partial x_\text{r} & \partial R_1/\partial y_\text{r} & \partial R_1/\partial z_\text{r} \\ \vdots & \vdots & \vdots \\ \partial R_{N_\text{v}}/\partial x_\text{r} & \partial R_{N_\text{v}}/\partial y_\text{r} & \partial R_{N_\text{v}}/\partial z_\text{r} \end{pmatrix}, \tag{4.4}$$

where N_v is the number of visible navigation satellites from the receiver's position. As derived in [28], assuming that the uncertainty matrix of the observations can be written in the form $\mathbf{Q}_\text{r} = \sigma^2\mathbf{I}$, where σ is the standard deviation of the observations and $\mathbf{I}$ is the identity matrix, the uncertainty matrix of the receiver position is given by

$$\mathbf{Q}_x = \sigma^2(\mathbf{A}^\top\mathbf{A})^{-1}. \tag{4.5}$$

Recalling the definition in (1.1)—dropping the clock bias term, as it does not affect the modeled navigation observations—and knowing that $\sqrt{\sigma_\text{E}^2 + \sigma_\text{N}^2 + \sigma_\text{U}^2} = \sigma\ \text{tr}\{(\mathbf{A}^\top\mathbf{A})^{-1}\}$, the PDOP remains as

$$\text{PDOP} = \text{tr}\{(\mathbf{A}^\top\mathbf{A})^{-1}\}. \tag{4.6}$$

It must be noted that for the observation model stated in (4.3), there is no concept of GDOP different from the PDOP.

The PDOP metric alone does not reflect the OD errors of the navigation satellites. The first-order estimation of the receiver positioning error incurred due to the OD error can be computed as

$$\Delta\mathbf{r}_\text{r} = (\mathbf{A}^\top\mathbf{A})^{-1}\mathbf{A}^\top\Delta\mathbf{R}, \tag{4.7}$$

where $\Delta\mathbf{R}$ is the ranging error caused by the OD error in the position of the navigation satellite. Equation (4.7) represents an iteration of the unweighted non-linear LS process used to solve the navigation problem. Thus, it serves to estimate the convergence error of the LS process due to ranging errors. The ranging error of the i-th navigation satellite can be computed as

$$\Delta R_i = (\mathbf{r}_{i,\text{est}} - \mathbf{r}_{i,\text{ref}}) \cdot \mathbf{u}_{\text{r},i}, \tag{4.8}$$

with $\mathbf{u}_{\text{r},i}$ being the unitary vector pointing from the receiver position to the i-th satellite's reference position. The $\Delta\mathbf{R}$ vector contains the values of ΔR_i for each satellite in view of the receiver.

These are epoch-wise metrics and, thus, in order to have single-value FoMs, the RMS of both the PDOP and the magnitude of $\Delta\mathbf{r}_\mathrm{r}$ can be evaluated. The RMS of any arbitrary time series, denoted as $S(t)$, can be computed as

$$S_\mathrm{RMS} = \sqrt{\frac{1}{N}\sum_{j=1}^{N}\left(S(t=t_j)\right)^2}, \tag{4.9}$$

where t_j with $j = \{1, N\}$ are the epochs at which the time series is being sampled, and N is the number of samples. Then, the equations used to compute the two mentioned FoMs are

$$\mathrm{PDOP}_\mathrm{RMS} = \sqrt{\frac{1}{N}\sum_{j=1}^{N}\mathrm{tr}\{(\mathbf{A}_j^\top\mathbf{A}_j)^{-1}\}}, \tag{4.10}$$

$$\Delta r_\mathrm{r,RMS} = \sqrt{\frac{1}{N}\sum_{j=1}^{N}||\Delta\mathbf{r}_{r,j}||} = \sqrt{\frac{1}{N}\sum_{j=1}^{N}||(\mathbf{A}_j^\top\mathbf{A}_j)^{-1}\mathbf{A}_j^\top\Delta\mathbf{R}_j||}. \tag{4.11}$$

In these equations, the subindex j is used to denote a quantity being evaluated at $t = t_j$, for example, $\mathbf{A}_j \equiv \mathbf{A}(t = t_j)$. Additionally, both the PDOP and Δr_r are strongly dependent on the geometric distribution of the satellites along the constellation's period. The constellation's period (T_const) is defined as the time that it takes for all satellites in the constellation to (approximately) repeat the same geometrical configuration. As all constellations considered in this thesis consist of orbits with equal values of the semi-major axis across satellites, the constellation's period is, at maximum, equal to the orbital period of the single satellite. Thus, in order to have an evaluation of the $\mathrm{PDOP}_\mathrm{RMS}$ and $\Delta r_\mathrm{r,RMS}$ that is representative of each configuration, they should be computed over time spans that are approximate multiples of the constellation's period.

Lastly, the model of the navigation observations formulated in (4.3) requires a minimum of 3 navigation satellites in view, called *3-fold visibility* or *3-fold coverage*, for the design matrix to possibly be full-rank. This is a required condition for a user to position itself using the navigation observations. Thus, the third FoM used to evaluate the LNS's performance on the user side is the time fraction of the constellation's period during which there is 3-fold coverage of the user location, represented as ξ. This can be computed as

$$\xi = \frac{T_{N_\mathrm{v}\geq 3}}{T_\mathrm{const}}, \tag{4.12}$$

where $T_{N_\mathrm{v}\geq 3}$ represents the time length of the period with 3-fold coverage.

Run time

The run time is the FoM that represents the computational cost of the OD process. The measured run time considers only the execution of the *Parameter estimation* and *Propagation of the estimated constellations* blocks in Figure 4.1, as they are the parts of the entire end-to-end simulation that would be performed during the real operation of a LNS.

Summary of the selected FoMs

Table 4.1 contains a summary of the FoMs used to evaluate the performance of the LNS, together with the equation used to compute them. Regarding the computation of the user-related FoMs, the assumed user location is the LSP, establishing a minimum elevation of 10° for a navigation satellite to count as visible from the lunar surface. The exact coordinates of the location are provided in Table 4.7 in MER frame. The evaluation of all

Table 4.1: List of FoMs used to evaluate the problem.

Figure of Merit (FoM)	Equation	Reference
Inter-satellite mean position RMSE	$\overline{\mathrm{RMSE}}_{\mathrm{pos}} = \frac{1}{N_\mathrm{s}} \sum_{i=1}^{N_\mathrm{s}} \sqrt{\frac{1}{N_i} \sum_{j=1}^{N_i} \Delta r_{i,j}^2}$	(4.2)
PDOP RMS	$\mathrm{PDOP}_{\mathrm{RMS}} = \sqrt{\frac{1}{N} \sum_{j=1}^{N} \mathrm{tr}\{(\mathbf{A}_j^\top \mathbf{A}_j)^{-1}\}}$	(4.10)
RMS of the positioning error estimate	$\Delta r_{\mathrm{r,RMS}} = \sqrt{\frac{1}{N} \sum_{j=1}^{N} \lvert\lvert(\mathbf{A}_j^\top \mathbf{A}_j)^{-1} \mathbf{A}_j^\top \Delta \mathbf{R}_j\rvert\rvert}$	(4.11)
Fraction of time with 3-fold coverage	$\xi = \frac{T_{N_\mathrm{v} \geq 3}}{T_{\mathrm{const}}}$	(4.12)
Run time	—	—

3 FoMs considers an interval of 20 s to sample the time series. The orbital periods of the analyzed orbits are ~ 12 h. Thus, a 20 s sampling interval is enough to properly capture all trends present in the corresponding time-continuous magnitudes.

The OD process distinguishes two time arcs: the estimation arc and the prediction arc. The estimation arc comprises the entire period of generation of the observations used to estimate the orbit. The already estimated orbit is propagated over a period occurring after the estimation arc. This is the prediction arc. The propagated orbit during the prediction arc serves to produce the navigation message broadcast by the satellites of the LNS. Thus, it is the accuracy of this prediction arc that represents the system's performance. For this reason, the FoMs are evaluated over the prediction arc, unless specified differently.

4.3. Model selection

To compute the FoMs from a given set of inputs, several model implementations are used to perform the tasks in Figure 4.1. The selection of models is mostly restricted to those available in the GODOT/GENEOS tools, as implementing such numerous models from scratch is unreasonably demanding for this thesis. However, it may be necessary to upgrade the models that are deemed insufficient to recreate the desired effects.

The functionality available in GODOT/GENEOS covers essentially every model needed to perform the analysis. GODOT is a flight dynamics library that provides functionality such as propagating orbits, computing observations, and solving parameter estimation problems. GODOT is used for the operation of interplanetary missions at ESOC and, thus, the quality of the models and algorithms it contains is enough to carry out the analysis. The following subsections introduce the selection of modeling choices together with the assumptions required for their use.

4.3.1. Frames and ephemerides

The definition of the dynamic and observation models requires a prior introduction of the relevant reference frames. The reference frames involved in the simulation problem are the following.

- *ICRF*. It is the basic reference frame, meaning that all other reference frames are, either directly or indirectly, defined with respect to it.
- *International Terrestrial Reference Frame (ITRF)*. The ITRF is the realization of the International Terrestrial Reference System (ITRS), a geocentric reference system whose orientation in time fulfills a

no-net-rotation condition relative to the horizontal tectonic motion, which implies that it rotates with the Earth [111]. The ITRF can be obtained from the ICRF by means of the so-called *Earth Orientation Parameters (EOPs)*. GODOT provides the files, in the proper format, containing the EOPs to obtain the ITRF2000 realization.

- *Lunar PA*. As introduced in § 2.4, this frame is defined following the principal directions of inertia of the lunar exterior. There are several models and ephemerides sources that can be used in its computation, and the main use of this frame is to implement the SH gravitational potential. For the sake of coherence, the PA frame realization chosen is the one based on DE 421, as the lunar SH model employed (mentioned later in § 4.3.2) is associated to that frame.

- *Lunar MER*. The MER is a lunar reference frame based on the Moon's orbital and rotation properties (as described in § 2.4). Similar to the PA frame, there are many possible realizations of this frame. On the other hand, as precision is less critical in the applications of the MER frame (the specification of the constellation's initial states and lunar surface locations), it is instantiated using the IAU model of the year 2009. The magnitude of the potential loss in precision between realizations of this frame, discussed in § 2.4, is not large enough to justify the computational effort of loading an additional ephemerides kernel for a more accurate instantiation.

- *Local North-East-Up (NEU)*. The definition of tracking stations on Earth, as well as lunar surface locations, involves providing their coordinates with respect to certain body-centered frames. Then, for any surface location,

$$\mathbf{e}_{\mathrm{N}} = -\sin(\phi)\cos(\lambda)\mathbf{X} - \sin(\phi)\sin(\lambda)\mathbf{Y} + \cos(\phi)\mathbf{Z}, \tag{4.13}$$

$$\mathbf{e}_{\mathrm{E}} = -\sin(\lambda)\mathbf{X} + \cos(\lambda)\mathbf{Y}, \tag{4.14}$$

$$\mathbf{e}_{\mathrm{U}} = \cos(\phi)\cos(\lambda)\mathbf{X} + \sin(\phi)\sin(\lambda)\mathbf{Y} + \sin(\phi)\mathbf{Z}, \tag{4.15}$$

  are the north, east and up directions, respectively. In these equations, ϕ is the latitude and λ is the longitude with respect to the corresponding body-centered frame. $\mathbf{X}$, $\mathbf{Y}$ and $\mathbf{Z}$ are the axes of the body-centered frame. These 3 directions serve as axes to build the local topocentric NEU frame of each surface location. These frames are used to compute the visibility with the satellites of the LNS and to evaluate certain models, such as the atmospheric models used in the computation of observations.

Apart from the frames, the evaluation of the models also requires knowledge of the states of the celestial bodies at any desired epoch. GODOT can import ephemerides kernels provided by NASA's Navigation and Ancillary Information Facility (NAIF) in its Planetary Data System (PDS)[1] to retrieve these data. These kernels can also be loaded to instantiate ephemerides-based reference frames, such as the lunar PA. Using the latest ephemerides available is desirable, as they are supposedly more accurate. Thus, the DE 440/441 source, the latest from the DE series, is chosen to compute the states of the celestial bodies.

[1]The SPICE kernels containing the ephemerides can be found in `https://naif.jpl.nasa.gov/pub/naif/generic_kernels/spk/planets/`.

4.3.2. Orbital propagation

The EoM used to propagate in time the state of motion of the navigation satellites is that of classical mechanics, derived from Newton's Second Law, that reads

$$\frac{\mathrm{d}^2\mathbf{r}}{\mathrm{d}t^2} = \sum^{\mathrm{b}} \mathbf{a}_{\mathrm{g,b}} + \mathbf{a}_{\mathrm{rel}} + \mathbf{a}_{\mathrm{SRP}}, \tag{4.16}$$

where m and $\mathbf{r}$ are the mass and state of an arbitrary satellite, $\mathbf{a}_{\mathrm{g,b}}$ is the gravitational acceleration due to body b, $\mathbf{a}_{\mathrm{rel}}$ is the relativistic correction of the gravitational acceleration, and $\mathbf{a}_{\mathrm{SRP}}$ is the SRP acceleration. The integration of this differential equation is performed in GODOT using a Cartesian state representation in ICRF and selecting TDB as time scale, following the IAU recommendation stated in § 2.4.

Gravity models

For the consideration of the gravitational acceleration induced by celestial bodies on the satellites, GODOT allows using a SH expansion of the bodies' gravitational potential. The basic formulation of the SH gravitational potential (from [112]) reads

$$U_{\mathrm{b}} = \frac{\mu_{\mathrm{b}}}{r} \sum_{n=0}^{\infty} \sum_{m=0}^{n} \frac{R_{\mathrm{b}}^n}{r^n} P_{n,m}(\sin(\phi))(C_{n,m}\cos(m\lambda) + S_{n,m}\sin(m\lambda)), \tag{4.17}$$

where μ_{b} is the gravitational parameter of the celestial body, R_{b} is the radius of the body, r is the distance from the center of the body to the CoM of the propagated object, $P_{n,m}$ is the Legendre polynomial of degree n and order m, and ϕ and λ are the latitude and longitude with respect to a body-fixed frame. The terms $C_{n,m}$ and $S_{n,m}$ are the coefficients of degree n and order m of the expansion, which characterize the potential of the different celestial bodies. For this thesis, the coefficients are considered to be known a priori and are inputs to the software. The acceleration associated to the gravitational potential U_{b} is computed by taking its gradient, so

$$\mathbf{a}_{\mathrm{g,b}} = \nabla U_{\mathrm{b}}. \tag{4.18}$$

The coefficients of the SH expansion can be provided to the software in the form of a standard Spherical Harmonic ASCII (SHA) file[2]. The SH model chosen for the Moon is the GRGM1200A, which derives from GRAIL data. GRAIL is the last mission to have produced lunar gravity data, and it entailed a great improvement in the characterization of lunar gravity compared to previous models [107]. The exact degree and order of the expansion derives from a sensitivity analysis of the propagated solution (see Chapter 6), through a trade-off between the accuracy of the solution and the computational resources.

The gravitational effect of *third bodies* on the satellites is a spherically symmetric gravitational potential. An exception to this is Earth, for which the relevance of the low degree and order terms of its SH expansion is to be studied during the sensitivity analysis, due to its relative proximity to the Moon. The used SH model for Earth's gravity is the EIGEN-5C model [113], which is readily available in GODOT. The list of other third bodies participating in the propagation is also decided based on the results of the sensitivity analysis in Chapter 6.

In order to account for the relativistic formulation of the gravitational accelerations, GODOT implements the model described in [114] based on Parameterized Post-Newtonian (PPN) parameters, following the framework of general relativity. The bodies considered to compute the relativistic contribution can be specified by the user. The choice of these bodies is based on the results of the sensitivity analysis in Chapter 6 as well.

[2]The format used is described under the name *shtools* here: `https://shtools.github.io/SHTOOLS/file-formats.html`

SRP models

Two models are available in GODOT for the acceleration caused by the SRP: a plate model and a cannonball model. The formulation of both models derives from the differential acceleration caused by a differential of surface area exposed to the solar radiation, which, from [112], is given by

$$\mathrm{d}\mathbf{a}_{\mathrm{SRP}} = -P_{\mathrm{S}}\frac{(1\,\mathrm{au})^2}{r^2}\frac{\mathrm{d}A}{m}\cos(\theta)((1-\varepsilon)\mathbf{e}_{\mathrm{S}} + 2\varepsilon\cos(\theta)\mathbf{n}), \tag{4.19}$$

where P_{S} is the mean solar radiation pressure at 1 au, r is the distance from the Sun to the differential of surface, m is the mass of the spacecraft, $\mathbf{e}_{\mathrm{S}}$ is the direction from the differential of surface to the Sun, $\mathbf{n}$ is the normal direction to the differential of surface, θ is the angle formed between $\mathbf{e}_{\mathrm{S}}$ and $\mathbf{n}$, and ε is the fraction of the incoming radiation reflected by the surface. A first assumption shared by both models is that the distance between two arbitrary points in the surface is sufficiently small in comparison to the distance to the Sun such that r and $\mathbf{e}_{\mathrm{S}}$ are constant. The plate model assumes that the surface is perfectly flat, so that $\mathbf{n}$, and, consequently, θ as well, are constant over the entire surface. Under this assumption, the integration of (4.19) yields

$$\mathbf{a}_{\mathrm{SRP,plate}} = -P_{\mathrm{S}}\frac{(1\,\mathrm{au})^2}{r^2}\frac{A}{m}\cos(\theta)((1-\varepsilon)\mathbf{e}_{\mathrm{S}} + 2\varepsilon\cos(\theta)\mathbf{n}), \tag{4.20}$$

with A being the total surface area exposed to the solar radiation. GODOT's implementation of the plate model makes the distinction between specular and diffusive reflection of radiation. Thus, the equation implemented in the software, which is a variation of (4.20), reads

$$\mathbf{a}_{\mathrm{SRP,plate}} = -P_{\mathrm{S}}\frac{(1\,\mathrm{au})^2}{r^2}\frac{A}{m}\cos(\theta)\left((1-C_{\mathrm{s}})\mathbf{e}_{\mathrm{S}} + 2\left(C_{\mathrm{s}}\cos(\theta) + \frac{C_{\mathrm{d}}}{3}\right)\mathbf{n}\right), \tag{4.21}$$

where C_{s} and C_{d} are the fractions of specularly and diffusively reflected radiation, respectively, also referred to as specular and diffusive reflection coefficients.

In the case of the cannonball model, the surface is assumed to be perfectly spherical. Introducing this assumption, the integration of (4.19) leads to

$$\mathbf{a}_{\mathrm{SRP,cannonball}} = -P_{\mathrm{S}}\frac{(1\,\mathrm{au})^2}{r^2}\frac{A}{m}C_{\mathrm{r}}\mathbf{e}_{\mathrm{S}}, \tag{4.22}$$

where $C_{\mathrm{r}} = (1+\varepsilon)$ is the so-called reflectivity coefficient of the surface. It must be noted that the resulting equation for the cannonball model is equivalent to having a plate perfectly facing the Sun with an area equal to that of the circular section through the sphere's center.

To mitigate the lack of knowledge about the LNS satellites' geometry, they are assumed to be similar in shape and dimensions to those used for the Galileo GNSS [115]. The Galileo satellites have a typical geometry for a navigation satellite (body + two solar panels on opposing sides) and their dimensions ensure the capability to perform navigation tasks. Thus, they are considered to be representative enough of the future LNS satellites. The satellite body is reproduced using a cannonball model. The area assigned to this model is computed as $A_{\mathrm{body}} = V_{\mathrm{body}}^{2/3}$, where V_{body} is the volume of the satellite's body computed from the three dimensions of its prismatic shape. The reflectivity coefficient is set to be $C_{\mathrm{r}} = 1.35$, which is a typical value used for cannonball models. The solar panels are considered using a plate model. The specular and diffusive reflection coefficients are approximated based on the values for gallium arsenide solar panels [116]. It should be noted that, based on the

Table 4.2: Satellite properties.

Parameter	Value	Parameter	Value
m	700 kg	A_{panel}	14.4 m^2
A_{body}	2.22 m^2	C_{s}	0.15
C_{r}	1.35	C_{d}	0.05

formulation of the SRP accelerations given in (4.21) and (4.22), there is no interaction between the cannonball and plate models used. This means that neither shadowing nor re-radiation from one surface onto another is accounted for in the implemented satellite model. All the geometrical parameters used to model the SRP effect are summarized in Table 4.2. The value of the mean solar radiation pressure at 1 au is $P_{\text{S}} = 4.57 \times 10^{-6}$ Pa, which is in close accordance with the value found in [112].

The pointing direction of the satellite's solar panels is dependent on the satellite's attitude. The satellite is assumed to keep a nadir pointing of the navigation antenna, thus leaving two degrees of freedom (satellite's yaw rotation and solar panel rotation) for the panels to face in the desired direction. The target pointing direction of the solar panels is the Sun direction ($\mathbf{e}_{\text{S}}$). As the satellite orbits the Moon and keeps its nadir pointing of the antenna, this pointing law requires that a correction of the panels' rotation is being applied at every moment to "follow" the Sun direction. This solar panel correction is a rotation about the normal to the local orbital plane, $\mathbf{e}_{\text{h}}$, which is given by

$$\mathbf{e}_{\text{h}} = \mathbf{e}_{\text{r}} \times \mathbf{e}_{\text{v}}. \tag{4.23}$$

In this equation, $\mathbf{e}_{\text{r}}$ is the radial direction of the satellite from the Moon's center and $\mathbf{e}_{\text{v}}$ is the velocity direction of the satellite with respect to the Moon's center. While the model used for the propagation of the estimated orbit assumes that the Sun pointing is perfect, the propagation of the reference orbit introduces a continuously present misalignment between the Sun direction and the true pointing direction. This misalignment is assumed to occur as a rotation along the $\mathbf{e}_{\text{h}}$ direction, as it is the main direction of the rotation to track the Sun. The true, "erroneous" pointing direction used in the reference orbit propagation, $\mathbf{e}_{\text{S,e}}$, is given by

$$\mathbf{e}_{\text{S,e}} = \cos(\delta_{\text{U}})\mathbf{e}_{\text{S}} + \sin(\delta_{\text{U}})\mathbf{e}_{\text{e}}, \tag{4.24}$$

where δ_{U} is the constant undershoot angle and $\mathbf{e}_e$ is an auxiliary error direction. The auxiliary error direction is computed as

$$\mathbf{e}_{\text{e}} = \mathbf{e}_{\text{h}} \times \mathbf{e}_{\text{S}}. \tag{4.25}$$

By the end of the last century, requirements on onboard pointing accuracy knowledge were already at the level of $\sim 0.001°$ [117]. Moreover, current considerations for the controlled pointing performance of satellite instruments set the accuracy level at an approximate $0.001°$ as well [118][119]. Bearing this in mind and with the intention of being conservative, a constant value of $\delta_{\text{U}} = 0.1°$ is chosen. By choosing this greater value, other imperfect modeling effects are also accounted for. A more complex strategy concerning a time-variable δ_{U} may have been a more realistic choice. However, due to the technical complexity involved in its implementation, and the consequent increased effort, the constant value strategy is deemed enough to represent the imperfect SRP modeling.

Finally, the total contribution of the SRP to the dynamics of the spacecraft is computed as

$$\mathbf{a}_{\text{SRP}} = \mathbf{a}_{\text{SRP,cannonball}} + \mathbf{a}_{\text{SRP,plate}}. \tag{4.26}$$

Numerical integration

For the numerical integration of the equations of motion, GODOT offers a variety of schemes. The several implementations of RK schemes are the following.

- Fehlberg78: 8-th order, variable step size method which uses 13 state derivative evaluations per step. It does not provide dense-output.
- Verner78: 8-th order, variable step size method equivalent to the Fehlberg78 method in every aspect.
- Verner787: 8-th order, variable step size method which uses 17 state derivative evaluations per step. The state output is identical to that of the Verner78 for the same input. It uses the additional 4 function evaluations compared to Verner78 to provide dense output through a 7-th order interpolating polynomial.
- Verner788: 8-th order, variable step size order method which uses 21 state derivative evaluations per step. The state output is identical to that of the Verner78 for the same input. It uses the additional 8 function evaluations compared to Verner78 to provide dense output through an 8-th order interpolating polynomial.

Apart from these, there is also a variable order, variable step size Adams method that uses an Adams-Bashforth predictor and an Adams-Moulton corrector. This method can provide dense output as well.

Due to the dynamics of the spacecraft suffering discontinuities at the entrance and exit of the eclipses, which would force the restart of the integration, multi-step methods like the Adams, which have a more costly restart, are less desirable. For this reason, the RK methods are preferred. In specific, the method providing dense output with the lowest-order interpolation polynomial (Verner787) is selected, as the only mid-propagation events to detect are the eclipse boundaries and, thus, the increase in accuracy for event detection does not compensate for the extra computational cost (the SRP is expected to be significantly smaller than the primary acceleration).

The tolerance level used for the numerical integration of the EoMs must be strict enough to ensure a sufficiently accurate orbital propagation while not excessively hindering the computational performance. The expectedly high number of terms of the lunar SH potential required, which would lead to rapidly changing dynamics close to the orbit's periselene, suggests that relative tolerance of the integrator needs to be low—even close to the finite-precision of the double-precision floating point representation. The value of tol^{r} is selected based on the results of the sensitivity analysis reported in § 6.1.

4.3.3. Computation of observations

The formulation of the two-way range tracking observations reads

$$\rho(t_{\text{r,D}}) = c(\Delta t_{\text{U}} + \Delta t_{\text{T}} + \Delta t_{\text{D}} - NT_{\text{ran}}) + b_{\text{ran}}, \tag{4.27}$$

where Δt_{U} is the time difference between the reception and transmission epochs of the uplink leg, Δt_{D} is the time difference between the reception and transmission epochs of the downlink leg, Δt_{T} is the transponder delay, b_{ran} is the range bias, and c is the speed of light. The range ambiguity is considered as an integer (N) times the

ambiguity of the range code (T_{ran}). The value of N is the highest possible that yields a positive range value. The range observations are time-tagged at epoch $t_{\text{r,D}}$, namely, the reception epoch of the downlink. The expression for the time difference during the uplink is

$$\Delta t_{\text{U}} = \Delta t_{\text{U}}^{\text{i}} + \Delta t_{\text{U}}^{\text{iono}} + \Delta t_{\text{U}}^{\text{tropo}}, \tag{4.28}$$

with $\Delta t_{\text{U}}^{\text{i}}$ being the "ideal" component of the uplink corresponding to the relativistic light-time without perturbations from the transmission media, $\Delta t_{\text{U}}^{\text{iono}}$ is the delay of the uplink due to the ionosphere, and $\Delta t_{\text{U}}^{\text{tropo}}$ is the delay of the uplink due to the troposphere. The evaluation of the atmospheric models uses the epoch of interaction with the ground station—that is, the epoch of transmission in the uplink ($t_{\text{t,U}}$) and the epoch of reception in the downlink ($t_{\text{r,D}}$). The formulation for the time difference of the downlink is equivalent. However, the epochs used to evaluate the ideal and atmospheric components are different between the uplink and downlink, thus introducing a difference between the values of both legs.

The two-way Doppler tracking observations are formulated as a range difference between epochs. To describe the Doppler observations, let the unambiguous, unbiased range observation be defined as

$$\tilde{\rho}(t_{\text{r,D}}) = c(\Delta t_{\text{U}} + \Delta t_{\text{T}} + \Delta t_{\text{D}}). \tag{4.29}$$

The equation of the unbiased Doppler observations in range-rate form is

$$\tilde{\dot{\rho}}(t_{\text{r,D}}^{\text{I}}) = \frac{\tilde{\rho}(t_{\text{r,D}}^{\text{I}} + T_{\text{dop}}) - \tilde{\rho}(t_{\text{r,D}}^{\text{I}})}{T_{\text{dop}}}, \tag{4.30}$$

where T_{dop} is the integration or count time. The Doppler observations are time-tagged at $t_{\text{r,D}}^{\text{I}}$, that is, at the reception epoch that marks the start of the count interval. The equation of the unbiased Doppler observations in frequency form is

$$\tilde{D}(t_{\text{r,D}}^{\text{I}}) = \frac{1}{T_{\text{dop}}} \int_{t_{\text{t,U}}^{\text{I}}}^{t_{\text{t,U}}^{\text{II}}} f_{\text{signal}} \mathrm{d}t = \frac{1}{T_{\text{dop}}} \int_{t_{\text{r,D}}^{\text{I}} - \tilde{\rho}(t_{\text{r,D}}^{\text{I}})/c}^{t_{\text{r,D}}^{\text{I}} + T_{\text{dop}} - \tilde{\rho}(t_{\text{r,D}}^{\text{I}} + T_{\text{dop}})/c} f_{\text{signal}} \mathrm{d}t, \tag{4.31}$$

where f_{signal} is the frequency of the tracking signal. Taking a constant f_{signal} in time, both (4.30) and (4.31) are essentially equivalent. This can be shown by integrating (4.31), obtaining

$$\begin{aligned} \tilde{D}(t_{\text{r,D}}^{\text{I}}) &= \frac{f_{\text{signal}}}{T_{\text{dop}}} \left(\left(t_{\text{r,D}}^{\text{I}} + T_{\text{dop}} - \frac{\tilde{\rho}(t_{\text{r,D}}^{\text{I}} + T_{\text{dop}})}{c} \right) - \left(t_{\text{r,D}}^{\text{I}} - \frac{\tilde{\rho}(t_{\text{r,D}}^{\text{I}})}{c} \right) \right) = \\ &= f_{\text{signal}} - \frac{f_{\text{signal}}}{c} \frac{\tilde{\rho}(t_{\text{r,D}}^{\text{I}} + T_{\text{dop}}) - \tilde{\rho}(t_{\text{r,D}}^{\text{I}})}{T_{\text{dop}}} = f_{\text{signal}} - \frac{f_{\text{signal}}}{c} \tilde{\dot{\rho}}(t_{\text{r,D}}^{\text{I}}). \end{aligned} \tag{4.32}$$

The linear relation between both forms of the Doppler observations allows continuing the discussion of certain observation effects only using the range-rate form without losing applicability to the frequency form. For example, the bias of the Doppler observations (b_{dop}) is given in range-rate units. Thus, the complete equation of the Doppler observations is

$$\dot{\rho}(t_{\text{r,D}}^{\text{I}}) = \frac{\tilde{\rho}(t_{\text{r,D}}^{\text{I}} + T_{\text{dop}}) - \tilde{\rho}(t_{\text{r,D}}^{\text{I}})}{T_{\text{dop}}} + b_{\text{dop}}. \tag{4.33}$$

The selection of the models used to compute the range and Doppler observations, together with the strategies followed to represent their imperfections, are now discussed.

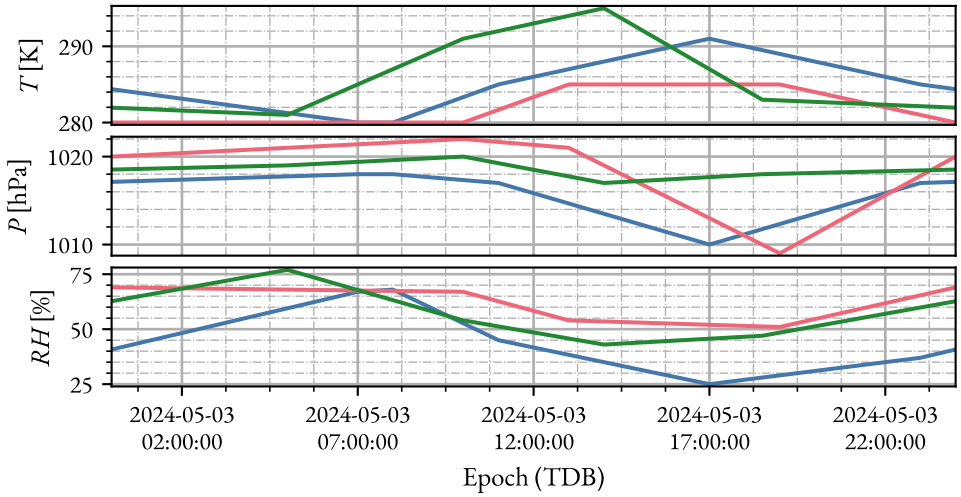

Figure 4.2: Daily profiles of the meteorological data at the 3 ground stations of the nominal station network.

Light-time solution with relativity correction

The geometrical component of range observations is given by a light-time solution method. The GODOT library uses the iterative method described in [120] that accounts for the relative motion between the station and spacecraft participants during the time of flight of the signal. This method includes both the direct relativistic effect induced by a number of user-defined celestial bodies (Moon, Earth and Sun for this thesis), which accounts for the increased path length traveled by the signal between the participants forming the link, and the indirect relativistic effect, which accounts for the difference in the coordinate velocity of light.

Atmospheric models

GODOT also implements the GLobal Neustrelitz Total electron Content Model (NTCM-GL) model to compute the ionospheric delay. This model estimates the vertical Total Electron Content (TEC) considering diurnal, seasonal, geomagnetic, and solar activity dependencies and corrects for the observation's slant. The solar activity data are provided by GODOT in an InterPolation File (IPF). A thorough description of the model can be found in [121]. The wet and dry zenith tropospheric delays are computed in GODOT using the Saastamoinen model, which depends purely on meteorological data at the station's location, that is, the temperature, pressure, and humidity content of the air. To correct for the observations' elevation, the Niell's mapping functions are implemented. The description of the delay model and the mapping functions can be found in [122] and [123], respectively. These models are assumed to have a high-enough complexity to realistically reproduce the atmospheric delays acting on the simulated observations, so no further models are deemed necessary.

The meteorological data used to compute the zenith tropospheric delay using the Saastamoinen model comprise a temperature, pressure, and relative humidity profile, which is different for each of the stations. Figure 4.2 shows the meteorological profiles for the 3 ground stations forming the nominal station network during a sample day. These profiles consist of a series of values of the 3 physical magnitudes over the span of a day, with linear interpolation between consecutive values. The data have been computed based on meteorological records for an average spring day at locations close to the ground stations, and is the same for all days.

Observation modeling errors

In reality, the values of the observations that are computed through models do not perfectly fit the real values of the observations, namely, there is certain error in modelling reality. In order to reproduce this observational modeling errors in the simulator, several effects are included to represent the uncertainty in different aspects.

- *Ionospheric delay.* As stated in [121], the fit of the provided TEC model to the data shows normally distributed residuals with a bias of -0.3 Total Electron Content Units (TECUs), and a RMS of 7.5 TECU. Under the assumption that the residuals are temporally and spatially independent, they can be computed as independent samples from a normal distribution. Thus, a normally distributed random component with a mean of $b_{\text{TEC}} = 0.3$ TECU and a standard deviation of $\sigma_{\text{TEC}} = 7.5$ TECU parameters is added to the model's reference TEC value when simulating an observation.

- *Tropospheric delay.* The value of the tropospheric delay included in the observation depends on the mapping function used to correct for the elevation angle of the link. The simulation of the observation uses the Niell's function, which has a relatively high level of complexity. The computation of residuals uses the simpler cosecant of the elevation angle, which is also provided by GODOT. Additionally, the value of the tropospheric delay at the zenith depends on the meteorological data at the station. To reproduce the imperfect knowledge of the meteorological conditions derived from sensor miscalibration and drift, a normally distributed random bias, constant over periods of 2 hours, is added to the meteorological data used for the simulation of observations. A period of 2 h is a good value to represent daily variations in the factors affecting the meteorological sensors. These factors include illumination conditions, precipitation conditions, perturbations due to human activity, etc. The approximate values of standard deviation used for all three temperature (σ_T) [124][125], pressure (σ_P) [126][127], and humidity content (σ_{RH}) [128][129] are retrieved from literature[3]. The values used in the simulations are included in Table 4.3.

- *White noise.* In addition to the modeled effects that impact the observations, there are other aspects, such as the multipath errors and the noise of the transmitter/receiver antenna, which are not modeled. To account for the uncertainty introduced by these effects, an additive white Gaussian noise component is directly added to the value of the observations. The order of magnitude of the observational noise found when tracking the LRO, reported in [27], serve the nominal value of the standard deviation assigned to the white noise—σ_{ran} for range observations and σ_{dop} for Doppler observations. These values are reported in Table 4.3. It is expected that the observations used in tracking the LNS satellites will be at least as good as those used for the LRO, so the values are conservative.

Other observation parameters

Further assumptions made in the modeling of the observations involve the ambiguity (T_{ran})—namely, the length of the code used for range tracking—, and the count or integration time of Doppler observations (T_{dop}). The ambiguity value is selected assuming a typical code length of 1023 chips with a chipping rate of $\sim$1 kHz, yielding $T_{\text{ran}} \approx 1$ s [130]. The integration time for the Doppler observations is set to $T_{\text{dop}} = 5$ s, which is the value used to track the LRO [27].

[3] It is acknowledged that the conditions presented in the cited references need not be closely comparable to those considered in the analysis at hand. However, obtaining values that are representative of the order of magnitude of the uncertainties is enough for the level of detail of the analysis performed in this thesis.

Table 4.3: Parameters of the observation models.

Parameter	Value	Parameter	Value
Nominal σ_{ran}	1 m	Nominal Δt_{T}	1 μs
Nominal σ_{dop}	1 mm s^{-1}	b_{TEC}	0.3 TECU
Nominal b_{ran}	10 m	σ_{TEC}	7.5 TECU
Nominal b_{dop}	10 mm s^{-1}	σ_T	1 °C
T_{ran}	1 s	σ_P	0.3 hPa
T_{dop}	5 s	σ_{RH}	2%

Finally, some assumptions are made regarding the geometric and hardware delay effects on the observations. The phase center of the antennas on both the ground stations and the satellites are assumed to be perfectly characterized and, thus, known at all epochs. This assumption is justified by the preliminary conditions of the analysis to be performed and the lack of knowledge regarding this aspect. The position of the satellites' antennas are assumed to be coincident with their CoM, as there is no information about the specific geometry of the satellites. The observation biases (b_{ran} and b_{dop}) introduced by both the ground stations' receivers/transmitters and the satellites' transponders and transponder delays (Δt_{T}) are assumed to be constant in time, and equal for all stations and transponders. The specific values used, presented in Table 4.3, derive from the values found in the tracking observations of the LRO [27]. Similarly to the noise values, it is expected that the tracking observations for the LNS satellites will be better or similar than those used for the LRO. Thus, the values in Table 4.3 are conservative.

Summary of the computation of observations

It has been made clear that the computation of the observations during their simulation must not be equal to their computation during the estimation stage to reproduce the imperfections of the models compared to reality. Thus, two different formulations appear for each of both range and Doppler observations.

- Simulation of observations: equations (4.27) and (4.33) are modified to include a white noise component. Additionally, the ionospheric and tropospheric delays are computed using the perturbed TEC and meteorological data following the description given in this section.
- Estimation process: the range and Doppler observations are directly modeled using the (4.27) and (4.33), respectively.

4.3.4. Estimation of parameters

The objective of the estimation algorithm is to minimize the RMS value of the observation residuals computed against a set of observations by varying a group of *solve-for* parameters. Nominally, the list of solve-for parameters includes the initial states and all parameters of the dynamic and observations models which are not considered to be perfectly characterized a priori. In this problem, the nominal solve-for parameters are

- all the components of the satellites' initial states: $\mathbf{x}_{0,i}$ with $i = \{1, \ldots, N_{\text{s}}\}$;
- the reflectivity properties: $C_{\text{r},i}, C_{\text{s},i}, C_{\text{d},i}$ with $i = \{1, \ldots, N_{\text{s}}\}$;

- the observation biases: b_{ran}, b_{dop};
- the transponder delay: Δt_{T}.

However, the list of solve-for parameters can vary attending to the specific conditions of a case. Let $\mathbf{x}_{\text{est}}$ be defined as the vector holding all solve-for parameters. The computation of the observation residual RMS of the k-th satellite is formulated as

$$\text{RMS}_{\text{res},k} = \sqrt{\frac{1}{N_{\text{ran},k} + N_{\text{dop},k}} \left(\sum_{i=1}^{N_{\text{ran},k}} \left(f_{\text{ran},k}(t_i, \mathbf{x}_{\text{est}}) - \rho_{i,k} \right)^2 + \sum_{j=1}^{N_{\text{dop},k}} \left(f_{\text{dop},k}(t_j, \mathbf{x}_{\text{est}}) - \dot{\rho}_{j,k} \right)^2 \right)}, \tag{4.34}$$

where $\rho_{i,k}$ is the i-th range observation, time-tagged at epoch t_i, $\dot{\rho}_{j,k}$ is the j-th Doppler observation, time-tagged at epoch t_j, and $N_{\text{ran},k}$ and $N_{\text{dop},k}$ are the total number of range and Doppler observations in the estimation arc of the k-th satellite, respectively. The functions $f_{\text{ran},k}(t, \mathbf{x}_{\text{est}})$ and $f_{\text{dop},k}(t, \mathbf{x}_{\text{est}})$ have the value of the modeled range and Doppler observations corresponding to the k-th satellite, respectively, time-tagged at any arbitrary epoch t along its orbit. It should be remarked that the dependence of both functions on other problem parameters, which are constant within the same estimation problem, is omitted for the sake of simplicity. The observation residual RMS of all satellites together is computed as

$$\text{RMS}_{\text{res}} = \sqrt{\sum_{k=1}^{N_{\text{s}}} \text{RMS}_{\text{res},k}^2}. \tag{4.35}$$

Then, the formulation of the unconstrained minimization problem is the following,

$$\min_{\mathbf{x}_{\text{est}}} \text{RMS}_{\text{res}}. \tag{4.36}$$

The parameter estimation algorithm used by GODOT to solve the problem stated in (4.36) is a Square Root Information Filter (SRIF). This is a batch sequential estimation filter that, according to [131], is mathematically equivalent to the classical WLS and has a better numerical performance. The implemented SRIF uses a variant of (4.34) in which each observation data set[4] is scaled according to a weighting factor. The values of the weighting factors are discussed in § 4.5. The detailed description of the estimation algorithm is of no special relevance to the thesis, so the interested reader is referred to [132] for its complete formulation.

During the first iteration of the estimation process, it is needed to use an initial guess for the value of the initial state vector to be estimated. As the required OD accuracy of the LNS is of the order of meters in position and millimeters per second in velocity, the chosen uncertainty in the initial state has a 1σ value of $\sim$10 m in position and $\sim$10 mm s^{-1}. Assuming that the estimation process is unbiased—that is, that the expected estimated orbit is the reference orbit—, the components of the initial guess can be obtained as independent samples of a normal distribution with a mean of 0. To approximate the stated level of uncertainty, values of $\sigma_{\text{pos}} = 10/\sqrt{3}$ m and $\sigma_{\text{vel}} = 10/\sqrt{3}$ mm s^{-1} are considered for the distribution of each of the position and velocity components, respectively.

[4] An observation data set contains the batch of either range or Doppler observations generated in a continuous pass of a satellite over a single station. The satellite going out of view from the station, even if only for its occultation by the Moon, interrupts the pass and splits the observations in different data sets.

It is assumed that there is some a priori knowledge about the reflectivity properties associated with the satellites' SRP models. Thus, the initial guesses for those parameters are computed as samples from normal distributions with means of 0 and with standard deviations of 5% of the true value of the parameters. This means that $\sigma_{C_r} = 0.0675$, $\sigma_{C_s} = 0.0075$ and $\sigma_{C_d} = 0.0025$. The initial guess for the observations biases and the transponder delays is set to 0, pessimistically assuming that there is no a priori knowledge of their values.

Two other parameters are involved in the estimation process. The first one is the outlier threshold (Θ_{out}), which is used to decide which observations to accept and which to reject within an observation data set. An observation is rejected if its residual y meets the condition

$$|y - \overline{y}_{\text{acc}}| > \Theta_{\text{out}} s_{y_{\text{acc}}}, \tag{4.37}$$

where $\overline{y}_{\text{acc}}$ is the mean of the residuals of the accepted observations in the data set, and $s_{y_{\text{acc}}}$ is the sample standard deviation of the residuals of the accepted observations in the data set. It should be noted that the selection of the accepted and rejected observations relies on knowing which are the residuals of the accepted observations, thus requiring an iterative process to make the selection. The process is initialized considering all observations as accepted. From there, the outliers are progressively rejected until two consecutive iterations have the same identified outliers. The second parameter is the convergence threshold (Θ_{conv}), which serves to stop the estimation process when sufficiently close to a solution of (4.36). The convergence of the estimation is assumed when the residual RMS of each observation data set shows a relative variation relative to the previous iteration below Θ_{conv}. The selection of values for these two parameters is discussed in § 6.2.

4.4. Software implementation

To perform the entire OD simulations, a software layer is to be developed to merge the different capabilities provided by GODOT[5] and GENEOS[6], accessing them through their Python interface. GENEOS, which is built on top of GODOT, is a suite of programs with standalone functionalities [133]. The programs in GENEOS are intended to be used for Earth-orbiting satellites, so their application to spacecraft in lunar orbit may require modifications.

Performing the end-to-end simulation depicted in Figure 4.1 requires creating a software tool to manage the use of the different GODOT and GENEOS functionalities. This is done from an Object Oriented Programming (OOP) approach, through custom classes that represent the different elements of the problem (satellite constellation, ground station network, etc.). This simulator layer handles the interaction with GODOT and GENEOS in the background, simplifying the setup of the simulation conditions and the analysis of large batches of simulation cases. To achieve this, it changes the way in which the inputs to the simulation are defined, modifies already existing functionality, and implements new functionality where needed. It also serves to evaluate and visualize the defined FoMs. The GODOT version used in the tool is *1.4.0*, and the GENEOS version is *1.8.0*. The Python version used to develop the simulator layer is *3.10.13*.

Interfaces with GODOT/GENEOS

The simulator layer works, among other things, with the management of a variety of files. The reason for this is that the interface with the GENEOS programs is based entirely on files. Additionally, certain setup tasks

[5] `https://godot.io.esa.int/`

[6] `https://gfe.io.esa.int/geneos/`

related to GODOT can be more easily performed using files. The configuration files inputted to GODOT and GENEOS are provided in JavaScript Object Notation (JSON) format. Two types of orbit files are handled: Orbit Ephemeris Message (OEM) [134], which is an ASCII text file format, and IPF, ESOC's flight dynamics internal binary file format. Other types of data outputted by GENEOS programs, such as time series of observations, are stored in JSON format as well.

Orbital propagation setup

The GODOT library is used to propagate the reference orbits of the satellite constellation. However, GODOT's implementation of orbital propagation does not allow propagating several spacecraft at a time. For that reason, the consideration of more than one satellite requires that the same dynamic models are instantiated for each of the spacecraft separately and that each of the propagations are triggered individually. All this process is controlled by the simulator layer, simplifying the handling of satellite constellations in GODOT.

Computation of visibility

The *Computation of visibility* for each ground station-satellite pair is implemented as part of the simulator layer. The visibility of a station-satellite pair considers two factors.

1. The elevation of the satellite as seen from the station's location. The elevation is computed using the station's topocentric frame as the angle formed between the station-satellite line of sight and the XY-plane. A station can see a satellite if its elevation is greater or equal than $e_{\min}$.
2. The occultation by the Moon. The orbital motion of the satellite may lead to periods during which the station-satellite line of sight is blocked by the Moon. This happens when two conditions are met. Figure 4.3 depicts this conditions through a schematic representation. First, the angle α between the station-satellite line of sight and the station-Moon's center direction is smaller than $\alpha_{\min} = \arctan\left(R_{\mathrm{L}}/d_{\mathrm{L}}\right)$, where R_{L} is the average lunar radius and d_{L} is the instantaneous distance between the station and the Moon. Second, the distance from the station to the satellite is greater than that from the station to the Moon's center.

A satellite is visible from a station whenever its elevation is above $e_{\min}$, and it is not occulted by the Moon. The outputs of these computations are a series of epoch pairs defining the start and end of the visibility intervals for each independent station-satellite pair. These results are printed to a JSON file following the format required by GENEOS for their use in the *Simulation of observations*.

Random Number Generators (RNGs)

The simulation of observations involves four different RNGs, each of which is used to compute

- the initial guess deviation of the solve-for parameters for the first iteration of the estimation process,
- the biases affecting the meteorological data,
- the random component of the TEC value of the ionospheric delay,
- the white noise component of the observations.

To ensure the statistical significance of the results included in this thesis, the simulation of each of the OD cases is run several times (more about this on Appendix B), using a different seed for the RNGs in each of the runs. Apart from this, in order to ensure that the random sequences used in each of these four aspects of the simulation

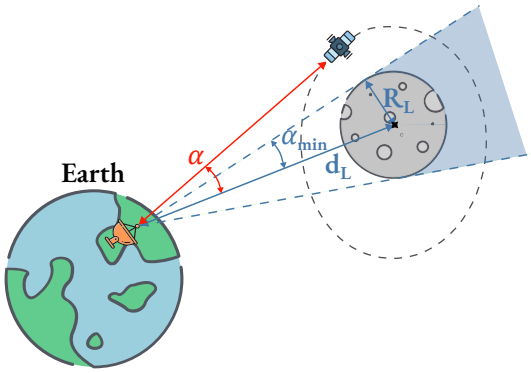

Figure 4.3: Schematic representation of the geometric conditions for the occultation of a station-satellite link by the Moon. The shaded area in the image represents the region where a satellite would be occulted from the station.

Table 4.4: Values of the seeds given to each of the RNGs in the first simulation run.

RNG	Seed
Meteorological data	1000
Initial guess deviation	2000
TEC of ionospheric delay	3000
White noise	4000

process are different, the different RNGs in the same simulation run use a different seed as well. By doing this, any possible correlation effect between the four random factors is avoided, leading to a more realistic representation of the randomness involved in the process.

The seed used for each of the RNGs in the first random run of each of the cases is presented in Table 4.4. The seeds assigned to the latter of two consecutive runs can be computed by adding 1 to the seeds of the former run. E.g., the seed of the RNG involved in the randomization of the meteorological data has a value of 1001 in the second run, 1002 in the third run, etc.

Computation of the FoMs

The computation of all the FoMs used to evaluate the system's performance uses newly implemented code. The procedure followed for their computation is the one presented in § 4.2. As specified in that section, the FoMs are evaluated during the prediction arc, unless specified differently. During that arc, the different satellites forming the LNS may go in and out of view from the receiver's location in the LSP. To account for that, the software checks the minimum elevation condition at each epoch of the time series, as explained for the computation of the visibility from the ground stations, using the topocentric frame at the lunar location. Only visible satellites contribute to the computation of the user-related FoMs at each epoch. Epochs without 3-fold coverage of the LSP are not considered for the computation of either the PDOP or the $\Delta\mathbf{r}_r$, so they do not have an impact on their final RMS value.

Each of the random runs of a single OD configuration is a different replication of the same OD case. The combination of the results of the several runs can serve to produce a more precise estimate of the FoMs associated with that OD configuration. This only adds value for those FoMs affected by random effects, which are $\overline{\text{RMSE}}_{\text{pos}}$, $\Delta r_{\text{r,RMS}}$ and the run time. Both the PDOP_{RMS} and ξ are geometrical values that are not affected by any simulated random effect, thus not benefitting from it. A first approach to merge the results of all random runs into an estimate of the FoMs could be to compute the mean (and the associated standard deviation) of the series of FoM values evaluated individually at each run. That would serve to estimate the average $\overline{\text{RMSE}}_{\text{pos}}$ and $\Delta r_{\text{r,RMS}}$ over

one prediction arc. However, the OD accuracy requirement of the system (introduced in Chapter 3) and the sought user positioning accuracy (mentioned in § 2.1) are not expressed in terms of a single prediction arc, but of the continuous operation of the system. To more representatively estimate the "long-term behavior" of the LNS system, the different random runs can be considered as hypothetically sequential. The term *hypothetically* is used to highlight the fact that they are truly not sequential—the defining epochs are the same for all of them; the initial states are the same, thus not necessarily matching the final state of any other run; and the initial relative position with respect to the Earth does not change. Nevertheless, they can be understood as different temporal instances of repetitive OD conditions. Doing so introduces the possibility to compute the RMS values of the FoMs over the prediction arcs of all random runs as if they were a singular time series. It must be noted that this is equivalent to computing the RMS of the series of $\overline{\mathrm{RMSE}}_{\mathrm{pos}}$ and $\Delta r_{\mathrm{r,RMS}}$ values of the individual random runs. Thus, the estimates of the FoMs are computed as

$$\begin{aligned} \widehat{\overline{\mathrm{RMSE}}}_{\mathrm{pos}} &= \sqrt{\frac{1}{N_{\mathrm{runs}}} \sum_{i=1}^{N_{\mathrm{runs}}} \left(\overline{\mathrm{RMSE}}_{\mathrm{pos}}^{(i)}\right)^2}, \\ \widehat{\Delta r}_{\mathrm{r,RMS}} &= \sqrt{\frac{1}{N_{\mathrm{runs}}} \sum_{i=1}^{N_{\mathrm{runs}}} \left(\Delta r_{\mathrm{r,RMS}}^{(i)}\right)^2}, \end{aligned} \tag{4.38}$$

where $\overline{\mathrm{RMSE}}_{\mathrm{pos}}^{(i)}$ and $\Delta r_{\mathrm{r,RMS}}^{(i)}$ represent the value of the corresponding FoM for the i-th random run. This formulation is used for the computation of any result in this thesis that involves several random runs. Thus, hereafter, it is assumed that the presented values are estimates and the hat is omitted in the notation for the sake of simplicity. The run time of the estimation process of any single case is computed as the arithmetic mean of the individual run times of each random replication for that case.

The use of several random runs in the estimation of the FoMs requires the examination of the convergence of the estimated quantities to a stable value. A convergence analysis can serve to determine whether a certain number of random runs is enough or not to obtain statistically significant values. Due to its nature, this thesis work involves the evaluation of many OD configurations, each of them with its associated convergence analysis. Presenting the convergence considerations together with the more relevant results of the thesis would be tedious for the reader. To avoid this, the convergence analyses and conclusions of almost all the results of this thesis are contained in Appendix B. Mentioning the number of runs used to produce the different results of further sections is avoided to prevent repetition, but are included in Appendix B.

Modifications to the GODOT/GENEOS source code

The core functionality used by the simulation tool is directly provided by the GODOT library. This library implements the models and algorithms involved in all the steps of the process depicted in Figure 4.1. The observation models present in GODOT are prepared to compute deterministic values of the different components affecting the observation. However, for the simulation of observations as devised in § 4.3.3, certain models—the tropospheric and ionospheric delay models—, require the incorporation of an optional random factor. Additionally, it is also needed to have control over the RNGs' seeds. These modifications are implemented in the GODOT source code as a part of this thesis work.

Apart from GODOT, the simulation tool uses 3 GENEOS programs, which are now described together with their corresponding modifications (if any).

- ***ObsSim*** serves to facilitate the handling of the generation of observations (*Simulation of observations* block in Figure 4.1). Using the already propagated orbits and their visibility intervals from each of the stations, *ObsSim* computes the time series of observations—range, Doppler, and/or direction observations—and prints them to a file. To do so, the program manages the configuration of the underlying GODOT models to include the desired effects on the computation of the observations. Thus, the source code of the program requires modifications to handle the configuration of the random components of the atmospheric models. Further modifications are required to be able to customize the simulation process to the extent required by this thesis. The configuration of the light-time computation model is adapted so that a user-defined model can be used to simulate the observations. Lastly, the capability to include random white noise in the observations is already implemented in *ObsSim*, but there is no control over the seed of the RNG used to sample it. That feature is also implemented for this thesis.

- ***Odp*** is the GENEOS program used to perform OD using a SRIF algorithm, as discussed in § 4.3.4. It performs the tasks encapsulated in the *Parameter estimation* and *Propagation of the estimated constellation* blocks of the diagram in Figure 4.1. The OD takes as inputs the simulated observations obtained from *ObsSim* and the initial guesses of the solve-for parameters, as well as any other model configuration required for the propagation of the orbits during the estimation and the generation of the modeled observations during the computation of residuals. *Odp* does not require any specific modification worth mentioning to be used in the context of this thesis.

- ***Prepro*** is a program that encapsulates a variety of observation preprocessing functionalities, among which are calibrating the observations, adding different delays and biases, modifying the observation uncertainties, and changing the observation representation (for example, from the Doppler frequency formulation to the range-rate formulation). The use made by the simulation tool of the *Prepro* program is minimal, as it only serves to compute tropospheric correction data from an inputted set of meteorological data. Similar to *Odp*, it requires no major modifications for this purpose.

Apart from any program-specific adaptations, it is also necessary to review and correct certain assumptions made in the GENEOS source code, such as the change from a terrestrial time scale to a barycentric time scale.

All the mentioned changes are applied to the C++ source code of GODOT and GENEOS, as well as to the Python binding where needed. As the described modifications do not involve the implementation of any new models, no specific verification or validation activities are required, as the already implemented models in GODOT are already tested by the developers (see the comparison against the NAvigation Package for Earth Orbiting Satellites (NAPEOS)[7] and the Advanced Modular Facility for Interplanetary Navigation (AMFIN) [8]). Moreover, the OD capabilities available in GENEOS are being subjected to a phase of operational validation by comparing against products of ongoing missions generated with NAPEOS [133]. The Sentinel-1A mission has already transitioned to using GENEOS as the main tool for operations. This reinforces the confidence placed in the validity of the results obtained from GENEOS—and, consequently, from GODOT—, and serves as a strong proof that a dedicated verification of the implemented models and algorithms is not required.

[7] `https://godot.io.esa.int/docs/1.4.0/comp/napeos.html`.
[8] `https://godot.io.esa.int/docs/1.4.0/comp/amfin.html`.

Table 4.5: Nominal orbital configuration of the satellite constellation ($N_s = 4$), given by the Keplerian elements with respect to the MER frame.

	Sat. 1	**Sat. 2**	**Sat. 3**	**Sat. 4**
Semi-major axis (a) [km]	6150	6150	6150	6150
Eccentricity (e) [-]	0.6	0.6	0.6	0.6
Inclination (i) [°]	51.7	51.7	51.7	51.7
RAAN (Ω) [°]	0	90	0	90
Argument of pericenter (ω) [°]	90	90	90	90
Mean anomaly (M) [°]	0	90	180	270

4.5. Nominal simulation setup

In order to perform the simulations reported in this thesis, a nominal setup is defined. This nominal simulation setup is used as the baseline for most of the simulated cases and has been retroactively established using findings from the following chapters, mainly from Chapter 6. Any case-specific modifications to this nominal setup is mentioned where applicable.

This section is devoted to the justification and specification of the values of the problem parameters that constitute the nominal simulation setup. The nominal values of many parameters are already introduced in previous sections of this chapter. Thus, this section only discusses those parameters that have not been given a value in advance, and provides references to the pertinent elements of this chapter for the rest of the parameters.

Satellite and constellation properties

The values selected for the properties of all satellites, similar to those of the Galileo satellites, are given in Table 4.2. The nominal orbital configuration of the constellation is based on the suggested values found in the literature for the instantiation of LNSs. Table 4.5 presents the Keplerian elements [112] of the nominal 4-satellite configuration, specified with respect to the lunar MER frame, inspired by [13] and [135], both of which propose similar constellation configurations. It is acknowledged that constellations consisting of more eccentric orbits with a higher semi-major axis are present in the literature [67]. However, the greater popularity of the constellation presented in Table 4.5 motivates is selection over any other options. Moreover, the selected configuration has a lower periselene altitude. This means that it is more strongly affected by the irregular lunar gravity field, expectedly creating an overall more demanding case for OD. Nevertheless, as the analysis performed in this thesis explores different orbital configurations, the selection of the nominal one is not a crucial decision. The nominal orbits have a period of approximately half a day, which is relevant to compare against the length of the estimation and prediction arcs.

For cases in which a single satellite is enough, as is the case of the verification in § 5.1 and the sensitivity analysis in Chapter 6, the orbit of *Satellite 1* from Table 4.5 is used.

Orbital propagation parameters

The sensitivity analysis reported later in this thesis serves to derive the required values of the parameters involved in the environmental and dynamic models used in the propagation of the reference orbit. The analysis concludes

Table 4.6: Nominal value of the dynamic and environmental parameters for the propagation of both the reference and estimated orbit.

Parameter	Value	Parameter	Value
$DO^{\mathrm{r}}_{\mathrm{L}}$	100	$DO^{\mathrm{e}}_{\mathrm{L}}$	20
$DO^{\mathrm{r}}_{\mathrm{E}}$	2	$DO^{\mathrm{e}}_{\mathrm{E}}$	2
tol^{r}	10^{-13}	tol^{e}	10^{-10}

Table 4.7: Coordinates of the nominal ground stations. Coordinates of terrestrial stations are given with respect to the ITRF frame, while coordinates of lunar locations are given with respect to the MER frame.

Station name	**X** [km]	**Y** [km]	**Z** [km]
Cebreros (CB)	4146.734	-370.174	4116.879
Malargüe (MG)	1823.343	-4850.457	-3708.972
New Norcia (NN)	-2414.067	4907.869	-3270.605
Lunar South Pole (LSP)	0.000	0.000	-1736.000

that only the gravitational effect of the Moon (L), the Earth (E), and the Sun (S) are required to propagate the reference orbit to the desired accuracy. The reader is referred to Chapter 6 for a detailed description of the strategy followed to obtain these values, which are given in Table 4.6.

Table 4.6 also contains the values of the propagation parameters pertinent to the estimated orbit. These values are chosen based on the intuition gained from the sensitivity analysis. However, similarly to the orbital configuration, the most impactful parameters of the propagation of the estimated orbit—$DO^{\mathrm{e}}_{\mathrm{L}}$ and tol^{e}—are inside the scope of the design analysis of this thesis, and, thus, their particular values are not of great importance.

The DE 440/441 ephemerides source is used to obtain those environmental parameters that refer to celestial bodies not appearing in Table 4.6, such as the gravitational parameters.

Ground station properties and user data

The nominal configuration considers a network of 3 ground stations ($N_{\mathrm{GS}} = 3$) placed at the locations of the ESA's Deep Space Antennas (DSAs)[136]. Table 4.7 provides the coordinates of these 3 stations. The value of the minimum elevation for the link between a satellite and a station is the same for all stations, and equal to $e_{\mathrm{min}} = 5°$. The minimum observation elevation is a parameter of the design analysis, so its nominal value is not of special relevance.

To compute the user-related FoMs, the user's location at the LSP is included as a station. Table 4.7 contains the coordinates of the LSP location. The nominal minimum elevation for the navigation link between a satellite and a user on the lunar surface is $e_{\mathrm{min,LSP}} = 10°$, to account for the irregular lunar topography.

Observation properties and meteorological data

The values of most properties pertaining to the computation of observations are provided in Table 4.3, except for f_{signal} and T_{obs}. Both of these parameters are considered for the design analysis, so there is no thorough reasoning

Table 4.8: Nominal value of the OD parameters.

Parameter	Value	Parameter	Value
w_{ran}	0.1 µm	w_{dop}	0.1 nm s^{-1}
w_{pos}	10 m	w_{vel}	10 mm s^{-1}
$w_{b_{\text{ran}}}$	10 m	$w_{b_{\text{dop}}}$	10 mm s^{-1}
$w_{\Delta t_{\text{T}}}$	1 µs	$w_{C_{\text{r}}}$	0.01
$w_{C_{\text{d}}}$	0.001	$w_{C_{\text{s}}}$	0.001
Θ_{out}	5	Θ_{conv}	0.001

behind the selection of their nominal values. The literature shows, as discussed in Chapter 2, that the X-band is the most popular choice of frequency band for the TT&C signal. This band comprises the range 8–12 GHz, and the selected nominal frequency value is $f_{\text{signal}} = 8$ GHz. As no applicable reference value for T_{obs} has been found in the literature, a nominal value of $T_{\text{obs}} = 5$ min is selected.

All meteorological input data is discussed in § 4.3.3, with the nominal daily profiles given in Figure 4.2, and their corresponding uncertainty values are provided in Table 4.3.

OD parameters

The nominal values assigned to the weight of the range and Doppler observations derive from a tuning process performed during the verification phase to ensure the convergence of the estimation process for the whole variety of simulation cases considered in this thesis. Table 4.8 shows the selected values ofthe observation weights, together with the weights assigned to each of the solve-for parameters. The solve-for parameter weights are based on the level of confidence in their initial state. E.g., assigning $w_{\text{pos}} = 10$ m implies that the initial guess of the position components of the initial state has an expected accuracy of 10 m. Note that the values of w_{pos} and w_{vel} are coherent in order of magnitude with the uncertainty in the initial state—σ_{pos} and σ_{vel}—, introduced in § 4.3.4. Something similar happens with $w_{b_{\text{ran}}}$ and $w_{b_{\text{dop}}}$, whose values are similar to those of the true observation biases. As the estimation is especially sensible to the reflectivity properties of the satellites' SRP model, the values of $w_{C_{\text{r}}}$, $w_{C_{\text{d}}}$ and $w_{C_{\text{s}}}$ are smaller than the values of $\sigma_{C_{\text{r}}}$, $\sigma_{C_{\text{d}}}$ and $\sigma_{C_{\text{s}}}$, respectively.

Finally, the threshold values used to check both the convergence of the estimation and the observation outliers, which are also included in Table 4.8, derive from the sensitivity analysis reported in Chapter 6.

Propagation, estimation, and prediction epochs

The epoch boundaries of the propagation, estimation, and prediction arcs are defined in terms of a reference epoch, t_{ref}. Both the estimation (T_{est}) and prediction arcs (T_{pred}) of the nominal configuration consist of two immediately consecutive 1-day-long periods, the estimation arc starting at t_{ref}. Accounting for the fact that nominal orbital period is 0.5 d, using $T_{\text{pred}} = 1$ d has the advantage of being a multiple of T_{const}, which means that the computation of the user-related FoMs is more realistic. These are initial guesses of the values, which are later assessed during the design analysis.

For the cases that do not consider a prediction arc, the simulation tool requires that the period over which the observations are simulated is completely comprised by the estimation arc, with a margin long enough to ensure

Table 4.9: Nominal value of the defining epochs of the simulation process.

t_{ref} = 2024-05-03T12:00:00.000 TDB, $T_{est} = T_{pred} = 1\,d$

Epoch	Value	Epoch	Value
Start estimation	t_{ref}	End estimation	$t_{ref} + T_{est}$
Start prediction	$t_{ref} + T_{est}$	End prediction	$t_{ref} + T_{est} + T_{pred}$
Start obs. simulation	$t_{ref} + 50\,s$	End obs. simulation	$t_{ref} + T_{est} - 50\,s$
Start propagation	$t_{ref} - 50\,s$	End propagation	$t_{ref} + T_{est} + T_{pred} + 50\,s$

the proper resolution of the light-time between the stations and the satellites. Thus, the starting epoch for generating observations is not coincident with the starting epoch of the estimation arc, but occurs 50 s later. Similarly, the final epoch for generating observations is 50 s earlier than the final epoch of the estimation arc. Lastly, the propagation arc of the reference orbit is chosen so that it comprises all other arcs, with a small margin to ensure that the reference orbit is properly defined at any required epoch of interest. Thus, the starting epoch of the propagation is 50 s earlier than the start of the estimation arc, and the final epoch of the propagation is 50 s later than the end of the prediction arc. Following these criteria, the values of the epochs that define the boundaries of the arcs are introduced in Table 4.9.

5

Verification and Validation

This chapter is dedicated to the description of the verification and validation tasks, discussed separately in two sections. The first section starts by explaining the approach and the specific considerations applicable for the verification of the simulation tool, to then report the results that show the proper simulation of the OD process. The second section is devoted to the validation of the tool by comparing the results with data from the GRAIL mission. Both the verification and validation processes aim to acquire confidence in the soundness and validity of further simulation results presented in this thesis.

5.1. Verification

The purpose of the verification tasks reported in this section is to examine the coherence of the results produced with the simulator described in Chapter 4. These tasks cover only the verification of the simulator layer implemented for the development of this thesis, as the more basic functionality on top of which it is built, provided by the GODOT package and the GENEOS programs, is considered to have been tested extensively enough to grant confidence in the results.

The approach followed for the verification of the simulator tool distinguishes three elements to test. Firstly, the orbital propagation inside the estimation module (performed using the GENEOS *Odp* program) is compared to the propagation of the reference orbit (performed directly with GODOT), expecting them to be effectively equivalent with an accuracy several orders of magnitude below the OD accuracy requirement of 3 m. Then, the coupling between the observation simulation module and the estimation module is tested by performing a complete simulation using ideal observations—no noises, biases, atmospheric effects, etc. Theoretically, the estimated orbit in this setup should be coincident with the reference orbit, thus serving to test the proper functioning of the entire simulation process in a simplified scenario. Finally, several estimation processes are performed adding *non-ideal* effects to the observations, checking the sensibility of the results and their coherence with the expected outcome based on a priori knowledge.

Table 5.1: Orbital configuration cases for verification.

Case ID	Element	Value
OREF	—	—
OA1	a	4650 km
OA2		9150 km
OE1	e	0.3
OE2		0.7
OI1	i	35°
OI2		90°
OR1	Ω	45°
OR2		90°

Table 5.2: Dynamic model cases for verification.

Case ID	Model description
D1	Lunar point mass gravity
D2	Lunar SH up to D/O 100
D3	Lunar SH up to D/O 100 + Terrestrial SH up to D/O 2 + Sun point mass
D4	Lunar SH up to D/O 100 + Terrestrial SH up to D/O 2 + Sun point mass + SRP ($\delta_U = 0$) + relativistic effects

5.1.1. Verification setup

The verification simulations consider a single lunar satellite. The inclusion of a greater number of satellites would not impact the results because the propagation and OD of each satellite is independent of the rest. To fully test the simulation processes, a series of test cases is defined to cover both different orbital configurations and dynamic model complexities. The objective of covering this variety of cases is to ensure that the verified behavior is applicable to the results appearing in both Chapter 6 and Chapter 7 regardless of the simulated scenario. In terms of orbital configuration, the test cases are defined as individual modifications to the Keplerian elements of the nominal orbit defined in § 4.5. Table 5.1 shows the modifications that define each of the cases.

Similarly, a second series of cases represents different levels of complexity of the dynamic and environmental model used to propagate the orbit. Table 5.2 presents a description of the dynamic models used in each of the cases. For all cases, the relative integration tolerance is set to $tol^r = 10^{-13}$, which is enough to properly represent the dynamics of the problem, as later discussed in Chapter 6.

The test cases for the verification are all the possible combinations of the orbital configuration cases in Table 5.1 and the dynamic model cases in Table 5.2. As the verification only aims at testing the proper behavior of the simulation + estimation process, no prediction arc is considered ($T_{\text{pred}} = 0$), and the FoMs are evaluated over the estimation arc. For the verification steps involving estimation, unless stated differently, the observations contain no noise, biases, delays, or atmospheric effects (both tropospheric and ionospheric effects are completely removed). The differences in simulation setup for verification with respect to the nominal setup of § 4.5 are summarized in Table 5.3. Furthermore, to evaluate the proper behavior of the simulation tool, the dynamic models of Table 5.2 are applied equally to the propagation of both the reference orbit and the estimated orbit. This suppresses the differences in dynamics and isolates the desired effects to test.

The accuracy of the estimation is assessed by means of the position RMSE (RMSE_{pos}) over the estimation arc—an adaptation of (4.2) to a single satellite, as there are no multiple satellites to compute the mean from. It should be noted that the first verification task is a pure comparison between propagations. For those simulations, because there is no estimated orbit, the RMSE_{pos} is computed using the difference between both propagations.

Table 5.3: Updates to the simulation parameters for verification.

Parameter	Value	Parameter	Value
T_{pred}	0	Δt_{T}	0
σ_{ran}	0	σ_{dop}	0
b_{ran}	0	b_{dop}	0

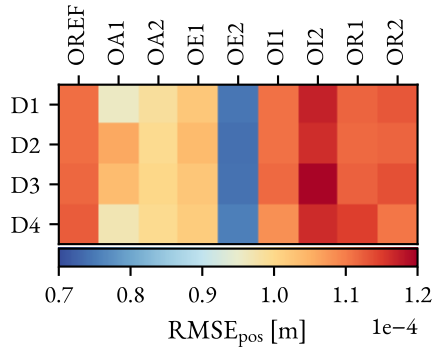

Figure 5.1: RMS of the position error between the propagation with GODOT and with GENEOS *Odp*.

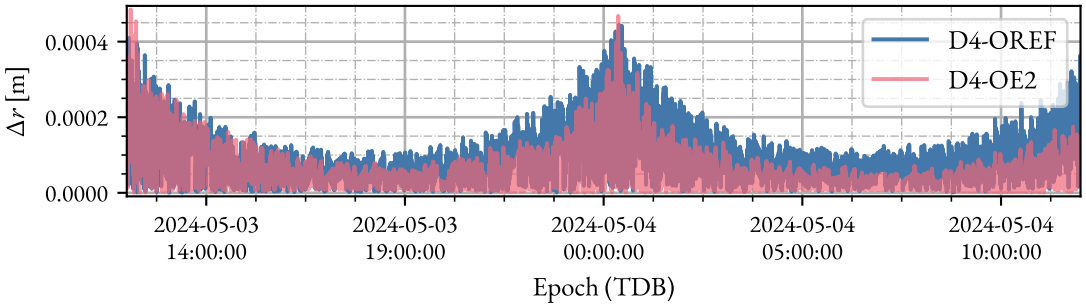

Figure 5.2: Time evolution of the position difference between the propagation using *Odp* and GODOT for two test cases.

5.1.2. Propagation with the OD module

The first verification step is to evaluate the differences, if any, between the propagation performed directly accessing GODOT functionality and that done by the *Odp* program. To do so, the same orbit is propagated using the same dynamic model following both strategies and the 3D position difference between both orbits is used for the comparison.

Figure 5.1 shows the RMS of the position differences between the two propagations for all possible combinations of cases. The error between orbits is of the order of $\sim 10^{-7}$ km. This corresponds to a relative error of $\sim 10^{-11}$, considering that $a \approx 6000$ km. Figure 5.2 shows the time evolution of the position difference for two specific combinations of cases—D4-OREF as a representation of the average case, and D4-OE2 as a representation of the OE2 cases, which show a lower RMSE$_{\text{pos}}$. It can be seen that, for both cases, the difference is mostly noise, which can be attributed to the numerical error both in the propagation and the interpolation of the orbit, with a varying amplitude. Considering the initial true anomaly and the orbit's period (approximately half a day), the noisy difference grows close to the pericenter and reduces close to the apocenter. The cause of these differences along the orbit is the increased sensitivity of the satellite's dynamics to minimal integration errors at low altitudes—the lunar gravity is stronger and higher degree and order terms of its SH expansion become more relevant. The cases with a higher eccentricity have a quicker pass through pericenter, so the time spent at low lunar altitudes is shorter, resulting in a smaller error RMS. In any case, the sufficiently small values of the differences at any of the epochs in the estimation arc do not incite further investigation of this effect.

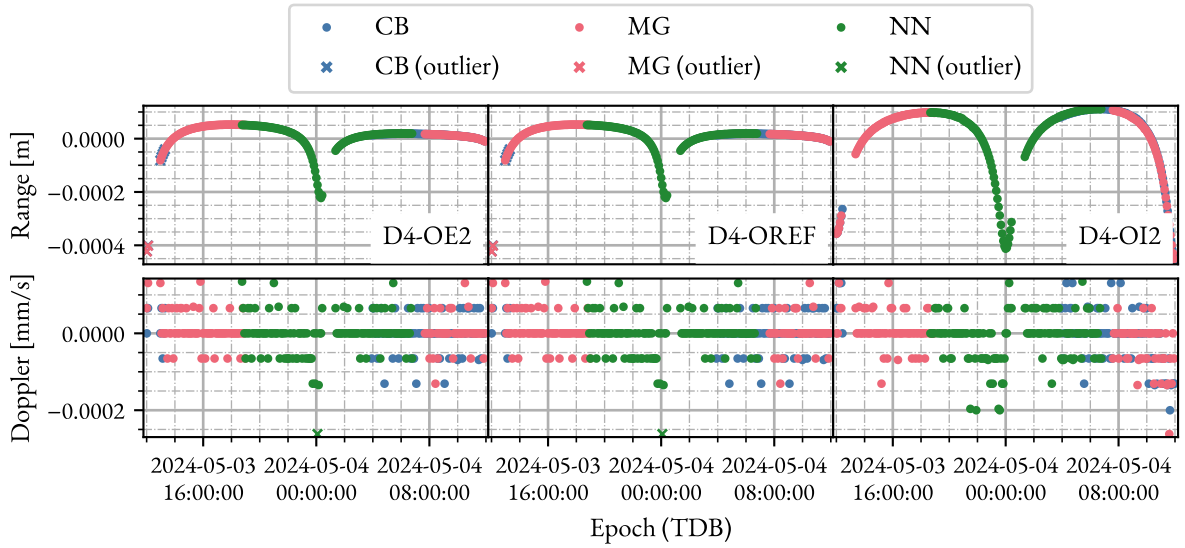

Figure 5.3: Observation residuals between the propagation using *Odp* and GODOT for 3 different test cases.

Figure 5.3 depicts the behavior of the observation residuals for the test cases with lowest (D4-OE2) and highest (D4-OI2) RMSE_{pos} using the most complex dynamics, as well as for the D4-OREF case, which serves as a representation of the average case. It must be noted that the three test cases compared share the same dynamic model so that the comparison is fair. The order of magnitude of the residuals is in accordance to the position difference observed in Figure 5.2. The range residuals show a trend that resembles the time evolution of the amplitude of the position difference noise. The Doppler residuals are grouped in several discrete levels. The reason for this traces back to the finite precision of the floating-point representation of numbers. The Doppler observations in range-rate form are computed through a difference of ranges between the start and end of the Doppler integration time. The ranges between ground stations on the Earth's surface and lunar satellites are of the order of 10^8 m, meaning that their precision in double-precision floating-point representation is of $\sim 10^{-7}$ m. Accounting for the integration time being $T_{\text{dop}} = 5$ s, the maximum achievable precision of the Doppler observations is $\sim 10^{-5}$–10^{-4} mm s^{-1}, which is coherent with the residuals in Figure 5.3.

From the presented results, it can be concluded that the propagation carried out inside the *Odp* program and directly with GODOT are equivalent and, thus, this difference has no impact on further results and conclusions.

5.1.3. Estimation with ideal observations

The following step in the verification is testing the end-to-end simulation process by performing OD with ideal observations. This means that the simulated observations do not include noise, biases, or atmospheric effects, but purely include the geometrical magnitudes that range and Doppler observations theoretically represent with the added relativistic effect. Using these ideal observations means that the residuals are expected to be 0 if the reference and estimated orbits are identical. The estimation considers the initial state vector and the satellite's reflectivity properties as solve-for parameters. As this batch of simulations considers neither observational noise nor atmospheric effects, the only random effect present in them is the deviation in the initial guess of the solve-for parameters.

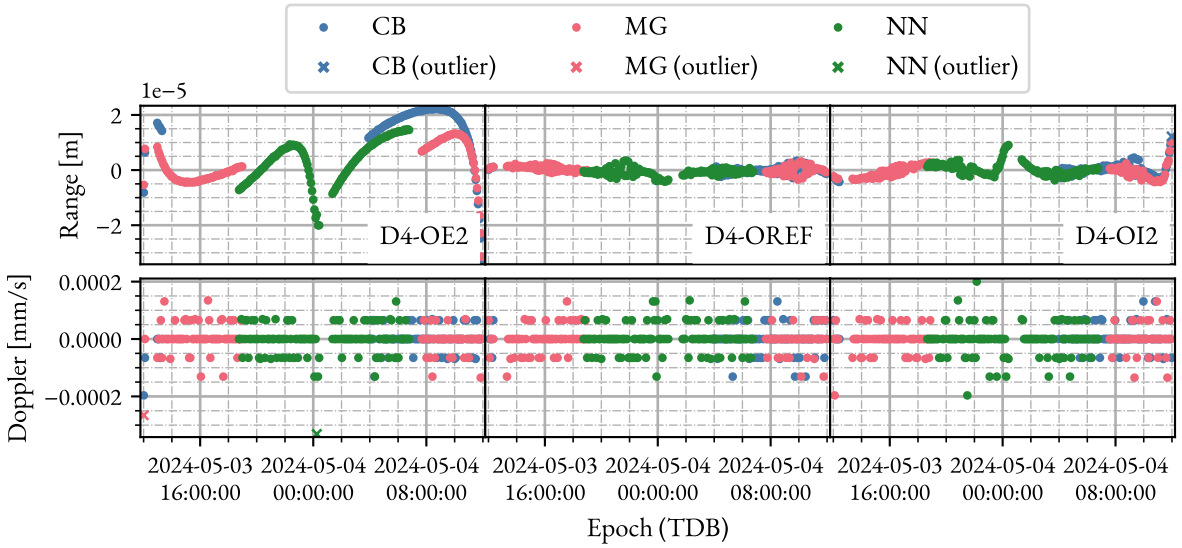

Figure 5.4: Observation residuals for the estimation with ideal observations for the first random run of 3 cases.

Figure 5.4 shows the reduction of the residuals relative to those in Figure 5.3 after the estimation with ideal observations. This implies that the estimation algorithm improves the solution given the minimization problem formulated in § 4.3.4. Figure 5.5 presents a summary of the RMSE_{pos} values for all test cases. The comparison of Figure 5.5 with Figure 5.1 shows that performing OD simulations using ideal observations leads to accuracies in the estimated orbits similar to the propagation accuracies. The combination of cases D4-OE2 is an exception to this, with the estimated orbit showing a mean RMSE_{pos} more than 3 times as large as the value computed from comparison of propagations. Still, the range residuals achieved with the estimation are one order of magnitude smaller than those without estimation. This implies that the orbital position differences decrease along the tracking line of sight, but increase in the orthogonal directions, likely due to the sensibility of the OD to the complexity of the spacecraft dynamics at low altitudes. The OE2 cases have the lowest periselene altitude among all orbit configuration cases, thus feeling the effect of the non-spherical lunar gravity more strongly. The D4 cases also consider other effects like the SRP, not present in other configuration cases of the dynamics, which complicate the dynamics even further. Because of this, the changes done by the estimation algorithm to $\mathbf{x}_{\text{est}}$ in order to reduce the range residuals introduce a comparable or even larger error in the orthogonal directions to the tracking line of sight. In any case, the achieved OD accuracy for the D4-OE2 case is ~ 0.1 mm, well below the target order of magnitude of ~ 1 m, so it is not a concern given the target order of magnitude of $\overline{\text{RMSE}}_{\text{pos}}$.

5.1.4. Estimation with non-ideal observations

To finish the verification, the impact of adding some *non-ideal* effects to the observations is examined. The effects considered in this verification step are those which have a known expected impact on the OD process, so that it is possible to confirm whether the results meet the expectations or not. These effects are: white noise, range and Doppler biases, and transponder delay.

White noise

To observe the effect of adding white noise to both range and Doppler observations, the simulations performed for the previous verification task (§ 5.1.3) are repeated with the sole addition of observational noise. The noise

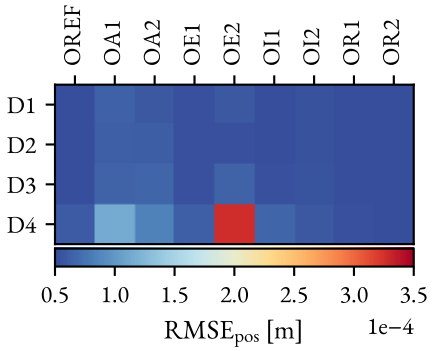

Figure 5.5: RMS of the position error for the estimation with ideal observations.

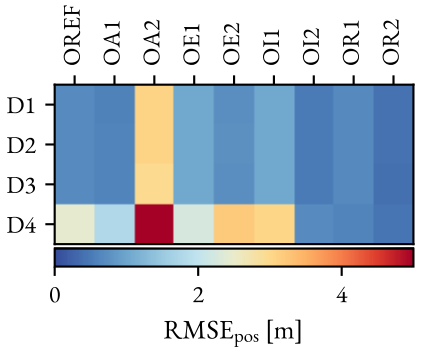

Figure 5.6: RMS of the position error for the estimation with observations affected by noise.

levels added to both types of observations are the nominal values, which are $\sigma_{\text{ran}} = 1\,\text{m}$ and $\sigma_{\text{dop}} = 1\,\text{mm}\,\text{s}^{-1}$. The satellite's initial state and reflectivity properties are the solve-for parameters of the estimation. This batch of simulations involves RNGs for the generation of the initial state deviations and the sampling of the white noise.

In this proposed setup, the simulated range and Doppler observations are the addition of a deterministic component—the previously called *ideal* value of the observation—, and a normally distributed noise component. Let $\mu_{\rho,i}$ and $\mu_{\dot{\rho},j}$ be the expected values of the distributions of the i-th range observation (ρ_i) and j-th Doppler observation ($\dot{\rho}_j$), respectively. The expected minimum of equation (4.34) (dropping the k subindex as there is only one satellite) is found when $f_{\text{ran}}(t_i, \mathbf{x}_{\text{est}}) = \mu_{\rho,i}$ and $f_{\text{dop}}(t_j, \mathbf{x}_{\text{est}}) = \mu_{\dot{\rho},j}$, for all i in $\{1, 2, \ldots, N_{\text{ran}}\}$ and j in $\{1, 2, \ldots, N_{\text{dop}}\}$. As the noise considered is white (having a mean value of 0), it happens that $\mu_{\rho,i} = \rho_i^{\text{i}}$ and $\mu_{\dot{\rho},j} = \dot{\rho}_j^{\text{i}}$, with ρ_i^{i} and $\dot{\rho}_j^{\text{i}}$ being the ideal values of the i-th range observation and the j-th Doppler observation, respectively. Thus, the residual RMS is expectedly minimized when all $f_{\text{ran}}(t_i, \mathbf{x}_{\text{est}}) = \rho_i^{\text{i}}$ and all $f_{\text{dop}}(t_j, \mathbf{x}_{\text{est}}) = \dot{\rho}_j^{\text{i}}$, which happens when the values of the parameters in $\mathbf{x}_{\text{est}}$ match the values of the true orbit[1]. This means that, even with noise, the estimation of the parameters remains unbiased. Consequently, the residuals obtained after the estimations should be normally distributed about 0, with a standard deviation value of σ_{ran} for the range residuals and of σ_{dop} for the Doppler residuals. Figure 5.7 confirms that the distributions of range and Doppler residuals across the different OD cases and simulation runs resemble the expected normal distributions.

Figure 5.6 shows the orbital accuracies of the estimations for all combinations of test cases. The observational white noise, while preserving the unbiased property of the estimation, causes the dispersion of the estimated values of $\mathbf{x}_{\text{est}}$. The dispersion of $\mathbf{x}_{\text{est}}$ around its ideal value results in differences between the propagation of the estimated and reference orbits—both the initial states and the dynamic models (through the reflectivity properties) are different. These differences in propagation emerge in the results as an increase in the mean RMSE_{pos} compared to the estimation with ideal observations shown in Figure 5.5, even reaching several meters. The different test cases suffer disparate losses in OD accuracy due to the noise in the observations. Case D4-OA2 shows a remarkably high RMSEpos compared to the rest. Nevertheless, it is not the objective of this verification to analyze the relation between noise and OD accuracy at different orbit configurations. These types of considerations are left to be discussed in Chapter 7.

[1]This does not imply that the actual estimated result is equal to the true orbit, but only that the expected result is equal to the true orbit.

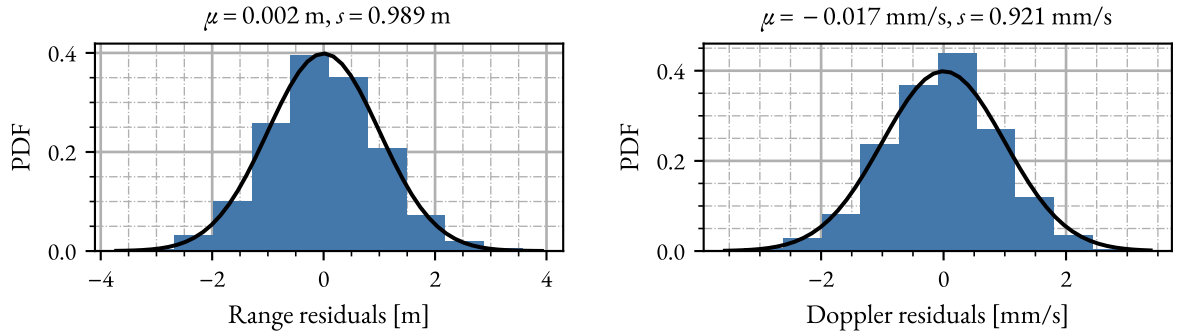

Figure 5.7: Distribution of the range and Doppler residuals of noisy observations for all runs with $N_{\text{runs}} = 45$ and all combinations of test cases. The solid black curve represents the Probability Density Function (PDF) of a 0 mean normal distribution with $\sigma = \sigma_{\text{ran}}$ in the range residuals and $\sigma = \sigma_{\text{dop}}$ in the Doppler residuals.

Biases

Other than random noise, the observations are also affected by biases, which act as an offset of the observations with respect to their ideal value. When performing OD, these biases are usually estimated together with the spacecraft's initial states and other properties. However, for the first set of simulations performed for this verification task, the observation biases are not included as solve-for parameters (only initial state and reflectivity properties) and are set to 0 during the estimation. The simulation of the observations uses the nominal bias values, $b_{\text{ran}} = 10$ m and $b_{\text{dop}} = 10$ mm s^{-1}, and no white noise.

In a large majority of cases, there are no values of the solve-for parameters that achieve a perfect fit of all biased observations. Namely, there is no $\mathbf{x}_{\text{est}}$ that achieves $f_{\text{ran}}(t_i, \mathbf{x}_{\text{est}}) = \rho_i$ and $f_{\text{dop}}(t_j, \mathbf{x}_{\text{est}}) = \dot{\rho}_j$ for all i in $\{1, 2, \ldots, N_{\text{ran}}\}$ and all j in $\{1, 2, \ldots, N_{\text{dop}}\}$. Consequently, after the estimation process, the resulting range and Doppler residuals are not reduced to (almost) 0 at all epochs, but show a certain temporal trend with values $\sim b_{\text{ran}}$ and $\sim b_{\text{dop}}$, respectively, as observed in Figure 5.8. Moreover, the estimated $\mathbf{x}_{\text{est}}$ that minimizes the residuals of the biased observations need not be (and usually is not) coincident with the $\mathbf{x}_{\text{est}}$ value of the estimation without biases. Consequently, the estimation of the parameters is biased, which significantly deteriorates the estimated orbit's accuracy, as seen in Figure 5.9 when compared against Figure 5.5. The mean values of RMSE_{pos} are of the order of meters and tens of meters for all the simulated cases, which are already worse than the OD accuracy requirement. The D4-OA2 case shows a specially high RMSE_{pos}, while its corresponding residuals are comparable to those of other test cases, as seen in Figure 5.8, due to the degradation of the orbital accuracy in the orthogonal components to the tracking line of sight during the estimation. Similarly to § 5.1.3, this happens for a test case using a more complex dynamic model, suggesting that it is the increased dynamic complexity what allows the estimation algorithm to improve the residual RMS at the expense of deteriorating the estimated orbit in the directions which are not observable. Lastly, this also highlights the different impact that the observation biases can have on the OD accuracy depending on the orbit's geometry and size.

To solve this issue, the biases are included as solve-for parameters of the problem. By doing this, the estimation algorithm can compensate for the offset present in all observation values to achieve an estimated $\mathbf{x}_{\text{est}}$ that almost perfectly fits the observations. Figure 5.10 shows that the result is a more accurate estimated orbit, close to the accuracy attained with ideal observations. Figure 5.11 shows that the order of magnitude of the residuals is also significantly reduced down to ~ 10 μm in range and ~ 0.1 μm s^{-1} in Doppler. This makes evident that

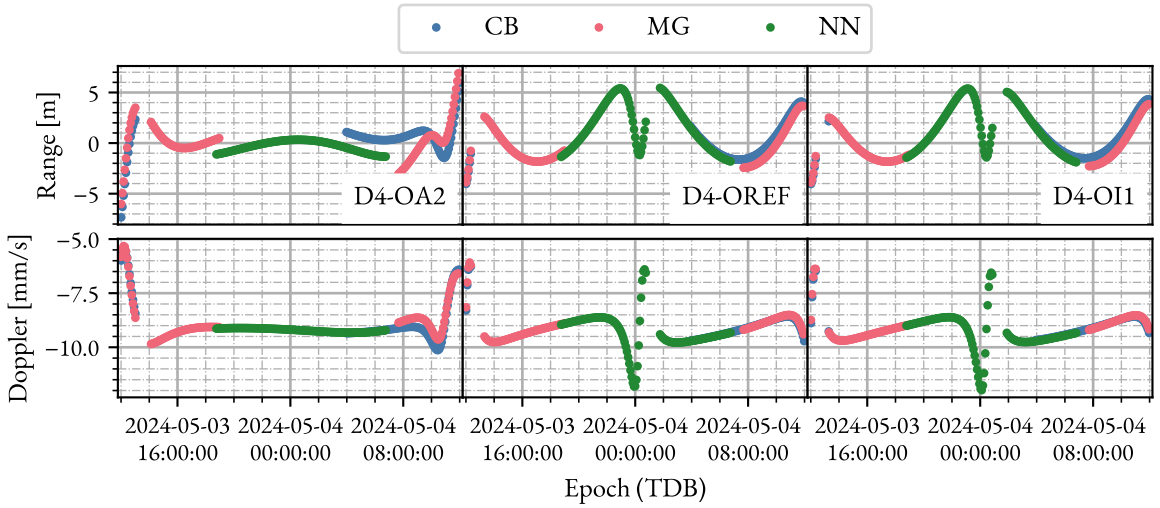

Figure 5.8: Observation residuals for the estimation with biased observations for the first random run of 3 cases, without estimating biases.

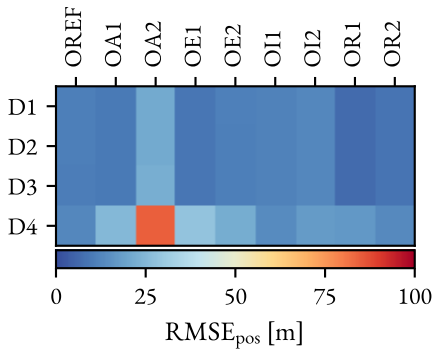

Figure 5.9: RMS of the position error for the estimation with biased observations, without estimating biases.

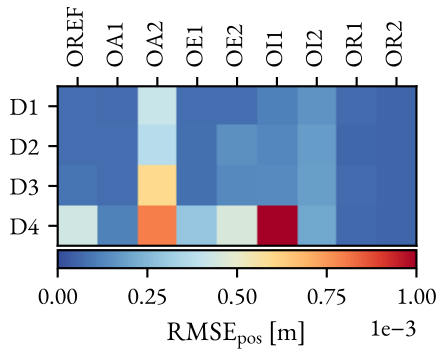

Figure 5.10: RMS of the position error for the estimation with biased observations, estimating biases.

the estimation algorithm is able to properly estimate the biases of the observations. The D4-OI1 case shows a remarkably higher RMSE_{pos} than the rest of cases, a difference that is not visible in the magnitude of the observation residuals in Figure 5.11. The tracking line of sight has a smaller out-of-plane component for lower inclination orbits. It is hypothesized that, due to the characteristics of the dynamic environment of the satellites, the out-of-plane component of the observation is more relevant to estimate the biases and, thus, the lower inclination orbit does so worse than the rest of cases. Still, the value of $\text{RMSE}_{\text{pos}} = 1\,\text{mm}$ is several orders of magnitude below the target accuracy, so the estimation of the biases is good-enough for all considered purposes.

Transponder delay

To test the effect of the transponder delay, the approach followed is similar to that of the observation biases. The transponder delay is set to a value of $\Delta t_{\text{T}} = 1\,\mu\text{s}$, with no observational noises or biases. At first, the transponder delay is not considered as a solve-for parameter and is set to 0 during the estimation, to evaluate its impact on the results. Later, it is estimated to observe the expected improvement in the OD accurracy. As it is also the case for the previous simulations, due to the randomness involved in the generation of the initial state deviation, a convergence analysis, reported in Appendix B, is required to ensure the validity of the results.

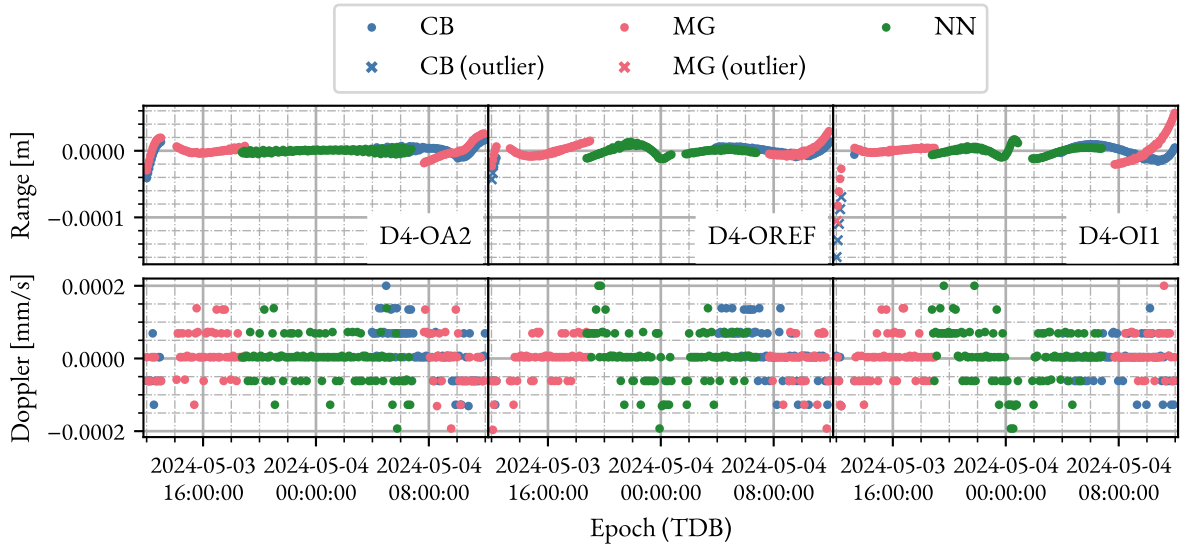

Figure 5.11: Observation residuals for the estimation with biased observations for the first random run of 3 cases, estimating biases.

The transponder delay has an effect on range observations similar to a bias. The time it takes the transponder to receive and transmit back the signal is an extra delay that amounts to a certain offset in the range observation (the offset is constant if the transponder delay is assumed constant). Nevertheless, this delay also causes the start of the downlink of the signal to occur later than it would without delay. During the period spanned by the delay, the spacecraft changes its state (position and velocity), affecting both the light-time of the downlink compared to its value without delay and the contribution of other factors such as the atmosphere. This second effect is smaller in magnitude than the formerly stated effect, but influences both range and Doppler observations. Similarly to what happens with the biased observations, the estimation does not find a value of $\mathbf{x}_{\text{est}}$ that properly fits the observations with delays. Figure 5.12 exhibits residuals of tens to hundreds of meters in range observations and tens of millimeters per second in Doppler observations when using observations with a delay. The effect of the delay biases the estimation of the parameters, which worsens the accuracy of the estimated orbit. Figure 5.13 shows the impact of the transponder delay on the accuracy of the estimation, with values of $\overline{\text{RMSE}}_{\text{pos}}$ of the order of the kilometer. The OD accuracy of the D4-OE2 case is specially degraded by the delay. This is likely due to the large speeds happening close to the pericenter of the more eccentric orbit, which results in a greater change in state of motion during the time elapsed by the transponder delay. This is visible in the range observation residuals in Figure 5.12, which are visibly greater at the pericenter pass (approximately at t = 2024-05-04T00:00:00 TDB) compared to those of the D4-OREF case. The combination of the OA2 orbit case with D1, D2 and D3 also show a remarkably high RMSE_{pos}. However, the residuals of case D4-OA2 in Figure 5.12 are overall smaller than those of other cases. No apparent reason is found for this, highlighting the unpredictability that derives from not estimating parameters related to significant effects that affect the observations.

When including the transponder delay as a solve-for parameter, the algorithm can estimate it and converge to the true orbit with a significantly increased accuracy. Figure 5.15 shows that, with this, the observation residuals obtained after the estimation show a much better fit, as they decrease several orders of magnitude, down to a sub-millimetric level. Additionally, Figure 5.14 exhibits a great reduction in orbital error with the estimation of

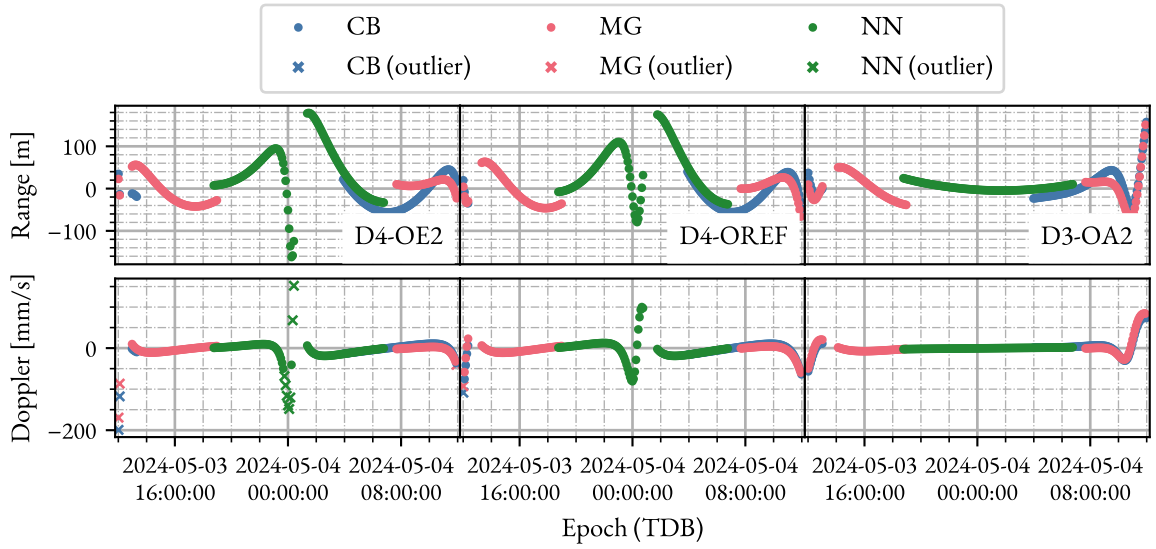

Figure 5.12: Observation residuals for the estimation with observations affected by transponder delay for the first random run of 3 cases, without estimating the transponder delay.

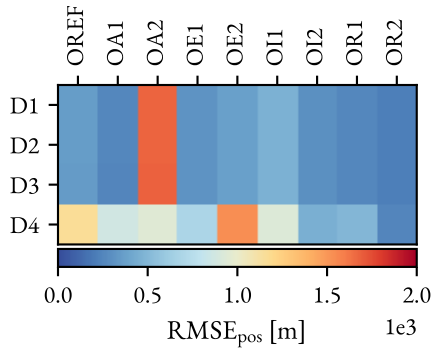

Figure 5.13: RMS of the position error for the estimation with observations affected by transponder delay, without estimating the transponder delay.

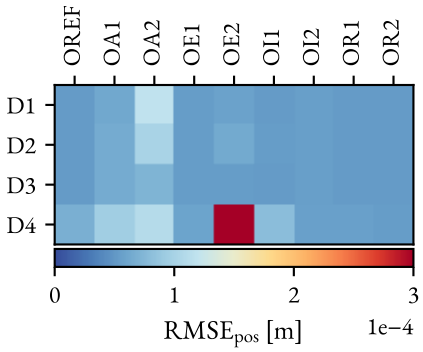

Figure 5.14: RMS of the position error for the estimation with observations affected by transponder delay, estimating the transponder delay.

the transponder delay. The D4-OE2 case still suffers the worst OD accuracy. The aforementioned reasoning for this still applied in this case. In any case, the $RMSE_{pos}$ values achieved are similar to those of the estimation with ideal observations depicted in Figure 5.5. This serves to verify the adequate handling of the transponder delay as a solve-for parameter.

5.2. Validation

Having checked the consistency of the results produced by the simulation tool, they must be contrasted against real external data to gain trust in their validity. Due to the lack of missions with characteristics similar to those expected for the LNS, there is no clear candidate ongoing or past mission to be used as a reference for validation. After thorough thought, the reference mission chosen for validation is GRAIL for two reasons. The first reason is that data from the GRAIL mission was used to produce the most accurate set of lunar SH coefficients up to date. Because of this, it is expected that the available GRAIL orbit data accurately represent its real orbit, and the

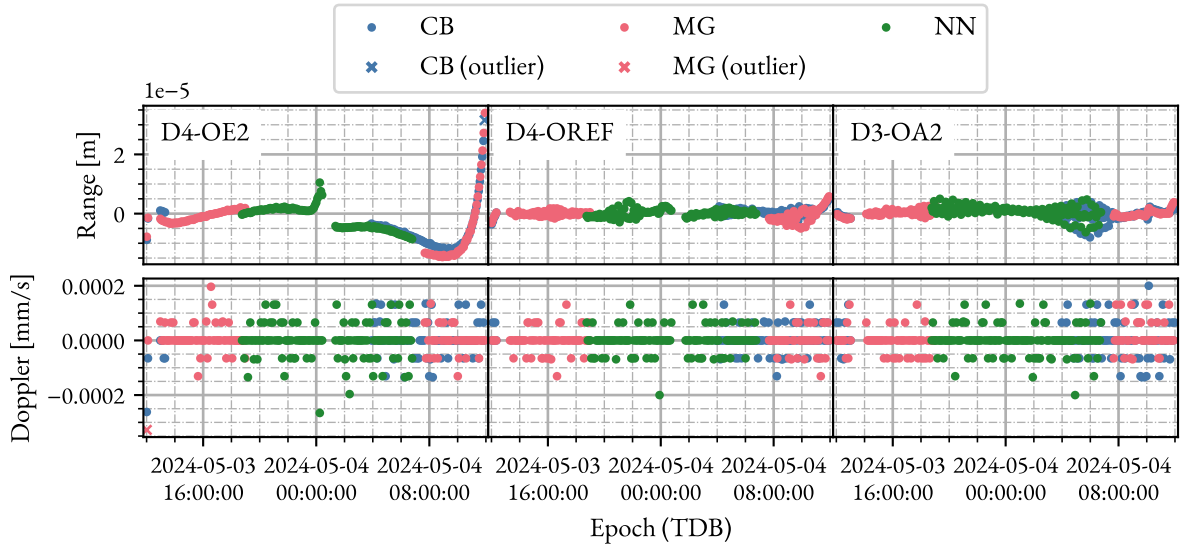

Figure 5.15: Observation residuals for the estimation with observations affected by transponder delay for the first random run of 3 cases, estimating the transponder delay.

coherence between the orbit product and the lunar gravitational model used to obtain it is ensured. A secondary motive for the decision is the easy availability of GRAIL orbit data and, to some extent, of the dynamic modeling choices made in the production of the orbit.

The validation starts by comparing an orbit propagated with the simulation tool to the external GRAIL orbit data. This comparison aims to assess the degree of accordance between the propagation implemented in the tool and a propagation used for operative lunar missions. After that, the external orbit is used to simulate range and Doppler observations, from which an orbit is estimated. This second step assesses the capability of the tool to estimate real lunar orbits from simulated range and Doppler observations.

5.2.1. GRAIL mission and orbit product

GRAIL was a two-probe NASA mission operated between 2011 and 2012 designed to map the gravitational field of the Moon with great accuracy to help determine its internal structure. The most reliable lunar SH coefficients currently available have been computed using data from the GRAIL mission. For this purpose, the probe was placed in a near-polar near-circular orbit at a mean altitude of 55 km above the lunar surface [92]. For the remainder of the section, when making reference to comparisons against the GRAIL orbit, the probe considered is GRAIL-A.

The orbit data for the GRAIL mission is available to the public in NAIF's PDS. The GRAIL orbit products found in this database[2] were produced using a lunar SH gravitational field up to degree and order 420, whose coefficients were computed from data of the mission, and the planetary ephemerides used were the DE 421. There are no further specifications about the dynamic model used. The reported accuracy of the given orbit data is at the level of a few meters.

[2]All publicly available data of the GRAIL mission can be accessed through: `https://naif.jpl.nasa.gov/pub/naif/pds/data/grail-l-spice-6-v1.0/grlsp_1000/`.

Table 5.4: Updates to the simulation parameters for validation.

Parameter	Value	Parameter	Value
t_{ref}	2012-03-01T12:01:06.000 TDB*	T_{obs}	30 s
T_{est}	0.25 d	T_{pred}	0
DO_{L}^{e}	420	tol^{e}	10^{-13}
m	130 kg	A_{body}	4 m^2
σ_{ran}	0.5 m	σ_{dop}	0.15 mm s^{-1}
w_{ran}	70 m	w_{dop}	70 mm s^{-1}

* This value of the epoch is selected to coincide with an epoch of GRAIL's orbit file.

5.2.2. Validation setup

Due to the disparity between the GRAIL mission and the LNS's orbits, the simulation of GRAIL's OD requires a significantly different setup. The value of t_{ref} must be changed to an epoch within the period of operations of GRAIL. Moreover, due to the low altitude of the orbit, it demands a greater resolution of the lunar SH expansion and a stricter integrator tolerance. To compensate for the increased computational effort derived from this raise in DO_{L}^{e} and tol^{e}, the estimation arc length is reduced to $T_{\text{est}} = 0.25$ d. Similarly to the verification, no prediction arc is considered, and the position difference is computed over the estimation arc. Additionally, the SRP acceleration considers a sole cannonball model due to the lack of information regarding the model used to produce the orbit. These simulations use the approximate spacecraft properties of GRAIL.

Regarding the simulation of observations, the quicker dynamics of GRAIL also require a greater frequency of observations to produce an accurate solution. The range and Doppler tracking data used in the GRAIL mission had a sampling interval of 60 s [137]. To compensate for the uncertainty in the modeling of the GRAIL orbit data, the value of T_{obs} used is reduced down to $T_{\text{obs}} = 30$ s. The simulated observations consider the nominal value for the biases of both range and Doppler, and for the transponder delay. The simulation also includes atmospheric effects. The simulations adjust the noise levels of the observations to $\sigma_{\text{ran}} = 0.5$ m and $\sigma_{\text{dop}} = 0.15$ mm s^{-1} so that they are representative of the tracking observations used during the operation of the mission [137].

The ephemerides source used to retrieve the positions of the celestial bodies is changed to DE 421 to be coincident with that used for the production of the external orbit. Lastly, due to the likely incoherence between the models of the true and estimated orbits, the relevance of the observations in the estimation process is reduced by raising their associated weights, tuning the values to improve the estimation accuracy. Table 5.4 contains a summary of the parameters used (only those different from the nominal configuration).

5.2.3. Validation of the orbital propagation

As mentioned, the first step of the validation consists in fitting a propagated orbit to the orbit data provided by NAIF. This is done by creating position observations in 3D (X, Y, Z components) and using the *Odp* program to estimate the initial state vector of the probe and its C_{r} for the SRP model. The position observations used are given a weight of 1 m in the estimation process.

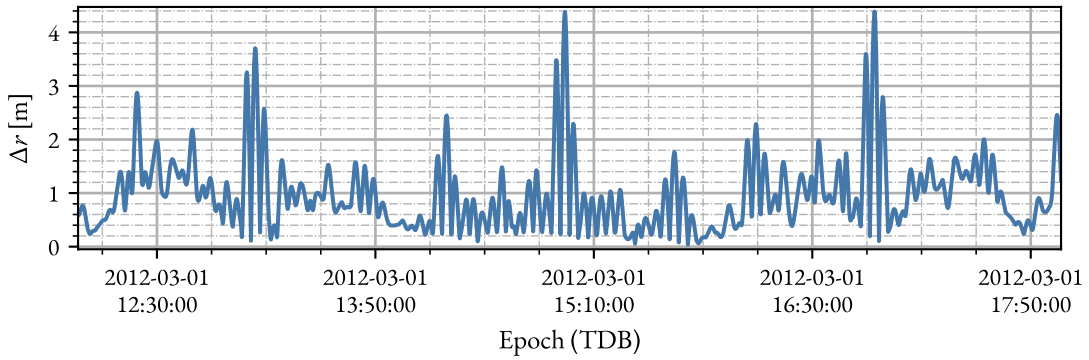

Figure 5.16: Comparison between the propagated orbit using the simulation tool and the GRAIL orbit provided by NAIF.

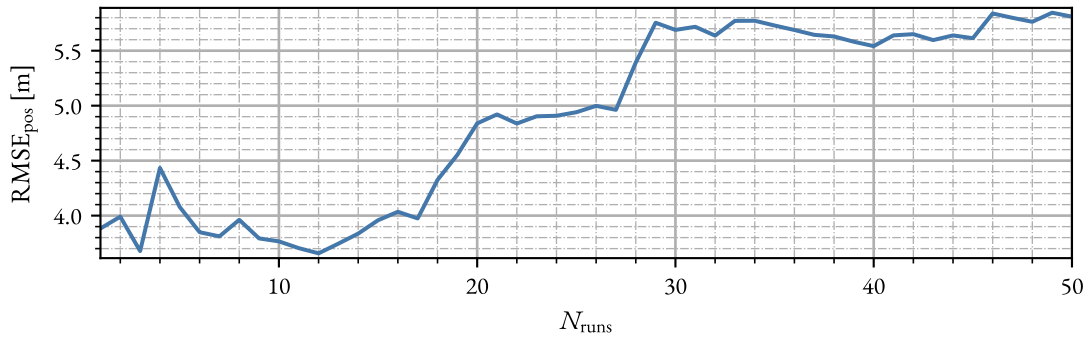

Figure 5.17: Evolution of the $RMSE_{pos}$ for the OD of GRAIL's orbit as a function of the number of runs.

Figure 5.16 shows that the propagation performed with the simulation tool is close to the orbit data retrieved from NAIF, with a $RMSE_{pos} \approx 1.2$ m. The accuracy level is of the same order of magnitude as the reported accuracy of the orbit product. This result provides great confidence that the propagations performed with the simulation tool represent adequately enough the motion of spacecraft in lunar orbit. Moreover, the impact of using a cannonball model instead of a more complex model seems to have a moderate impact on the propagation over 6 h (approximately three orbital periods).

5.2.4. Validation of the OD

The second and last step of the validation process consists in estimating the external GRAIL orbit using simulated range and Doppler observations. The solve-for parameters are the initial state vector and the C_r value associated to the cannonball SRP model.

Figure 5.17 displays the convergence of the estimated $RMSE_{pos}$ with an increasing number of random runs. After run number 30, the mean value of $RMSE_{pos}$ remains within ±5% of 5.7 m. Thus, there is confidence that the OD of GRAIL's orbit converges to its true orbit and estimates it with $RMSE_{pos} \approx 5.7$ m. Given the uncertainty in the modeling assumptions used to propagate the reference and estimated orbits, the accuracy level of the presented results provides a great confidence in the validity of the OD simulation process described in Chapter 4.

5.3. Conclusions from the verification and validation

The verification tasks reported in this chapter evidence the reliability of the tool's end-to-end simulation capabilities used to produce further results. These qualities are tested over a broad range of orbit and dynamic configurations so that there is confidence in the good behavior of the tool in the variety of cases assessed in Chapter 7.

The OD simulation process has also been validated against the orbit product from the GRAIL mission, leading to estimated orbital accuracies similar to those of the external product used, even when dealing with a notable uncertainty in the modeling choices. This provides a strong degree of assurance of the validity of the simulation of observations + OD process to recreate a realistic scenario and produce representative results.

6

Sensitivity analysis

Prior to the design analysis of the OD system of the LNS, it is required to perform a previous analysis to investigate the effect of those parameters that are not included in the design stage. These parameters are those used to represent the "true" dynamical environment of the spacecraft—namely, those involved in the propagation of the reference orbit—, together with some parameters of the estimation process which may affect the quality of the convergence. The objective of the analysis is to select values for these parameters so that the results obtained during the design analysis are representative of a real environment.

The selection of the nominal values presented along Chapter 4 reflects the conclusions of the analysis performed in this chapter.

6.1. Orbital propagation

The reference orbits produced at the first stage of the simulation process represent the true orbit of the LNS satellites. Because of this, their accuracies must be high enough so that the FoMs used in the analysis are not significantly impacted by their propagation errors. A sensitivity analysis of the reference orbit accuracy serves to find adequate values for the propagation parameters by establishing a trade-off between accuracy and computational effort. The selected approach to do so is to first establish a reference model, considered to be of greater accuracy than needed, to later simplify it until the target accuracy is reached.

Table 6.1: Reference environmental and dynamic model for the sensitivity analysis.

$DO^{\mathrm{r}}_{\mathrm{L}}$	420
$DO^{\mathrm{r}}_{\mathrm{E}}$	4
Point mass	Sun, Jupiter, Saturn, Venus, Mars
Massive bodies for relativity	Moon, Earth, Sun
tol^{r}	10^{-14}

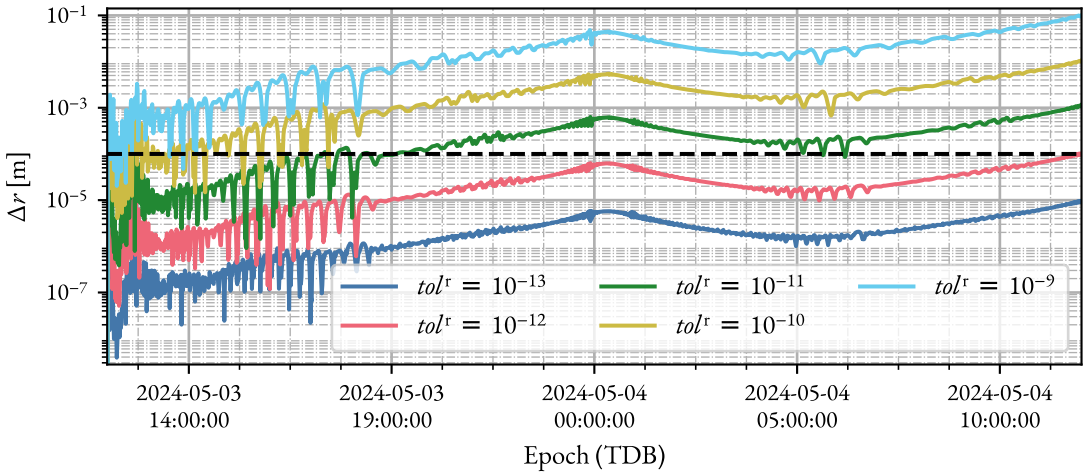

Figure 6.1: Time evolution of the position difference for increasing values of relative integrator tolerance using the nominal orbit configuration. The threshold value is marked with a black dashed line.

Table 6.1 presents the parameter values defining the reference dynamic and environmental model used for the sensitivity analysis. The reference DO^{r}_{L} is chosen based on the value used for the propagation of GRAIL's orbit. As the orbit of the LNS satellites is expected to be higher in altitude, the required DO^{r}_{L} is expectedly below that. The relative relevance of the SH components of higher degree and order decay rapidly with the distance. Thus, for the Earth's gravity, a much smaller value of DO^{r}_{E} is chosen compared to the lunar SH. Apart from the Moon and Earth, the gravities of the remaining most prominent bodies are modeled as point masses. The reference model includes only the relativistic effect of the Moon, Earth, and Sun, as they are the most likely bodies to have a significant influence on the propagation. Finally, the integrator tolerance is set close to the finite precision of the floating-point representation. It should be noted that the values in Table 6.1 are not final, and that they can be "expanded" (more point mass bodies or higher SH degree and order) if deemed necessary.

The propagation accuracy is evaluated by means of the maximum 3D position difference between the "simplified" propagation and the reference one over a representative propagation interval of 1 day. As the expected OD errors are in the orders of the meter (according to the requirement stated in Chapter 3), and to ensure that the propagation error is well below that accuracy, the threshold value for this metric is set to 1 cm. The only exception to this is the integrator tolerance, for which an even lower threshold of 0.1 mm is set to ensure that integration errors are not the dominant source of error. This last choice has a negative impact on the computational cost. However, the design analysis only requires propagating new reference orbits when inspecting different orbital configurations, whereas the same reference orbit can be reused to study the impact of any other parameter. Thus, the assurance of more accurate results has been chosen over a mild reduction in computational cost.

6.1.1. Nominal orbit configuration

The analysis uses the nominal orbit configuration presented in § 4.5. Figure 6.1 shows the impact of raising the tolerance from the reference level. The results are coherent with the expectations—an increase of N orders of magnitude on the tolerance translates into an increase of N orders of magnitude on the position difference. Attending to the established threshold, also shown in the plot, a value of $tol^{r} = 10^{-12}$ could be used, as it barely reaches the accuracy threshold, but the more conservative $tol^{r} = 10^{-13}$ is chosen.

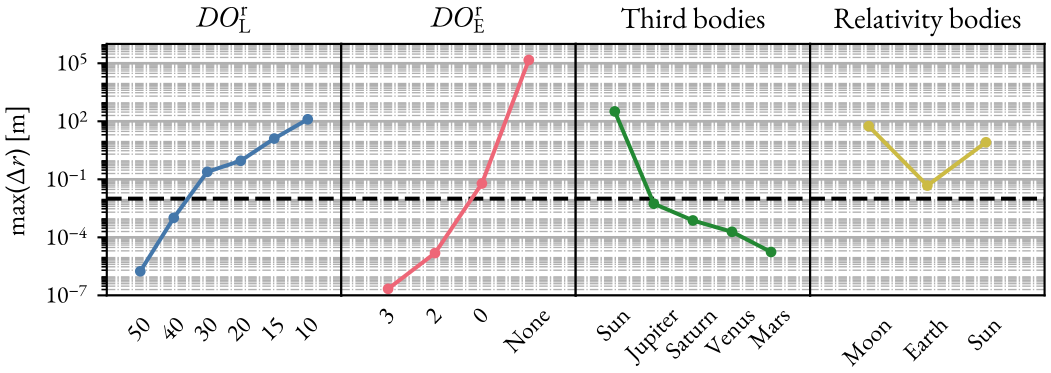

Figure 6.2: Impact of simplifying the dynamic and environmental model on the propagation for the nominal orbit configuration. The threshold value is marked with a black dashed line.

Table 6.2: Most restrictive orbit configuration. The Keplerian elements are specified with respect to the MER frame.

a [km]	e [-]	i [°]	Ω [°]	ω [°]	θ [°]
6150	0.7	51.7	0	90	0

Figure 6.2 presents the results of the sensitivity analysis of the rest of parameters of the model. The curves referring to the third bodies and the massive bodies for relativity represent the effect of individually excluding those celestial bodies from the reference model in Table 6.1. As expected, lowering DO_L^r and DO_E^r leads to a monotonic increase in the position difference. Both the lunar and terrestrial SH expansions must include terms up to degree and order 40 and 2, respectively, to meet the accuracy threshold. The Sun is the next celestial body in order of relevance, and the only one that needs to be considered as a point mass. Finally, the propagation must account for the relativistic effect of the Moon, the Earth, and the Sun.

6.1.2. Most restrictive orbit configuration

The design analysis of the OD system reported in Chapter 7 considers several orbit configurations. Some of them modify the value of a and e with respect to the nominal orbit, thus also affecting the periselene altitude. Due to the significant irregularity of the lunar potential, which becomes more prominent at lower altitudes, orbit configurations presenting a lower periselene altitude may require the use of a greater number of lunar SH terms or a lower integrator tolerance. For this reason, a "most restrictive" orbit configuration is defined setting the lowest periselene altitude found in later analyses. Table 6.2 introduces the Keplerian elements associated to this configuration.

Figure 6.3 shows the maximum orbital error incurred by propagating using different model simplifications with respect to the reference model given in Table 6.1. Differently from the nominal configuration, this "most restrictive" configuration requires that the lunar gravity considers at least $DO_L^r = 100$. On the other hand, $tol^r = 10^{-13}$ is still enough to meet the stricter requirement imposed on that parameter. The rest of model choices remain unaffected as well. Table 6.3 contains the final environmental and dynamic model choices for propagating the reference orbit. These choices aim to ensure that the accuracy threshold is met for all the orbit configurations present in the analyses.

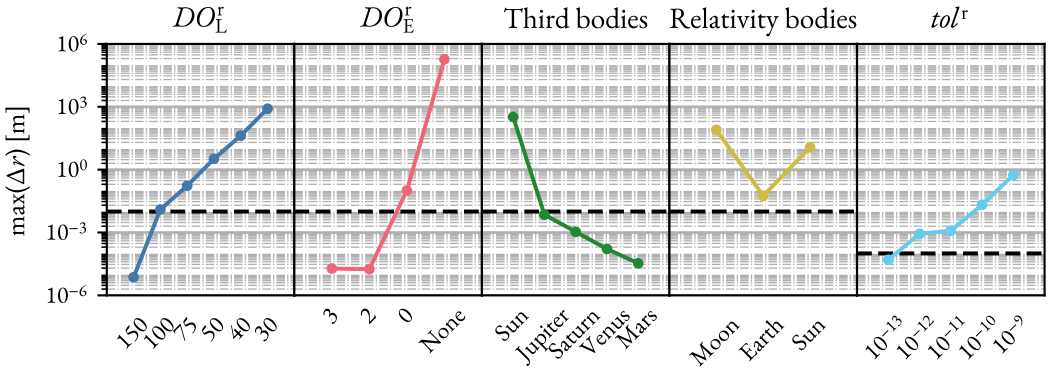

Figure 6.3: Impact of simplifying the dynamic and environmental model on the propagation for the "most restrictive" orbit configuration. The threshold value is marked with a black dashed line.

Table 6.3: Final environmental and dynamic model based on the results of the analysis.

DO^r_L	100
DO^r_E	2
Point mass	Sun
Massive bodies for relativity	Moon, Earth, Sun
tol^r	10^{-13}

6.2. OD parameters

In addition to the observation and parameter weights, there are two other parameters involved in the estimation algorithm. These are the outlier threshold (Θ_{out}) and the convergence threshold (Θ_{conv}). Unlike the parameter weights—which are decided on the basis of a priori assumptions—and the observation weights—which are selected to ensure the convergence of the estimation process—, there are no reasoned values to give to the threshold parameters without exploring their impact on the resulting estimated solution. Because of this, several OD simulations are run varying Θ_{out} and Θ_{conv} separately.

To perform the analysis, a range of values for both threshold parameters must be first defined. These ranges are built starting from a justifiable parameter value, and then including values both above and below that. A reasonably expected value of the outlier threshold is $\Theta_{out} = 6$, as it means that erroneously modeled observations, whose residuals usually differ by many sample standard deviations from the mean, are marked as outliers, while keeping a large volume of "valid" observations. Consequently, a suitable range of values is $\Theta_{out} \in [2, 11]$. To properly test the impact of Θ_{out} on the results, two scenarios are used. The first scenario considers the observation modeling strategy defined in § 4.3.3 for both the simulation and estimations stages. The second scenario does the same, but fails at correcting the tropospheric delay at both the first and last observation on each continuous tracking pass of a station (trying to recreate a bad processing of the first and last observations of each pass). This second scenario includes observations with significantly larger residuals which, if not marked as outliers, would have a notable detrimental effect on the estimation accuracy.

Regarding the convergence threshold, the chosen central value of the studied range is $\Theta_{conv} = 10^{-3}$, as a 0.1% change in the residual RMS is expected to be already negligible for the estimated solution, and it is not

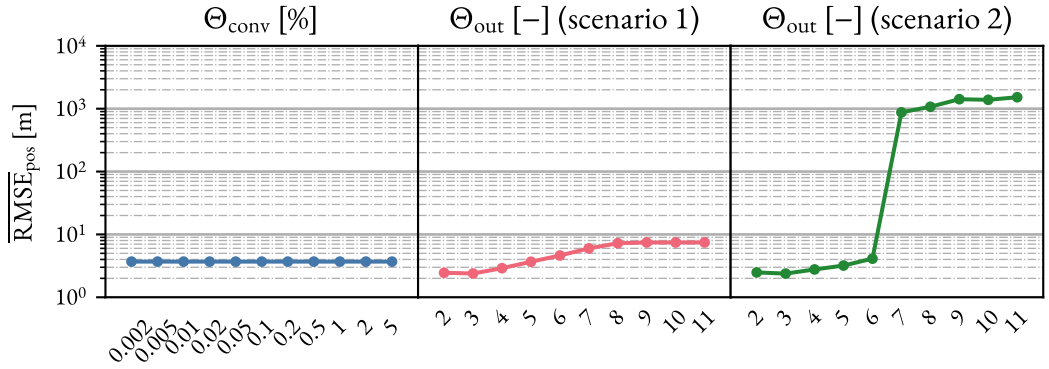

Figure 6.4: Impact of Θ_{conv} and Θ_{out} on the OD accuracy.

a strict-enough value to cause an inability to converge. Thus, the decided range for the analysis is $\Theta_{conv} \in [2 \times 10^{-5}, 5 \times 10^{-2}]$. It must be remarked that the value of Θ_{out} for all cases of the analysis of Θ_{conv} is set to be $\Theta_{out} = 6$, while the value of Θ_{conv} for all cases of Θ_{out} is set to be $\Theta_{conv} = 10^{-3}$.

Figure 6.4 displays the results of the analysis using the nominal configuration introduced in § 4.5. Varying Θ_{conv} over a broad range of values does not have any apparent impact on the OD accuracy. Based on the aforementioned reasoning, the chosen final value is $\Theta_{conv} = 10^{-3}$, in case other OD setups show a more complicated convergence behavior.

Figure 6.4 also shows the effect of the Θ_{out} value on the OD accuracy for both of the defined scenarios. In the first scenario (all observations corrected for the tropospheric delay), Θ_{out} has a mild impact on $\overline{RMSE}_{pos}$. Lower valuesof Θ_{out} lead to better OD accuracies. This feature can be likely attributed to the effective reduction in observational noise occurring when marking the observations with a greater noise component as outliers. No variation in $\overline{RMSE}_{pos}$ is observed when increasing Θ_{out} above 8, indicating that there are no residuals that deviate more than 8 sample standard deviations from the mean value. However, as previously stated, this is not a very realistic scenario, as there are no erroneously modeled observations, which are those that are truly relevant to be marked as outliers. In the second scenario (missing the tropospheric delay correction of some observations), the OD accuracy notably deteriorates for $\Theta_{out} > 6$. For $\Theta_{out} \leq 6$, all erroneously modeled observations are identified as outliers and the accuracy is barely unaffected. It must be remarked that the obtained results depend on the magnitude of the modeling errors and on the number of erroneously modeled observations. Thus, they need not entirely apply to a real set of observations. To make a realistic choice for the scenario described in this section, a final value of $\Theta_{out} = 5$ is decided to ensure that hypothetical erroneously modeled observations are identified as outliers and that no (or almost none) observations are rejected solely due to noise considerations. Nevertheless, the selection of the definitive value of Θ_{out} is mostly arbitrary, as all the simulations used in the design analysis in Chapter 7 use the same approach as the first scenario of this analysis.

7

OD design analysis

This chapter is devoted to the development of a series of analyses, all with the objective of producing a final set of recommended specifications for the OD system of a LNS. To do so, it is first needed to characterize the response of the FoMs to the parameters of the problem. Having identified the parameters that drive the system's performance, the problem can be reduced to enable a more detailed analysis, which has as outcomes the recommended values of the system specifications. Lastly, a section is dedicated to evaluating the effect of the different sources of uncertainty on the system's performance using the recommended specifications.

7.1. Parameter selection

From the entire list of problem parameters discussed in previous chapters, many can potentially impact the performance of the LNS, and, more specifically, of the OD system. The first objective of the design analysis is to determine the problem parameters that drive the system's performance. For this reason, in this first step, all potentially impactful parameters are defined. The studied parameters can be divided into groups according to the aspect of the OD process in which they are involved.

Orbit configuration

The orbit configuration of the different satellites that form the constellation can affect both the accuracy of the OD system—as it may change the periselene altitude, the observation conditions (face-on versus edge-on observation[1]), etc.—and the performance on the user's end—as it may change the relative position of the LNS satellites from the user's location. In order to account for all of these effects, the analysis of the constellation's configuration uses 5 parameters.

Figure 7.1 depicts the two parameters related to the orbits' RAAN. The first parameter is the so-called *RAAN offset* (Ω_0). This parameter represents the value of Ω of the first orbital plane of the configuration, that is, of

[1]An orbit being tracked *face-on* means that the projection of the normal direction to the spacecraft's orbital plane onto the lunar orbital plane points, approximately, along the line of sight of the tracking observations (practically, the EM direction). On the contrary, an orbit being tracked *edge-on* means that the projection of the normal direction to the spacecraft's orbital plane onto the lunar orbital plane is, approximately, perpendicular to the line of sight of the tracking observations.

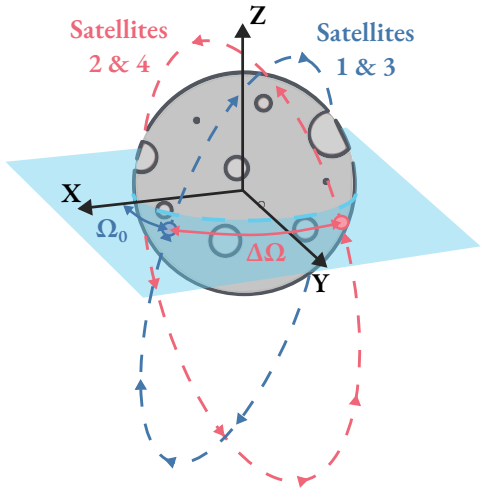

Figure 7.1: Schematic representation of the Ω_0 and $\Delta\Omega$ parameters.

the plane containing the orbits of satellites 1 and 3. The nominal orbit configuration of Table 4.5 has $\Omega_0 = 0°$. The second parameter is the so-called *RAAN difference* ($\Delta\Omega$), which is the RAAN separation between the two orbital planes of the initial orbits of the satellites. Changing the value of $\Delta\Omega$ affects satellites 2 and 4 in Table 4.5, with the nominal configuration having a value of $\Delta\Omega = 90°$.

The effect of varying Ω_0 for a fixed $\Delta\Omega$ can be understood as a rotation of the initial orbits about the Z-axis. For example, when considering $\Omega_0 = 45°$ keeping $\Delta\Omega = 90°$, the orbits of those satellites with a nominal $\Omega = 0°$ change into $\Omega = 45°$, and those with nominal $\Omega = 90°$ change into $\Omega = 135°$. By modifying this parameter, the observation conditions of the two orbital planes change—an orbit with $\Omega = 0°$ or $\Omega = 180°$ shows an exact edge-on condition from Earth, while an orbit with $\Omega = 90°$ or $\Omega = 270°$ shows an approximate face-on condition (it is not exact as the inclination is not 90°. Because of the nominal configuration having $\Delta\Omega = 90°$, from an Earth tracking point of view, all values $\Omega_0 = \Omega_0^* + k \cdot 90°$, for any integer k, produce practically equivalent configurations. For this reason, the values of Ω_0 are in the range $\Omega_0 \in [0, 90)°$. For a user in the LSP, changes in this parameter lead to essentially identical configurations of the satellites in the sky, so any impact on the user-related performance is expected to be due to the improvement or deterioration of the OD accuracy.

The values of $\Delta\Omega$ can range from 0° to 180°. Nevertheless, the configurations are practically symmetric with respect to $\Delta\Omega = 90°$—for example, the values $\Delta\Omega = 80°$ and $\Delta\Omega = 100°$ lead to identical geometrical configurations except for the relative position of the ascending/descending nodes. Therefore, the range considered is $\Delta\Omega \in [0, 90]°$. Modifying this parameter only changes the observation conditions of 2 out of 4 satellites. Moreover, as opposed to the variation of Ω_0, changes in $\Delta\Omega$ affect the relative configuration of the satellites in the sky as seen from the LSP, so the impact on the user-related FoMs is expected to be greater compared to that of Ω_0.

The remaining 3 parameters are the semi-major axis (a), eccentricity (e), and inclination (i) of all satellites in the constellation. The nominal configuration in Table 4.5 considers that these 3 Keplerian elements are equal for all satellites, and that is maintained here. It is acknowledged that this need not be the case in reality. However, a

simultaneous and equal change of these elements to all satellites is enough to get a first notion of their impact on the OD system. The optimization of the LNS's orbit configuration is out of the scope of this analysis. The ranges of values of a and e are limited in the lower and upper bounds, respectively, by the minimum periselene altitude. It is undesirable to lower the periselene below an altitude of 100 km. Using the nominal value of $e = 0.6$ leads to a minimum $a \approx 4650$ km, and using the nominal value of $a = 6150$ km leads to a maximum $e \approx 0.7$. The upper limit of the range of values for a is given by the constellations proposed in literature, which reach values of ~ 9000 km [67], thus leading to a final range of $a \in [4650, 9150]$km. The lower limit of e is selected to still provide some preferential coverage of the LSP compared to the North Pole. The range of values of e used is $e \in [0.3, 0.7]$. Finally, the values of i are in the range $i \in [40, 90]°$. Inclination values below 40° have a poor coverage of the LSP and values above 90° are essentially equivalent to their supplementary angles.

The analysis does not consider any variations of ω or M with respect to their nominal values expressed in Table 4.5. The reason for this is that there is no apparent benefit in changing either of those from their nominal values. Modifying the orbits' ω so that their apocenters are closer to the lunar equator reduces the coverage of the LSP, and the equidistant configuration of M is needed to maximize the 3-fold coverage of the LSP. Achieving a continuous 3-fold coverage is already a challenge for several orbit configurations, so the modification of these two parameters is undesirable. Additionally, having the satellites with different initial values of M helps in averaging out the possible effect of starting the estimation at different positions along the orbit. Regarding ω, there is no a priori reason to believe that its modification can have a positive impact on the OD accuracy. For these reasons, the values of ω and M remain equal to their nominal values found in Table 4.5.

Orbit propagation

From the dynamic and environmental model parameters included in the sensitivity analysis reported in § 6.1, two of them are of special interest for the analysis. These are the maximum degree and order of the lunar SH ($DO_{\mathrm{L}}^{\mathrm{e}}$) and the relative tolerance of the integrator (tol^{e}). Together with the rest of the parameters, both of them have a significant impact on the accuracy of the propagation. However, compared to the others, these two parameters have the greatest impact on the computational cost of the propagation in the range of values required for them. E.g., using a point mass approach for Earth's gravity instead of a SH expansion up to degree and order 2 leads to a comparable orbital error as reducing the maximum degree and order of the lunar SH from 150 to 75, as observed in Figure 6.3. However, the reduction in computational effort derived from the simplification of the terrestrial gravity model is considerably smaller than the reduction achieved by the simplification of the lunar gravity model.

The ranges of values for these two parameters derive from the results reported in § 6.1. A maximum $DO_{\mathrm{L}}^{\mathrm{e}} = 75$ is considered, as it is enough to propagate the "most restrictive" orbit configuration defined in the sensitivity analysis for 1 day with an accuracy better than the meter. The range of values used is $DO_{\mathrm{L}}^{\mathrm{e}} \in [5, 75]$, as a drop below 5 does not seem a reasonable choice due to the strong irregularity of lunar gravity. For tol^{e}, the range of values $tol^{\mathrm{e}} \in [10^{-11}, 10^{-6}]$ includes values leading to orbital errors over 1 day well below the meter and values expectedly leading to hundreds of meters of error.

Observation properties

From the many parameters affecting the range and Doppler observations, those chosen for the design analysis are the observational noise, the observational bias, the transponder delay and the signal frequency. All three

noise, bias and transponder delay cannot be modeled a priori (at least accurately enough) and, thus, seem logical options to include in the analysis. The signal frequency affects the observations through the atmospheric delays. Therefore, as the values of the atmospheric delays change with a varying f_{signal}, the impact of the imperfect atmospheric modeling may also vary, possibly affecting the accuracy of the OD.

Both the observational noise of the range and Doppler observations are varied simultaneously using the *noise factor* (F_σ). The noise factor serves as a scaling factor for the nominal value of both σ_{ran} and σ_{dop}. Based on the values found in the literature for lunar missions (LRO [27], Lunar Prospector [138] and Chang'e missions [139]), range and Doppler noise tend to maintain a proportion of $\sigma_{ran}/\sigma_{dop} \sim 1000$ s. Thus, it is chosen to follow this single-parameter approach to simplify the analysis and reduce the volume of simulations while not significantly affecting the realism of the results. To include both more optimistic and pessimistic results than the nominal configuration, the values of F_σ used in the analysis are within $F_\sigma \in [0.1, 10]$.

The inclusion of biases in range and Doppler observations, as shown in § 5.1.4, incur little, if any, loss in the accuracy of the estimated orbit if the biases are considered as solve-for parameters of the problem. Nevertheless, when accounting for other factors that affect the observations, such as atmospheric delays, the estimation of the station biases may be degraded and lead to a deteriorated estimation of the initial state. For this reason, it is chosen to vary the observation biases in a range including one order of magnitude above and below their nominal values. This results in the final intervals being $b_{\text{ran}} \in [1, 100]$m and $b_{\text{dop}} \in [1, 100]\,\text{mm}\,\text{s}^{-1}$. The same discussion applies to the transponder delay as well. Therefore, the value of Δt_{T} is varied in the range $\Delta t_{\text{T}} \in [0.1, 10]\,\mu$s.

The range of values of f_{signal} are chosen to cover the entire X-band mentioned in the literature for the TT&C link. This means that values in the interval $f_{\text{signal}} \in [8, 12]$GHz are explored in the analysis.

Tracking properties

The scheduling of the generation of observations is influenced mainly by two parameters: the minimum elevation for link (e_{min}) and the time interval between observations (T_{obs}). Both of them are included in the design analysis. The range of e_{min} starts from 0° and goes up to a value large enough to avoid the large residuals occurring at very low elevations, but still not large enough to cause very significant gaps in the visibility of the constellation from Earth. Thus, the range of values used is $e_{\text{min}} \in [0, 30]°$. The interval between observations is varied between approximately one order of magnitude below and above the nominal value, leading to a range of $T_{\text{obs}} \in [30, 2400]$s.

The volume of observations used in the estimation, apart from T_{obs}, also depends on the length of the estimation arc. As mentioned in § 1.4, the 3D observability of the satellite's orbits from Earth is heavily dependent on the motion of the Moon along its orbit. Thus, the analysis considers a wide range of values of T_{est} to evaluate the relevance of the 3D observability in the resulting estimation, with values in the interval $T_{\text{est}} \in [1/8, 8]$d.

The resulting estimated orbit is used to generate the ephemerides of the navigation satellites during the prediction arc. The longer T_{pred}, the more the propagation expectedly diverges from the true orbit, leading to greater orbital errors. Thus, having values of T_{pred} longer than 1 d is not suitable. On the other hand, having a short T_{pred} implies needing to compute the OD solution with a higher frequency to ensure the continuous availability of satellite ephemerides. Because of this, it is considered to have T_{pred} below 2 h. With this, the final values analyzed for T_{pred} are in the interval $T_{\text{pred}} \in [2, 24]$h.

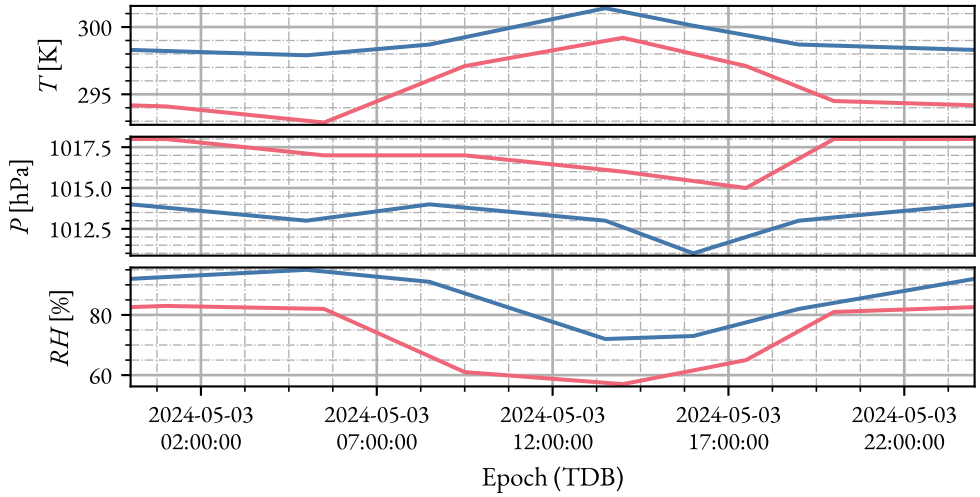

Figure 7.2: Daily profiles of the meteorological data at the 2 additional ground stations.

Table 7.1: Coordinates of the additional ground stations in ITRF.

Station name	**X** [km]	**Y** [km]	**Z** [km]
South Point (SO)	-5488.1369057	-2482.2197618	2075.7117712
Kourou (KR)	3839.7170150	-5059.4955070	579.8764430

Station network

The nominal ground station network used to track the navigation satellites provides a continuous visibility of the lunar orbits (assuming $e_{\min} = 5°$), with the sole interruption being due to occultation by the Moon. Logically, this is beneficial for the OD, since data from (almost) the entire estimation arc are being considered for the estimation. The discontinuous visibility of the lunar orbits from Earth due to a lack of overlap between ground stations may negatively impact the accuracy of the estimation, as there is no information on the orbits during the visibility gaps. To evaluate this effect, three cases are considered in which each of the three nominal stations introduced in Table 4.7 is not used for tracking.

Furthermore, it is interesting to explore the possible benefits of reinforcing the network with additional stations at new locations. To make the extra stations as positively impactful on the OD accuracy as possible, they should be placed at locations from which the lunar orbits can be observed close to the zenith. Accounting for the Earth's rotation and the lunar motion around the Earth, this condition is best met close to the equator. Thus, the new stations are placed at low latitudes. The largest longitude difference in the nominal network occurs between New Norcia and Malargüe, leading to a notably small overlap between these stations. During that small period of overlap, both stations observe the lunar orbits at a low elevation, thus acquiring worse-quality tracking data. Because of this, adding an extra station at a longitudinally intermediate location between New Norcia and Malargüe can significantly improve the OD solution. The only realistic candidate location for a station to be relatively close to the equator and in the middle of the Pacific Ocean is Hawaii, US. The coordinates of the South Point Satellite Station at Hawaii, operated by the Swedish Space Corporation, are used to locate the extra station.

Table 7.2: Summary of the parameters of the design analysis.

	Parameter	Range of values	Parameter	Range of values
Orbit configuration	Ω_0	$[0, 90)°$	$\Delta\Omega_1$	$[0, 90]°$
	i	$[40, 90]°$	e	$[0.3, 0.7]$
	a	$[4650, 9150]$km		
Orbit propagation	$DO_{\mathrm{L}}^{\mathrm{e}}$	$[5, 75]$	tol^{e}	$[10^{-11}, 10^{-6}]$
Observation properties	F_σ	$[0.1, 10]$	f_{signal}	$[8, 12]$GHz
	b_{ran}	$[1, 100]$m	b_{dop}	$[1, 100]$mm s^{-1}
	Δt_{T}	$[0.1, 10]\mu$s		
Tracking properties	e_{min}	$[0, 30]°$	T_{obs}	$[30, 2400]$s
	T_{est}	$[0.125, 8]$d	T_{pred}	$[2, 24]$h

Another approach to the reinforcement of the network is to consider an extra station that (almost) exactly overlaps with a station from the nominal network. This strategy increases the unbalance in time of the volume of tracking observations, meaning that some periods have a much greater frequency of acquisition of observations than others. This situation is implemented by considering an additional station placed at Kourou, French Guiana, where there are already ESA operated facilities (a spaceport). The coordinates of these facilities serve to locate the second additional station and are given in Table 7.1 together with those of the South Point station. Figure 7.2 shows the meteorological data profiles during a sample day for both these extra stations.

Summary of the parameters for the analysis

Table 7.2 contains a compilation of all the parameters (excluding the station network) and their respective range of values for the analysis reported in this chapter. For the variation of the station network, 7 cases are defined with respect to the nominal network of stations:

1. removing Cebreros,
2. removing Malargüe,
3. removing New Norcia,
4. the nominal network,
5. adding South Point,
6. adding Kourou,
7. adding both South Point and Kourou.

These cases, together with the variation of the parameters in Table 7.2, comprise all the cases included in the preliminary phase of the design analysis.

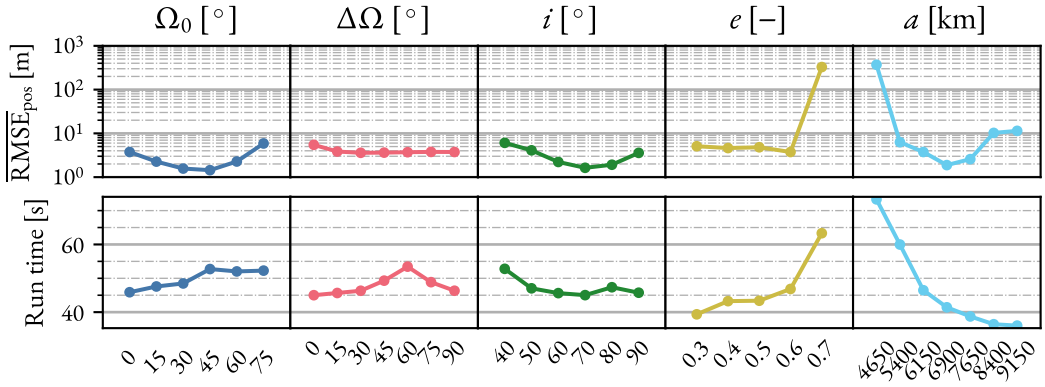

Figure 7.3: Influence of the orbit configuration parameters on the OD accuracy.

7.2. Preliminary analysis

The number of parameters that affect the OD problem is too large to have a proper understanding of the relation between them and FoMs that represent the LNS's performance. Because of this, it is necessary to first reduce the dimensionality of the problem before diving into the selection of adequate OD system specifications. To do this, a preliminary sensitivity analysis can be used to evaluate the impact that the different parameters have on the FoM. This preliminary analysis consists of one-by-one variations of each of the parameters mentioned in § 7.1, while keeping the rest of parameters with their nominal values. The outcome of the analysis can serve to find the most impactful problem parameters, namely, the OD accuracy drivers. Those parameters are kept for a more detailed posterior analysis, while the rest are fixed to their most fitting values, attending to the results. The criterion for selecting the fixed values of the least relevant parameters is not unique and is discussed after presenting and discussing the results of the preliminary analysis.

7.2.1. OD accuracy

Figures 7.3 to 7.6 show the results of the preliminary analysis regarding the accuracy of the OD represented through the $\overline{\text{RMSE}}_{\text{pos}}$, as well as the estimation run time. Figure 7.3 shows that the value of $\overline{\text{RMSE}}_{\text{pos}}$ is minimum at $\Omega_0 \approx 30{-}45°$ and peaks at $\Delta\Omega = 0°$, suggesting that an edge-on tracking condition results in a reduced OD performance compared to the approximate face-on condition or some intermediate situation between both. This is further investigated by computing the $\overline{\text{RMSE}}_{\text{pos}}$ of satellites in planes with $\Omega = 0°$ (edge-on), $\Omega = 90°$ (face-on[2]), and $\Omega = \{45°, 135°\}$ (intermediate), using all random runs from the cases $\Omega_0 = \{0°, 45°\}$. The results are presented in Table 7.3, confirming that the edge-on tracking has a detrimental effect on the accuracy of the estimation. Tracking in an intermediate condition shows little difference with respect to tracking in face-on. Values of Ω_0 close to either 0° or 90° at the nominal $\Delta\Omega = 90°$ means having two of the satellites being tracked close to edge-on, worsening the accuracy. At $\Omega_0 \approx 45°$, all satellites are tracked in an intermediate condition and, thus, the accuracy is better. It must be noted that, effectively, varying Ω_0 is equivalent to analyzing different epochs along the lunar orbit around Earth. For example, the case $\Omega_0 = -90°$ is equivalent to analyzing the system's performance one quarter of a lunar period (≈ 7 d) after t_{ref}. Thus, based on the results in Figure 7.3,

[2] It is not an exact face-on condition, as the inclination is not 90°, so the tracking observations still have a significant component in the in-plane directions of the orbit.

Table 7.3: OD accuracy of a satellite at different tracking conditions.

Tracking condition	$\overline{\mathbf{RMSE}}_{\text{pos}}$ [m]
Edge-on ($\Omega = 0°$)	6.366
Face-on ($\Omega = 90°$)	1.465
Intermediate ($\Omega = 45°$)	1.329
Intermediate ($\Omega = 135°$)	1.702

the OD accuracy is approximately periodic with half the period of the lunar orbit. The worst performances along the periodic cycle are found when any of the orbital planes are close to the edge-on tracking condition. At the nominal $\Omega_0 = 0°$, the value $\Delta\Omega = 0°$ leads to all 4 satellites being tracked in edge-on, producing the worst accuracies. For any other value of $\Delta\Omega$, one orbital plane moves away from the edge-on condition and the accuracy improves.

The eccentricity and the semi-major axis have the most noticeable impact on the OD accuracy in Figure 7.3. The worst accuracy is found either at the lowest value of a or the highest value of e, both corresponding to similarly low periselene altitudes. Accurately propagating the orbit at such low lunar altitudes ($\sim$100 km) likely requires a value of the DO^{e}_{L} greater than the nominal value of 20. These cases also show the longest run times, which indicates the relation between the more complicated OD conditions and the longer run times. Raising the value of a above 8000 km negatively affects the accuracy as well. It is hypothesized that the reason behind this is the increase in period of the satellites' orbits, which causes a reduction in the number of observed orbital revolutions over a constant T_{est}. Another possible reason is the increased relative relevance of the SRP acceleration compared to the lunar gravity. This would cause the mismatch in SRP modeling between the estimated and the true orbits to become more relevant, leading to a loss in accuracy.

The variation of $\overline{\text{RMSE}}_{\text{pos}}$ with the inclination in Figure 7.3 shows that the best performance is achieved when $i \approx 60$–$70°$. The reason for the loss in performance at higher and lower inclination values is not clear. When tracking in a face-on configuration, a lower inclination means that the lines of sight of the observations are closer to parallel to the orbital plane. This results in a better observability of the orbit in the in-plane directions. On the contrary, a higher inclination means that the lines of sight of the observations are closer to perpendicular to the orbital plane, which results in a better observability of the out-of-plane component. It is hypothesized that the intermediate inclinations achieve a good trade-off between the information offered by the observations in the in-plane and out-of-plane directions, yielding a better OD accuracy. The change in the in-plane and out-of-plane components of accelerations such as the SRP or the third bodies' gravities with a varying inclination may also be responsible for the observed trend.

Figure 7.4 depicts the effect of the parameters of the dynamic model on the $\overline{\text{RMSE}}_{\text{pos}}$. Both the DO^{e}_{L} and tol^{e} show a similar trend. Increasing the dynamic model fidelity (increasing DO^{e}_{L} and reducing tol^{e}) improves the OD accuracy before reaching a point at which further model improvements have no impact on the $\overline{\text{RMSE}}_{\text{pos}}$. The existence of this "floor value" can be attributed to the rest of model imperfections outside the dynamic model (observational noise, atmospheric effects, etc.). The improvement of the dynamic model beyond a certain point leads to accuracy improvements that are orders of magnitude smaller than the $\overline{\text{RMSE}}_{\text{pos}}$ value induced

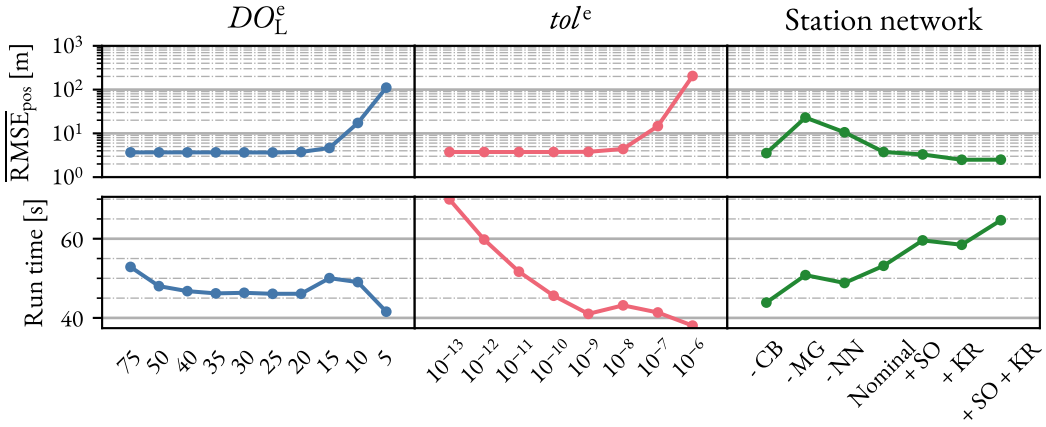

Figure 7.4: Influence of the propagation parameters and station network on the OD accuracy.

by the other factors. The "floor value" of $\overline{\text{RMSE}}_{pos} \approx 3$ m is achieved with $DO_L^e = 20$ and $tol^e = 10^{-9}$. This is coherent with the results presented in the sensitivity analysis of the orbital propagation reported in § 6.1. Figures 6.1 and 6.2 show that, for the nominal orbit, improving the dynamic model beyond $DO_L^r = 20$ and $tol^r = 10^{-9}$ yields sub-metric propagation errors, thus explaining the lack of OD accuracy improvement beyond these values. There is a clear relation between the run time and both DO_L^e and tol^e, with the higher fidelity models requiring longer run times. As the fidelity of the model decreases, the run times can increase again, as the estimation becomes more complicated and requires more iterations.

The effect of changing the network of ground stations used for tracking is also shown in Figure 7.4. The reduction in the number of stations has a notably different impact depending on which station is subtracted. Removing either Malargüe or New Norcia leads to an accuracy loss of barely 1 order of magnitude. On the other hand, removing Cebreros shows little impact on the accuracy. When attending at the visibility periods of the lunar orbits from each of these 3 stations, which can be done by looking at the residual plots in the verification section (e.g., Figure 5.3), Cebreros almost completely overlaps with the other 2 stations. Thus, removing Cebreros from the network only creates a brief gap in the otherwise continuous generation of observations (at least with $e_{min} = 5°$). Removing any of the other 2 stations yields a significantly wider gap in the generation of observations, thus being more detrimental to the performance of the OD. The addition of extra stations to the network seems to lead to little improvement in accuracy. Only the addition of a station at Kourou seems to have some positive impact on the OD, while a station at South Point adds no value. The reason behind this difference between stations is not completely clear, and the limited impact on the OD accuracy does not motivate further investigation. Adding and removing stations from the problem changes significantly the estimation run time. Less stations means a lower volume of observations to process, and consequently lower run times, and vice versa.

Regarding the observation properties, Figure 7.5 shows that neither the observation bias (range and Doppler) nor the transponder delay have a visible impact on the OD accuracy. This was expected, as they are all solve-for parameters of the estimation problem, and their effect on the OD solution is "removed" during the minimization of the residual RMS. The variation in f_{signal}, which affects the OD through the ionospheric delay of the observations, shows no noticeable impact on the $\overline{\text{RMSE}}_{pos}$ either. On the other hand, the $\overline{\text{RMSE}}_{pos}$ presents a clear direct relation with the noise factor F_σ. This strong relation suggests that the observational noise is one of

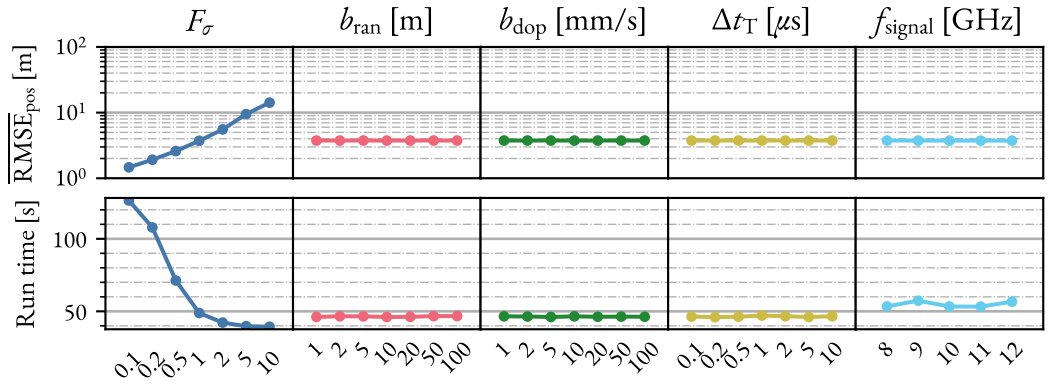

Figure 7.5: Influence of the observation properties on the OD accuracy.

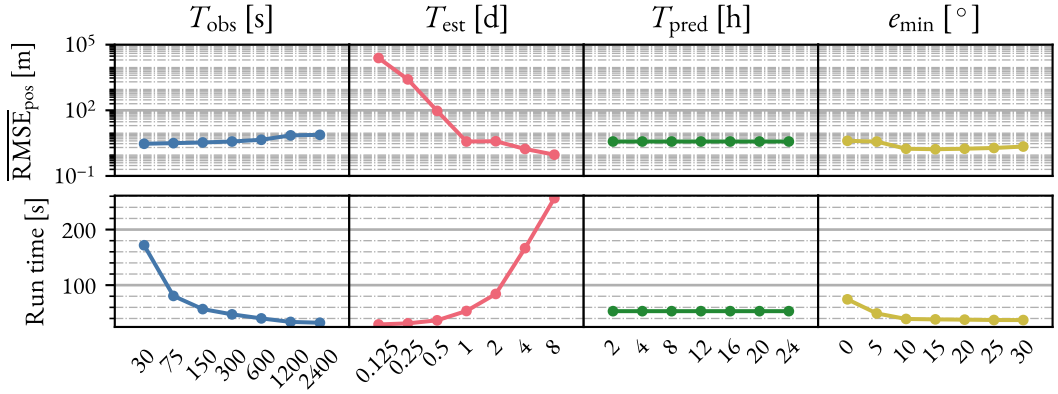

Figure 7.6: Influence of the tracking properties on the OD accuracy.

the most determining factors of the $\overline{\text{RMSE}}_{\text{pos}}$, highlighting the relevance of properly modeling the observations to obtain an accurate OD solution. However, the improvement in accuracy achieved by lowering the noise decreases as the noise level decreases. This is likely due to other effects, such as atmospheric modeling errors and propagation errors, becoming more prominent sources of error. Lower noise levels relate to high run times, likely due to requiring more iterations to converge to a better OD solution.

Lastly, Figure 7.6 shows the effect of the tracking parameters. Starting with T_{obs}, the major change in $\overline{\text{RMSE}}_{\text{pos}}$ is observed between $T_{\text{obs}} = 300$ s and $T_{\text{obs}} = 1200$ s, where the error is more than doubled. Reducing T_{obs} an entire order of magnitude below 300 s improves the accuracy by barely a meter, but increases the estimation run time in more than triple. The length of the estimation arc has a strong impact on the $\overline{\text{RMSE}}_{\text{pos}}$. For values of $T_{\text{est}} < 1$ d, the obtained accuracy is far worse than the requirement imposed on the system. The reason for this is both the reduced amount of observations available for the estimation and the more limited information used regarding the dynamic environment of the spacecraft, due to the shorter distance traveled by the spacecraft in their orbits. Increasing T_{est} beyond the nominal value of 1 d leads to better observability of the orbit in 3D, which is helpful in the estimation process to lessen the influence of observational noise and other imperfect modeling effects. High values of T_{est} achieve better accuracies at the expense of a severely increased estimation run time. The best values of e_{min} in terms of $\overline{\text{RMSE}}_{\text{pos}}$ are in the range 10–20°. For smaller values than that, the atmospheric model used to compute the residuals during the estimation is not accurate enough, and thus the OD

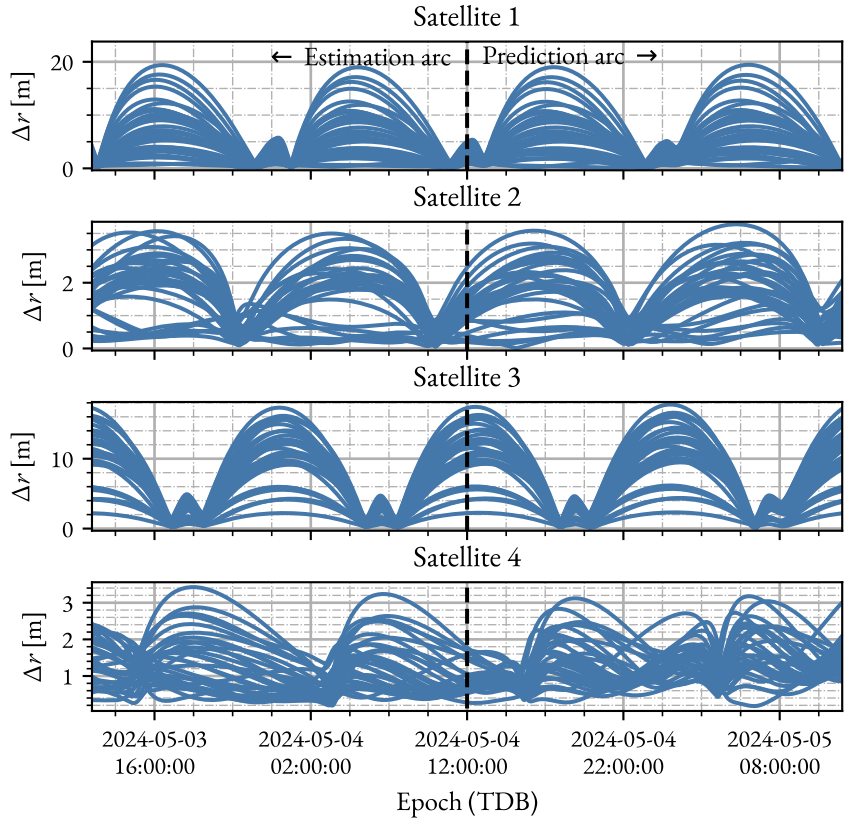

Figure 7.7: Time evolution of the position difference for all the LNS satellites during both the estimation and prediction arcs, using all random runs of the nominal configuration.

accuracy is negatively affected. Values of $e_{\text{min}} > 20°$ lead to a reduced volume of observations, due to the shorter periods of visibility from each station, while not significantly improving the quality of the observations. As a result, the $\overline{\text{RMSE}}_{\text{pos}}$ raises slightly. Very low values of e_{min} result in slightly higher run times, due to the larger volume of observations and the more complicated convergence due to using more badly modeled observations.

The behavior of $\overline{\text{RMSE}}_{\text{pos}}$ with varying T_{pred} displayed in Figure 7.6 is specially interesting. Against a first intuition, the length of the prediction arc does not seem to affect the performance of the OD system. One would expect that, as T_{pred} increases, the estimated orbit diverges from the true orbit and, as a result, the $\overline{\text{RMSE}}_{\text{pos}}$ increases. To better understand this behavior, Figure 7.7 represents the $\Delta r_i(t)$, as given in (4.1), for 30 random runs of all 4 satellites with the nominal configuration ($T_{\text{pred}} = 24\,\text{h}$). The epoch range in Figure 7.7 spans both the estimation and prediction arcs. The position differences for all 4 satellites show similar values both during the estimation and the prediction arcs. The reason behind this seems to be that the propagation errors, which should cause an increase of $\Delta r_i(t)$ in time during the propagation arc, are significantly smaller than the errors coming from the estimation. Then, it is hypothesized that, for higher values of T_{pred}, the degradation of the propagation would dominate over the estimation errors, and the OD accuracy would deteriorate as T_{pred} increases. Additionally, for better observation conditions (lower observational noise, longer estimation arc, etc.), it would be expected that the degradation of the prediction becomes noticeable in the considered range of 2–24 h.

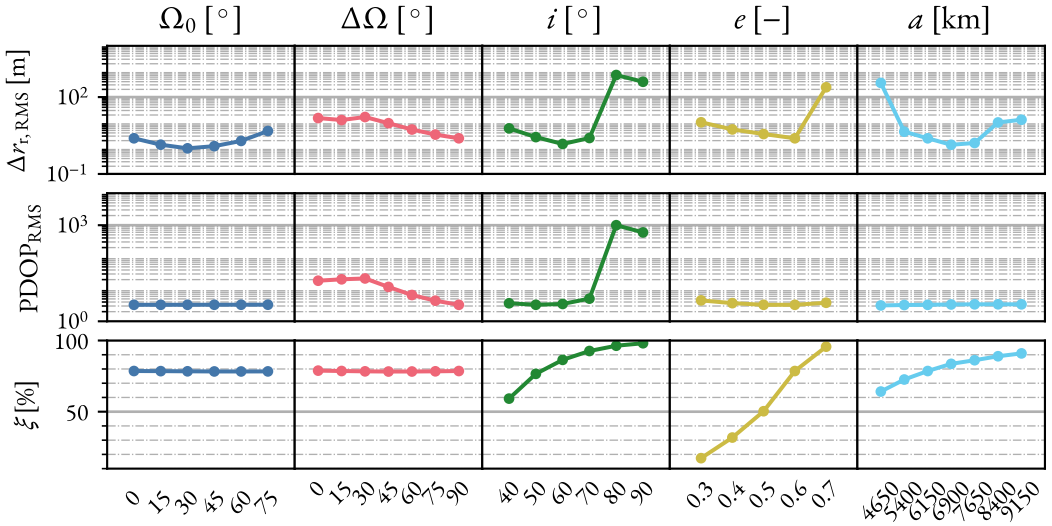

Figure 7.8: Influence of the orbit configuration parameters on the system's performance on the user's side.

7.2.2. User performance

As mentioned in § 4.2, the user positioning error depends both on the OD accuracy of the LNS and on the geometrical distribution of the satellites relative to the user's location. Both the PDOP and the fraction of 3-fold coverage are only affected by the distribution of the satellites. While the accuracy of the estimated orbits depends on many of the parameters in this preliminary analysis, the geometrical distribution of the satellites is only affected by the orbit configuration parameters. Thus, it is expected that the impact of this group of parameters on the user-related FoMs is more notable than that of other parameters.

Figure 7.8 shows the relation between the orbit configuration parameters and the user-related FoMs. The variation of Ω_0 has no impact on the PDOP and 3-fold coverage, which makes sense, as the changing Ω_0 roughly means rotating the satellites' configuration around the Z-axis of the lunar frame[3]. Thus, a polar location only observes an approximately equal change in the azimuth of all the satellites at any epoch, so the geometric configuration is essentially the same. This can be confirmed by looking at Figure 7.9, which shows the distribution of satellites in the sky at a certain epoch for 3 values of Ω_0. The result of this is that the $\Delta r_{r,RMS}$ curve is proportional to that of the $\overline{\text{RMSE}}_{pos}$. It must be noted that the values of $\Delta r_{r,RMS}$ are below the corresponding values of $\overline{\text{RMSE}}_{pos}$, which may seem counterintuitive at first, as the error in the user positioning should in principle not be lower than the error of the satellites' ephemerides. The reason for this is that only the component of the ephemerides error along each satellite's ranging direction to the user has an impact on $\Delta r_{r,RMS}$. Thus, the results imply that the trends observed in $\overline{\text{RMSE}}_{pos}$ are extensible to just the ranging component of the ephemerides error and, consequently, to $\Delta r_{r,RMS}$ as well.

The effect of $\Delta\Omega$ on the PDOP in Figure 7.8 has a simple explanation. For low values of $\Delta\Omega$, the two orbital planes of the constellation are close to parallel, thus leading to a poor spread of the satellites in the sky and PDOP values of ≈ 20. No improvement is observed when initially raising $\Delta\Omega$ from 0° to 30°. As it further increases past 30°, the two orbital planes of the constellation become closer to perpendicular, and the satellites spread over

[3]This is only true when considering the lunar point mass gravity, as including other dynamic effects results in slightly different orbits when changing Ω_0. However, the impact of those other effects is negligible for the purpose of this discussion.

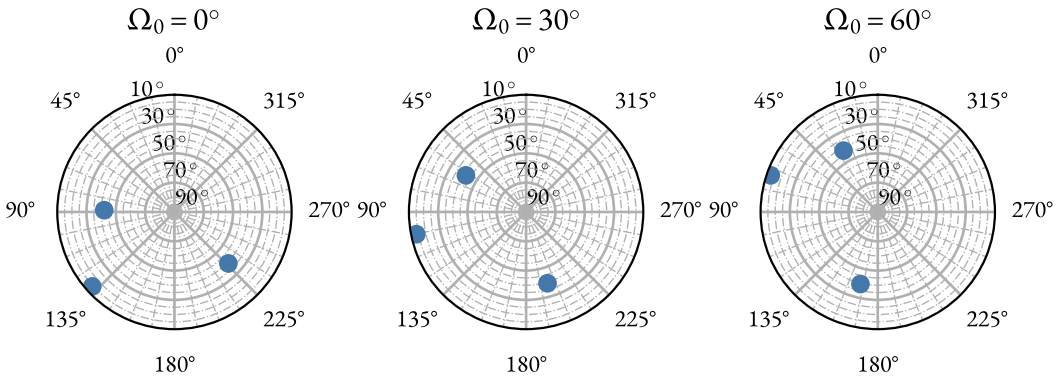

Figure 7.9: Polar view of the satellites from the LSP at $t = t_{ref} + T_{est} + T_{pred}/5 =$ 2024-05-04T16:48:00.000TDB for different values of Ω_0.

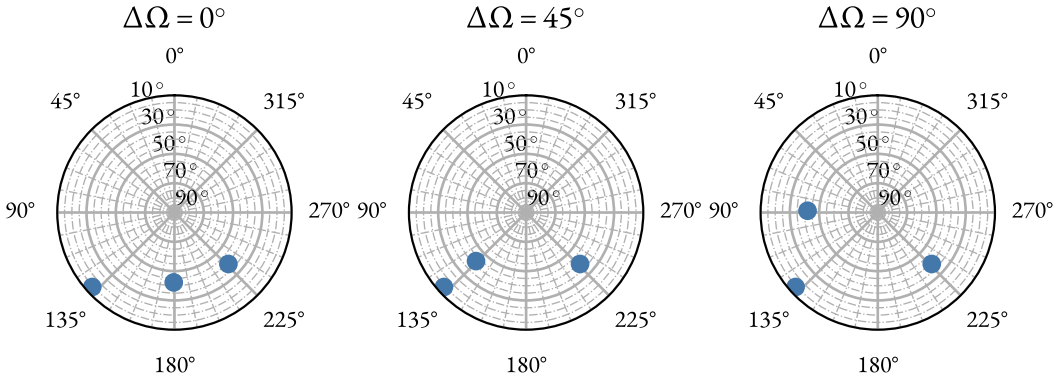

Figure 7.10: Polar view of the satellites from the LSP at $t = t_{ref} + T_{est} + T_{pred}/5 =$ 2024-05-04T16:48:00.000TDB for different values of $\Delta\Omega$.

the sky as seen from the user's location, improving their geometrical configuration and lowering the PDOP to ≈ 3. Figure 7.10 shows the spread of the satellites at the same epoch as $\Delta\Omega$ increases. This improvement in the geometric distribution also leads to an improved $\Delta r_{r,RMS}$. As the $\overline{\text{RMSE}}_{pos}$ is only slightly impacted by changes in $\Delta\Omega$ (except when having $\Delta\Omega = 0°$), the behavior of $\Delta r_{r,RMS}$ is dominated by the behavior of the PDOP. The 3-fold coverage of the LSP shows no variations for different values of $\Delta\Omega$, as the orbital planes change, but the orbits' shapes within their planes are the same.

Figure 7.8 shows an abrupt loss of user performance when using orbits above certain values of i. When considering values of $i > 70°$, the PDOP and, as a consequence, the $\Delta r_{r,RMS}$ suffer a sudden increase of more than two orders of magnitude. The 3-fold coverage of the LSP improves monotonically with increasing values of i. Figure 7.11 explains this effect. Increasing the inclination moves the apocenter of the orbits closer to the local zenith of the LSP, which makes the satellites visible over greater true anomaly arcs and, consequently, over longer time periods.

Lastly, both e and a are seen to have little impact on the quality of the geometrical configuration of the satellites to observe the LSP, so their PDOP curves are roughly flat. Only e appears to have a slight impact, reaching a minimum around $e = 0.6$. The result of this is that the behavior of $\Delta r_{r,RMS}$ for these two parameters is completely determined by the OD accuracy. Similarly to $\Delta\Omega_0$, the $\Delta r_{r,RMS}$ curve achieved when modifying

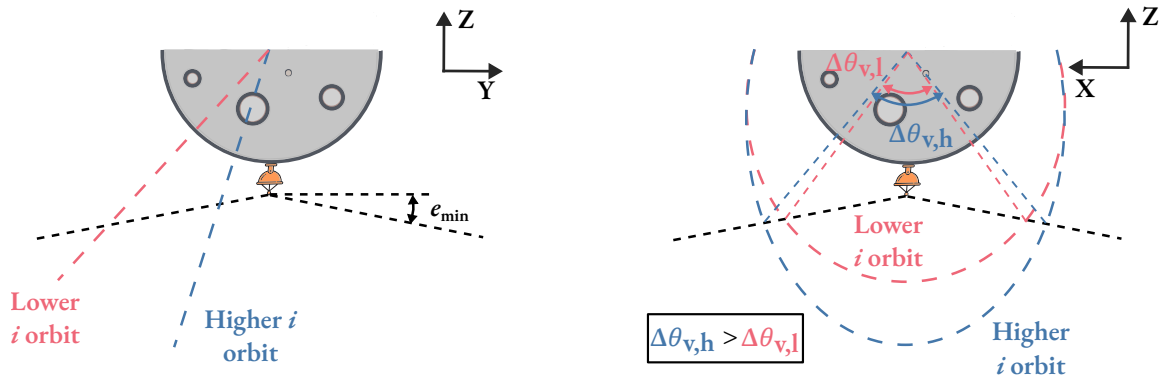

Figure 7.11: Schematic representation of the effect of i on the time of coverage of the LSP. The true anomaly arc with coverage is greater for orbits with a higher i. A longer true anomaly arc translates directly into a longer fraction of the orbital period due to the constant value of e.

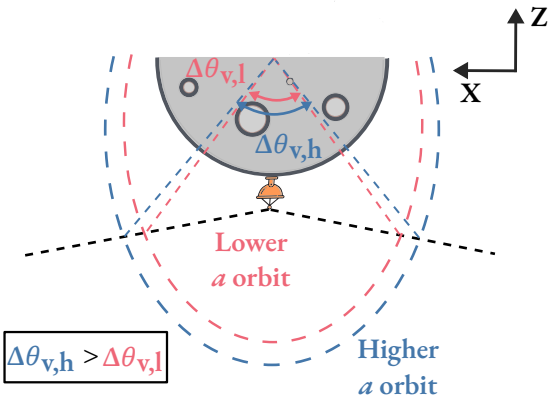

Figure 7.12: Schematic representation of the effect of a on the time of coverage of the LSP. The true anomaly arc with coverage is greater for orbits with a higher a. A longer true arc translates directly into a longer fraction of the orbital period due to the constant value of e.

these parameters is practically proportional to the curve of $\overline{\text{RMSE}}_{\text{pos}}$, reinforcing the observation that the trends shown by the $\overline{\text{RMSE}}_{\text{pos}}$ are extensible to just the ranging component of the ephemerides error. The 3-fold coverage is greatly affected by both a and e, monotonically increasing with the values of these two parameters. Figure 7.12 graphically describes the increased coverage of the LSP due to an increase in a. A higher a leads to a rise in altitude over the lunar surface at all points along the orbits. As a result, the satellites are visible from the LSP over greater true anomaly arcs, similar to what happens with increasing i. A rise in e means that the satellites are in the vicinity of their orbits' apocenters during a greater fraction of the orbital period, thus being individually visible from the LSP over longer time arcs. It is not possible to do the same graphical representation with the variation of e, as the fraction of the orbital period spent coasting over specific true anomaly arcs changes with varying e and the discussion is not purely geometrical.

The rest of problem parameters have no effect on the geometric distribution of the satellites. Thus, their PDOP_{RMS} and ξ curves do not show interesting features. As a result of this, the OD error completely dominates the behavior of the user positioning error. Thus, it is not worth dedicating a separate discussion to this topic.

7.2.3. Problem reduction

Having observed the individual influence of the problem parameters on the FoMs, it is possible to make some choices that help reduce the dimensionality of the problem. These choices are directed toward focusing the final part of the analysis on the parameters that drive the performance of the LNS, and doing so in a way that can yield meaningful conclusions about the design of the OD system.

The entire set of parameters considered in this preliminary phase of the analysis contains both design and non-design variables of the OD system. The design variables or parameters are those over which there is an active control during the system's design. They include, among others, the estimation and prediction arc lengths and the propagation parameters. The values of the design parameters are the OD system specifications. On the contrary, the non-design variables or parameters are inputs to the design over which there is no control. The impossibility of deciding over these variables can derive from various factors. Some variables, like the observational noise, relate to environmental aspects that cannot be modeled. Others, like the transponder delay, represent a certain technological limitation. The parameters that attend to design considerations of other parts of the LNS, such as the orbit configuration, which depends, for example, on the power and fuel budget, are also considered non-design variables from the perspective of the OD system. The goal of this problem reduction stage is to select the design parameters with the greatest impact on the OD accuracy while giving reasoned values to the rest of design parameters and the non-design parameters.

Orbit configuration

Despite the orbit configuration parameters being considered non-design variables of the OD system, their impact on the different FoMs is significant. Thus, to examine for the effect of having different orbit configurations during the second phase of the design analysis, 3 configuration are defined.

A *Nominal configuration.* This orbit configuration, as stated in § 4.5, is interesting because it is the most repeated configuration found in the literature. The only parameter that does not have its nominal value is Ω_0. As discussed in the previous section, the value of Ω_0 does not affect the constellation's geometry itself, but serves to represent the effect of the Moon orbiting the Earth. Thus, it is unavoidable that the Ω_0 of any given constellation continuously changes in time. Because of this, to select the most pessimistic scenario, the value $\Omega_0 = 75°$, which yields the greatest $\overline{\text{RMSE}}_{\text{pos}}$, is selected. Table 4.5 contains the Keplerian elements of this nominal configuration, while its associated orbit configuration parameters, as defined in this chapter, are given in Table 7.4.

B *"Best user performance" configuration.* This orbit configuration shows the best user performance solely attending to PDOP and 3-fold coverage criteria, based on the results presented in Figure 7.8. It must be stated that it is not the objective to find an "optimal" orbit configuration, but to qualitatively assess the previous results regarding these two user-related FoMs and select a configuration that performs notably well on both of them. The choice of $\Delta\Omega = 90°$ and $a = 9150$ km are evident, as they show either a better or an equal PDOP and 3-fold coverage compared to any other values of those parameters. The chosen eccentricity is $e = 0.7$, sacrificing a small increase in PDOP to reach a significantly greater 3-fold coverage. On the other hand, a value of $i = 60°$ provides a good trade-off between both FoMs. For the same reason as in configuration A, $\Omega_0 = 75°$ is used. These values are summarized in Table 7.4.

C *"Most demanding" configuration.* This third configuration has the intention of assessing the design of the

Table 7.4: Value of the parameters for the 3 orbit configurations defined for the reduced problem.

	Ω_0	$\Delta\Omega$	i	e	a
Nominal	75°	90°	51.7°	0.6	6150 km
"Best user performance"	75°	90°	60°	0.7	9150 km
"Worst case"	75°	90°	40°	0.7	6150 km

OD system in the most demanding scenario. To do this, the values of the orbit configuration parameters are those showing the worst OD accuracy, attending to Figure 7.3, with two exceptions. Considering $a = 4650$ km and $e = 0.7$ is not possible because the periselene of the orbits would be below the lunar surface. Thus, it is selected to use $a = 6150$ km with the "most restrictive" value of $e = 0.7$, a combination that yields a periselene slightly above 100 km in altitude. The second exception is the value of $\Delta\Omega$. It is discussed in the previous section that $\Delta\Omega = 0°$ yields the worst OD accuracy because, for the nominal $\Omega_0 = 0°$, that configuration has simultaneous edge-on tracking of all satellites in the constellation, which is detrimental for the accuracy. At a different value of Ω_0, this is not applicable. In any case, having a constellation with all 4 satellites in the same orbital plane does not seem to be sensible from the user performance perspective. Thus, it is chosen to use $\Delta\Omega = 90°$, which is the most sensible option and leads to an OD accuracy comparable to any other $\Delta\Omega$ value than 0°. The values of the orbit configuration parameters are shown in Table 7.4. It must be noted that the period of the orbits in this configuration is of approximately 1 d (double the orbital period of the other two configurations).

Fixed parameters

Among the rest of problem parameters, it is simple to separate the parameters that drive the OD accuracy from those with little influence on it. In order to reduce the dimensionality of the problem, only those design parameters which are identified as accuracy drivers remain as variable parameters, while the rest are fixed to a sensible value.

The remaining non-design problem parameters are: b_{ran}, b_{dop}, Δt_{T}, f_{signal}. All three of b_{an}, b_{dop} and Δt_{T} show no effect on the accuracy of the estimated solution. This is coherent with the setup used for the estimation problem, as thes are solve-for parameters of the estimation. Furthermore, f_{signal} does not show any visible effect on the OD accuracy either. Because of this, all these parameters are fixed to their nominal value.

Both T_{obs} and e_{min} have a visible effect on the OD accuracy. However, variations of these parameters over broad ranges of values do not account for a change in $\overline{\text{RMSE}}_{\text{pos}}$ of even an order of magnitude. The results of the preliminary analysis show that there is little improvement in using values of $T_{\text{obs}} < 600$ s, while the run time grows notably. Therefore, a value of $T_{\text{obs}} = 300$ s is a conservative option (as using $T_{\text{obs}} = 600$ s may lead to unacceptable losses in accuracy in different scenarios) while not penalizing greatly the run time of the estimation. Using $e_{\text{min}} = 15°$ is a sensible choice as well, as it leads to the best OD accuracy without a notable impact on the run time. There is no apparent good reason to choose a different value.

Removing certain ground stations from the problem shows a considerable impact on the accuracy of the estimation. This proves the relevance of the different ground stations and of having continuous visibility of the lunar orbits. Nevertheless, from a nominal operations perspective, it is not sensible to consider just two ground

Table 7.5: Fixed parameters for the final part of the design analysis.

Non-decision parameter	Value	Decision parameter	Value
b_{ran}	10 m	T_{obs}	300 s
b_{dop}	10 mm s^{-1}	e_{min}	15°
Δt_{T}	1 μs	T_{pred}	24 h
f_{signal}	8 GHz	Station network	Nominal (CB, MG & NN)

stations, as it would lead to a very poor configuration in terms of robustness. Adding extra stations shows little benefit for the system, not enough to justify the increased cost that would be incurred with their inclusion. Thus, the most reasonable choice is to consider the nominal network of stations for the tracking of the LNS.

The prediction arc length is the last parameter that does not significantly affect the accuracy of the OD solution within a logical range of values. The reason for this is investigated in the previous section and is found that the degradation of the propagation smaller in magnitude than the accuracy of the achieved estimated orbit. A propagation accuracy of the order of the meter has been found to not require a very high-fidelity model of the satellite's dynamics. Thus, it is assumed that T_{pred} does not have a relevant influence when looking at OD accuracies of the order of the meter. Because of this, it is decided to fix it to a constant value. Regardless, the theoretically most conservative value of $T_{\text{pred}} = 24$ h is selected and the effect of varying T_{pred} on the recommended OD specifications is investigated after the system design is complete.

Table 7.5 presents a summary of the parameter that are fixed for the final part of the analysis, along with their selected values.

Main parameters of the analysis

The remaining parameters—DO_{L}^{e}, tol^{e}, F_σ and T_{est}—are those that drive the accuracy of the OD solution in terms of RMSE_{pos}. Thus, these 4 parameters remain variable during the final part of the analysis. While DO_{L}^{e}, tol^{e} and T_{est} are design parameters of the OD system, the noise of the observations is not. Thus, it is included in the analysis following a special approach: different noise levels are considered, and different OD system specifications are determined for each of those levels. The levels included in the analysis are the following.

1. *Nominal noise level:* $F_\sigma = 1$. Using a noise level of 1 m in range and 1 mm s^{-1} in Doppler is a conservative option. Even if these values are derived from the operational tracking of the LRO, the technological advancements over the last 15 years have entailed a reduction in the observational noise.
2. *Reduced noise level:* $F_\sigma = 0.2$. Both the tracking of the GRAIL mission [137] and recent investigations about the OD of LNSs [52] consider noise values of the order of a few decimeters in range and a few tenths of millimeters per second in Doppler. Thus, this value of F_σ is more representative of the current accuracy capabilities in producing tracking observations.

It would be desirable to analyze a higher number of noise levels. However, the computational effort involved in each of the analyses does not allow exploring more values. The combination of each noise level with each of the defined orbital configurations leads to a total of 6 cases in which the OD system is analyzed. Table 7.6 summarizes the orbit and noise configurations associated to each of these cases.

Table 7.6: Cases of interest for the final design analysis of the OD system.

	Nominal orbit configuration	**Best user performance orbit configuration**	**Most demanding orbit configuration**
Nominal noise level	A1	B1	C1
Reduced noise level	A2	B2	C2

7.3. Parameter design of the OD system

Having decided on the scenarios to study, it is left to perform the final stage of the analysis to produce a recommendation for the OD system specifications. To do this, a general strategy is defined, selecting the method used to both specify the design space and evaluate the system's performance within that design space. Later, this strategy is applied to each of the 6 cases specified in Table 7.6, obtaining a set of system specifications for each of them.

7.3.1. Design strategy

The analysis for the design of the OD system involves 4 steps. The first one is to select the values of $DO^{\mathrm{e}}_{\mathrm{L}}$, tol^{e} and T_{est} that act as boundaries of the design space. These boundary values need not be the same for each of the cases. Thus, each case is studied independently to find the values that ensure the system's capability to meet the requirement. The second step is to sample the 3D design space formed by the parameters. This is done through a Monte Carlo (MC) approach using a quasi-random low-discrepancy sequence to generate a cloud of points that cover the entirety of the space. Then, each of the defined points is evaluated by computing its OD solution and its corresponding values of the FoM. The value of the $\overline{\mathrm{RMSE}}_{\mathrm{pos}}$ at each point is used to compute the isosurface corresponding to the 2 m requirement in accuracy. Lastly, the requirement isosurface serves to select the recommended design point. The values of $\overline{\mathrm{RMSE}}_{\mathrm{pos}}$ associated to the selected point are computed to ensure that it meets the requirement.

Specification of the design space

In order to have a set of meaningful values for the parameter of the analysis, it is relevant to select adequate boundaries for the design space. This means that the boundaries should span a reasonable range of values of the parameters that allow to meet the OD accuracy requirement of 2 m. To do so, the influence of each of the parameters is first studied by doing an individual variation of $DO^{\mathrm{e}}_{\mathrm{L}}$, tol^{e} and T_{est} while keeping the remaining 2 parameters constant at a given value. The range of values considered for this 1-by-1 variation of parameters is decided based on the knowledge and intuition gained from the preliminary analysis. Thus, the range of values may differ from one case to the other and are specified later with the discussion of each of the cases.

For the analysis, it is convenient to specify the design space in terms of normalized parameters. The normalization seeks to transform the range of values for each parameter into the unit interval—that is, the $[0, 1]$ interval. This is useful to standardize the design space of all cases and convenient based on the sampling strategy described later. During the preliminary analysis, some parameters have shown that their influence on the $\overline{\mathrm{RMSE}}_{\mathrm{pos}}$ is well observed by varying them in a logarithmic scale. Both tol^{e} and T_{est} are among them. Because of this, the

normalization of these 2 parameters also changes their scale. With this, the normalization of the parameters is given by

$$\begin{aligned}
\delta &= \frac{DO_{\mathrm{L}}^{\mathrm{e}} - \left(DO_{\mathrm{L}}^{\mathrm{e}}\right)^{\mathrm{L}}}{\left(DO_{\mathrm{L}}^{\mathrm{e}}\right)^{\mathrm{U}} - \left(DO_{\mathrm{L}}^{\mathrm{e}}\right)^{\mathrm{L}}}, \\
\rho &= \frac{\log_{10}\left(tol^{\mathrm{e}}\right) - \log_{10}\left(\left(tol^{\mathrm{e}}\right)^{\mathrm{L}}\right)}{\log_{10}\left(\left(tol^{\mathrm{e}}\right)^{\mathrm{U}}\right) - \log_{10}\left(\left(tol^{\mathrm{e}}\right)^{\mathrm{L}}\right)}, \\
\tau &= \frac{\log_2\left(T_{\mathrm{est}}\right) - \log_2\left(\left(T_{\mathrm{est}}\right)^{\mathrm{L}}\right)}{\log_2\left(\left(T_{\mathrm{est}}\right)^{\mathrm{U}}\right) - \log_2\left(\left(T_{\mathrm{est}}\right)^{\mathrm{L}}\right)},
\end{aligned} \tag{7.1}$$

where δ, ρ and τ are the normalized $DO_{\mathrm{L}}^{\mathrm{e}}$, tol^{e}, T_{est}, respectively. The notation $(X)^{\mathrm{L}}$ and $(X)^{\mathrm{U}}$ represents the lower and upper bounds of any parameter X, respectively. Thus, the design space of any scenario is the cube formed by the variation of the normalized parameters in the unit interval.

Monte Carlo approach

Once the design space is known, it is sampled using a MC strategy. Instead of using a regular pseudo-random sequence to compute the sample points in the design space, the analysis uses the Soboĺ sequence. The Soboĺ sequence is a quasi-random low-discrepancy sequence that produces values in a unit N-dimensional supercube. It is said to be "quasi-random low-discrepancy" because its values can be deterministically computed and they uniformly cover the N-dimensional space, along with any of its lower-dimensional projections. For the purpose of the sequence, its "randomness properties" are not of special interest, so there is no drawback in using the Soboĺ sequence. In fact, due to the sequence ensuring the uniform coverage of the space, it is more convenient than any arbitrary pseudo-random sequence. The Soboĺ sequence is accessed through the Python's *scipy* module, using its scrambling option and setting the seed to 5000.

As mentioned, the Soboĺ sequence produces values in the continuous unit hypercube. However, the parameter δ has a series of valid discrete values corresponding to the integer values of $DO_{\mathrm{L}}^{\mathrm{e}}$. For that reason, the sampled points of the sequence are rounded in δ to the closest valid discrete value.

Having defined the sampling strategy, it is left to decide the number of samples (N_{points}) used in the analysis. Using a larger number of points is desirable, as it means that the sampling of the design space is denser and the representation of the FoMs in the space is more precise. However, the computational effort of the analysis grows proportionally to the number of points. As the computational cost associated to a single point is already considerably high, due to the need of considering multiple random runs to achieve statistical significance, this sets an upper limit on the number of points that can be used. Figure 7.13 shows the coverage of the 3D space achieved by different values of N_{points}. The value $N_{\mathrm{points}} = 500$ covers the design space densely enough to produce representative results, while still being realistic within the time constraints of this thesis.

Simulation environment

Ideally, all the simulations required for the presented analysis should be computed in a single controlled computational environment. Nevertheless, the large volume of simulations demands the use of more than one computational environment so that they can be finished within the time frame of this thesis. Taking into account

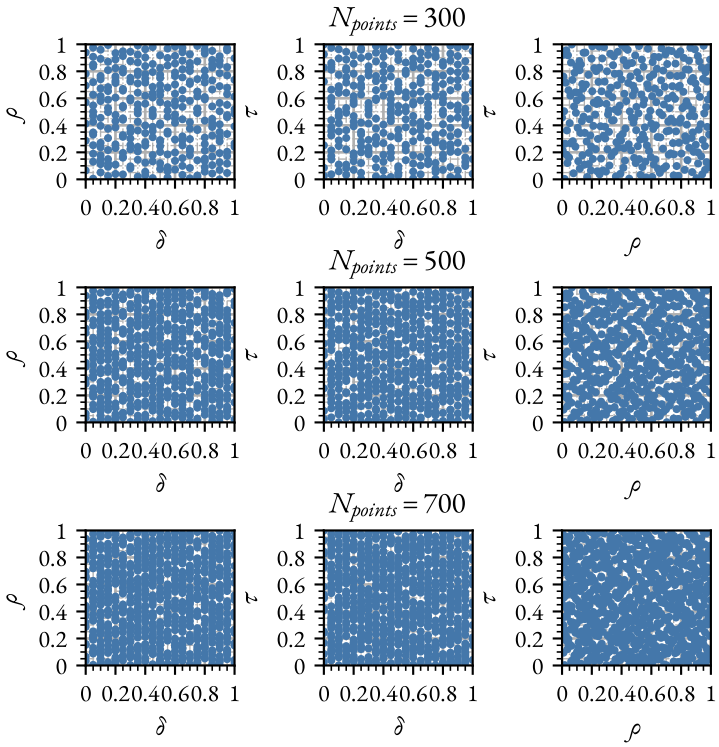

Figure 7.13: Coverage of the 3D design space by the Sobol sequence for several numbers of samples. The δ parameter can have 21 possible discrete values.

the accuracy levels required for the analysis, this is not expected to have any notable impact on the values of the FoMs. On the other hand, it can have a significant impact on the run time of the estimation. Because of this, any given random run is computed in the same environment for all points of the MC. The analyses of all 6 cases meet this rule. This is done to reduce the effect of potential differences in run time between environments, so that the results are as representative as possible.

Post-processing of the results

Once the raw results—the values of the FoMs at all points—are computed, they need to be processed in a way that allows choosing a set of final values for the parameters. First, the raw results are interpolated to a regular rectangular grid using Radial Basis Function (RBF) interpolation. The RBF interpolation is chosen over the simpler linear interpolation as it lightly smoothens the interpolated result, leading to an almost identical isosurface, but easier to visualize. This interpolation functionality is accessed through Python's *scipy* module. The isosurface corresponding to $\overline{\text{RMSE}}_{\text{pos}} = 2$ m is then computed from the interpolated data using the Lewiner's marching cubes method provided by the Python's *skimage* module. This isosurface (approximately) marks the boundary between the regions of the design space above and below the $\overline{\text{RMSE}}_{\text{pos}} = 2$ m requirement. This can be used to decide the best value of the OD parameters for each of the cases.

It must be remarked that, due to the selection of the RBFs interpolation method, the differences of several orders of magnitude in $\overline{\text{RMSE}}_{\text{pos}}$ among points in the design space affect the quality of the interpolation negatively. To deal with this, both the interpolation and the subsequent computation of the isosurface are done using the base-10 logarithm of the $\overline{\text{RMSE}}_{\text{pos}}$. Doing this avoids the issue of having regions with highly disparate

$\overline{\text{RMSE}}_{\text{pos}}$ values, while not degrading the accuracy of the isosurface computation—there is no practical difference between computing the isosurface corresponding to $\log_{10}\left(\overline{\text{RMSE}}_{\text{pos}}\right) = \log_{10}(2\,\text{m})$ or the one corresponding to $\overline{\text{RMSE}}_{\text{pos}} = 2\,\text{m}$.

Design point selection

The isosurface corresponding to the OD accuracy requirement value approximates the limit between the region that fulfills the requirement and the region that does not. Evidently, the desired design point lies inside the fulfilled requirement region. The preliminary analysis shows that, for the remaining design parameters, there is a trade-off between accuracy and computational cost—that is, raising or lowering the value of these 3 parameters to reduce $\overline{\text{RMSE}}_{\text{pos}}$ leads to an increase in run time. Thus, it is also desired that the design point lies close to the isosurface, to avoid using more computational resources than needed. Figure 7.4 and Figure 7.6 show that the run time grows monotonically with decreasing tol^{e} and with increasing T_{est}. Consequently, the sought design point has the highest possible value of ρ and the lowest possible value of τ. Theoretically, evaluating a SH expansion using a higher maximum degree and order involves a greater computational cost. The relation between DO^{e}_{L} and run time in Figure 7.4 is not as evident as for the other 2 parameters. Nevertheless, this might just be an implementation-specific feature of GODOT. Because of this, a design point with a lower δ is desirable. Still, based on the results, this last criterion has a low priority, meaning that it only applies when it does not conflict with any of the aforementioned criteria.

7.3.2. OD system specifications for the nominal orbit configuration

Starting with the nominal orbit configuration, Figure 7.14 and Figure 7.15 show the influence of the 3 design parameters of the reduced problem on the OD accuracy for cases A1 and A2, respectively. The selection of the range of values for each of the parameters derives from the results in § 7.2. The individual variation of the parameters considers the following values when kept constant: $DO^{\text{e}}_{\text{L}} = 20$, $tol^{\text{e}} = 10^{-10}$ and $T_{\text{est}} = 1\,\text{d}$. The trends shown by the curves corresponding to cases A1 and A2 are similar. For values of $DO^{\text{e}}_{\text{L}} \leq 15$ and $tol^{\text{e}} \geq 10^{-8}$, the $\overline{\text{RMSE}}_{\text{pos}}$ values are almost identical in A1 and A2. This suggests that, for those values, the lower fidelity of the dynamic model limits the accuracy of the OD, dominating over observational noise considerations. Both A1 and A2 show that the OD accuracy does not further improve when using $DO^{\text{e}}_{\text{L}} \geq 20$ and $tol^{\text{e}} \leq 10^{-9}$. Case A2 has a lower floor value in the achievable accuracy, reaching $\overline{\text{RMSE}}_{\text{pos}} \approx 0.5\,\text{m}$, compared to A1, which does not go below $\overline{\text{RMSE}}_{\text{pos}} \approx 1.5\,\text{m}$. In these ranges of values, the observational noise is the limiting factor on the accuracy, so the lower noise of scenario A2 allows for a better accuracy. Regarding T_{est}, the lower noise of A2 reduces the $\overline{\text{RMSE}}_{\text{pos}}$ compared to A1 for values of $T_{\text{est}} \leq 2\,\text{d}$ by approximately half an order of magnitude. For greater values, the noise level does not seem to be very relevant, as the curves of both A1 and A2 show similar values. Furthermore, the OD accuracy seems to deteriorate for the higher values of T_{est}. This can be attributed to the degradation of the propagation with the increasing propagation interval. It is likely that using a higher fidelity dynamic model would enable better accuracies at $T_{\text{est}} > 2$.

The results in Figure 7.14 and Figure 7.15 serve to decide the lower and upper boundaries to be used for the normalization of the design parameters. These boundaries are summarized in Table 7.7. They limit the range of interest of each of the parameters, inside which the $\overline{\text{RMSE}}_{\text{pos}}$ curves intersect the 2 m requirement for both cases A1 and A2. The values in Table 7.7 specify the design space used for the analysis of A1 and A2. After this, the design space is sampled as described in § 7.3.1, and the analysis can continue independently for each case.

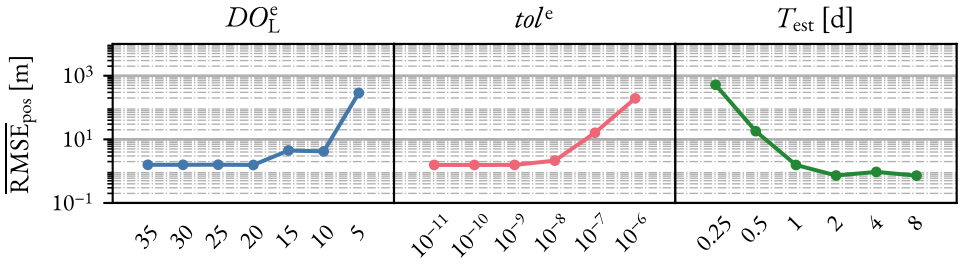

Figure 7.14: Influence of the individual variation of the design parameters on the OD accuracy for the case A1.

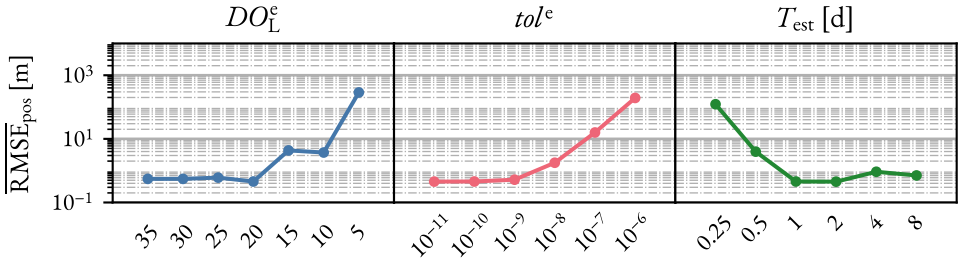

Figure 7.15: Influence of the individual variation of the design parameters on the OD accuracy for the case A2.

Table 7.7: Boundaries of the design parameters for the nominal orbit configuration (configuration A).

Parameter	Lower boundary	Upper boundary
DO^{e}_{L}	10	30
tol^{e}	10^{-10}	10^{-7}
T_{est}	0.5 d	8 d

Case A1: nominal noise level

Figures 7.16 to 7.18 show the values of different FoMs at 500 points throughout the design space. This is done by means of the 3 principal 2D projections of the cubic design space, as these views are useful to identify the relations between the FoMs and the parameters. Figure 7.16 allows identifying trends of the OD accuracy with each of the 3 normalized parameters. The $\overline{\text{RMSE}}_{\text{pos}}$ increases with decreasing δ or τ, and with increasing ρ. Figure 7.17 shows that the run time of the estimation is completely dominated by τ. The normalized parameter ρ also has a visible influence on the run time, which is especially noticeable at high values of τ, where the highest run time values are found in the range $\rho = [0.1, 0.4]$. All these trends are coherent with the observations derived from the results in § 7.2. Regarding the user positioning accuracy, the distribution of $\Delta r_{\text{r,RMS}}$ values displayed in Figure 7.18 closely resembles that of the $\overline{\text{RMSE}}_{\text{pos}}$. This observation reinforces the observation made in § 7.2 that the $\overline{\text{RMSE}}_{\text{pos}}$ is closely related to $\Delta r_{\text{r,RMS}}$, which would make it a suitable FoM to evaluate the OD accuracy.

Figure 7.19 shows the requirement contour surface inside the design space of A1. The surface divides the design space into two regions. The "quasi-convex" space delimited by the surface contains the design points with $\overline{\text{RMSE}}_{\text{pos}} < 2$ m (hereon referenced as *valid* points). Points on the remaining of the design space are above the OD accuracy requirement. The shape of the isosurface is remarkable, consisting of three parts which are approximately parallel to the boundaries of the design space. The first one, and the flattest, lies at $\tau \approx 0.2$ and

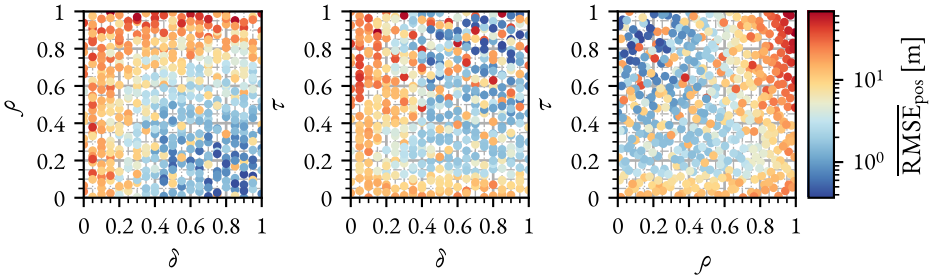

Figure 7.16: OD accuracy of the sampled design space using $N_{\text{points}} = 500$ for the case A1.

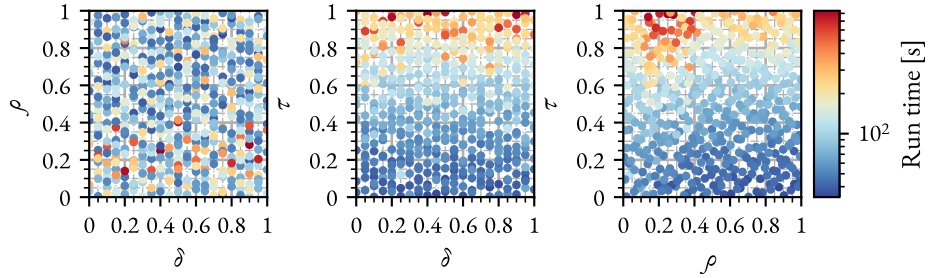

Figure 7.17: Run time of the sampled design space using $N_{\text{points}} = 500$ for the case A1.

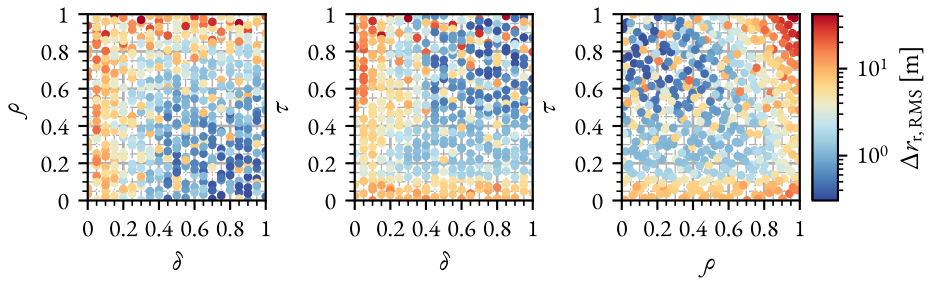

Figure 7.18: User positioning error of the sampled design space using $N_{\text{points}} = 500$ for the case A1.

sets a lower boundary for the estimation arc length of the points meeting the requirement. The second part lies at $\delta \approx 0.4$, with values below 0.4 at high τ and near $\tau = 0.2$, and higher values in between. It marks the minimum degree and order of the lunar potential to achieve the requirement. Lastly, the most irregular part ranges from $\rho \approx 0.4$ at higher values of τ to $\rho \approx 0.65$ at $\tau \approx 0.2$. It acts as the upper limit of the integrator tolerance to meet the requirement. The isosurface showing lower required values of ρ at higher τ can be explained by the fact that each of the steps in the propagation needs to be more accurate to compensate for the longer propagation interval to achieve an adequate accuracy level for the estimation. However, this does not seem to apply to the lunar SH, as a longer estimation arc (higher τ) requires fewer terms of the expansion (lower δ) to attain an equivalent accuracy level.

Attending to the criteria in § 7.3.1, the design point selected for A1 is represented in Figure 7.19 using a black dot. It is close to the isosurface and has a low τ, a low δ and a high ρ while lying inside the valid region. Table 7.8 contains the values of the normalized parameters, together with their equivalent values of the original design parameters. The value of $\overline{\text{RMSE}}_{\text{pos}}$ of this design point confirms that it is a valid point close to the requirement.

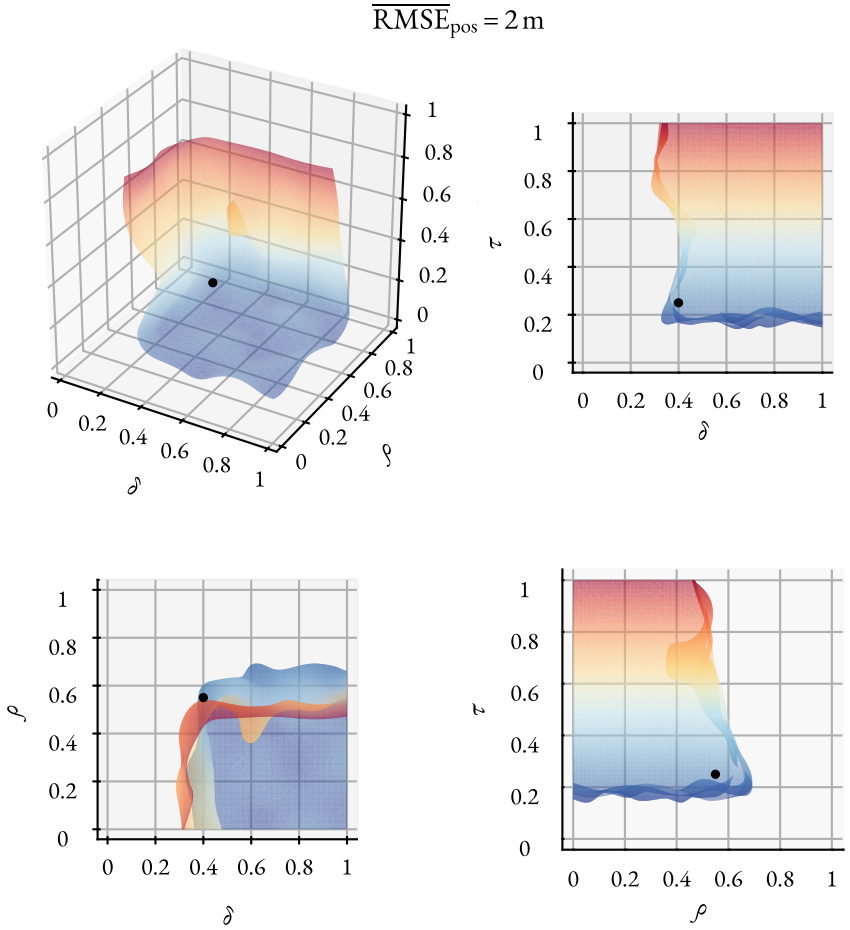

Figure 7.19: Isosurface correponding to the OD accuracy requirement for the scenario A1.

Table 7.8: Recommended value of the design parameters and their associated OD accuracy for the case A1.

$\overline{\text{RMSE}}_{\text{pos}} = 1.95\,\text{m}$

Normalized parameter	Value		Parameter	Value
δ	0.40	$\rightarrow$	DO^{e}_{L}	18
ρ	0.55	$\rightarrow$	tol^{e}	4.5×10^{-9}
τ	0.25	$\rightarrow$	T_{est}	1.0 d

Case A2: reduced noise level

The trends observed for the case A2 are similar to those of A1. Figure 7.20 shows that the main difference between these two scenarios in terms of $\overline{\text{RMSE}}_{\text{pos}}$ occurs at low values of τ, where A2 achieves lower values of this FoM. Apart from this, a slight overall reduction in $\overline{\text{RMSE}}_{\text{pos}}$ is visible at design points with a high δ, low ρ, and high τ, where the values are already the lowest in case A1. Nevertheless, both A1 and A2 share the same minimum value of $\overline{\text{RMSE}}_{\text{pos}} \approx 0.4\,\text{m}$. Regarding the run time displayed in Figure 7.21, τ remains as the parameter with the strongest impact. The effect of a low ρ on the estimation run time is more clearly observed as well. Once again, there is a close relation between the values of $\overline{\text{RMSE}}_{\text{pos}}$ in Figure 7.20 and the values of

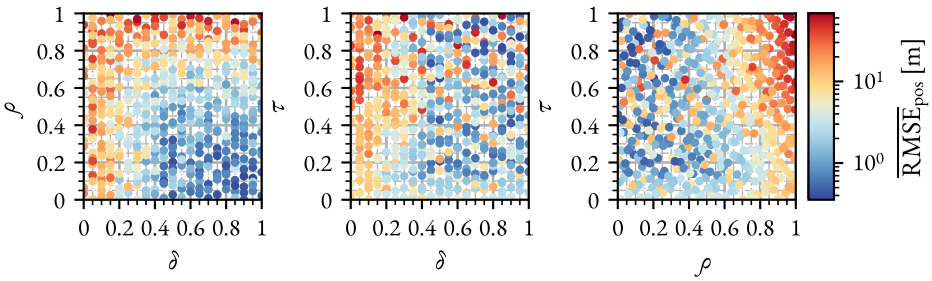

Figure 7.20: OD accuracy of the sampled design space using $N_{\text{points}} = 500$ for the case A2.

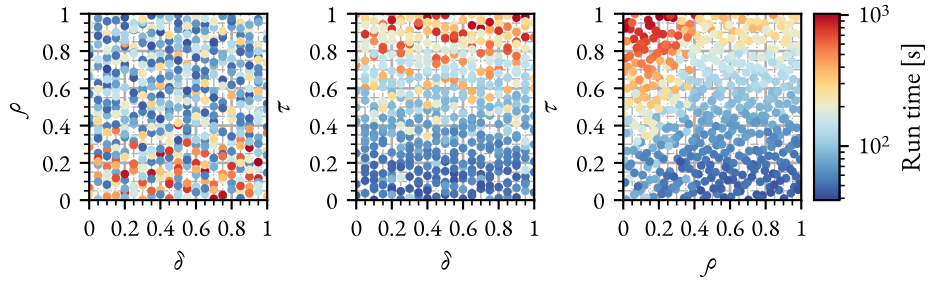

Figure 7.21: Run time of the sampled design space using $N_{\text{points}} = 500$ for the case A2.

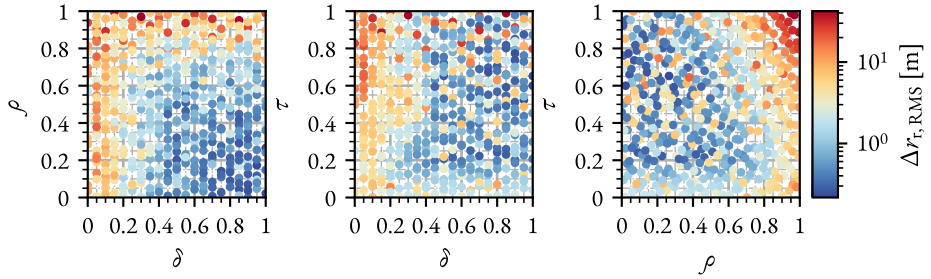

Figure 7.22: User positioning error of the sampled design space using $N_{\text{points}} = 500$ for the case A2.

$\Delta r_{\text{r,RMS}}$ in Figure 7.22 throughout the design space, further highlighting the adequacy of the $\overline{\text{RMSE}}_{\text{pos}}$ as a means of evaluating the OD accuracy due to its tight relation to the user positioning accuracy.

The requirement isosurface associated to A2, which can be observed in Figure 7.23, has an almost identical shape to that of A1 in Figure 7.23. Similar to A1, the valid region is the approximately convex region of the design space created by the isosurface. Both surfaces are practically equal at $\tau > 0.5$, as the OD accuracy is dominated by the fidelity of the dynamic model and, thus, noise differences have no impact. The most remarkable difference relates to the lower limit in τ of the valid region. For A2, the valid region extends to the lower value of $\tau \approx 0.08$, or even $\tau \approx 0.05$ at specific values of δ and ρ. This reduction in the required τ could be expected, as it is in line with the results in Figures 7.15 and 7.20. Apart from this, the remaining features are similar to those displayed in case A1. The dependency of the ρ values of the surface on τ is also visible in Figure 7.23. As the valid region of A2 includes shorter estimation arcs, the range of valid integrator tolerances also extends, reaching values of $\rho > 0.7$ at $\tau \approx 0.1$. The shorter arcs involve fewer integration time steps, so the allowable error at each step to obtain a certain propagation accuracy is greater and, thus, the required tolerance is less strict.

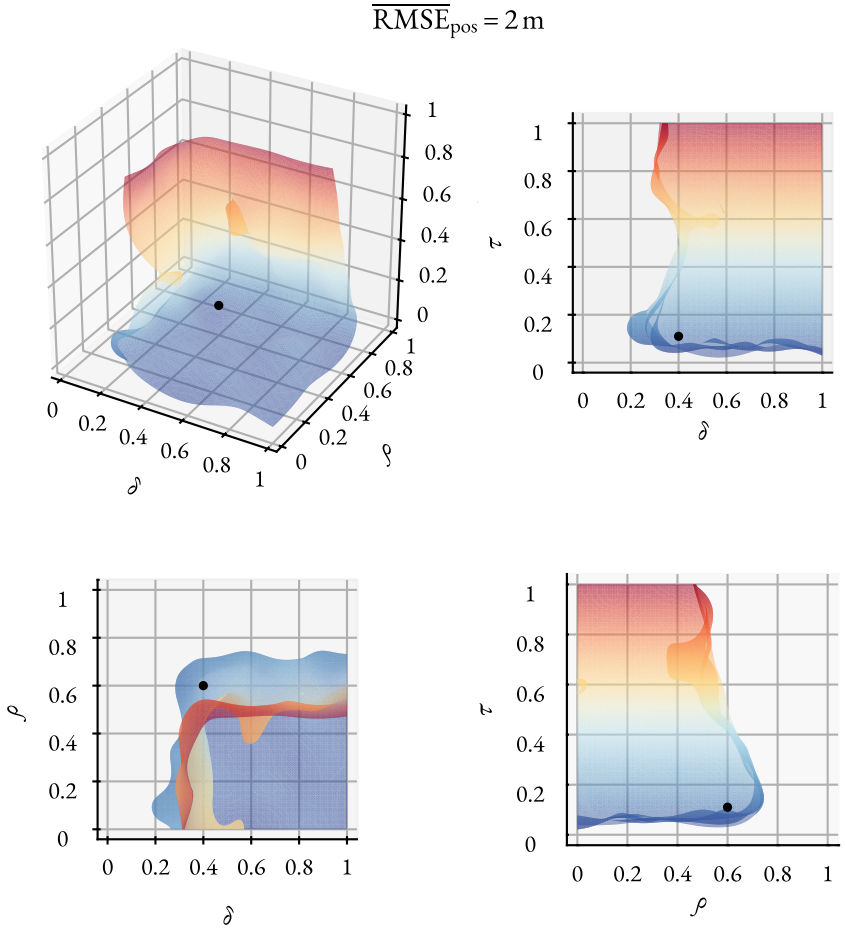

Figure 7.23: Isosurface correponding to the OD accuracy requirement for the scenario A2.

Table 7.9: Recommended value of the design parameters and their associated OD accuracy for the case A2.

$\overline{\text{RMSE}}_{\text{pos}} = 1.94\,\text{m}$

Normalized parameter	Value		Parameter	Value
δ	0.40	$\rightarrow$	DO^{e}_{L}	18
ρ	0.60	$\rightarrow$	tol^{e}	6.3×10^{-9}
τ	0.11	$\rightarrow$	T_{est}	0.68 d

The values of the normalized parameters corresponding to the chosen design point of A2 are given in Table 7.9. Figure 7.23 shows the location of this point in the design space. Its location relative to the shape of the requirement isosurface is similar to that of A1: the point is inside the valid region, with a low δ, high ρ, and low τ. The selected design point reflects the discussed differences in the requirement isosurface of scenario A2 compared to A1. The reduction in the noise level leads to a value of τ that is remarkably lower, which translates into an approximate reduction of 30% in T_{est} with respect to A1. The selected value of ρ increases compared to A1, resulting in an increase of 40% in tol^{e}. The choice of $\delta = 0.4$ is shared in both scenarios. Table 7.9 presents the value of $\overline{\text{RMSE}}_{\text{pos}}$ associated to the chosen design point, confirming that it meets the requirement.

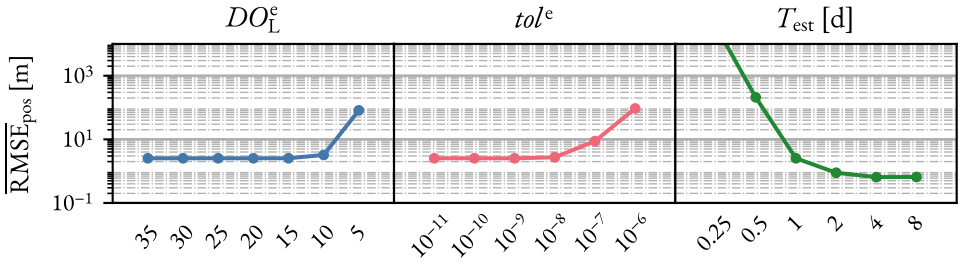

Figure 7.24: Influence of the individual variation of the design parameters on the OD accuracy for the case B1.

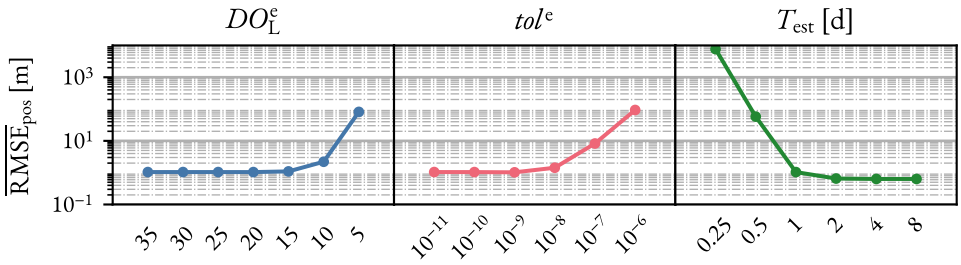

Figure 7.25: Influence of the individual variation of the design parameters on the OD accuracy for the case B2.

7.3.3. OD system specifications for the best user performance orbit configuration

The preliminary analysis reported in § 7.2 shows that the OD conditions of the best user performance orbit configuration are less favorable than those of configuration A. Thus, the a priori expectation is that cases B1 and B2 require higher values of DO^{e}_{L} and T_{est}, as well as lower values of tol^{e}, to achieve comparable OD accuracies to cases A1 and A2. Figures 7.24 and 7.25 display the results of the 1-by-1 analysis of the impact of the 3 design parameters on the OD accuracy for scenarios B1 and B2, respectively. The range of values considered in the analysis is the same used for the configuration A, due to the lack of solid reasons to do differently. The constant value of the design parameters outside their own individual analysis are: $DO^{e}_{L} = 20$, $tol^{e} = 10^{-10}$ and $T_{est} = 1$ d. The general trends resemble those of Figures 7.14 and 7.15. Using $DO^{e}_{L} > 20$ and $tol^{e} < 10^{-9}$ does not have a noticeable impact on $\overline{RMSE}_{pos}$. Compared to configuration A, Figures 7.24 and 7.25 show that reducing T_{est} has a stronger detrimental effect on the accuracy in this orbit configuration. Moreover, the loss in accuracy experienced at high values of T_{est} in scenarios A1 and A2 is not present in either B1 or B2.

Table 7.10 summarizes the boundaries for the 3 design parameters used to analyze both cases B1 and B2. The values of these boundaries serve to specify a design space which includes the ranges of values of interest of the parameters, that is, where the values are close to the $\overline{RMSE}_{pos} = 2$ m requirement. It should be noted that the boundaries for DO^{e}_{L} and tol^{e} are different from those used for the nominal orbit, given in Table 7.7. Both boundaries of DO^{e}_{L} are lower for cases B1 and B2, while the boundaries for tol^{e} are higher. This affects the normalization of the parameters and, thus, should be kept in mind during the comparison of the results of cases B1 and B2 against those of cases A1 and A2. Nevertheless, the normalization used for T_{est} in all these cases is, indeed, the same and, thus, a direct comparison of values of τ is possible.

Table 7.10: Boundaries of the design parameters for the best user performance orbit configuration (configuration B).

Parameter	Lower boundary	Upper boundary
DO^{e}_{L}	5	20
tol^{e}	10^{-9}	10^{-6}
T_{est}	0.5 d	8 d

Case B1: nominal noise level

The behavior of the FoMs within the design space of case B1 shows the same features as the previous cases A1 and A2. A dedicated discussion in relation to this does not add any significant value. Because of this, any relevant differences with the previously discussed cases are mentioned during the assessment of the isosurface depicted in Figure 7.26. For the sake of completeness, the plots showing the values of the FoMs at the sample points of the design space are reported in Appendix C.

The isosurface represented in Figure 7.26 has an overall shape that resembles that of cases A1 and A2. There is a clear lower limit of the valid region at $\tau \approx 0.3$, meaning that the estimation arcs required by this case are longer compared to previous cases. Furthermore, the already identified decrease in ρ with increasing τ is more accentuated in this case, reaching values of $\rho \approx 0.1$ at $\tau = 1$. It is hypothesized that the stronger interaction between the integrator tolerance and the estimation arc is due to the greater eccentricity of the orbits in configuration B compared to A. Regarding the limits of the valid region in terms of δ, the surface changes from values of $\delta \approx 0.6$ at $\tau \approx 0.3$ to $\delta \approx 0.5$ as τ increases, noticeably shifting to higher values of δ again when approaching $\tau = 1$. This is similar to the observations made for cases A1 and A2, in which the minimum required δ is found at values of $\tau \approx 0.8$ as well.

Figure 7.26 also shows the selected design point for the case B1. The selection of this point follows the criteria explained in § 7.3.1 and already discussed for cases A1 and A2. Table 7.11 contains the values of both the normalized parameters and the original parameters for this point, together with its corresponding value of the OD accuracy. The design point chosen can be compared against that of configuration A at the same noise level (case A1), in Table 7.8, to analyze the impact of changing the orbit configuration. Case B1 requires a lower DO^{e}_{L} and a greater tol^{e} compared to A1, meaning that the OD is less strict on those parameters. On the contrary, the value of T_{est} required by B1 is higher than that of A1, which implies that configuration B is more demanding in terms of estimation arc than A.

Table 7.11: Recommended value of the design parameters for the case B1.

$\overline{\text{RMSE}}_{pos} = 1.81$ m

Normalized parameter	Value		Parameter	Value
δ	0.65	$\rightarrow$	DO^{e}_{L}	15
ρ	0.34	$\rightarrow$	tol^{e}	1.0×10^{-8}
τ	0.35	$\rightarrow$	T_{est}	1.3 d

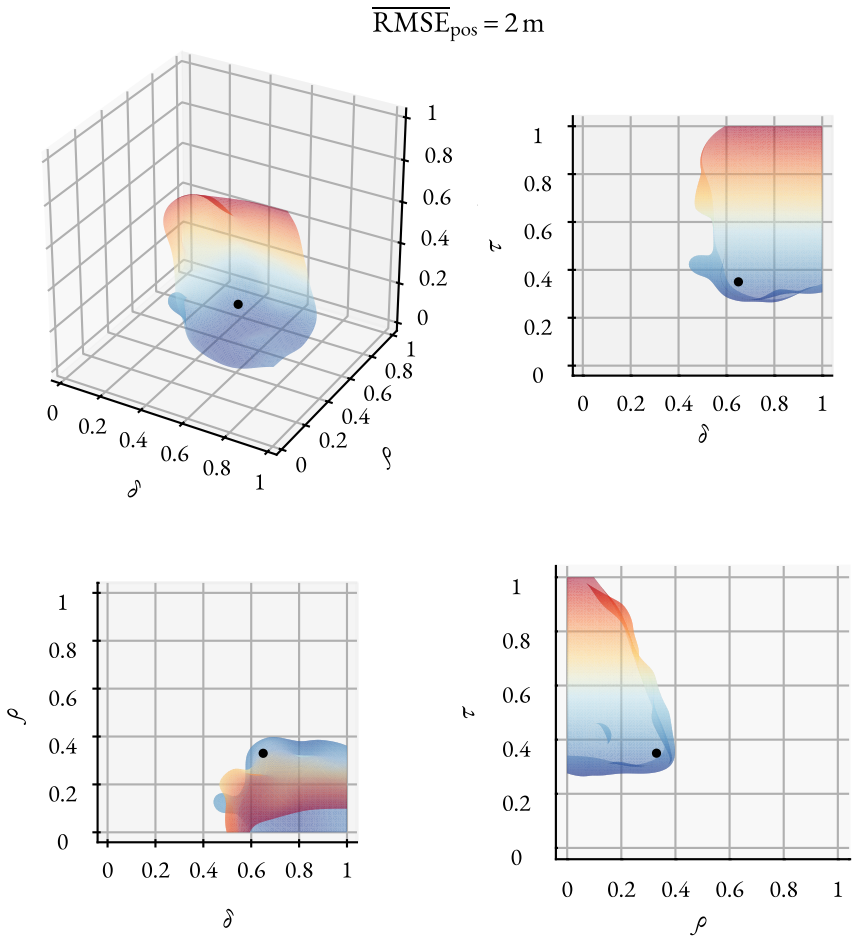

Figure 7.26: Isosurface correponding to the OD accuracy requirement for the case B1.

Case B2: reduced noise level

Similar to case B1, the overall behavior of the FoMs in the design space of case B2 has no major differences with respect to the previously discussed cases. Thus, the comparison between this case and the former ones is done on the basis of the requirement isosurface in Figure 7.27 and the selected design point. The interested reader can find the plots with the FoMs evaluated at the MC points in Appendix C.

Figure 7.27 shows the requirement isosurface for the case B2. There is a strong similarity between the surface of case B2 and that of case B1 in Figure 7.26. The only relevant differences between both happen at the lower limit of the valid region in terms of τ, namely, for $\tau < 0.4$. This effect is identified in the comparison between cases A1 and A2 as well. Longer estimation arcs allow a better "filtering" of the observational noise, and the accuracy is limited by the fidelity of the dynamic model. Thus, noise differences only become relevant at low values of τ. The reduced noise extends the lower limit from $\tau \approx 0.3$ to $\tau \approx 0.2$. For these low values of τ, the required ρ increases up to $\rho \approx 0.45$.

Table 7.12 contains the parameter values associated to the recommended design point for case B2, which is also shown in Figure 7.27. Comparing this point against that of case A2 reveals that B2 requires more relaxed values of DO^{e}_{L} and tol^{e}, but a higher T_{est}, similarly to the relation between A1 and B1. This suggests that the change in orbit configuration has a roughly equal impact on the OD system design regardless of the noise level of the

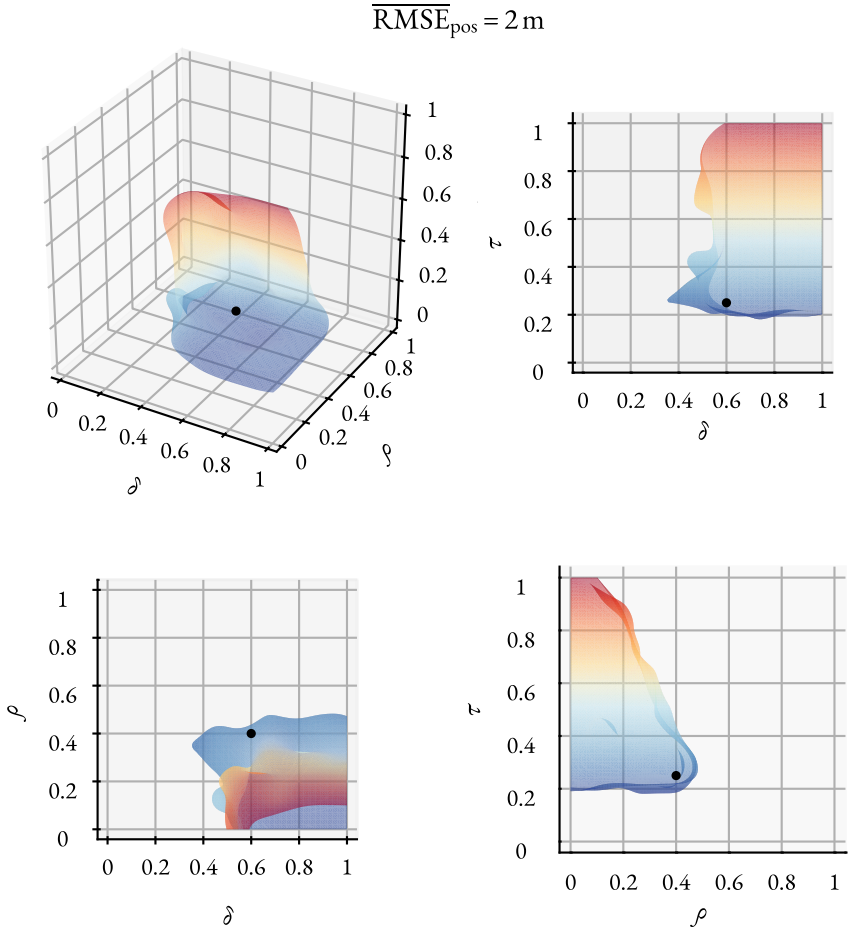

Figure 7.27: Isosurface correponding to the OD accuracy requirement for the case B2.

Table 7.12: Recommended value of the design parameters for the case B2.

$\overline{\mathrm{RMSE}}_{\mathrm{pos}} = 1.81\,\mathrm{m}$

Normalized parameter	Value		Parameter	Value
δ	0.60	$\rightarrow$	$DO_{\mathrm{L}}^{\mathrm{e}}$	14
ρ	0.40	$\rightarrow$	tol^{e}	1.6×10^{-8}
τ	0.25	$\rightarrow$	T_{est}	1.0 d

observations. Moreover, the difference between B1 and B2 is comparable to that between A1 and A2, implying that the effect on the system's design of having a reduced (or increased) observational noise is essentially the same regardless of the orbit configuration.

7.3.4. OD system specifications for the most demanding orbit configuration

The most demanding orbit configuration defined after the preliminary analysis in § 7.2 shows an OD accuracy that is several orders of magnitude worse than those of the other two configurations. For this reason, the range of values of $DO_{\mathrm{L}}^{\mathrm{e}}$ explored to set the boundaries of cases C1 and C2 is different from the ones used in the previous cases. The maximum value of $DO_{\mathrm{L}}^{\mathrm{e}}$ considered is 90. As the propagation of the reference orbit uses $DO_{\mathrm{L}}^{\mathrm{r}} = 100$,

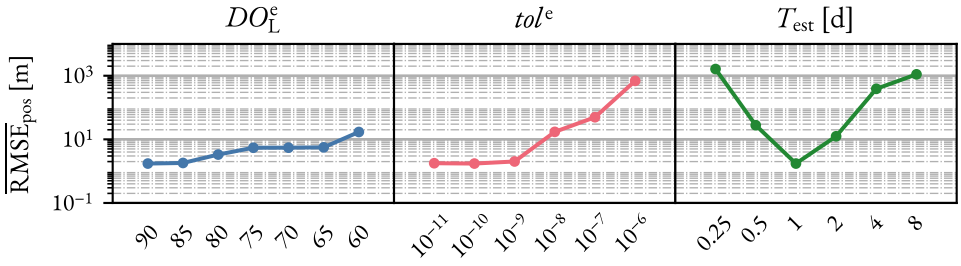

Figure 7.28: Influence of the individual variation of the design parameters on the OD accuracy for the case C1.

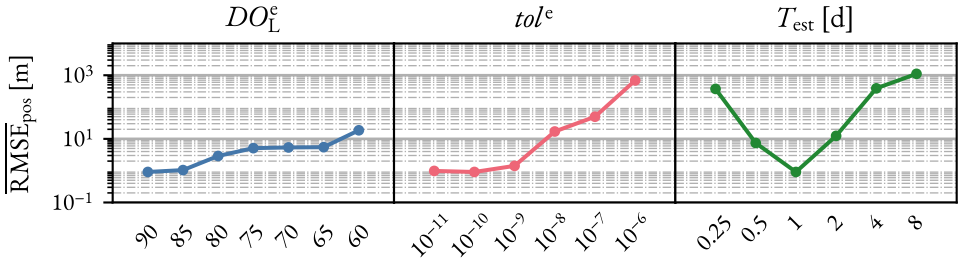

Figure 7.29: Influence of the individual variation of the design parameters on the OD accuracy for the case C2.

it is not suitable to use values of $DO^{e}_{L} > 90$, as the dynamics used during the estimation would be excessively similar to the "true" dynamics. Eliminating the differences between the true dynamics and the dynamics used for the estimation could lead to results that are not representative of the real OD environment. The constant values of the parameters outside their individual variations are: $DO^{e}_{L} = 90$, $tol^{e} = 10^{-10}$, $T_{est} = 1$ d.

Figures 7.28 and 7.29 show the influence of the 1-by-1 variations of the 3 design parameters of the reduced problem on the OD accuracy. In terms of the observed trends, a few differences can be spotted with respect to the previous cases. The increase in DO^{e}_{L} does not lead to reaching a lower limit of $\overline{RMSE}_{pos}$, as happens in Figures 7.14, 7.15, 7.24 and 7.25, but to a monotonic decrease in the FoM. Another remarkable difference is the behavior of $\overline{RMSE}_{pos}$ with T_{est}. Some previous cases show a slight loss of OD accuracy when considering $T_{est} > 2$ d. For both cases C1 and C2, the detrimental impact of raising T_{est} starts from $T_{est} = 1$ d and the accuracy losses incurred by raising its value beyond that are of one or more orders of magnitude. The reason behind this is the faster degradation of the propagation in configuration C, as the periselene altitude is remarkably lower than those of A or B. This feature highlights the high difficulty of performing OD in this configuration.

Taking into account the results in Figures 7.28 and 7.29, Table 7.13 presents the chosen values of the parameter boundaries for both cases C1 and C2. The criterion followed for the selection of these values is the same from previous cases: spanning the parameter values at which the resulting $\overline{RMSE}_{pos}$ is close to its 2 m requirement. Figure 7.28 shows that reaching such level of accuracy is barely possible with the nominal noise level. Having a reduced noise helps to achieve the 2 m accuracy level, as seen in Figure 7.29.

Case C1: nominal noise level

Figures 7.30 to 7.32 show the values of the FoMs at the 500 MC points used to sample the design space. Figure 7.30 reveals that the relations between $\overline{RMSE}_{pos}$ and the parameters are coherent with those observed in their individual variations in Figure 7.28. Compared with previous cases, the OD accuracy is more clearly

Table 7.13: Boundaries of the reduced problem parameters for the most demanding orbit configuration (configuration C).

Parameter	Lower boundary	Upper boundary
$DO_{\mathrm{L}}^{\mathrm{e}}$	60	90
tol^{e}	10^{-10}	10^{-7}
T_{est}	0.5 d	4 d

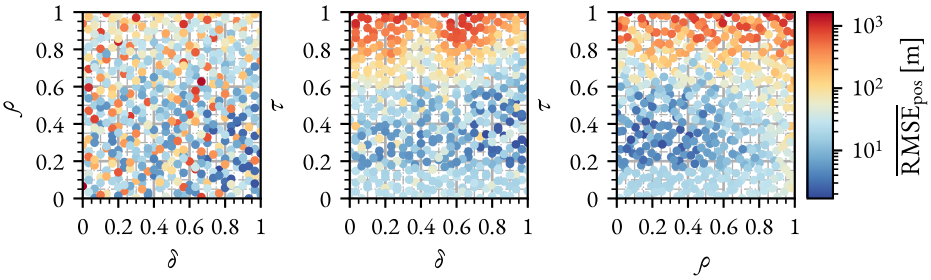

Figure 7.30: OD accuracy of the sampled design space using $N_{\mathrm{points}} = 500$ for the case C1.

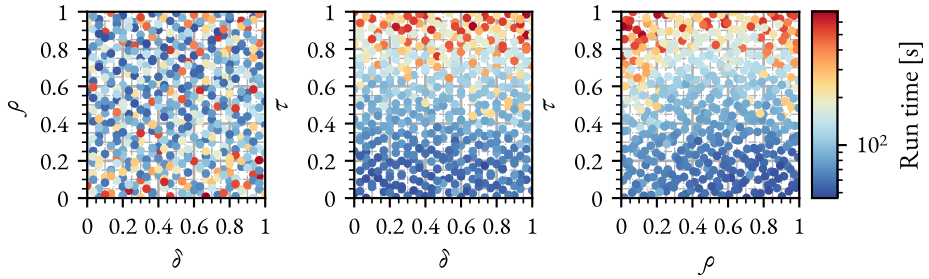

Figure 7.31: Run time of the sampled design space using $N_{\mathrm{points}} = 500$ for the case C1.

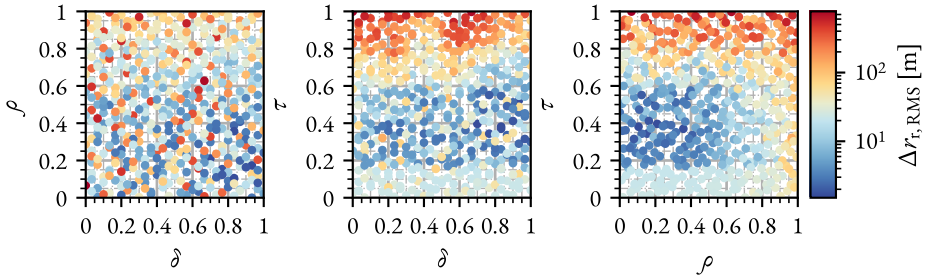

Figure 7.32: User positioning error of the sampled design space using $N_{\mathrm{points}} = 500$ for the case C1.

dominated by the estimation arc length, with the best values being found between $\tau \approx 0.3$ and $\tau \approx 0.5$. The impact of ρ and, especially, δ on this FoM in this case is significantly less accentuated relative to other cases. Nevertheless, the lowest $\overline{\mathrm{RMSE}}_{\mathrm{pos}}$ points are still found at high values of δ and low values of ρ. Regarding the run time, Figure 7.31 shows that τ remains as the main driver, and neither δ nor ρ have a remarkable impact on it. Lastly, the user positioning errors exhibited in Figure 7.32 reaffirm the close relation that exists between $\overline{\mathrm{RMSE}}_{\mathrm{pos}}$ and $\Delta r_{\mathrm{r,RMS}}$, even in these more demanding conditions.

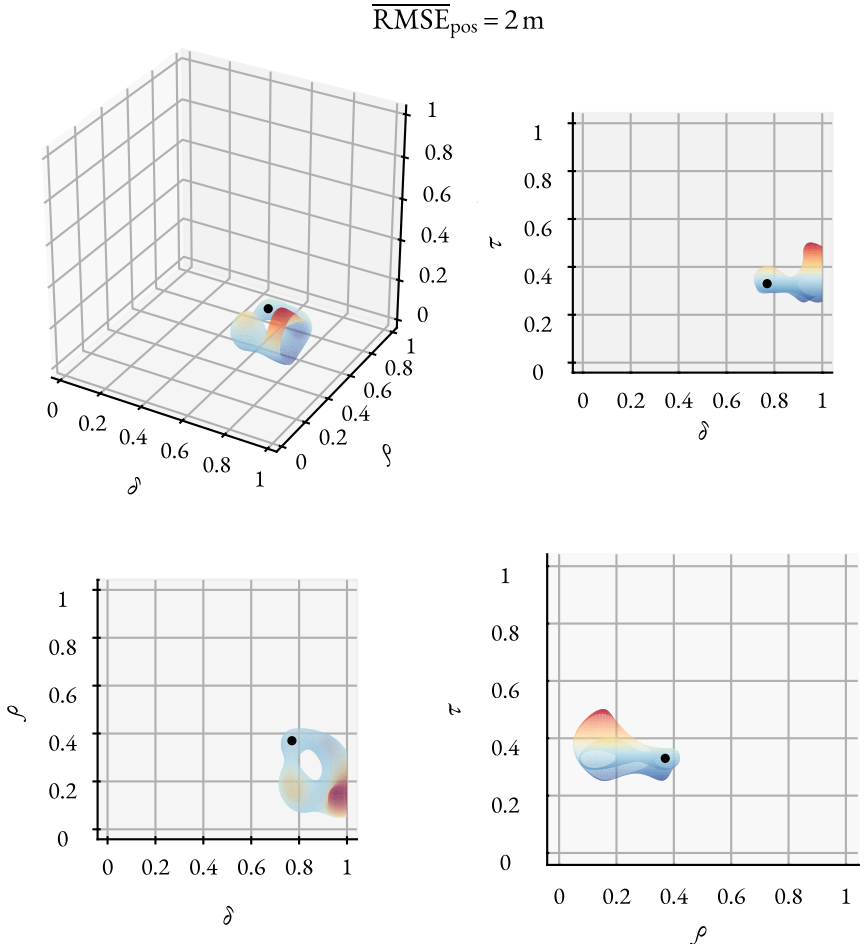

Figure 7.33: Isosurface correponding to the OD accuracy requirement for the case C1.

Figure 7.33 presents the requirement isosurface for case C1, which is the most different from the cases analyzed. The minimal valid region for the case C1 lies on the inside of the surface. It is contained within $\tau \approx 0.3$ and $\tau \approx 0.5$, once again showing that long estimation arcs do not serve to meet the accuracy requirement. A more surprising observation relates to the location of the valid region in terms of ρ. Values of $\rho \approx 0$ are outside the valid region, meaning that a more strict integrator tolerance induces a degradation of the accuracy. There is no clear reason for this. This can be attributed to the distribution of points used to sample the design space not properly representing the true behavior of $\overline{\text{RMSE}}_{\text{pos}}$ inside the design space. However, this seems unlikely, as the separation between the surface and the $\rho = 0$ value seems too large to be caused by this effect. Lastly, the shape of the surface indicates that it is not possible to meet the requirement for values of $\delta \approx 0.85$ and $\rho \approx 0.3$, while it is possible to do so with higher and lower values of those two parameters. No explanation is found for this.

Along with the requirement isosurface, Figure 7.33 shows the recommended design point within the design space of case C1. Table 7.14 contains the values of the normalized parameters corresponding to this point, together with their associated values of the original reduced problem parameters. Compared to other cases with a nominal observational noise (A1 and B1), this recommended design point has a value of DO_{L}^{e} more than 4 times higher, as well as a remarkably lower tol^{e} (between half and one order of magnitude). The more strict values of DO_{L}^{e} and tol^{e} required for case C1 could be expected, as its particular orbit configuration is chosen for analysis due

Table 7.14: Recommended value of the design parameters for the case C1.

$\overline{\text{RMSE}}_{\text{pos}} = 1.79\,\text{m}$

Normalized parameter	Value		Parameter	Value
δ	0.77	$\rightarrow$	DO_{L}^{e}	83
ρ	0.37	$\rightarrow$	tol^{e}	1.2×10^{-9}
τ	0.33	$\rightarrow$	T_{est}	1.0 d

Table 7.15: Recommended value of the design parameters for the case C2.

$\overline{\text{RMSE}}_{\text{pos}} = 1.80\,\text{m}$

Normalized parameter	Value		Parameter	Value
δ	0.77	$\rightarrow$	DO_{L}^{e}	83
ρ	0.40	$\rightarrow$	tol^{e}	1.8×10^{-9}
τ	0.23	$\rightarrow$	T_{est}	0.81 d

to it being more demanding. On the contrary, the recommended T_{est} for C1 is identical to that of A1 and even lower than that of B1. This is positive as the run time is almost exclusively driven by T_{est}, meaning that the choice of orbit configuration does not have a huge impact on the computational cost of the estimation.

Case C2: reduced noise level

The overall behavior of the FoMs throughout the design space of case C2 closely resembles Figures 7.30 to 7.32. Thus, no additional discussion is dedicated to this. The interested reader can find the plots showing the values of the FoMs at the MC points of case C2 in Appendix C.

The requirement isosurface of case C2, displayed in Figure 7.34 has, in rough terms, an intermediate shape between that of case C1 and those of previous cases. Similarly to Cases A1, A2, B1, and B2, this surface sets reasonably uniform limiting values of the valid region for the 3 parameters. The valid region coincides, approximately, with the volume defined by $0.75 \leq \delta \leq 1$, $0 \leq \rho \leq 0.45$, and $0.2 \leq \tau \leq 0.45$. On the other hand, it shares with the isosurface of C1 that they both show an upper limit of $\tau \approx 0.45$ for the valid region—a feature that is not present in any of the previous cases. Longer estimation arcs exhibit a worse OD accuracy because of the degradation of the propagation due to the longer propagation interval. This is a limitation that derives from the specific orbit configuration shared by cases C1 and C2, not from the observational noise. Thus, it is sensible that both C1 and C2 show a similar upper limit for the estimation arc length.

Table 7.15 presents the recommended value of the design parameters for case C2. The selection of this point attends to the criteria stated in § 7.3.1. The effect of reducing the observational noise with respect to C1 is similar to the one observed between the A1-A2 and B1-B2 pairs. The length of the estimation arc is reduced by an approximate 20%, as fewer observations are required to filter out the lower noise. Having a shorter arc means that each integration step need not be as accurate, which consequently leads to an allowable integrator tolerance that is about 50% higher. Comparing the recommended design point against those of A2 and B2, C2 requires a similar value of T_{est}, while the needed DO_{L}^{e} and tol^{e} are more strict—that is, a greater DO_{L}^{e} and a lower tol^{e}.

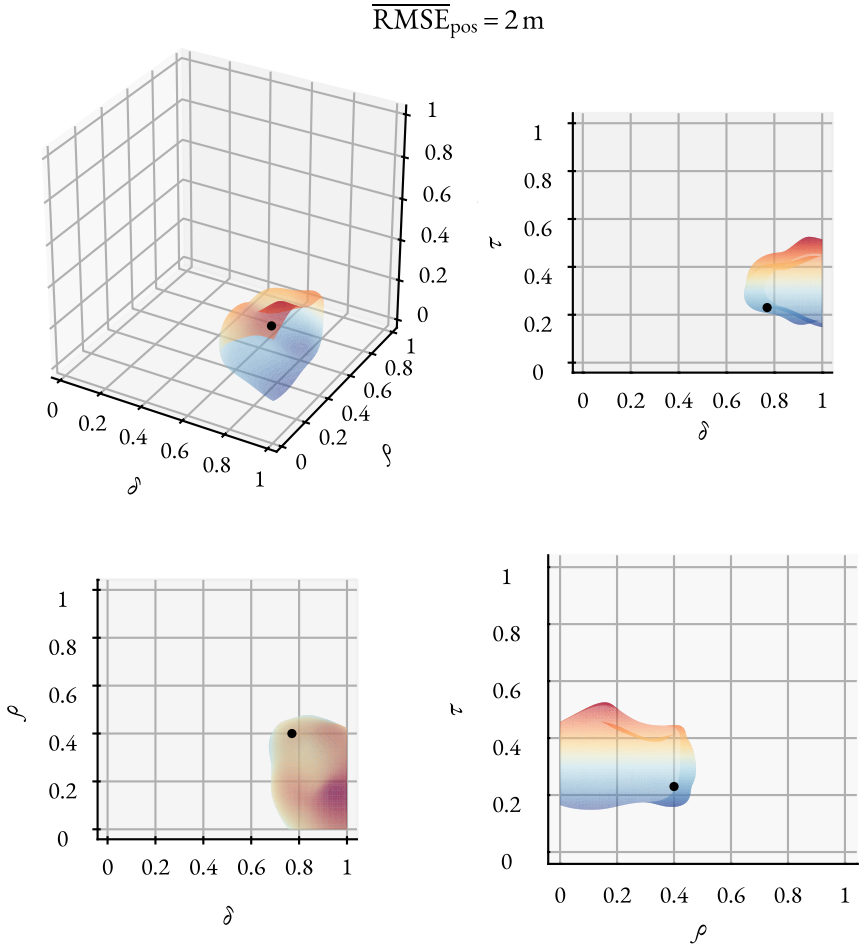

Figure 7.34: Isosurface correponding to the OD accuracy requirement for the case C2.

7.3.5. Impact of the prediction arc on the OD accuracy

Having produced a recommendation for the OD system specifications in the 6 defined cases, the effect of the prediction arc length on the final OD accuracy remains for analysis. The results of the preliminary analysis reported in § 7.2 show that, when using the nominal values of all the simulation parameters (§ 4.5), the length of the prediction arc has no visible impact on the resulting value of $\overline{\mathrm{RMSE}}_{\mathrm{pos}}$. The identified reason for this is the greater relative relevance of the errors incurred during the estimation compared to the degradation of the propagation along the prediction arc. The recommended system specifications derived from the preliminary analysis and from the examination of the different cases reveal significant differences with respect to the nominal values. This can possibly affect the relation between of estimation and propagation errors, making the prediction arc length a relevant parameter for the proposed sets of OD system specifications.

Table 7.16 shows the variation of the OD accuracy with the length of the prediction arc. A general improvement of the accuracy is achieved by shortening the prediction arc. The enhancements do not occur uniformly for all cases. The results indicate that case B2 is especially sensitive to the prediction arc length, experiencing the greatest reductions of $\overline{\mathrm{RMSE}}_{\mathrm{pos}}$ compared to the rest of the cases. On the other hand, case A2 suffers a slight loss of accuracy at $T_{\mathrm{pred}} = 3\,\mathrm{h}$, failing to meet the requirement by a 2.5%. For that specific case, it is possible to slightly improve the OD specifications—for example, raising $DO^{\mathrm{e}}_{\mathrm{L}}$ and T_{est}, or lowering tol^{e}—to ensure meeting the

Table 7.16: Values of $\overline{\text{RMSE}}_{\text{pos}}$ for the 6 analyzed cases at different prediction arc lengths.

	A1	**A2**	**B1**	**B2**	**C1**	**C2**
$T_{\text{pred}} = 3\,\text{h}$	1.49 m	2.05 m	1.68 m	0.64 m	1.15 m	1.29 m
$T_{\text{pred}} = 6\,\text{h}$	1.82 m	1.71 m	1.61 m	0.77 m	1.47 m	1.23 m
$T_{\text{pred}} = 12\,\text{h}$	1.87 m	1.93 m	1.52 m	1.24 m	1.66 m	1.38 m
$T_{\text{pred}} = 24\,\text{h}$	1.95 m	1.94 m	1.81 m	1.81 m	1.79 m	1.80 m

requirement at every prediction arc length. However, Figure 7.7 shows that the orbital errors have an oscillatory behavior in time that appears to coincide with the orbital period. These oscillations do not seem a product of randomness, as they repeat in a majority of the replications. Thus, the values of $\overline{\text{RMSE}}_{\text{pos}}$ computed with short prediction arcs may not be perfectly representative of the long-term accuracy of the OD, as the arcs may coincide with periods of abnormally good or bad accuracy. Furthermore, the analyzed orbit configurations consider the worst tracking condition along the lunar orbit ($\Omega_0 = 75°$). Thus, the OD accuracy at different points of the lunar orbit is expectedly better than the results presented in this section. Because of all of these reasons, it is decided not to modify the recommended OD specifications for case A2.

7.3.6. Relation between OD accuracy and user positioning accuracy

The discussion of previous results reported in this chapter highlights the similar behavior presented by $\overline{\text{RMSE}}_{\text{pos}}$ and $\Delta r_{\text{r,RMS}}$. Figure 7.35 shows the relation between the OD accuracy FoM and the user positioning accuracy FoM. The analysis considers each orbit configuration separately, as they result in different geometrical arrangements relative to a user in the LSP, and only uses points with $\overline{\text{RMSE}}_{\text{pos}} < 10$ m, to focus on the range of values of interest. All 3 configurations show a correlation coefficient between both FoMs greater than 0.78 and a residual RMS below 1.5 m, with the dispersion of the points being greater at higher values of $\overline{\text{RMSE}}_{\text{pos}}$. The relation between both FoMs is particularly remarkable, with higher correlation and lower residuals, for configuration A.

It is also worth highlighting the effect of the orbit configuration on the slope of the linear fit. Orbit configuration C has the strongest response of $\Delta r_{\text{r,RMS}}$ to $\overline{\text{RMSE}}_{\text{pos}}$ (the highest linear coefficient of the fit), which can be attributed to it having the highest PDOP_{RMS} of all 3 configurations—configuration C has $\text{PDOP}_{\text{RMS}} \approx 4.1$, while both A and B have $\text{PDOP}_{\text{RMS}} \approx 2.9$. Nevertheless, the differences in the linear coefficients of the fit of configurations A and B cannot be explained through the PDOP_{RMS}, as both have very similar values. This suggests that the position errors incurred when performing the OD of orbit configuration B have a greater component along the ranging direction—which is close to the radial direction of the orbit—than those of configuration A. No explanation has been found for this behavior based on the previously reported results.

7.4. Summary of the recommended OD system specifications

Table 7.17 contains the final recommended values for the design parameters of the OD system in the 6 defined cases. The required value of DO^{e}_{L} depends mostly on the orbit configuration, while both tol^{e} and T_{est} are impacted by both the orbit configuration and the noise level. The discussion about this is given in § 7.3. § 7.2 explains the reasoning behind the selection of the recommended values of T_{obs} and e_{min}, as well as the recommended ground station network for tracking.

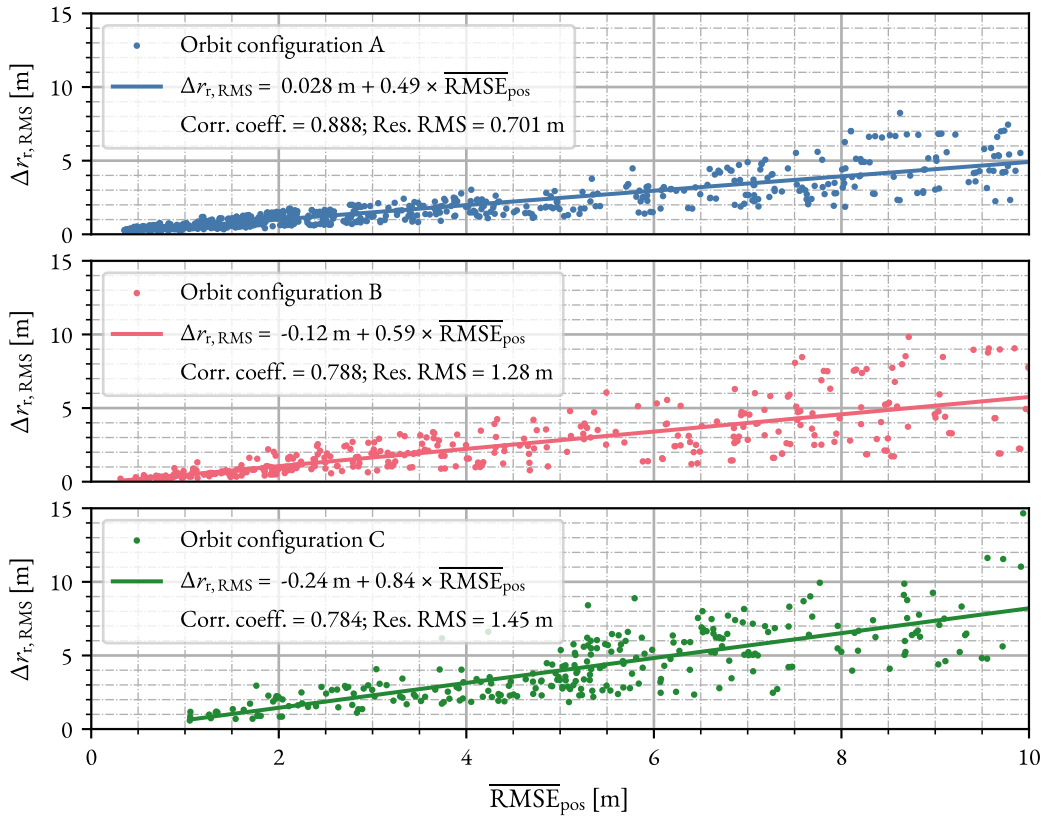

Figure 7.35: Relation between $\overline{\text{RMSE}}_{\text{pos}}$ and $\Delta r_{\text{r,RMS}}$ for the 3 orbit configurations. Each point represents one sample of the Sobol sequence of either the nominal or reduced noise level with $\overline{\text{RMSE}}_{\text{pos}} < 10$ m. The line corresponds to the linear fit to the points. The plot also shows the correlation coefficient between the 2 FoMs and the residuals RMS of the fit.

Table 7.17: Recommended values of the OD system decision variables for the LNS.

	DO^{e}_{L}	tol^{e}	T_{est} [d]	T_{pred} [h]	T_{obs} [s]	e_{min} [°]	Station network
A1	18	4.5×10^{-9}	1.0	$6 \leq T_{\text{pred}} \leq 24$	300	15	Nominal (CB, MG & NN)
A2	18	6.3×10^{-9}	0.68				
B1	15	1.0×10^{-8}	1.3				
B2	14	1.6×10^{-8}	1.0				
C1	83	1.2×10^{-9}	1.0				
C2	83	1.8×10^{-9}	0.81				

The recommendation regarding T_{pred} is not a single value, but an interval. Using short prediction arcs entails computing the OD solution with a high frequency. Using 6-hour-long prediction arcs already satisfies the accuracy requirement comfortably, and the results do not show a clear benefit in lowering it further in many cases. Thus, the recommendation is to use prediction arcs longer than 6 h, although this is not a strong limitation as the computational cost of the OD solution in terms of run time is low (of the order of a couple of minutes). The recommended upper limit for T_{pred} is set based on the range of validity of the results reported in this thesis. The values of all other design variables are chosen assuming a maximum $T_{\text{pred}} = 24$ h. This thesis does not explore

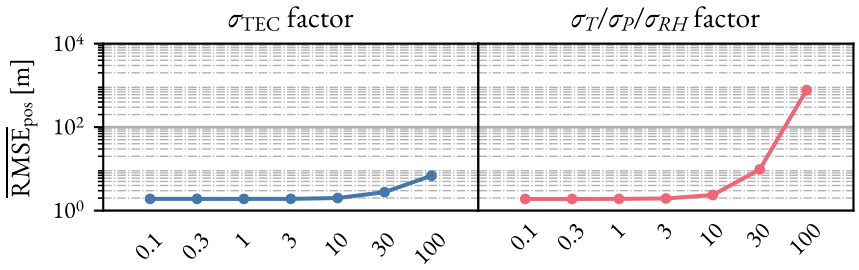

Figure 7.36: Influence of the uncertainties affecting the atmospheric models on the OD accuracy of case A1.

longer prediction arcs, although they could be possible. Furthermore, the recommendation for T_{pred} is flexible to accommodate for possibly unaccounted effects, such as the impact of performing the OD at different epochs, which is briefly analyzed in Appendix D.

7.5. Influence of uncertainties on the OD system's performance

Having achieved a final recommendation for the OD system specifications in each of the 6 defined scenarios, it is left to evaluate the impact of the uncertainties involved in the OD problem on the system's performance. To do this, the levels of uncertainty affecting the different aspects of the problem are varied in a 1-by-1 fashion (similar to what is done in § 7.2) to observe their impact on the OD accuracy. The parameters involved in the analysis are:

- the uncertainty in the initial guess of the satellites' positions (σ_{pos}),
- the uncertainty in the initial guess of the satellites' velocities (σ_{vel}),
- the uncertainty in the initial guess of the satellites' reflectivity properties (σ_{C_r}, σ_{C_d}, σ_{C_s}),
- the uncertainty in the TEC of the ionospheric model (σ_{TEC}),
- the uncertainty in the meteorological data affecting the tropospheric correction (σ_T, σ_P, σ_{RH}).

It must be noted that some parameters are grouped into a single item. This is done to limit the resources required for this study. The objective of this final part of the design analysis is not to perfectly characterize the individual response of the OD system's performance to the mentioned uncertainties, but to better understand the order of magnitude of their impact and identify which are the most relevant factors that may affect the accuracy. The applied simplification allows drawing meaningful conclusions and, thus, reaching the aforementioned objective, while employing a more reasonable amount of resources. For every of the individual variations in the analysis, the parameters are varied between 0.1 and 100 times their nominal value (the nominal values are defined in § 4.5). To do so, a scale factor is defined for each of the items of the previous list. The analysis is repeated for each of the 6 cases defined at the end of § 7.2.

From the results, the uncertainty in the initial guesses of the solve-for parameters has no visible effect on the resulting accuracy of the converged OD processes for any of the cases. Nevertheless, using a σ_{vel} which is 100 times higher than its nominal value, that is, $\sigma_{\text{vel}} = 1\,\text{m}\,\text{s}^{-1}$, leads to convergence issues in the estimation—approximately 10% of the estimations diverge. This means that the a priori knowledge about the solve-for parameters can be worse than that assumed in this thesis work without an effect on the results. This provides a greater confidence on the outcome of the analyses reported in this thesis.

Figure 7.36 shows the impact of the two scale factors associated to atmospheric effects on the $\overline{\text{RMSE}}_{\text{pos}}$ for case A1. Both of these uncertainties have a significant impact on the OD accuracy. The increased uncertainty in the TEC of the ionospheric model starts having a visible effect when being 10 times as large as the nominal value. For values beyond that, the loss in accuracy becomes significant until reaching approximately 5 m. Raising the uncertainty in the meteorological data leads to a similar, but more accentuated, behavior, showing values of $\overline{\text{RMSE}}_{\text{pos}}$ of several hundreds of meters. When scaling the meteorological uncertainty times 100, an approximate 10% of the estimations fail to converge. The nominal ionospheric and meteorological uncertainties are representative of the order of magnitude of the imperfect knowledge of these atmospheric effects. The presented results regarding imperfect atmospheric modeling may be optimistic. Still, the observations imply that the characterization of these two effects has to be at least 10 times worse than it is assumed in this thesis to have a significant detrimental impact on the OD accuracy of the system. Thus, it can be concluded that the modeled atmospheric uncertainties are not a driving factor of the system's performance.

Although not identical to Figure 7.36, the figures corresponding to the rest of the cases do not reveal new relevant information nor incite interesting discussion. For the sake of completeness, they can be found in Appendix C. Lastly, it is not found necessary to adapt the recommended values of the design parameters given in Table 7.17 based on the impact of the problem uncertainties on the accuracy of the OD.

8

Conclusions and Recommendations

This thesis addresses the design of the OD system for the operations of a LNS consisting of 4 satellites placed in elliptical lunar orbits. The design is guided by the requirement set on the minimum accuracy of the OD solution. To achieve the requirement, the analysis explores the impact of the system parameters on the estimated OD solution, and aims toward providing recommended OD system specifications. The OD parameters involved in the analysis affect the orbit configuration of the lunar satellites, the modeling of the satellites' dynamics, the network of ground stations used for tracking, the tracking strategy, and the properties of the tracking observations. The thesis also assesses the relation between the accuracy of the OD and the quality of the positioning service that it provides to a receiver on the Lunar South Pole (LSP), which has been declared a region of interest for lunar activity in the short-term future.

An end-to-end simulation tool has been implemented to perform the analysis of the OD based on the functionality provided by the GODOT and GENEOS packages. The simulation tool handles the propagation of the navigation satellites' reference orbits, the computation of station-satellite visibility periods, the simulation of observations, the parameter estimation, and the computation of the FoMs used to evaluate the system's performance.

The design process for the OD system starts by selecting the parameters for the analysis. The large number of parameters makes it practically impossible to perform a detailed analysis of the problem. Because of that, a preliminary phase of the analysis studies the impact of the parameters on the system's performance. This preliminary stage reveals that the design parameters having a greater impact on the OD accuracy are the maximum degree and order of the SH expansion of the lunar gravitational potential ($DO_{\mathrm{L}}^{\mathrm{e}}$) and the relative integrator tolerance (tol^{e}) used in the estimation, as well as the length of the estimation arc (T_{est}). Apart from these, other non-design parameters having a substantial influence on the accuracy are the orbit configuration parameters—semi-major axis, eccentricity, inclination and RAAN—and the noise level of the tracking observations. Tracking geometries leading to observations with a small out-of-plane component show OD accuracies approximately 4 times worse than those with a greater observability of the out-of-plane direction. The OD error during the prediction arc shows an oscillatory behavior caused by errors in the estimation, which dominates over the degradation of the propagation and leads to a limited impact of the prediction arc length on the OD accuracy.

The design analysis is continued by performing a Monte Carlo (MC) analysis on the design space of a series of 6 cases of interest spanning different orbit configurations (A, B and C)—which represent the most frequent configuration in the literature, the configuration providing the best user performance, and the most demanding configuration for OD—and observational noise levels (1 and 2)—a conservative value and a value representative of the current state of technology. It is observed that the behavior of the FoMs with the design parameters is highly dependent on the orbit configuration. Configurations A and B show that the best OD accuracy is achieved using the highest possible $DO^{\mathrm{e}}_{\mathrm{L}}$ and T_{est}, and the lowest possible tol^{e} for the considered range of values. That same design point also leads to the longest estimation run time. On the contrary, configuration C, which is more challenging for the OD, shows an optimal value of the estimation arc at around $T_{\mathrm{est}} = 1$ d. A correlation coefficient greater than 0.78 is observed between the OD accuracy and the user positioning accuracy for all cases of interest. This suggests that a requirement in user accuracy can be directly translated into a requirement in $\overline{\mathrm{RMSE}}_{\mathrm{pos}}$.

The results from the MC are then used to compute the requirement isosurface and select the recommended system specifications for all 6 cases. Comparing the several cases reveals that reducing the observational noise by a factor of 5 entails a reduction in T_{est} of ≈ 20–30%. Due to having a shorter propagation, the required tol^{e} is also relaxed, increasing by ≈ 40–60%. The changes in orbit configuration affect all 3 design parameters. The values of $DO^{\mathrm{e}}_{\mathrm{L}}$ range from 14 in the best-behaved configuration to 83 in the most demanding one. Variations in the orbits can also account for differences in tol^{e} of one order of magnitude. The recommended values of T_{est} are approximately between 0.7 d and 1.3 d for all cases of interest. The impact of the prediction arc length is re-assessed using the recommended specifications, showing that the improvement in the OD accuracy achieved by shortening the prediction arc is not uniform for all cases. This is attributed to the oscillatory behavior of the orbital errors during the prediction arc.

The last step of the analysis involves studying the influence of the different sources of uncertainty on the resulting values of the FoMs. The uncertainty in the initial guess of the solve-for parameters during the OD shows no impact on the accuracy of the converged solutions. However, velocity uncertainties of 1 m s^{-1} already cause the divergence in the estimation of an approximate 10% of the cases. The quality of the current data used to model the ionospheric and tropospheric delays is also found to be high enough so that they do not have a principal role in determining the OD accuracy. However, ionospheric and, especially, meteorological uncertainties ranging from 10 to 100 times the nominal levels can severely degrade the accuracy, causing average OD errors up to almost 3 orders of magnitude greater than the 2 m requirement, and complicate the convergence of the estimation.

Using the results and conclusions derived from this work, we can try to answer the research questions formulated at the beginning of the thesis.

RQ-1. How can the accuracy requirements imposed on the OD solution of a LNS be met?

The research done considers the OD of a LNS based on Elliptical Lunar Frozen Orbits (ELFOs). It shows that a requirement of 2 m on the $\overline{\mathrm{RMSE}}_{\mathrm{pos}}$ is attainable using range and Doppler tracking from ground stations on the Earth's surface with the current technology and scientific knowledge.

RQ-1.1. What are the OD design parameters that drive the accuracy of the OD solution?
The OD of the LNS exhibits a considerable sensitivity to many of the design parameters of the problem. Nevertheless, it is possible to identify a reduced set of parameters that drive the accuracy of the solution. These are the degree and order of the lunar gravitational potential ($DO_{\mathrm{L}}^{\mathrm{e}}$), the relative integrator tolerance (tol^{e}) and the estimation arc length (T_{est}).

RQ-1.2. What is the sensitivity of the OD solution to the identified accuracy drivers?
The OD accuracy is most responsive to T_{est}, especially for values below $T_{\mathrm{est}} = 1$ d, for which a variation of a couple of hours can result in an order of magnitude difference in $\overline{\mathrm{RMSE}}_{\mathrm{pos}}$. In general, the accuracy of the OD improves with increasing T_{est}. Nevertheless, raising T_{est} past a certain limit causes a degradation of the accuracy. A higher fidelity dynamic model—that is, a higher $DO_{\mathrm{L}}^{\mathrm{e}}$ and a lower tol^{e}—leads to a better accuracy until reaching a limit, from which no further improvement is observed. This minimum $\overline{\mathrm{RMSE}}_{\mathrm{pos}}$ achievable by improving the dynamic model depends on the observational noise—a decrease of 80% in noise leads to an approximate 50% reduction in the minimum achievable error.

RQ-1.3. What are the values of the OD design parameters needed to meet the defined accuracy requirements?
Due to the dependence of the OD accuracy on non-design parameters—for example, the orbit configuration of the constellation and the noise of the observations—, it is not possible to derive a unique set of recommended values for the design parameters of the system. Still, it is possible to provide some indicative values for them. For the estimation and prediction arc lengths, the recommended ranges of values are $T_{\mathrm{est}} = 0.7$–1.3 d and $T_{\mathrm{pred}} = 6$–24 h. It is not required to use values of $DO_{\mathrm{L}}^{\mathrm{e}}$ beyond 83, even when considering orbits with a very low periselene altitude (down to 100 km in altitude). The recommended values for tol^{e} lie between 10^{-9} and 2×10^{-8}, although the maximum acceptable tolerance varies significantly depending on the orbit configuration and the noise level. Lastly, in terms of tracking, it is recommended to use a station network with 3 ground stations that provide continuous tracking of the lunar orbits, tracking at a minimum elevation of $e_{\mathrm{min}} = 15°$ with an interval between observations of $T_{\mathrm{obs}} = 300$ s.

RQ-1.4. How are the recommended OD system specifications affected by uncertainties?
The uncertainty in the initial guesses of the solve-for parameters does not affect the OD accuracy when varied in the range of 0.1–100 times their nominal values. On the contrary, the accuracy of the OD is negatively affected when increasing the uncertainty involved with the atmospheric delays (both from the ionosphere and the troposphere). This effect becomes visible when the atmospheric uncertainties are above 10 times their nominal values. The nominal values of these uncertainties derive from the current scientific knowledge about the atmosphere. Thus, these results suggest that, given the current measurement and modeling knowledge of the atmosphere, these uncertainties do not significantly impact the OD accuracy of the system. It is concluded that the recommended values of the design parameters need not be changed due to uncertainty considerations other than the noise in the observations.

RQ-2. What is the relation between the OD accuracy of a LNS and the accuracy of the positioning capabilities that it offers?
The results obtained from the various analysis performed in this thesis expose a close correlation between the average accuracy of the OD of all satellites in the constellation ($\overline{\mathrm{RMSE}}_{\mathrm{pos}}$) and the error experienced by a

navigation receiver on the LSP ($\Delta r_{\mathrm{r,RMS}}$). All 3 orbit configurations studied in detail during the design analysis show a correlation coefficient greater than 0.78. Computing the linear fit to the data reveals that the slope of $\Delta r_{\mathrm{r,RMS}}$ relative to $\overline{\mathrm{RMSE}}_{\mathrm{pos}}$ depends on the orbit configuration, and that this dependence cannot be explained solely based on the PDOP, suggesting that the orbit configuration can have an impact on the magnitude of the OD error component along the ranging direction to the LSP.

The analyses presented in this thesis report only represent a first step toward a more detailed design of the OD system of a future LNS. Thus, I provide several recommendations to extend the work done in this thesis.

1. **Examine the impact that data gaps have on the accuracy of the OD.** The results presented in this thesis rely on the assumption that the ground stations perform continuous tracking of the lunar satellites whenever they are in view. This may not be realistic in an actual operational environment in which the stations may stop producing valid observations over certain time intervals. The OD design analysis reveals that breaking the continuous coverage by removing stations from the tracking network can lead to OD accuracy losses of up to one order of magnitude. Therefore, I recommend analyzing the impact of the frequency and duration of data gaps on the OD accuracy.

2. **Analyze the potential improvement in the accuracy of the OD solution derived from adding new sources of tracking data.** Advanced stages of the lunar navigation programs propose lunar stations or satellites in LLO as means of improving the OD of the navigation satellites. These new elements would provide more geometrically diverse tracking observations, which are beneficial for the OD. This thesis identifies a factor of 4 difference in OD accuracy when tracking lunar orbits in edge-on versus face-on using ground stations on Earth, and hypothesizes that the very limited observability of the lunar orbits from Earth is responsible for this difference. Adding lunar sources of tracking observations to the study would allow testing this hypothesis and evaluating the magnitude of the potential accuracy improvement.

3. **Characterize the possible time dependence of the OD system's performance over different time scales.** This thesis considers a single reference epoch along the entire design analysis. Changing the reference epoch affects the relative position of the celestial bodies involved in the problem. The design analysis partially assesses the effect of the lunar orbit around the Earth and identifies a significant dependence of the OD performance on this motion. Apart from this, the change in epoch also impacts the atmospheric delays on the tracking signal through variations in solar activity and meteorological data. Including monthly and yearly variations of the reference epoch in the analysis can help assess the influence of these factors on the OD accuracy and characterize the system's performance on longer time scales.

4. **Include the effect of the navigation message fit to the estimated ephemerides in the computation of the OD errors.** The OD errors assessed in this thesis only include the difference between the estimated and the true satellite ephemerides. Nevertheless, the navigation message conveyed to the users is not an exact representation of the estimated ephemerides, leading to an additional error component. Accounting for the error in the navigation message fit would allow evaluating the OD accuracy using the broadcast ephemerides instead of the estimated ephemerides—which is more useful as the broadcast ephemerides are the ones employed by the navigation user. Thus, it becomes relevant to produce better estimates of the user positioning accuracy. The consideration of this message fit error relies on the prior design of the navigation message for the LNSs.

5. **Update the design of the OD system as more new information about the system becomes available.** The results of this thesis show large differences in the recommended specifications for the OD system depending on the orbit configuration of the satellites and the noise of the tracking observations. Therefore, to find the system specifications that apply to the future LNSs, it is key to update the design reported in this thesis with the final orbit configuration that will be used to instantiate the system and with more specific estimates of the expected tracking noise levels.

References

[1] "Moonlight Programme," ESA, 2022.

[2] "The Global Exploration Roadmap," ISECG, 2018. [Online]. Available: www.globalspaceexploration.org.

[3] "NASA's Lunar Exploration Program Overview," NASA, 2020. [Online]. Available: https://www.nasa.gov/specials/artemis/index.html.

[4] "Argonaut." (2022), [Online]. Available: https://www.esa.int/Science_Exploration/Human_and_Robotic_Exploration/Exploration/Argonaut (visited on 12/22/2023).

[5] N. Schörghofer and R. Rufu, "Past extent of lunar permanently shadowed areas," *Science Advances*, vol. 9, 37 2023. DOI: 10.1126/sciadv.adh4302.

[6] S. Li, P. G. Lucey, R. E. Milliken, *et al.*, "Direct evidence of surface exposed water ice in the lunar polar regions," *Proceedings of the National Academy of Sciences of the United States of America*, vol. 115, pp. 8907–8912, 36 Sep. 2018, ISSN: 10916490. DOI: 10.1073/pnas.1802345115.

[7] P. O. Hayne, A. Hendrix, E. Sefton-Nash, *et al.*, "Evidence for exposed water ice in the Moon's south polar regions from Lunar Reconnaissance Orbiter ultraviolet albedo and temperature measurements," *Icarus*, vol. 255, pp. 58–69, Jul. 2015, ISSN: 10902643. DOI: 10.1016/j.icarus.2015.03.032.

[8] M. Anand, I. A. Crawford, M. Balat-Pichelin, *et al.*, "A brief review of chemical and mineralogical resources on the Moon and likely initial in situ resource utilization (ISRU) applications," *Planetary and Space Science*, vol. 74, pp. 42–48, 1 2012, ISSN: 00320633. DOI: 10.1016/j.pss.2012.08.012.

[9] E. M. Mazarico, G. A. Neumann, D. E. Smith, M. T. Zuber, and M. H. Torrence, "Illumination conditions of the lunar polar regions using LOLA topography," *Icarus*, vol. 211, pp. 1066–1081, 2 2011.

[10] "Gateway." (2024), [Online]. Available: https://www.esa.int/Science_Exploration/Human_and_Robotic_Exploration/Exploration/Gateway (visited on 01/20/2024).

[11] "NASA's Gateway Program." (2024), [Online]. Available: https://www.nasa.gov/reference/nasas-gateway-program/ (visited on 01/20/2024).

[12] *Global Exploration Roadmap Critical Technology Needs*, 2019. [Online]. Available: https://www.globalspaceexploration.org/wp-content/uploads/2019/12/2019_GER_Technologies_Portfolio_ver.IR-2019.12.13.pdf.

[13] M. Murata, M. Koga, Y. Nakajima, *et al.*, "Lunar Navigation Satellite System: Mission, System Overview, and Demonstration," in *Proc. 39th International Communications Satellite Systems Conference*, Oct. 2022.

[14] "Lunar Surface Navigation System." (2022), [Online]. Available: https://technology.nasa.gov/patent/LAR-TOPS-361 (visited on 01/10/2024).

[15] D. J. Grebow, "Generating Periodic Orbits in the Circular Restricted Three-Body Problem with Applications to Lunar South Pole Coverage," M.S. thesis, Purdue University, 2006.

[16] R. W. Farquhar, "Lunar communications with libration-point satellites," *Journal of Spacecraft and Rockets*, vol. 4, pp. 1383–1384, 10 1967, ISSN: 00224650. DOI: 10.2514/3.29095.

[17] T. A. Ely, "Stable Constellations of Frozen Elliptical Inclined Lunar Orbits," *Journal of Astronautical Sciences*, vol. 53, pp. 301–316, 3 2005.

[18] J. S. Schier, J. J. Rush, W. D. Williams, and P. Vrotsos, "Space Communication Architecture Supporting Exploration and Science: Plans and Studies for 2010-2030," in *Proc. 1st Space Exploration Conference: Continuing the Voyage of Discovery*, 2005.

[19] D. Guzzetti, E. M. Zimovan, K. C. Howell, and D. C. Davis, "Stationkeeping Analysis for Spacecraft in Lunar Near Rectilinear Halo Orbits," in *Proc. 27th AAS/AIAA Space Flight Mechanics Meeting*, 2017, pp. 3199–3218.

[20] M. Schonfeldt, A. Grenier, A. Delepaut, *et al.*, "A system study about a lunar navigation satellite transmitter system," in *Proc. 2020 European Navigation Conference, ENC 2020*, Institute of Electrical and Electronics Engineers Inc., Nov. 2020, ISBN: 9783944976273. DOI: 10.23919/ENC48637.2020.9317521.

[21] E. Strömgren, "Current knowledge of orbits in the three body problem," Copenhaguen Observatory, 1933.

[22] R. A. Broucke and W. G. Melbourne, "Periodic Orbits in the Restricted Three-Body Problem With Earth-Moon Masses," NASA, Tech. Rep., 1968.

[23] R. Whitley and R. Martinez, "Options for Staging Orbits in Cis-Lunar Space," in *Proc. IEEE Annual Aerospace Conference*, vol. 4, 2016.

[24] A. Delépaut, M. Schönfeldt, P. Giordano, *et al.*, "A system study for cislunar radio navigation leveraging the use of realistic Galileo and GPS signals," in *Proc. 32nd International Technical Meeting of the Satellite Division of the Institute of Navigation, ION GNSS+ 2019*, 2019, pp. 1199–1219, ISBN: 0936406232. DOI: 10.33012/2019.17084.

[25] C. Stallo, H. Bookmap, D. Cretoni, *et al.*, *A Roadmap to Future Space Connectivity*. Springer, 2023, pp. 243–270.

[26] W. R. Wollenhaupt, "Apollo orbit determination and navigation," in *Proc. AIAA 8th Aerospace Sciences Meeting*, Jan. 1970. DOI: 10.2514/6.1970-27.

[27] E. Mazarico, G. A. Neumann, M. K. Barker, S. Goossens, D. E. Smith, and M. T. Zuber, "Orbit determination of the Lunar Reconnaissance Orbiter: Status after seven years," *Planetary and Space Science*, vol. 162, pp. 2–19, Nov. 2018, ISSN: 00320633. DOI: 10.1016/j.pss.2017.10.004.

[28] R. B. Langley, P. J. Teunissen, and O. Montenbruck, *Handbook of Global Navigation Satellite Systems*. Springer, 2017, pp. 3–24.

[29] L. Müller, K. Chen, G. Möller, M. Rothacher, B. Soja, and L. Lopez, "Real-time navigation solutions of low-cost off-the-shelf GNSS receivers on board the Astrocast constellation satellites," *Advances in Space Research*, Jan. 2023, ISSN: 18791948. DOI: 10.1016/j.asr.2023.10.001.

[30] A. Piccolo, A. Zin, S. Zago, L. Badano, and L. Marradi, "Navigating in Geostationary Orbit with a GNSS Receiver: A Further Analysis to In-Flight Results," in *Proc. 2023 IEEE 10th International Workshop on Metrology for AeroSpace, MetroAeroSpace 2023 - Proceedings*, Institute of Electrical and Electronics Engineers Inc., 2023, pp. 615–620, ISBN: 9781665456906. DOI: 10.1109/MetroAeroSpace57412.2023.10190030.

[31] E. Mazarico, X. Sun, J. M. Torre, *et al.*, "First two-way laser ranging to a lunar orbiter: infrared observations from the Grasse station to LRO's retro-reflector array," *Earth, Planets and Space*, vol. 72, 1 Dec. 2020, ISSN: 18805981. DOI: 10.1186/s40623-020-01243-w.

[32] C. Stallo, E. E. Zini, D. Cretoni, *et al.*, "Candidate System concepts for a Lunar Satellite Navigation System," in *Proc. NAVITEC 2022*, 2022. [Online]. Available: https://www.researchgate.net/publication/359849815.

[33] F. Kikuchi, Q. Liu, N. Petrova, *et al.*, "Differential Phase Delay Estimation in VRAD Mission of SELENE (KAGUYA)," *2009, Transactions of the Japan Society for Aeronautical and Space Sciences, Space Technology Japan*, 2009.

[34] W. M. Folkner and J. S. Border, "Orbiter-Orbiter and Orbiter-Lander Tracking Using Same-Beam Interferometry," NASA, Tech. Rep., 1992.

[35] O. Montenbruck and P. Steigenberger, *Position, Navigation, and Timing Technologies in the 21st Century: Integrated Satellite Navigation, Sensor Systems and Civil Applications*, 1st ed. John Wiley & Sons, Inc., 2021, vol. 1, pp. 233–258.

[36] Y. Jia, Y. Zou, J. Ping, C. Xue, J. Yan, and Y. Ning, "The scientific objectives and payloads of Chang'E-4 mission," *Planetary and Space Science*, vol. 162, pp. 207–215, Nov. 2018, ISSN: 00320633. DOI: 10.1016/j.pss.2018.02.011.

[37] "Farside Seismic Suite (FSS)." (2024), [Online]. Available: https://www.jpl.nasa.gov/missions/the-farside-seismic-suite (visited on 01/25/2024).

[38] S. Speretta, A. Cervone, P. Sundaramoorthy, *et al.*, *Space Operations: Inspiring Humankind's Future*. Springer International Publishing, Jan. 2019, pp. 103–134, ISBN: 9783030115364. DOI: 10.1007/978-3-030-11536-4.

[39] "ESA, NASA Race to the Moon for First Lunar GNSS Fix." (2021), [Online]. Available: https://insidegnss.com/esa-nasa-race-to-the-moon-for-first-lunar-gnss-fix/ (visited on 01/08/2024).

[40] J. A. Christian, "A Tutorial on Horizon-Based Optical Navigation and Attitude Determination with Space Imaging Systems," *IEEE Access*, vol. 9, pp. 19 819–19 853, 2021, ISSN: 21693536. DOI: 10.1109/ACCESS.2021.3051914.

[41] "LunaNet Interoperability Specification Document," NASA, 2023. [Online]. Available: https://www.nasa.gov/directorates/somd/space-communications-navigation-program/lunanet-interoperability-specification/.

[42] D. J. Israel, J. W. Mitchell, M. A. Johnson, *et al.*, "LunaNet: a Flexible and Extensible Lunar Exploration Communications and Navigation Infrastructure," in *Proc. 2020 IEEE Aerospace Conference*, 2020.

[43] K. Schauer. "LunaNet: Empowering Artemis with Communications and Navigation Interoperability." (2021), [Online]. Available: https://www.nasa.gov/humans-in-space/lunanet-empowering-artemis-with-communications-and-navigation-interoperability/ (visited on 01/25/2024).

[44] C. Gramling, J. Crenshaw, and L. Mann, "Interoperable Services to Mitigate Lunar Position, Navigation, and Timing Challenges," in *Proc. 73rd International Astronautical Congress*, 2022.

[45] "Who's ready to serve the lunar missions?" (2020), [Online]. Available: https://www.esa.int/Applications/Connectivity_and_Secure_Communications/Who_s_ready_to_serve_the_lunar_missions (visited on 01/14/2024).

[46] P. Giordano, A. Grenier, P. Zoccarato, *et al.*, "Moonlight navigation service-how to land on peaks of eternal light," in *Proc. 72nd International Astronautical Congress (IAC)*, 2021, pp. 25–29.

[47] "Lunar Communication Relay and Navigation Systems (LCRNS)." (2024), [Online]. Available: https://tempo.gsfc.nasa.gov/projects/LCRNS (visited on 01/16/2024).

[48] "Satnav from Earth to the Moon." (2023), [Online]. Available: https://www.esa.int/ESA_Multimedia/Images/2023/06/Satnav_from_Earth_to_the_Moon (visited on 01/20/2024).

[49] N. O. Harlé, S. Bywater, C. Cranstoun, *et al.*, "Forward(ing) from the moon – lunar pathfinder data relay satellite, paving the way for communication and navigation constellation," in *Proc. 39th International Communications Satellite Systems Conference (ICSSC 2022)*, 2022, ISBN: 7824804925.

[50] J. Parker, F. Melman, M. Murata, and R. V. Moreno, "Lunar Navigation Services: A Global View from the Next Frontier," in *GoToWebinar*, 2024.

[51] A. Grenier, P. Giordano, L. Bucci, *et al.*, "Positioning and Velocity Performance Levels for a Lunar Lander using a Dedicated Lunar Communication and Navigation System," *Navigation, Journal of the Institute of Navigation*, vol. 69, 2 Jun. 2022, ISSN: 21614296. DOI: 10.33012/navi.513.

[52] C. Stallo, C. D. Lauro, M. Carosi, *et al.*, "Lunar Navigation System ODTS Signal in Space Error Analysis," *Engineering Proceedings*, vol. 54, 1 Dec. 2023. DOI: 10.3390/enc2023-15468.

[53] "Lunar Communications Relay and Navigation Systems (LCRNS) Lunar Relay Services Requirements Document (SRD)." (2022), [Online]. Available: https://ipdtdms.gsfc.nasa.gov/ (visited on 02/05/2024).

[54] A. Delépaut, P. Giordano, J. Ventura-Traveset, *et al.*, "Use of GNSS for lunar missions and plans for lunar in-orbit development," *Advances in Space Research*, vol. 66, pp. 2739–2756, 12 Dec. 2020, ISSN: 18791948. DOI: 10.1016/j.asr.2020.05.018.

[55] P. Blunt, V. Capuano, S. Ghamari, M. Rico, and P.-A. Farine, "Ultra-high sensitivity state-of-the-art receiver for space applications," in *Proc. ESA NAVITEC 2016*, 2016. [Online]. Available: https://www.researchgate.net/publication/315677584.

[56] "The moon – where no satnav has gone before." (2022), [Online]. Available: https://www.esa.int/Applications/Navigation/The_Moon_where_no_satnav_has_gone_before (visited on 01/12/2024).

[57] G. Impresario, G. D'Amore, C. Stallo, L. Ansalone, and A. Tuozzi, "GNSS and GALILEO for Cis-lunar and Moon Navigation," in *Proc. 2018 IEEE 4th International Forum on Research and Technology for Society and Industry (RTSI)*, IEEE, Sep. 2018, ISBN: 9781538662823.

[58] E. A. Mikrin, M. V. Mikhailov, I. V. Orlovskii, S. N. Rozhkov, A. S. Semenov, and I. A. Krasnopol'skii, "Circumlunar Spacecraft Navigation Using the Measurements from Global Navigation Satellite Systems GLONASS, GPS, Galileo and BeiDou," *Gyroscopy and Navigation*, vol. 10, pp. 187–195, 4 Oct. 2019, ISSN: 20751109. DOI: 10.1134/S2075108719040126.

[59] V. Capuano, P. Blunt, C. Botteron, and P. A. Farine, "Orbital filter aiding of a high sensitivity gps receiver for lunar missions," vol. 1, The Institute of Navigation, 2016, pp. 245–262, ISBN: 9781510821613. DOI: 10.33012/2016.13422.

[60] E. A. Mikrin, M. V. Mikhailov, I. V. Orlovskii, S. N. Rozhkov, and I. A. Krasnopol'skii, "Satellite navigation of lunar orbiting spacecraft and objects on the lunar surface," *Gyroscopy and Navigation*, vol. 10, pp. 54–61, 2 Apr. 2019, ISSN: 20751109. DOI: 10.1134/S2075108719020068.

[61] J. R. Carpenter, D. C. Folta, M. C. Moreau, and D. A. Quinn, "Libration Point Navigation Concepts Supporting the Vision for Space Exploration," in *Proc. Astrodynamics Specialist Conference and Exhibit*, Aug. 2004.

[62] D. Romagnoli and C. Circi, "Lissajous trajectories for lunar global positioning and communication systems," *Celestial Mechanics and Dynamical Astronomy*, vol. 107, pp. 409–425, 4 2010, ISSN: 09232958. DOI: 10.1007/s10569-010-9279-1.

[63] Y. Ren and J. Shan, "Libration point orbits for lunar global positioning systems," *Advances in Space Research*, vol. 51, pp. 1065–1079, 7 Apr. 2013, ISSN: 02731177. DOI: 10.1016/j.asr.2012.10.022.

[64] C. Circi, D. Romagnoli, and F. Fumenti, "Halo orbit dynamics and properties for a lunar global positioning system design," *Monthly Notices of the Royal Astronomical Society*, vol. 442, pp. 3511–3527, 4 2014, ISSN: 13652966. DOI: 10.1093/mnras/stu1085.

[65] J. Ware and F. Davarian, "Lunar Communications Services with Emphasis on Commercialization," in *Proc. IEEE Aerospace Conference*, vol. 2022-March, IEEE Computer Society, 2022, ISBN: 9781665437608. DOI: 10.1109/AERO53065.2022.9843705.

[66] L. Capdevila, D. Guzzetti, K. Howell, L. Capdevila, and K. C. Howell, "Various transfer options from Earth into Distant Retrograde Orbits in the vicinity of the Moon," *Advances in Astronautical Sciences*, 2014. [Online]. Available: https://www.researchgate.net/publication/287054622.

[67] S. Bhamidipati, T. Mina, and G. Gao, "A Case Study Analysis for Designing a Lunar Navigation Satellite System with Time Transfer from the Earth GPS," *Navigation, Journal of the Institute of Navigation*, vol. 70, 4 Dec. 2023, ISSN: 21614296. DOI: 10.33012/navi.599.

[68] R. Zhang, Y. Wang, Y. Shi, C. Zhang, and H. Zhang, "Performance analysis of impulsive station-keeping strategies for cis-lunar orbits with the ephemeris model," *Acta Astronautica*, vol. 198, pp. 152–160, Sep. 2022, ISSN: 00945765. DOI: 10.1016/j.actaastro.2022.05.054.

[69] S. K. Singh, R. Woollands, E. Taheri, and J. Junkins, "Feasibility of quasi-frozen, near-polar and extremely low-altitude lunar orbits," *Acta Astronautica*, vol. 166, pp. 450–468, Jan. 2020, ISSN: 00945765. DOI: 10.1016/j.actaastro.2019.10.037.

[70] A. J. Brown, "A Minimum delta-V Orbit Maintenance Strategy for Low-Altitude Missions Using Burn Parameter Optimization," in *Proc. 2011 AAS Astrodynamics Specialist Conference*, 2011.

[71] M. Beckman and R. Lamb, "Stationkeeping for the Lunar Reconnaissance Orbiter (LRO)," in *Proc. 20th International Symposium on Space Flight Dynamics*, 2007.

[72] A. Tselousova, S. Trofimov, and M. Shirobokov, "Station-keeping in high near-circular polar orbits around the moon," *Acta Astronautica*, vol. 188, pp. 185–192, Nov. 2021, ISSN: 00945765. DOI: 10.1016/j.actaastro.2021.07.025.

[73] C. P. Newman, D. C. Davis, R. J. Whitley, J. R. Guinn, and M. S. Ryne, "Stationkeeping, Orbit Determination, and Attitude Control for Spacecraft in Near Rectilinear Halo Orbits," in *Proc. AAS Astrodynamics Specialists Conference*, 2018.

[74] V. Muralidharan, A. Weiss, and U. Kalabić, "Control strategy for long-term station-keeping on near-rectilinear halo orbits," in *Proc. AIAA Scitech 2020 Forum*, vol. 1 PartF, American Institute of Aeronautics and Astronautics Inc, AIAA, 2020, ISBN: 9781624105951. DOI: 10.2514/6.2020-1459.

[75] N. Kumagai and K. Oguri, "Robust NRHO Station-keeping Planning with Maneuver Location Optimization under Operational Uncertainties," in *Proc. AAS/AIAA Astrodynamics Specialist Conference*, 2023. [Online]. Available: https://www.researchgate.net/publication/373238991.

[76] S. Ueda and S.-I. Sakaui, "Low-Energy Lunar Transfer with Specific Landing Conditions," *Transactions of the Japan Society for Aeronautical and Space Sciences, Aerospace Technology Japan*, vol. 19, pp. 334–343, 3 2021. DOI: 10.2322/tastj.19.334.

[77] M. Loucks, K. Post, and J. Carrico, "Lunar Near Rectilinear Orbits And Cis-Lunar Transfer Trajectories In Support Of The Deep Space Proving Ground," in *Proc. 26th AAS / AIAA Space Flight Mechanics Meeting*, 2016. [Online]. Available: https://www.researchgate.net/publication/327050185.

[78] T. Ikenaga, K. Yamanaka, S. Ueda, and N. Ishii, "Study on the low-energy ballistic lunar transfer orbit for future cargo mission to gateway," in *Proc. AIAA Scitech 2020 Forum*, vol. 1 PartF, American Institute of Aeronautics and Astronautics Inc, AIAA, 2020, ISBN: 9781624105951. DOI: 10.2514/6.2020-0794.

[79] T. Gardner, B. Cheetham, J. S. Parker, *et al.*, "CAPSTONE: Mission Updates and Ongoing Efforts at the Moon," in *Proc. ASCEND 2023*, American Institute of Aeronautics and Astronautics (AIAA), Oct. 2023. DOI: 10.2514/6.2023-4611.

[80] C. Stallo, E. E. Zini, C. D. Lauro, *et al.*, "Orbit Determination and Time Transfer in Selenodetic Reference Frames For a Lunar Radio Navigation System," in *Proc. 8th International Colloquium on Scientific and Fundamental Aspects ofGNSS*, 2022. [Online]. Available: https://www.researchgate.net/publication/365892036.

[81] M. D. Benedetto, G. Boscagli, F. D. Marchi, *et al.*, "An architecture for a Lunar Navigation system: Orbit Determination and Time Synchronization," in *Proc. 8th International ESA Colloquium on Scientific and Fundamental Aspects of GNSS*, Editeur officiel, 2022.

[82] J. Ventura-Traveset, "Lunar Pathfinder & Moonlight," in *ICG WG-B Presentation*, 2023.

[83] M. Murata, I. Kawano, and S. Kogure, "Lunar Navigation Satellite System and Positioning Accuracy Evaluation," in *Proc. International Technical Meeting of The Institute of Navigation, ITM*, vol. 2022-January, Institute of Navigation, 2022, pp. 582–586, ISBN: 9780936406305. DOI: 10.33012/2022.18220.

[84] S. Liu, J. Yan, Q. He, J. Cao, M. Ye, and J. P. Barriot, "Precise positioning of Chang'e 3 lander based on Helmert-VCE-aided weighting method using phase delay data from Chinese VLBI Network," *Advances in Space Research*, vol. 66, pp. 1485–1494, 6 Sep. 2020, ISSN: 18791948. DOI: 10.1016/j.asr.2020.05.034.

[85] Z. Xin, L. I. Qing-hui, W. U. Ya-jun, M. A. Jun-wu, and D. E. Tao, "Study on VLBI Differential Delay of Lunar Rendezvous and Docking," *Chinese Astronomy and Astrophysics*, vol. 44, pp. 356–370, 3 Jul. 2020, ISSN: 02751062. DOI: 10.1016/j.chinastron.2020.08.006.

[86] S. Kaplev, M. Titov, T. Valentirova, I. Mozharov, A. Bolkunov, and V. Yaremchuk, "Lunar PNT system concept and simulation results," *Open Astronomy*, vol. 31, pp. 110–117, 1 Jan. 2022, ISSN: 25436376. DOI: 10.1515/astro-2022-0014.

[87] Q. Zhao, C. Wang, J. Guo, *et al.*, "Enhanced orbit determination for BeiDou satellites with FengYun-3C onboard GNSS data," *GPS Solutions*, vol. 21, pp. 1179–1190, 3 Jul. 2017, ISSN: 15211886. DOI: 10.1007/s10291-017-0604-y.

[88] U. Hugentobler and O. Montenbruck, *Handbook of Global Navigation Satellite Systems*. Springer, 2017, pp. 59–90.

[89] E. Mazarico, D. D. Rowlands, G. A. Neumann, *et al.*, "Orbit determination of the Lunar Reconnaissance Orbiter," *Journal of Geodesy*, vol. 86, pp. 193–207, 3 Mar. 2012, ISSN: 09497714. DOI: 10.1007/s00190-011-0509-4.

[90] S. Slojkowski, "Lunar Reconnaissance orbiter Orbit Determination Accuracy Analysis," in *Proc. International Symposium on Space Flight Dynamics*, 2014.

[91] S. Bertone, D. Arnold, V. Girardin, M. Lasser, U. Meyer, and A. Jäggi, "Assessing Reduced-Dynamic Parametrizations for GRAIL Orbit Determination and the Recovery of Independent Lunar Gravity Field Solutions," *Earth and Space Science*, vol. 8, 6 Jun. 2021, ISSN: 23335084. DOI: 10.1029/2020EA001454.

[92] M. T. Zuber, D. E. Smith, M. M. Watkins, *et al.*, "Gravity Field of the Moon from the Gravity Recovery and Interior Laboratory (GRAIL) Mission," *Science*, 2013.

[93] E. G. Fahnestock, R. S. Park, D. N. Yuan, and A. S. Konopliv, "Spacecraft thermal and optical modeling impacts on estimation of The GRAIL lunar gravity field," in *Proc. AIAA/AAS Astrodynamics Specialist Conference 2012*, 2012, ISBN: 9781624101823. DOI: 10.2514/6.2012-4428.

[94] Y. R. Kim, Y. J. Song, J. Bae, and B. Y. Kim, "Influence of the Choice of Lunar Gravity Model on Orbit Determination for Lunar Orbiters," *Mathematical Problems in Engineering*, 2018, ISSN: 15635147. DOI: 10.1155/2018/5145419.

[95] D. Strugarek, K. Sośnica, and A. Jäggi, "Characteristics of GOCE orbits based on Satellite Laser Ranging," *Advances in Space Research*, vol. 63, pp. 417–431, 1 Jan. 2019, ISSN: 18791948. DOI: 10.1016/j.asr.2018.08.033.

[96] "Tropospheric delay." (2011), [Online]. Available: https://gssc.esa.int/navipedia/index.php/Tropospheric_Delay#:~:text=The%20tropospheric%20delay%20depends%20on,the%20dry%20and%20wet%20components..

[97] A. Hauschild, *Handbook of Global Navigation Satellite Systems*. Springer, 2017, pp. 561–582.

[98] "DSN Telecommunications Link Design Handbook: Sequential Ranging," JPL, Tech. Rep., 2019. [Online]. Available: https://deepspace.jpl.nasa.gov/dsndocs/810-005/.

[99] C. Stallo, C. D. Lauro, M. Carosi, *et al.*, "Performance Analysis of Lunar Radio Navigation ODTS System," in *Proc. International Technical Meeting of The Institute of Navigation, ITM*, vol. 1, Institute of Navigation, 2023, pp. 190–203, ISBN: 9781713871378. DOI: 10.33012/2023.18595.

[100] R. B. Roncoli, "Lunar Constants and Models Document," JPL, 2005.

[101] R. S. Park, W. M. Folkner, J. G. Williams, and D. H. Boggs, "The JPL Planetary and Lunar Ephemerides DE440 and DE441," *The Astronomical Journal*, vol. 161, p. 105, 3 Mar. 2021, ISSN: 0004-6256. DOI: 10.3847/1538-3881/abd414.

[102] S. Goossens, T. J. Sabaka, J. B. Nicholas, *et al.*, "High-resolution local gravity model of the south pole of the Moon from GRAIL extended mission data," *Geophysical Research Letters*, vol. 41, pp. 3367–3374, 10 May 2014, ISSN: 19448007. DOI: 10.1002/2014GL060178.

[103] S. Goossens, T. J. Sabaka, M. A. Wieczorek, *et al.*, "High-Resolution Gravity Field Models from GRAIL Data and Implications for Models of the Density Structure of the Moon's Crust," *Journal of Geophysical Research: Planets*, vol. 125, 2 Feb. 2020, ISSN: 21699100. DOI: 10.1029/2019JE006086.

[104] "A Standardized Lunar Coordinate System for the Lunar Reconnaissance Orbiter and Lunar Datasets," NASA, Tech. Rep., 2008.

[105] W. M. Folkner, J. G. Williams, D. H. Boggs, R. S. Park, and P. Kuchynka, "The Planetary and Lunar Ephemerides DE430 and DE431," JPL, Tech. Rep., 2014.

[106] J. G. Williams, D. H. Boggs, and W. M. Folkner, "DE430 Lunar Orbit, Physical Librations, and Surface Coordinates," JPL, Tech. Rep., Jul. 2013.

[107] A. S. Konopliv, R. S. Park, D. N. Yuan, *et al.*, "The JPL lunar gravity field to spherical harmonic degree 660 from the GRAIL Primary Mission," *Journal of Geophysical Research: Planets*, vol. 118, pp. 1415–1434, 7 Jul. 2013, ISSN: 21699100. DOI: 10.1002/jgre.20097.

[108] "Resolution of the XXI General Assembly," IAU, 1991.

[109] "Resolution B3," IAU, 2006.

[110] "IERS Technical Note 36, Conventions," IERS, 2010.

[111] "The International Terrestrial Reference System." (2013), [Online]. Available: https://www.iers.org/IERS/EN/Science/ITRS/ITRS.html (visited on 02/15/2024).

[112] O. Montenbruck and G. Eberhard, *Satellite Orbits: Models, Methods and Applications*. Springer, 2000.

[113] C. Förste, F. Flechtner, R. Schmid, *et al.*, "EIGEN-5C: A new global combined high-resolution GRACE-based gravity field model of the GFZ-GRGS cooperation," in *Proc. General Assembly European Geosciences Union*, 2008, pp. 13–18.

[114] T. D. Moyer, *Formulation for Observed and Computed Values of Deep Space Network Data Types for Navigation*. NASA, 2000.

[115] *GALILEO: European Satellite Navigation System (Space Segment)*. [Online]. Available: https://www.ohb-system.de/files/images/mediathek/downloads/190603_OHB-System_Galileo_FOC-Satellites_2019-05.pdf.

[116] Y. Cao, Z. Wu, L. Bai, and H. Zhang, "Measurement of optical characteristics of solar panels used on satellite," in *Proc. 9th International Symposium on Antennas, Propagation and EM Theory*, 2010, ISBN: 9781424469086.

[117] A. G. Santo, S. C. Lee, and R. E. Gold, "NEAR Spacecraft and Instrumentation," *Journal of the Astronautical Sciences*, vol. 43, pp. 373–397, 4 1995.

[118] L. Li, L. Yuan, L. Wang, R. Zheng, Y. Wu, and X. Wang, "Recent advances in precision measurement & pointing control of spacecraft," *Chinese Journal of Aeronautics*, vol. 34, pp. 191–209, 10 2021.

[119] G. T. Yermoldina, B. T. Suimenbayev, V. K. Sysoev, and Z. B. Suimenbayeva, "Features of space solar power station control system," *Acta Astronautica*, vol. 158, pp. 111–120, 2019.

[120] T. D. Moyer, "Mathematical Formulation of the Double-Precision Orbit Determination Program (DPODP)," JPL, Tech. Rep., 1971.

[121] N. Jakowski, M. M. Hoque, and C. Mayer, "A new global TEC model for estimating transionospheric radio wave propagation errors," *Journal of Geodesy*, vol. 85, pp. 965–974, 12 Dec. 2011, ISSN: 09497714. DOI: 10.1007/s00190-011-0455-1.

[122] J. Saastamoinen, *The Use of Artificial Satellites for Geodesy*. American Geophysical Union, Mar. 1972, vol. 15, pp. 247–251. DOI: 10.1029/gm015p0247.

[123] A. E. Niell, "Global mapping functions for the atmosphere delay at radio wavelengths," *Journal of Geophysical Research: Solid Earth*, vol. 101, pp. 3227–3246, 2 Feb. 1996, ISSN: 21699356. DOI: 10.1029/95jb03048.

[124] J. M. Mitchell, "On the causes of instrumentally observed secular temperature trends," *Journal of Meteorology*, vol. 10, 1953.

[125] D. W. Thompson, J. J. Kennedy, J. M. Wallace, and P. D. Jones, "A large discontinuity in the mid-twentieth century in observed global-mean surface temperature," *Nature*, vol. 453, pp. 646–649, 7195 May 2008, ISSN: 14764687. DOI: 10.1038/nature06982.

[126] *Guide to Instruments and Methods of Observation*. WMO, 2018, vol. 1.

[127] R. S. Ramasamy, V. Krishnamoorthy, R. Manickavasagam, *et al.*, "Estimation of Uncertainty in the Atmospheric Pressure Measurement From the Indian Ocean Moored Buoy Systems," *Marine Technology Society Journal*, vol. 55, 1 2021.

[128] M. Heinonen and M. Keskus, "Uncertainty in humidity measurements," in *EUROMET Workshop P758*, 2006.

[129] Y. Liu, H. Mo, and X. Wang, "Influence Factors and Uncertainty Analysis of Relative Humidity Measured by Psychrometer," *Journal of Physics: Conference Series*, vol. 2500, 1 2023, ISSN: 17426596. DOI: 10.1088/1742-6596/2500/1/012006.

[130] H. Chen, J. Liu, L. Long, Z. Xu, Y. Meng, and H. Zhang, "Lunar far side positioning enabled by a CubeSat system deployed in an Earth-Moon halo orbit Lunar Far Side Positioning enabled by a CubeSat System deployed in an Earth-Moon Halo Orbit," *Advances in Space Research*, vol. 64, 1 2019. DOI: 10.1016/j.asr.2019.03.031Ãŕ.

[131] F. Budnik, T. A. Morley, and R. A. Mackenzie, "ESOC's System for Interplanetary Orbit Determination," in *Proc. 18th International Symposium on Space Flight Dynamics*, 2004.

[132] G. J. Bierman, *Factorization Methods for Discrete Sequential Estimation*. Academic Press, Inc., 1977.

[133] P. R. Bosch, A. Vasconcelos, L. Dubois, L. Jauregui, and J. F. Mallol, "GENEOS - The new ESOC Earth Observation Flight Dynamics Software based on GODOT - Design, Capabilities and Operational Validation," in *Proc. 29th International Symposium on Space Flight Dynamics (ISSFD)*, 2024, pp. 22–26. [Online]. Available: https://www.space-codev.org.

[134] "Orbit data messages: Recommendation for space data system standards," CCSDS, 2023.

[135] S. Bhamidipati, T. Mina, A. Sanchez, and G. Gao, "Satellite Constellation Design for a Lunar Navigation and Communication System," *Navigation, Journal of the Institute of Navigation*, vol. 70, 4 2023, ISSN: 21614296. DOI: 10.33012/navi.613.

[136] ESA. "Estrack: Esa's global ground station network." (2024), [Online]. Available: https://www.esa.int/Enabling_Support/Operations/ESA_Ground_Stations/Estrack_ESA_s_global_ground_station_network (visited on 03/20/2024).

[137] T.-H. You, P. Antreasian, S. Broschart, *et al.*, "Gravity Recovery and Interior Laboratory Mission (GRAIL) Orbit Determination," in *Proc. 23rd International Symposium on Space Flight Dynamics*, 2012. [Online]. Available: https://www.researchgate.net/publication/265727708.

[138] E. Lee, Y. Kim, M. Kim, and S.-Y. Park, "Development, demonstration and validation of the deep space orbit determination software using lunar prospector tracking data," *Journal of Astronomy and Space Sciences*, vol. 34, pp. 213–223, 3 2017, ISSN: 20931409. DOI: 10.5140/JASS.2017.34.3.213.

[139] S. Liu, J. Yan, J. Cao, *et al.*, "Review of the Precise Orbit Determination for Chinese Lunar Exploration Projects," *Earth and Space Science*, vol. 8, 4 Apr. 2021, ISSN: 23335084. DOI: 10.1029/2020EA001361.

A

Research plan

Figure A.1 represents the task division of this thesis, together with the time allocated to each task. The first step of the thesis is the literature study, which consists in collecting the ideas and information on the topic of LNSs which form the background knowledge of the thesis. This task is assigned approximately two months of work, due to the great effort involved in searching for information about the broad variety of topics involved in the thesis, and extracting the relevant pieces of information from each source. The literature study also includes the formulation of the research questions to be answered in the thesis. The product of the literature study are Chapters 1 to 3.

The next task is to implement the OD simulation capabilities based on the already existing functionality in GODOT/GENEOS. This is divided into three main functionalities that correspond to each of the fundamental elements of the OD simulation: propagating orbits, simulating observations, and estimating parameters. The implementation of each of these parts depends on the implementation of the previous one. Thus, Figure A.1 shows that they are allocated sequentially. The progressive development of the simulation tool, along with the information gathered during the literature study, exposes the entire list of parameters involved in the OD process. Having identified all parameters, a reduced list must be derived with the parameters to include in the design analysis of the OD system. The parameters of the estimation algorithm having a purely mathematical meaning—the weights of the observations and the weights of the estimated parameters, among others—are left out of the design analysis, as their values do not have any physical implications in the problem and are dependent on the estimation algorithm itself and its implementation.

The implementation of the simulator also exhibits the available and missing functionalities in the GODOT and GENEOS libraries. This results in the need for modifications and implementations to cover all the capabilities required for the design analysis of the OD system.

Once the full capabilities are available, the validation and verification of the simulator are performed to increase the confidence on the results. The validation of OD capabilities of the simulator is to be done by comparing against orbit data of past lunar missions like LRO or GRAIL. The values of certain parameters involved in

representing the reality, together with some other parameters of the estimation algorithm, are fixed through a sensitivity analysis. The values coming from the sensitivity analysis can be different from those used in the verification and validation. Thus, these tasks must be performed simultaneously to make retroactive adjustments as they progress, as allocated in Figure A.1.

All previous tasks serve to prepare the final OD design analysis. This analysis stage involves the computation of the results, their interpretation and, lastly, the production of the written report for the thesis. These 3 tasks are the longest of the thesis, as observed in Figure A.1, as they aim to fulfill the objective of the thesis, which is answering the research questions.

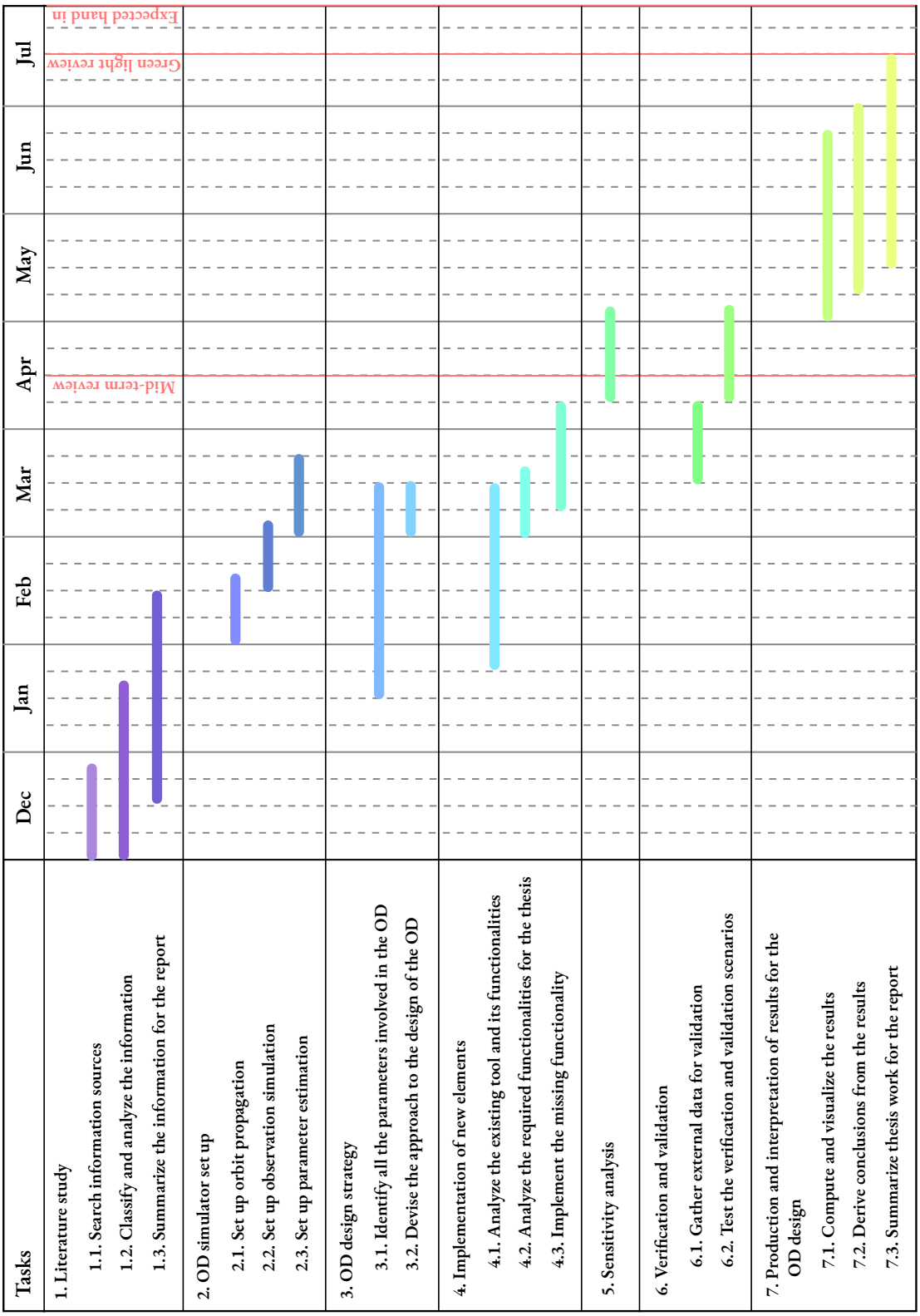

Figure A.1: Gantt diagram to plan the thesis work.

B

Convergence analysis

The objective of this appendix is to evaluate the statistical convergence of the different simulation results reported along this thesis. The need for this type of analysis arises from the use of multiple random runs, each with a different initialization of the RNGs involved in the simulation, to estimate the values of certain FoMs. This convergence analysis aims to ensure that the reported results are statistically meaningful, attending to the purpose they serve.

The approach to study the convergence is the same for all groups of results. An initial number of random runs is considered for every OD case, which is selected to be $N_{\text{runs}} = 30$ based on some initial tests. From this, the $\overline{\text{RMSE}}_{\text{pos}}$[1] can be estimated using an increasing number of simulation results from the available runs to evaluate the variation incurred by using more runs. To do this, the following auxiliary FoM is defined:

$$\overline{\text{RMSE}}_{\text{pos}}^{(l,m)} = \sqrt{\frac{1}{m-l}\sum_{i=l}^{m}\left(\overline{\text{RMSE}}_{\text{pos}}^{(i)}\right)^2}, \quad \text{with } m > l. \tag{B.1}$$

This auxiliary FoM represents the estimated value of $\overline{\text{RMSE}}_{\text{pos}}$ using the random runs from number l to number m. The convergence analysis evaluates this new FoM using $l = 1$ and $m = N_{\text{runs}} - N$ and computes the relative difference of the obtained values with respect to that of using $l = 1$ and $m = N_{\text{runs}}$. The relative difference corresponding to any arbitrary N is computed as

$$\Delta\overline{\text{RMSE}}_{\text{pos}}^{(N_{\text{runs}},N)} = \frac{\left|\overline{\text{RMSE}}_{\text{pos}}^{(1,N_{\text{runs}})} - \overline{\text{RMSE}}_{\text{pos}}^{(1,N_{\text{runs}}-N)}\right|}{\overline{\text{RMSE}}_{\text{pos}}^{(1,N_{\text{runs}})}}. \tag{B.2}$$

To assume the convergence of the result, the maximum relative difference using $N = \{1, \ldots, 5\}$ must not exceed a certain threshold. The value of the threshold depends on the purpose of the analyzed result. Those results whose objective is to identify trends in the behavior of the OD of the LNS consider a less strict threshold than the final values of the recommended OD system specifications. Lastly, in case that the initial value of $N_{\text{runs}} = 30$ is

[1] This explanation also applies to RMSE_{pos} for the pieces of results involving a single satellite.

insufficient to achieve the imposed threshold, a new batch of random runs is computed, repeating the procedure until reaching a satisfactory number of runs.

It must be remarked that the convergence analysis solely attends to the values of $\overline{\text{RMSE}}_{\text{pos}}$, as it is the principal FoM of the problem on which the requirement is imposed. However, due to the relation between the OD accuracy and the user positioning error, the presented convergence analysis also provides confidence in the significance of the $\Delta r_{\text{r,RMS}}$ results where applicable.

B.1. Verification

The verification results reported in Chapter 5 serve to test the proper behavior of the simulation tool under different simulation conditions. Thus, it is important to have relatively high confidence in the results obtained. However, the verification considers several cases in which the value of $\overline{\text{RMSE}}_{\text{pos}}$ should ideally be 0 (for example, the estimation with ideal observations). The obtained estimation of the FoM is not 0, but has millimetric or submillimetric values due to the numerical considerations. For these cases, using a different number of random seeds may lead to a very small difference in absolute terms, which still translates into a relatively large relative difference. This can be not only a matter of statistical convergence, but of the mentioned numerical limitations as well. Therefore, two different thresholds are considered. The cases with ideal observations, observation biases (estimated) and transponder delay (estimated) use a value of 20%. The rest of the cases use a value of 5%.

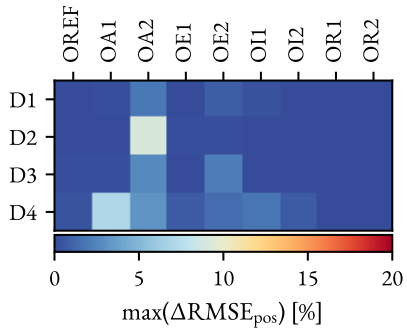

Figure B.1: Convergence results of the verification simulations with ideal observations for $N_{\text{runs}} = 30$.

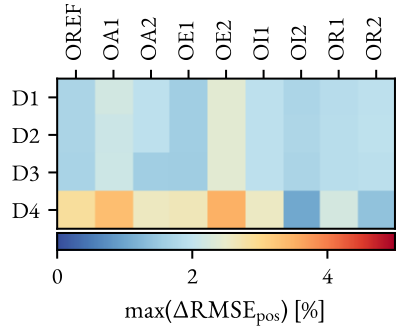

Figure B.2: Convergence results of the verification simulations with observations affected by noise for $N_{\text{runs}} = 45$.

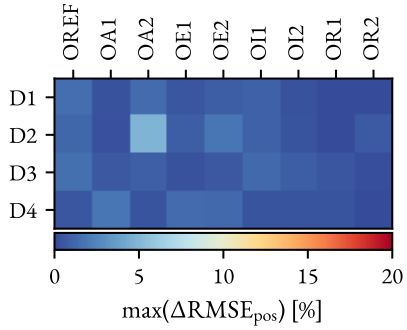

Figure B.3: Convergence results of the verification simulations with biased observations for $N_{\text{runs}} = 30$, estimating biases.

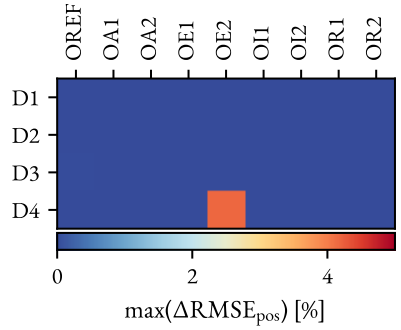

Figure B.4: Convergence results of the verification simulations with biased observations for $N_{\text{runs}} = 30$, without estimating biases.

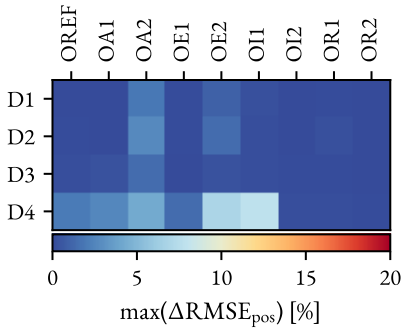

Figure B.5: Convergence results of the verification simulations with observations affected by transponder delay for $N_{\text{runs}} = 30$, estimating the transponder delay.

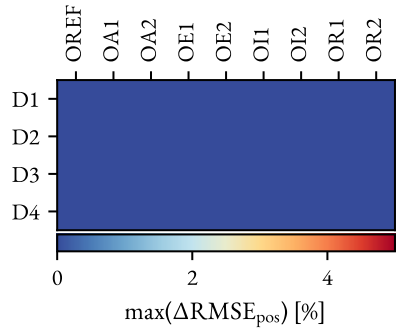

Figure B.6: Convergence results of the verification simulations with observations affected by transponder delay for $N_{\text{runs}} = 30$, without estimating the transponder delay.

Figures B.1 to B.6 show the maximum relative difference computed with $N \leq 5$ for all the simulation results. Those groups of results that do not converge with the initial $N_{\text{runs}} = 30$ consider new batches of 5 random runs until reaching convergence. It is observed that different groups require distinct numbers of runs to converge.

B.2. Sensitivity analysis

Chapter 6 discusses the selection of the outlier and convergence thresholds for the estimation algorithm by testing a range of values of these two parameters. It is relevant to ensure that the results of this analysis are precise enough to confidently select the values of these estimation parameters for later simulations. Nevertheless, it is not necessary to obtain remarkable precise results, as it would increase the computational cost of the analysis. Therefore, the threshold for convergence is set at 5%. Figure B.7 shows that $N_{\text{runs}} = 30$ is enough to achieve a convergence of the results below the established threshold.

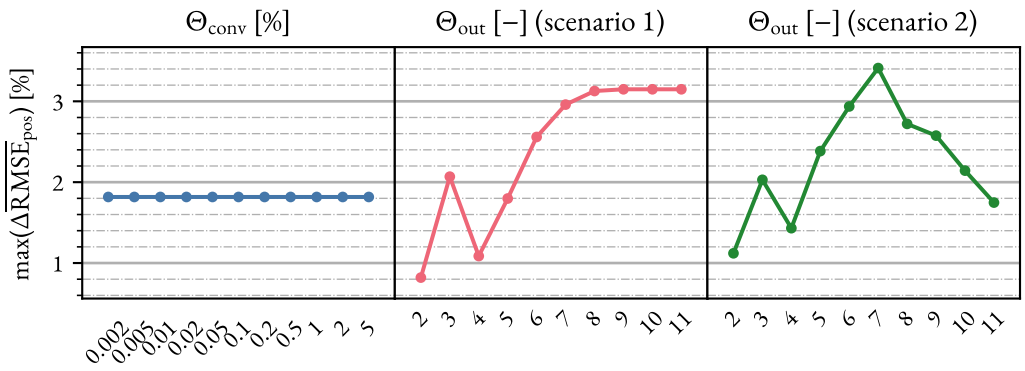

Figure B.7: Convergence results of the sensitivity analysis to the estimation convergence and outlier thresholds for $N_{\text{runs}} = 30$.

B.3. Design analysis

B.3.1. Preliminary analysis

The preliminary analysis reported in § 7.2 examines the relation between the FoMs and the many problem parameters, with the objective of identifying the most influential parameters on the system's performance. To achieve this purpose, the results analyzed must be precise enough to derive strong conclusions that can be useful for the later phase of the analysis, as well as to produce the final recommendation for the OD system specifications. For that reason, a threshold of 5% seems suitable for this group of results.

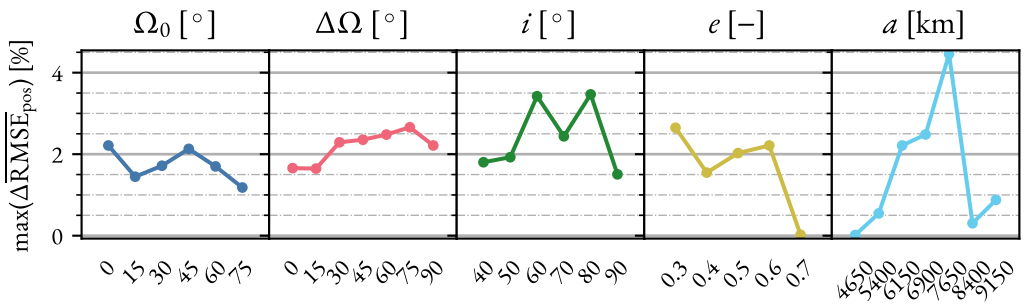

Figure B.8: Convergence results of the preliminary design analysis of the orbit configuration parameters for $N_{\mathrm{runs}} = 30$.

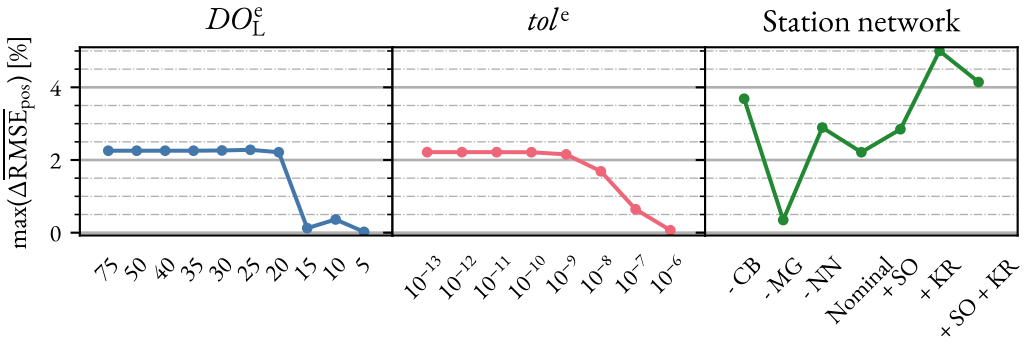

Figure B.9: Convergence results of the preliminary design analysis of the propagation parameters and station network for $N_{\mathrm{runs}} = 30$.

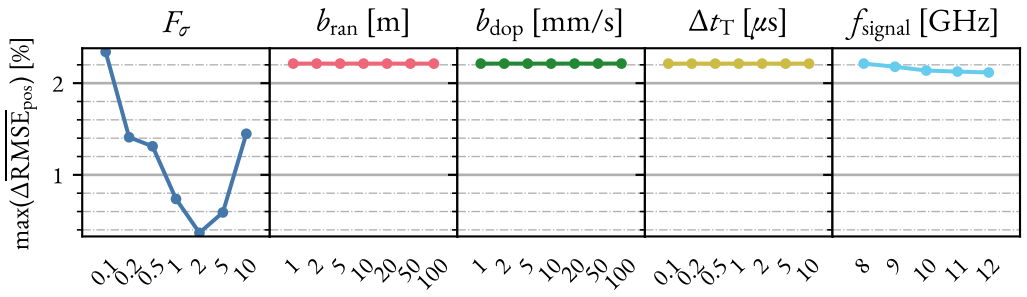

Figure B.10: Convergence results of the preliminary design analysis of the observation properties for $N_{\mathrm{runs}} = 30$ (except F_σ, which uses $N_{\mathrm{runs}} = 35$).

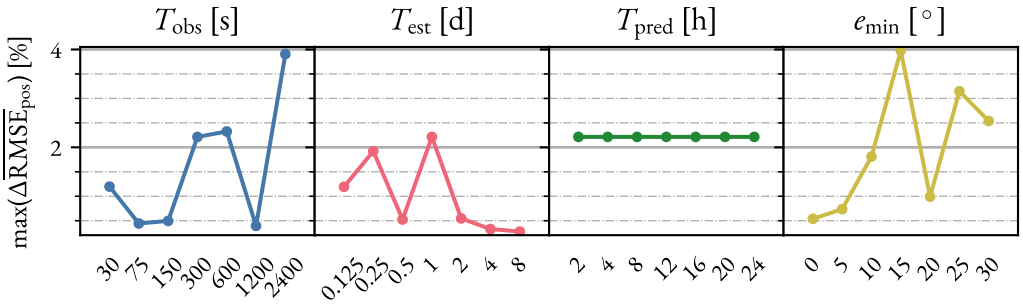

Figure B.11: Convergence results of the preliminary design analysis of the tracking properties for $N_{runs} = 30$ (except e_{min}, which uses $N_{runs} = 35$).

The maximum relative difference values for each of the parameter variations are displayed in Figures B.8 to B.11. The parameters for which using the base value of N_{runs} is not enough, consider 5 more runs. That increment is sufficient to satisfy the threshold.

B.3.2. Monte Carlo (MC) sampling

To sample the design space for each of the cases analyzed in § 7.3, the number of points must be high enough to cover uniformly enough the entire space. Because of this, the space is sampled using 500 points. Each random run for the 500 sample points of each of the 6 scenarios already involves a great computational cost. Because of this, the number of random runs associated to each of these points is limited to 30, without performing any convergence check. The sampling of the design space serves to examine the overall trends of the FoMs throughout the space and to compute an approximation of the requirement isosurface to help find the recommended design point. To meet these purposes, a strict convergence is not deemed critical.

Figures B.12 to B.17 show the maximum relative difference using $N \leq 5$ for the 6 cases of the final parameter design analysis. For every case, almost all, if not all, sample points achieve a maximum relative difference below the 5% level considered for results in other contexts. Thus, it is assumed that the statistical convergence of the MC samples is good enough to adequately display the trends of the FoMs in the design space and to compute a representative requirement isosurface.

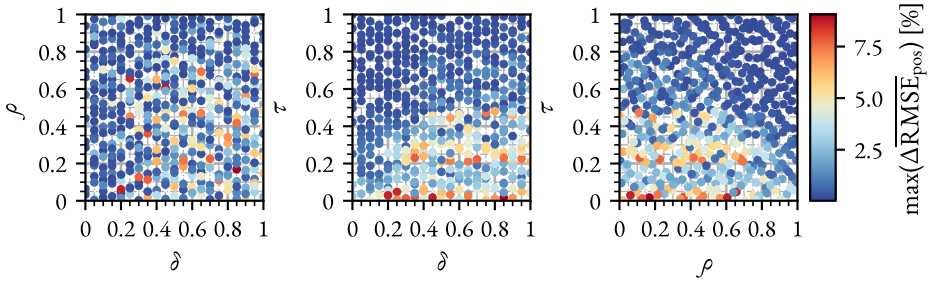

Figure B.12: Convergence results of the sampled design space of case A1 for $N_{runs} = 30$.

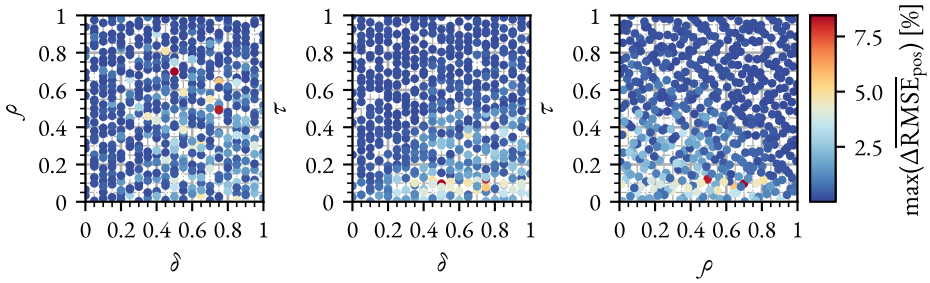

Figure B.13: Convergence results of the sampled design space of case A2 for $N_{\text{runs}} = 30$.

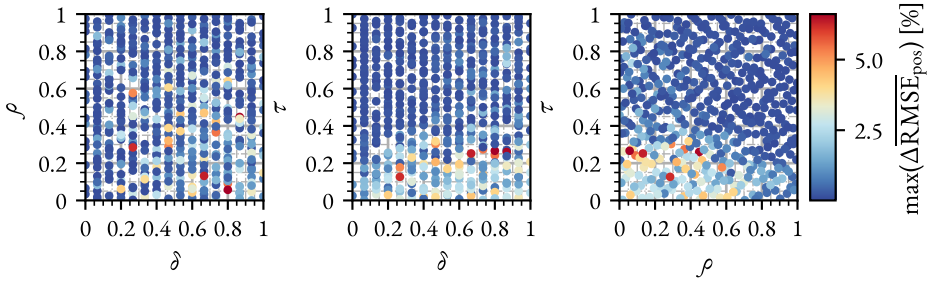

Figure B.14: Convergence results of the sampled design space of case B1 for $N_{\text{runs}} = 30$.

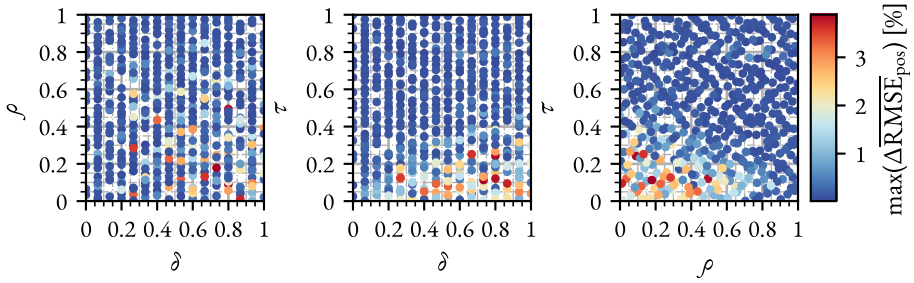

Figure B.15: Convergence results of the sampled design space of case B2 for $N_{\text{runs}} = 30$.

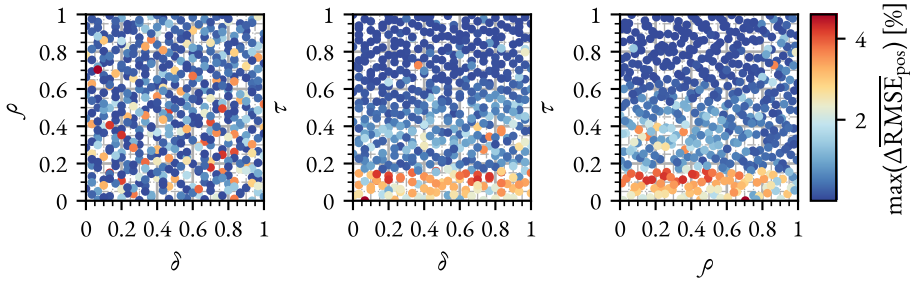

Figure B.16: Convergence results of the sampled design space of case C1 for $N_{\text{runs}} = 30$.

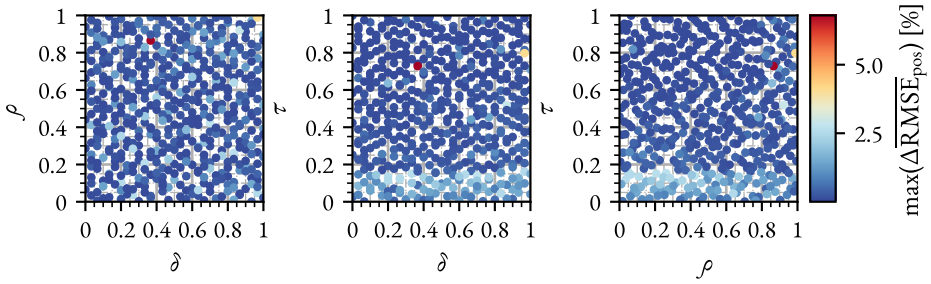

Figure B.17: Convergence results of the sampled design space of case C2 for $N_{\text{runs}} = 30$.

B.3.3. Recommended design points

The recommended design points constitute the central results of this thesis. Therefore, accuracy in their computation is most critical. The chosen convergence threshold for these results is set to 2%. As the $\overline{\text{RMSE}}_{\text{pos}}$ of all recommended points is analyzed over different prediction arc lengths, the convergence of each case considers the maximum $\Delta\overline{\text{RMSE}}_{\text{pos}}$ with $N \leq 5$ among all studied values of T_{pred}. Table B.1 contains the relative differences obtained for all 6 cases. The required number of runs to reach the set convergence threshold varies notably between cases, with some cases requiring 15 more runs than others.

Table B.1: Convergence results (in terms of $\max(\Delta\overline{\text{RMSE}}_{\text{pos}})$) of the recommended design parameter values for the 6 analyzed cases at different prediction arc lengths. The value of N_{runs} for each case is specified in parentheses.

	A1 (55)	**A2** (55)	**B1** (50)	**B2** (40)	**C1** (40)	**C2** (45)
$T_{\text{pred}} = 3\,\text{h}$	1.67%	1.38%	1.35%	1.66%	0.67%	2.00%
$T_{\text{pred}} = 6\,\text{h}$	1.77%	1.23%	0.93%	1.31%	1.53%	1.47%
$T_{\text{pred}} = 12\,\text{h}$	1.97%	1.40%	0.72%	0.93%	1.43%	1.22%
$T_{\text{pred}} = 24\,\text{h}$	1.94%	1.38%	1.19%	0.38%	1.37%	0.88%

B.3.4. Analysis of the problem uncertainties

Lastly, a final analysis is done to evaluate the influence of the different sources of uncertainties on the computed OD accuracies. This last stage only has the objective of qualitatively characterizing the response of the accuracy to the uncertainties. Thus, the statistical convergence of the results is not of great importance. All simulated cases use the base value of $N_{\text{runs}} = 30$. Regarding the variations of the three uncertainties in the initial guesses for the estimation algorithm, which are not shown in a plot in § 7.5, all values converge with a maximum relative difference in $\overline{\text{RMSE}}_{\text{pos}}$ below 5%. Figure B.18 exhibits that the maximum relative difference in the results of the ionospheric TEC remains below 5%. The higher values of the uncertainty in the meteorological data show a much worse convergence. Nevertheless, the discussion included in § 7.5 is equally valid regardless of these results. The convergence for cases other than A2 are not included because of their close similarity to Figure B.18.

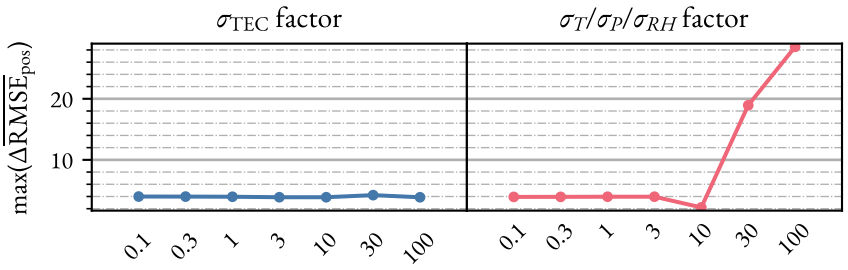

Figure B.18: Convergence results of the influence of the problem uncertainties on the OD accuracy for the case A1 with $N_{\mathrm{runs}} = 30$.

C

Additional figures

This appendix contains those figures that are omitted from Chapter 7. These figures do not add a significant value to the discussion because of their close resemblance to other figures already present in that chapter. However, they are included here for the sake of the completeness of the results.

C.1. Preliminary phase of the OD system design

The preliminary stage of the design analysis discusses the effect that the individual variation of the problem parameters has on the user-related FoMs. Figures C.1 to C.3 show the impact of changing all parameters except those related to the orbit configuration on the user-related FoMs. As the orbits of the satellites are not changing, neither $\mathrm{PDOP}_{\mathrm{RMS}}$ nor ξ change with the variation of these parameters. As a consequence, the values of $\Delta r_{\mathrm{r,RMS}}$ are completely determined by the OD accuracy and, thus, the corresponding curves are similar to those of $\overline{\mathrm{RMSE}}_{\mathrm{pos}}$ in Figures 7.4 to 7.6.

C.2. Parameter design of the OD system

Within the design of the OD system, § 7.3 presents a discussion of the values of the FoMs throughout the design spaces of the 6 defined cases. Figures C.4 to C.9 show that the distribution of values of the FoMs for cases B1 and B2 have very similar trends to those observed and discussed for cases A1 and A2. Something similar happens with Figures C.10 to C.12, which manifest the similarity in the values of the FoMs for case C2 in comparison to C1.

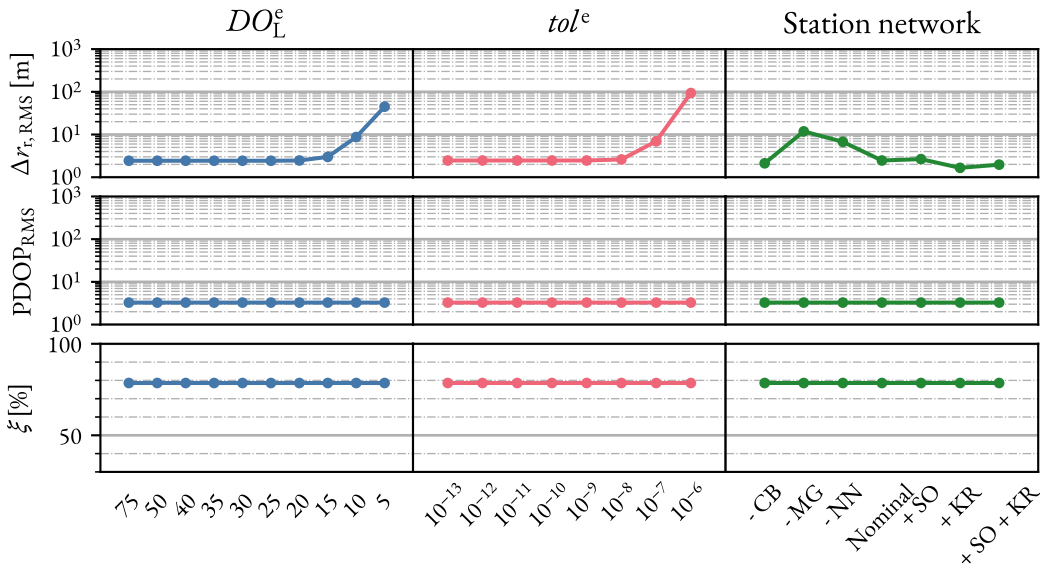

Figure C.1: Influence of the propagation parameters and station network on the user-related FoMs.

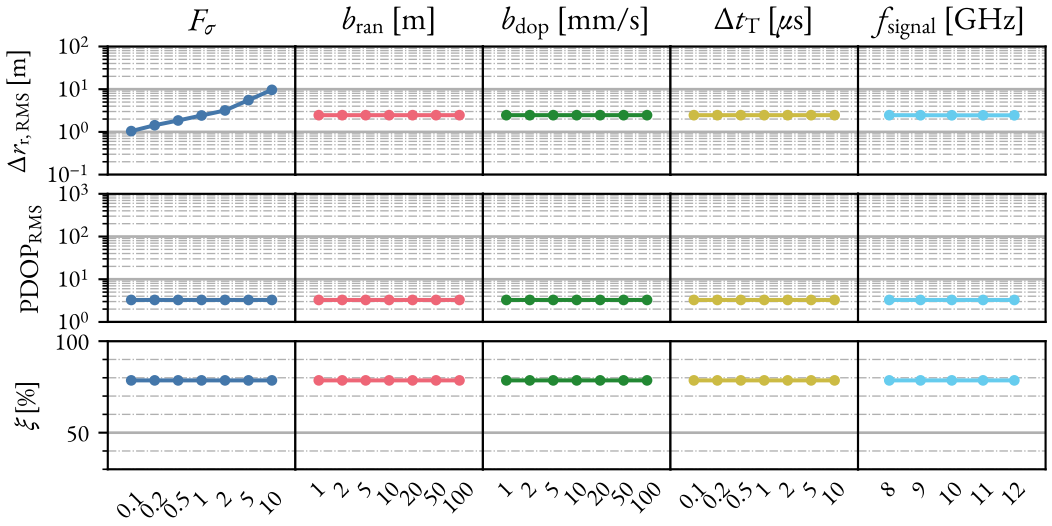

Figure C.2: Influence of the observation properties on the user-related FoMs.

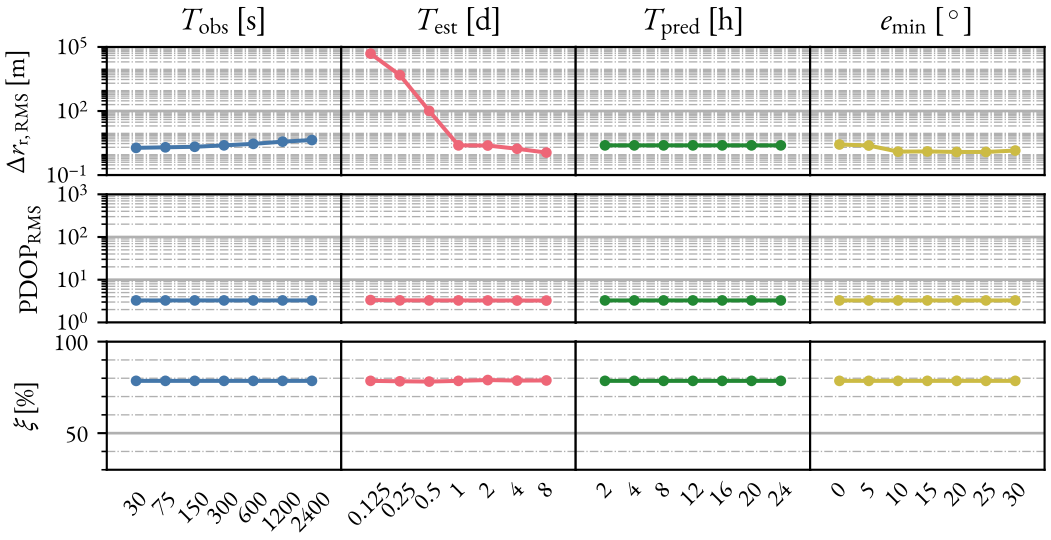

Figure C.3: Influence of the tracking properties on the user-related FoMs.

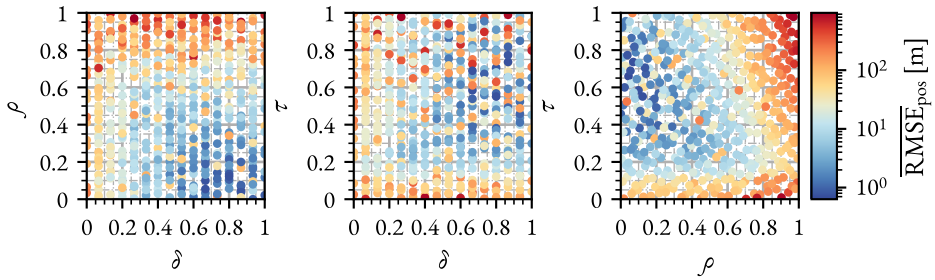

Figure C.4: OD accuracy of the sampled design space using $N_{points} = 500$ for the case B1.

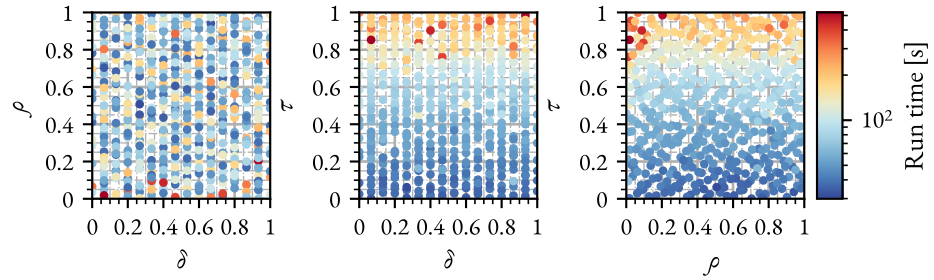

Figure C.5: Run time of the sampled design space using $N_{points} = 500$ for the case B1.

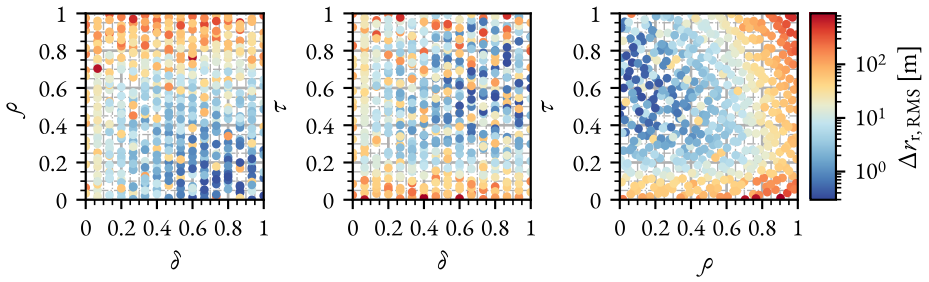

Figure C.6: User positioning error of the sampled design space using $N_{\mathrm{points}} = 500$ for the case B1.

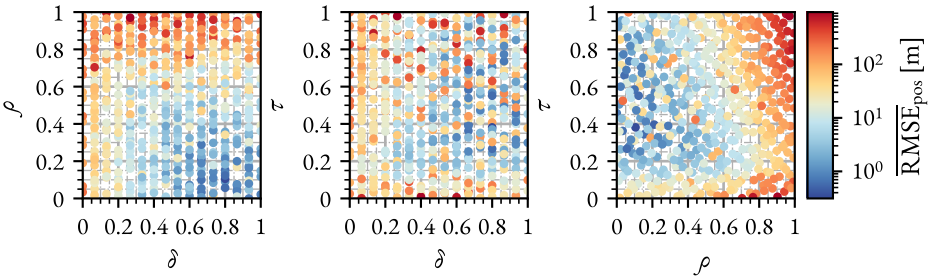

Figure C.7: OD accuracy of the sampled design space using $N_{\mathrm{points}} = 500$ for the case B2.

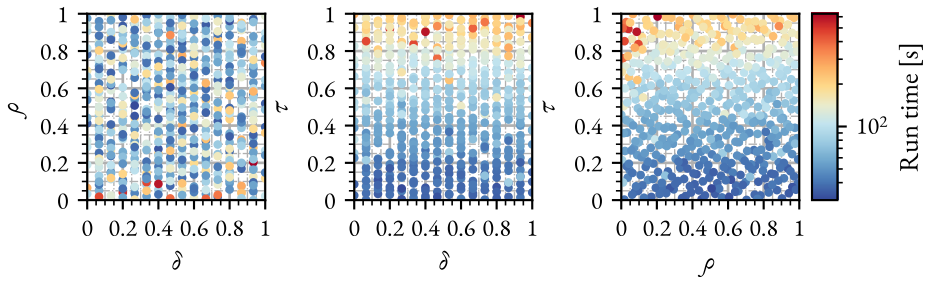

Figure C.8: Run time of the sampled design space using $N_{\mathrm{points}} = 500$ for the case B2.

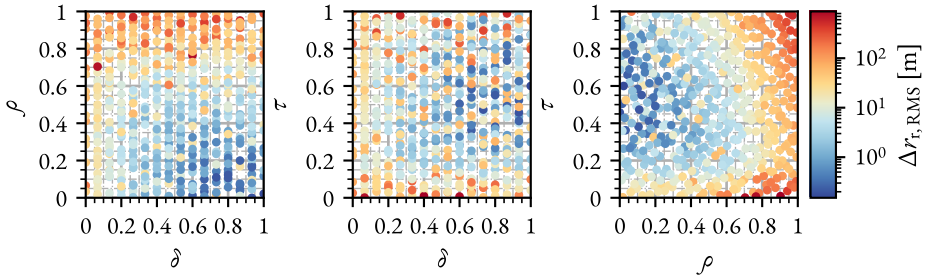

Figure C.9: User positioning error of the sampled design space using $N_{\mathrm{points}} = 500$ for the case B2.

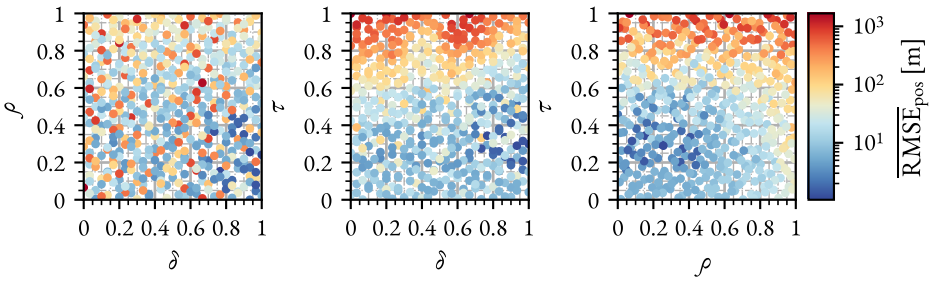

Figure C.10: OD accuracy of the sampled design space using $N_{\mathrm{points}} = 500$ for the case C2.

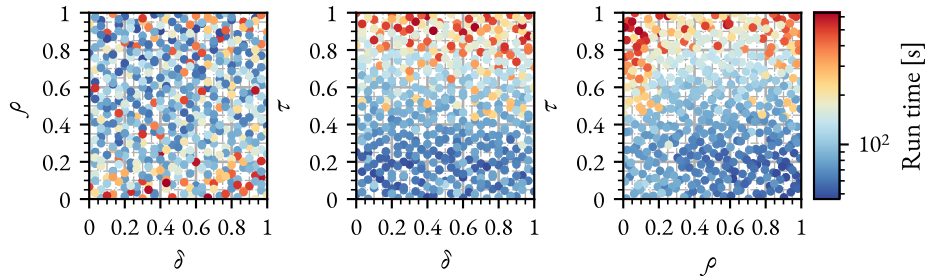

Figure C.11: Run time of the sampled design space using $N_{\mathrm{points}} = 500$ for the case C2.

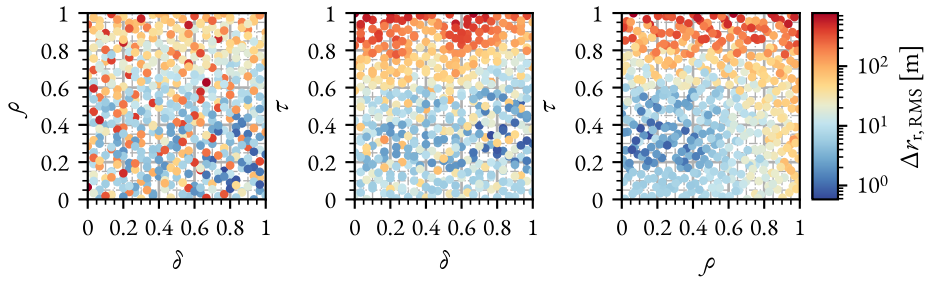

Figure C.12: User positioning error of the sampled design space using $N_{\mathrm{points}} = 500$ for the case C2.

C.3. Influence of uncertainties on the OD system's performance

At the end of the design analysis, § 7.5 reports a study of the impact of the different sources of uncertainty of the problem on the OD accuracy. Although the simulations of the analysis are performed using the recommended OD system specifications of all 6 cases, the discussion uses case A1 as representative of the rest. Figures C.13 to C.17 show the influence of the uncertainty related to the atmospheric components of the observations on the rest of the cases.

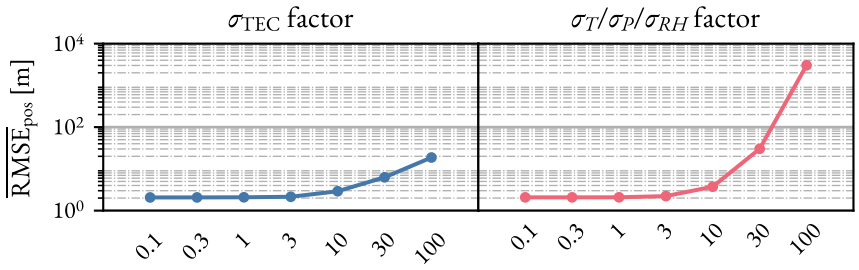

Figure C.13: Influence of the uncertainties affecting the atmospheric models on the OD accuracy of case A2.

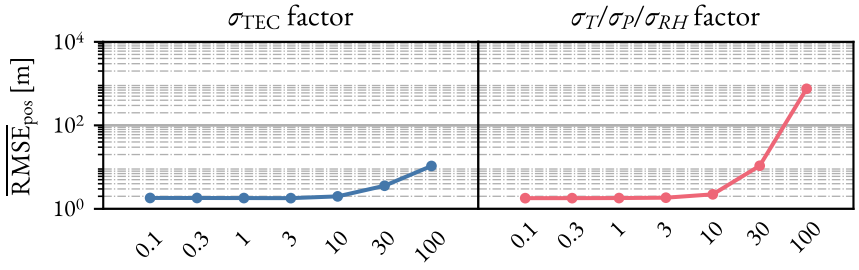

Figure C.14: Influence of the uncertainties affecting the atmospheric models on the OD accuracy of case B1.

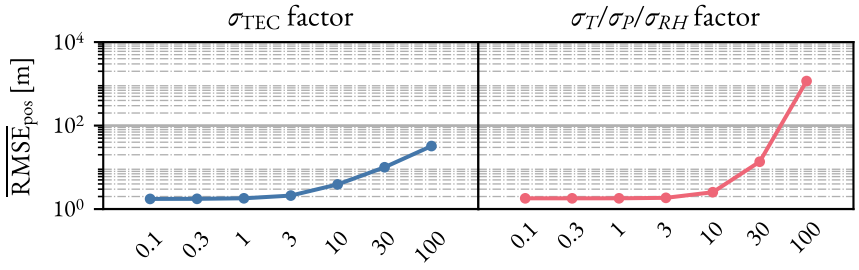

Figure C.15: Influence of the uncertainties affecting the atmospheric models on the OD accuracy of case B2.

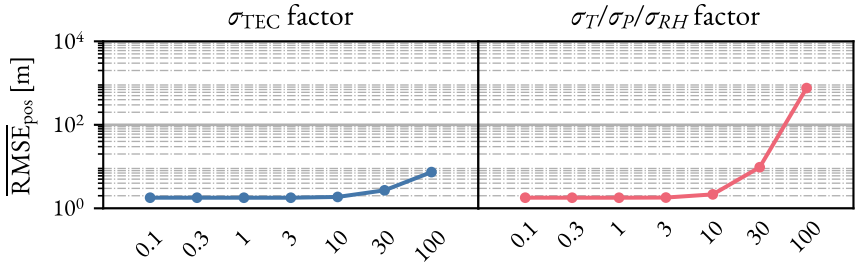

Figure C.16: Influence of the uncertainties affecting the atmospheric models on the OD accuracy of case C1.

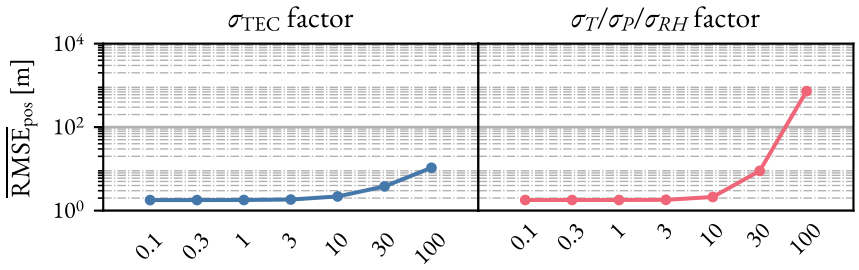

Figure C.17: Influence of the uncertainties affecting the atmospheric models on the OD accuracy of case C2.

D

Influence of the epoch on the OD accuracy

The entirety of the results reported in this thesis assume a certain reference epoch to perform the OD simulations. This chapter aims to evaluate the impact of the reference epoch on the accuracy of the OD. Due to the time constraints of the thesis, this analysis is brief and does not have any impact on the final recommended specification for the OD system of the LNS. Its objective is to examine the variability of the reported results over a broad range of epochs to acquire knowledge about their validity at any arbitrary epoch.

A change in the reference epoch considered for the analysis impacts the relative position and orientation of the celestial bodies, which, in turn, affect the problem in many ways. Among others, the relative relevance of the different gravitational accelerations on the spacecraft changes, as well as the visibility conditions of the satellites from the ground stations (due to the declination of the lunar orbit relative to the Earth's equator). Based on this, it would be expected to possibly encounter certain differences in the OD at monthly and yearly time scales. It must also be noticed that a change in the reference epoch also affects the meteorological and solar activity data used in the computation of the atmospheric components of the observations. The time evolution of the solar activity used for the simulation of the observations is identical to that used during their reconstruction to compute the observation residuals. Thus, this is not expected to introduce observable differences in the results. Regarding the meteorological data, due to the considerable effort involved in the implementation of its dependence on the epoch, the same temperature, pressure, and relative humidity profiles in Figure 4.2 are considered.

The case A1 defined at the end of § 7.2 serves as the test case for this analysis. Figure D.1 shows the impact of changing the reference epoch, t_{ref}, over one lunar orbital period (approximately 28 d, close to one month) and over one terrestrial orbital period (approximately 12 months of 30 d on average). Along these different epochs, the value of $\overline{\text{RMSE}}_{\text{pos}}$ varies within a meter of the value of $\overline{\text{RMSE}}_{\text{pos}} = 1.91$ m reported for case A1 in § 7.3. Despite the change in the reference epoch, involving the motion of the Moon along its orbit, the initial states of the satellites, which are defined with respect to a lunar body-fixed frame, are the same. This means that the

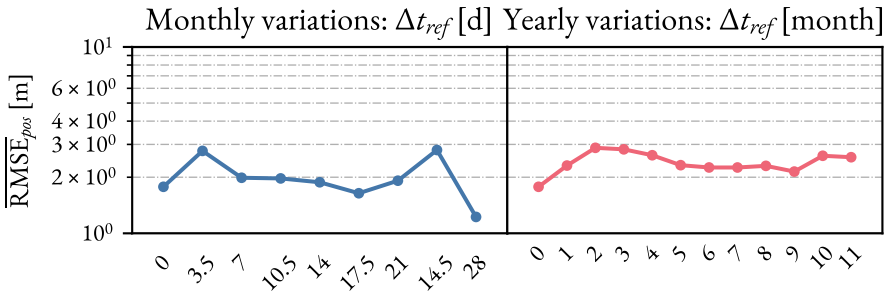

Figure D.1: Changes in the OD performance due to monthly and yearly variation of the reference epoch.

variability observed in Figure D.1 cannot be attributed to a difference in the tracking condition (edge-on or face-on) of the orbits.

It is complicated to assess the implications of these results on the recommended OD specifications from Chapter 7. The recommended specifications derive from assumptions which are conservative, such as using a notably long prediction arc of 24 h and considering the worst tracking condition for the LNS. It is highly likely that these conservative assumptions can compensate for the "long-term variability" of the OD system's performance so that the requirement is still met (or, at least, nearly met).